TECHNISCHE UNIVERSITÄT MÜNCHEN
Physik-Department E62 - Dense and strange hadronic matter

(Strange) Meson Production in Pion-Nucleus Collisions at 1.7 GeV/c

-

Strong Absorption of Hadrons with Hidden and Open Strangeness

Joana Katharina Wirth

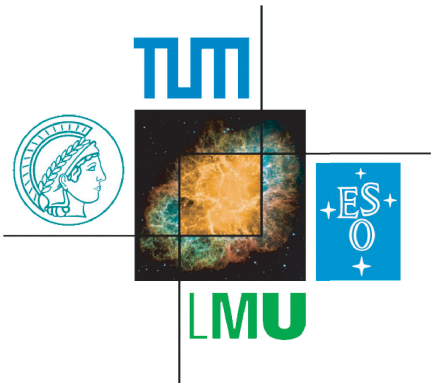

TECHNISCHE UNIVERSITÄT MÜNCHEN
Physik-Department E62 - Dense and strange hadronic matter

(Strange) Meson Production in Pion-Nucleus Collisions at 1.7 GeV/c

-

Strong Absorption of Hadrons with Hidden and Open Strangeness

Joana Katharina Wirth

Vollständiger Abdruck der von der Fakultät für Physik der Technischen Universität München zur Erlangung des akademischen Grades eines

Doktors der Naturwissenschaften (Dr. rer. nat.)

genehmigten Dissertation.

Vorsitzender:		apl. Prof. Dr. Nobert Kaiser
Prüfer der Dissertation:	1.	Prof. Dr. Laura Fabbietti
	2.	Prof. Dr. Peter Fierlinger

Die Dissertation wurde am 04.09.2019 bei der Technischen Universität München eingereicht und durch die Fakultät für Physik am 27.09.2019 angenommen.

Zusammenfassung

Mehrere Experimente haben die Auswirkungen der Kernmaterie auf die Eigenschaften von Hadronen bei Schwerionenkollisionen (HIC) untersucht, bei denen die Baryonendichten ρ_B die normale Kerndichte überschreiten. Solche Effekte werden jedoch bereits in normalen Kerndichten ρ_0 erwartet und können in Hadron-Kern-Reaktionen untersucht werden. Bei diesen ist die Dynamik weniger komplex. Von besonderer Bedeutung ist die Untersuchung der Hadronenwechselwirkungen in der Kernmaterie, da sie der Hauptbestandteil der Zustandsgleichung sind, die dichte Materie oder sogar makroskopische Phänomene wie Neutronensterne und Neutronensternfusion beschreibt. Insbesondere eignen sich Pion-Kern-Reaktionen für die detaillierte Untersuchung von Hadroneneigenschaften in Kernmaterie. Aufgrund des großen inelastischen πN-Wirkungsquerschnitts erfolgt die Hadronenproduktion in der Nähe der Oberfläche des Kerns. Dies führt im Durchschnitt zu einem längeren Weg, der erzeugten Hadronen innerhalb der Kernmaterie. Dazu werden die Produktion und die Eigenschaften von $\pi^{\pm}$, $K^{\pm}$ und ϕ Mesonen in kalter Kernmaterie, die in $\pi^- + \mathrm{C}$ und $\pi^- + \mathrm{W}$ Reaktionen bei einem Impuls des einfallenden Strahls von 1,7 GeV/c erzeugt wird, mit dem HADES-Experiment am SIS18/GSI untersucht.

In dieser Arbeit wird eine umfassende (Doppel-)Differentialanalyse der geladenen Pionproduktion in beiden Kollisionssystemen in zwei verschiedenen zweidimensionalen Observablen ($p_T - y$, $p - \theta$) vorgestellt. So konnten die Rapiditätsverteilungen dN/dy extrahiert werden. Die zeigen starke Streueffekte für beide geladenen Pionen im schwereren Nucleus (W), welche die Verteilung im Vergleich zu dem leichteren Nucleus (C) zur Rückwärtsrapidität verschiebt. Darüber hinaus konnte der integrierte differenzielle inelastische Produktionswirkunsgsquerschnitt ($\Delta\sigma$) für π^+ ($0 \leq y < 1.9(1.8)$) und π^- ($0.1 \leq y < 1.9$) innerhalb der HADES-Akzeptanz abgeleitet werden. Die umfassende experimentelle Messungen der HARP-Kooperation [A$^+$09d] können auf einen geringeren Impuls des einfallenden Pion-Strahls (1,7 GeV/c) ausgedehnt werden. Dabei wurde eine auffällige Abhängigkeit vom Impuls des einfallenden Strahls festgestellt, der für die positiv geladenen Pionen stärker ist. Der Vergleich dreier anerkannter Transportmodelle (GiBUU [BGG$^+$12], UrQMD [B$^+$99b] und SMASH [W$^+$16]) mit den Ergebnissen zeigte jedoch, dass es (derzeit) keine zufriedenstellende theoretische Beschreibung der (doppel-)differentielen Wirkungsquerschnitte der geladenen Pionen in Pion-Kern-Reaktionen gibt. Die präsentierten Ergebnisse können daher als Referenz für Transportmodellberechnungen dienen, welche die Interpretation von Schwerionenkollisionen im geringen GeV-Energiebereich verbessern. Auch im Rahmen astroteilchenphysikalischer Experimente sind geladene Pionenwirkunsquerschnitte ein wichtiger Bestandteil für die Berechnung des atmosphärischen Neutrinoflusses und des Beschleunigerneutrinoflusses.

Die Modifikation des (Anti-)Kaons in der Kernmaterie, die bereits bei endlichen Baryonendichten sichtbar sein sollte, ist von besonderem Interesse. Für beide, K^+ und K^-, werden die (Doppel-)Differentiellenverteilungen in $\pi^- + \mathrm{C}$ und $\pi^- + \mathrm{W}$ Kollisionen für beide zweidimensionalen Observablen, $p_T - y$ und $p - \theta$, extrahiert. Ähnlich wie bei den geladenen Pionen verschiebt die (elastische) Streuung die K^+-Rapiditätsverteilung in Richtung Rückwärtsrapidität im schwereren Nucleus (W). Im Gegensatz dazu sieht die Form der K^--Rapiditätsverteilung für beide nuklearen Umgebungen ähnlich aus. Darüber hinaus konnte der integrierte Produktionswirkungsquerschnitt innerhalb der HADES-Akzeptanz für K^+ ($0 \leq y < 1.1$) und K^- ($0.2 \leq y < 1.0$) in $\pi^- + \mathrm{C}$ und $\pi^- + \mathrm{W}$ Reaktionen gemessen werden. Für das Kaon (K^+, K^0) wurde das repulsive KN-Potenzial mit einer moderaten Stärke ($20 - 40$ MeV) in verschiedenen Experimenten untersucht. Im Vergleich

zu den gleichen Transportmodellberechnungen ist keines in der Lage, die experimentellen K^+-Daten zu beschreiben. Im Gegensatz zu GiBUU enthalten die vorgestellten Versionen von UrQMD und SMASH weder nukleares NN-Potenzial noch nukleares KN-Potenziale. Um Aufschluss über die Existenz das KN-Potenzial zu geben, wäre eine detaillierte Abstimmung der in diesem Modell implementierten elementaren Kaon-Produktionswirkungsquerschnitte erforderlich. Das Verhältnis des inklusiven Kaon-Produktionswirkungsquerschnitts $R(\sigma_A^K/\sigma_C^K)$, der voraussichtlich besonders empfindlich auf die Auswirkungen des KN-Potenzials reagiert, wird mit Vorhersagen aus GiBUU und früheren Messungen verglichen. Eine bessere Übereinstimmung mit GiBUU einschließlich eines mittleren ChPT KN Potenzials konnte beobachtet werden. Andererseits sind für die K^- Absorptionsprozesse (z.B. $K^-N \to Y\pi$) dominierend. Ein direkter Hinweis auf die Absorption ergibt sich aus dem Vergleich des Verhältnisses K^-/K^+, das bei Kollisionen mit dem schweren Nucleus (W) und dem leichteren Nucleus (C) gemessen wird. Das gemessene Doppelverhältnis von $(K^-/K^+)_{\mathrm{W}}/(K^-/K^+)_{\mathrm{C}} = 0{,}319 \pm 0{,}009(\mathrm{stat})^{+0{,}014}_{-0{,}012}(\mathrm{syst})$ liegt weit unter der erwarteten (Anti-)Kaon-Produktionsreferenz basierend auf elementaren πN Reaktionen, was direkt auf eine beträchtliche K^- Absorption in schweren Kernen (W) im Vergleich zu dem leichten Kernen (C) hinweist. Die Vorhersagen für K^- in GiBUU sind vielversprechend, während UrQMD und SMASH nicht in der Lage sind, den K^--Wirkungsquerschnitt in beiden nuklearen Umgebungen gleichzeitig zu reproduzieren. Die starke K^--Absorption in der Kernmaterie hat direkte Auswirkungen auf eine verbesserte Beschreibung von Schwerionenkollisionen und die Zustandsgleichung von Neutronensternen.

Das Verhalten von ϕ-Mesonen in der Kernmaterie ist komplex und wird seit Jahrzehnten diskutiert. Gemäß der OZI-Regel, die Prozesse mit unterbrochenen Quark-Linien behindert, wird erwartet, dass die ϕN-Koppelstärke unterdrückt wird. Andererseits prognostizieren chirale effektive Feldtheorie-Modelle eine wesentliche Modifikation der mittleren Breite, die sich aus der mittleren Modifikation der Kaonschleife und der direkten ϕN-Kopplung ergibt. Auf der Grundlage der integrierten differenzierten ϕ Produktionsquerschnitte ($\Delta\sigma$) innerhalb der HADES-Akzeptanz ($0{,}4 \leq y < 1{,}0$ und $150 \leq p_T < 650$ MeV/c) in beiden Kollisionssystemen wird die ϕ-Absorption im Hinblick auf das Transparenz-Verhältnis diskutiert. Das extrahierte ϕ-Transparenzverhältnis von $T(\sigma^\phi_{\mathrm{W}}/\sigma^\phi_{\mathrm{C}}) = 0{,}18 \pm 0{,}02(\mathrm{stat}) \pm 0{,}01(\mathrm{syst})^{+0{,}04}_{-0{,}03}(\mathrm{norm})$ ist niedriger als in den Messungen von ANKE [P$^+$11] und CLAS [W$^+$10]. Sowohl, die Ergebnisse von ANKE als auch die von CLAS wurden einem effektiven ϕN-Absorptionswirkungsquerschnitt zugeordnet, der größer ist, als der freie. Darüber hinaus wird ein direkter Hinweis auf die Absorption von ϕ-Mesonen in Kernmaterie aus dem Vergleich des Verhältnisses von ϕ/K^- gemessen in Kollisionen mit dem schweren Nucleus (W) und dem leichteren Nucleus (C) gewonnen. Die gemessenen ϕ/K^--Verhältnisse in $\pi^- + \mathrm{C}$ und $\pi^- + \mathrm{W}$ Reaktionen innerhalb der HADES-Akzeptanz sind gleich mit $0{,}55 \pm 0{,}04(\mathrm{stat})^{+0{,}06}_{-0{,}07}(\mathrm{syst})$ und $0{,}63 \pm 0{,}06(\mathrm{stat})^{+0{,}11}_{-0{,}11}(\mathrm{syst})$. Die ähnlichen Verhältnisse, die in den beiden verschiedenen Reaktionen gemessen wurden, deuten auf eine nicht vernachlässigbare Absorption von ϕ-Mesonen hin. Der experimentelle Beweis für die starke Kopplung zwischen der ϕ- und K^--Dynamik innerhalb der Kernmaterie ist relevant, um realistischere Zustandsgleichungen dichter Kernmaterie mit Strangeness-Gehalt, bei Schwerionenkollisionen, aber möglicherweise auch bei Neutronensternen zu liefern. Tatsälich kann das ϕ-Meson als Vermittler von Hyperon-Hyperon-Interaktionen fungieren.

Abstract

Several experiments have investigated the effects of nuclear matter on the properties of hadrons in heavy-ion collisions (HIC) where baryon densities ρ_B exceed the normal nuclear density. However, such effects are already expected at normal nuclear densities ρ_0 and hence they can be investigated in hadron-nucleus reactions where the dynamics are less complex. The study of the hadron interactions in nuclear matter is in particular relevant, since they are the key ingredient of the equation-of-state, which describes dense matter or even macroscopic phenomena like neutron stars and neutron star merger. In particular, pion-nucleus reactions are suitable for the detailed studies of hadrons in-medium properties. Due to the large πN inelastic cross-section, hadron production occurs close to the upstream surface of the nucleus, leading on average to a longer path of the produced hadrons inside nuclear matter. For this purpose, the production and properties of $\pi^{\pm}$, $K^{\pm}$ and ϕ mesons in cold nuclear matter generated in $\pi^- + \mathrm{C}$ and $\pi^- + \mathrm{W}$ reactions at an incident beam momentum of 1.7 GeV/c are investigated with the HADES experiment at SIS18/GSI.

In this work an inclusive (double-)differential analysis of the charged pion production in both collision systems in two sets of kinematic variables ($p_T - y$, $p - \theta$) is presented. Thus, the rapidity density distributions dN/dy could be retrieved, which show strong scattering effects for both charged pions in the heavier target (W) as the distributions are shifted to backward rapidity with respect to the ones in the lighter target (C). In addition, the integrated differential inelastic production cross-section ($\Delta\sigma$) for π^+ ($0 \leq y < 1.9(1.8)$) and π^- ($0.1 \leq y < 1.9$) inside the HADES acceptance could be deduced. The comprehensive experimental campaign performed by the HARP Collaboration [A$^+$09d] could be extended to lower incident pion beam momentum (1.7 GeV/c) and revealed a striking dependence on the incoming beam momentum, which is stronger for the positively charged pions. The comparison to three state-of-the-art transport models (GiBUU [BGG$^+$12], UrQMD [B$^+$99b] and SMASH [W$^+$16]) with the results, however, demonstrated that (currently) there is no satisfactory theoretical description of the (double-)differential charged pion cross-sections in pion-nucleus reactions. Hence, the presented results can serve as a reference for transport model calculations improving the interpretation of heavy-ion collisions in the few GeV energy range. Also in the context of astroparticle physics experiments, charged pion cross-sections are an important ingredient for calculations of the atmospheric neutrino flux and of the accelerator neutrino flux.

The modification of the (anti-)kaon in nuclear matter, which should be already apparent at finite baryon densities, is of particular interest. For both, K^+ and K^-, the (double-)differential distributions are extracted in $\pi^- + \mathrm{C}$ and $\pi^- + \mathrm{W}$ collisions for both sets of kinematic variables, $p_T - y$ and $p - \theta$. Similar to the charged pions, (elastic) scattering shifts the K^+ rapidity density distribution to backward rapidity in the heavier target (W). Contrary, the shape of the K^- rapidity density distributions looks similar for both nuclear environments. Moreover, the integrated production cross-section within the HADES acceptance for K^+ ($0 \leq y < 1.1$) and K^- ($0.2 \leq y < 1.0$) in $\pi^- + \mathrm{C}$ and $\pi^- + \mathrm{W}$ reactions could be measured. For the kaon (K^+, K^0) the repulsive KN potential has been studied in various experiments having a moderate strength ($20-40$ MeV). In the comparison to the same transport model calculations, none is able to describe the experimental K^+ data. In contrast to GiBUU, the presented versions of UrQMD and SMASH contain neither mean-field NN potential nor in-medium KN potentials. To conclude about the KN potential, a detailed tuning of the elementary kaon production cross-sections implemented in these model would be needed. The ratio of the inclusive kaon production cross-section $R(\sigma_A^K/\sigma_C^K)$,

which is expected to be particularly sensitive to the effects of the KN potential, is compared to predictions from GiBUU and earlier measurements. A better agreement with GiBUU including a in-medium ChPT KN potential is observed. On the contrary, for the K^- absorption processes (e.g $K^-N \to Y\pi$) are dominating. A direct indication of absorption is deduced from the comparison of the K^-/K^+ ratio measured in collisions with the heavy target (W) and the lighter target (C). The measured double ratio of $(K^-/K^+)_{\mathrm{W}}/(K^-/K^+)_{\mathrm{C}} = 0.319 \pm 0.009(\mathrm{stat})^{+0.014}_{-0.012}(\mathrm{syst})$ is far below the expected (anti-)kaon production reference based on elementary πN reactions, directly indicating a sizable K^- absorption in heavy nuclei (W) with respect to light nuclei (C). The predictions for K^- in GiBUU are promising, while UrQMD and SMASH are not able to reproduce the K^- cross-section simultaneously in both nuclear environments. The strong K^- absorption within nuclear matter has direct consequences for an improved description of heavy-ion collisions and the equation-of-state of neutron stars.

The behavior of ϕ mesons in nuclear matter is complex and has been debated for decades. According to the OZI rule, which hinders processes with disconnected quark lines, the ϕN coupling strength is expected to be suppressed. On the other hand, chiral effective field theory models predict a substantial modification of the in-medium width, which arise from in-medium modification of kaon loop and direct ϕN coupling. On the basis of the integrated differential ϕ production cross-sections ($\Delta\sigma$) within the HADES acceptance ($0.4 \leq y < 1.0$ and $150 \leq p_T < 650$ MeV/c) in both collisions systems the ϕ absorption is discussed in terms of the transparency ratio. The extracted ϕ transparency ratio of $T(\sigma^{\phi}_{\mathrm{W}}/\sigma^{\phi}_{\mathrm{C}}) = 0.18 \pm 0.02(\mathrm{stat}) \pm 0.01(\mathrm{syst})^{+0.04}_{-0.03}(\mathrm{norm})$ is lower than observed by ANKE [P$^+$11] and CLAS [W$^+$10] measurements. Both, ANKE and CLAS, results have been attributed to an effective ϕN absorption cross-section larger than the free one. In addition, a direct indication of ϕ absorption within nuclear matter is extracted from the comparison of the ϕ/K^- ratio measured in collisions with the heavy target (W) and the lighter target (C). The measured ϕ/K^- ratios in π^- + C and π^- + W reactions within the HADES acceptance are found to be equal to $0.55 \pm 0.04(\mathrm{stat})^{+0.06}_{-0.07}(\mathrm{syst})$ and to $0.63 \pm 0.06(\mathrm{stat})^{+0.11}_{-0.11}(\mathrm{syst})$, respectively. The similar ratios measured in the two different reactions point to a non-negligible ϕ absorption. The experimental evidence of the strong coupling between the ϕ and K^- dynamics within nuclear matter is relevant to provide more realistic equation-of-state of dense nuclear matter with strangeness content, in heavy-ion collisions, but possibly also in neutron stars. Indeed, the ϕ meson can act as mediator of hyperon-hyperon interactions.

Contents

1 Introduction

1.1 The Standard Model of Particle Physics

The Standard Model (SM) of particles physics covers the description of the most fundamental particles, the fermions with spin $s = 1/2$, and was formulated in the 1970s. In addition, the Standard Model describes the fundamental interactions between these particles. Fermions are divided into two groups, quarks and leptons. Depending on the mass, three different quark families (u,d), (c,s) and (t,b) are distinguished. Since single quarks have never been observed in nature, quarks exist in bound states, the hadrons. Hadrons either consist of three constituent (anti-)quarks ($qqq, \bar{q}\bar{q}\bar{q}$), so-called baryons, or consist of quark-anti-quark pairs ($q\bar{q}$) called mesons. Similar to quarks, leptons are divided into three families (e^+,e^-), (μ^+,μ^-) and (τ^+,τ^-) together with their corresponding neutrinos ($\bar{\nu}$,ν). All fermions with their properties (charge, mass and spin) are represented in Fig. 1.1.

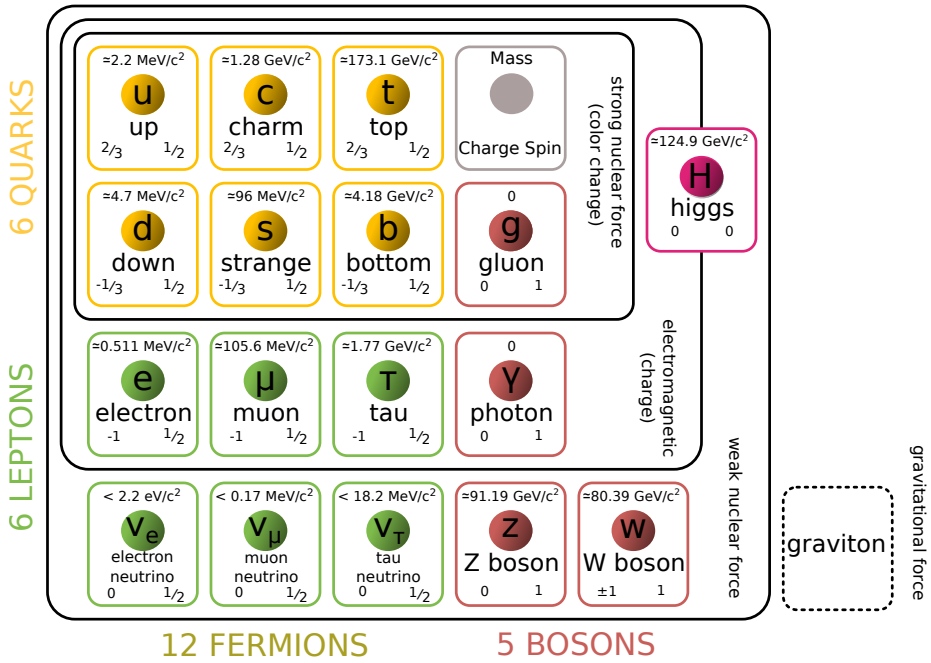

Figure 1.1: Detailed scheme of the Standard Model. Figure adapted from [Mau19].

Four different fundamental forces - the gravitational, the electromagnetic, the weak and the strong force - are known to present time, while the last three forces are contained in the Standard Model. All forces are described by the (virtual) exchange of (gauge) bosons summarized in Fig. 1.1 colored in red/pink, whereas the graviton is indicated in black. In general, the range of forces depends on the mass of the exchange boson. The gravitational force acting between massive particles is not only the weakest, but also the least known in comparison to the others. The graviton with

a spin of $s = 2$ is the hypothetical elementary particle that mediates gravity, which has yet to be discovered experimentally. Since it is supposed to be massless, the gravitational force has an infinite range. As the gravitational force is very weak compared to the other three forces on macroscopic scales it is neglected. Field theory is employed for the description of the three forces of the SM. The electromagnetic force acts between charged particles, e.g. hadrons and leptons, and is mediated by the exchange of photons ($s = 1$). As the photons do not have any rest mass, the range of the electromagnetic force is infinite. The underlying quantum field theory is the quantum electrodynamics (QED), in which, for example, the binding between electrons and nuclei is described. A third force, called the weak interaction, is involved in processes such as the weak decay of strange hadrons (e.g. $K_s^0 \to \pi^+\pi^-$). Here (rather) heavy W^+, W^- and Z^0 bosons ($s = 1$) with masses in the order of $80 - 90$ GeV/c^2 are exchanged. Therefore, the weak interaction acts only at small distances. The gluons are the force carriers of the strong interaction that couples to the color charge of the quarks. Each (anti-)quark carries one of the following colors: (anti-)blue, (anti-)red or (anti-)green. Due to the so-called confinement, only color-neutral particles exist, which means that hadrons consist either of three different colors or a color-anti-color pair. The underlying quantum field theory is the quantum chromodynamics (QCD). Further details are discussed in Section 1.2. The Higgs boson [Hig64] predicted by the Standard Model was recently discovered at CERN[1] [A$^+$12a, C$^+$12]. This boson is responsible for the mass generation of fundamental gauge bosons ($W^\pm$, Z^0), quarks and leptons.
Although the predictions of the Standard Model have been validated in various experiments, some important questions remain unanswered. The fundamental forces are not unified with respect to a single quantum field theory as the inclusion of the gravitational force is in particular challenging. Moreover, the imbalance of matter and antimatter in the universe cannot be explained by CP violation alone. In contrast to the experimentally observed neutrinos oscillations, the Standard Model predicts massless neutrinos. Furthermore, the existence of dark matter and dark energy cannot be explained within the Standard Model.

1.2 Quantum Chromodynamics and Chiral Symmetry

The strong interaction was successfully described in the context of quantum chromodynamics (QCD). It is a non-abelian gauge theory based on $SU(3)$ symmetry. Analogous to QED, where the charge defines the local symmetry, QCD introduces the color charge as an internal degree of freedom. There are a total of three charge colors and (anti-)quark carry one of these colors: (anti-)blue, (anti-)red or (anti-)green. The exchange bosons of the strong interaction are the gluons, which also interact among themselves, resulting in effects such as color confinement and asymptotic freedom. The potential $V(r)$ of QCD is given by the following expression:

$$V_s(r) = -\frac{4}{3}\frac{\alpha_s(r)}{r} + kr \tag{1.1}$$

with

$\alpha_s(r)$: strong coupling constant
r : distance between quarks
k : energy density term ($k \approx 1$ GeV/fm)

1 Conseil européen pour la recherche nucléaire

The first term of QCD potential (Eq. (1.1)) is dominating at small distance and shows a similar behavior like coloumb force in QED ($\propto \frac{\alpha}{r}$). For small distances corresponding to very high momentum transfers q^2, the strong coupling constant $\alpha_s(r)$, also called running coupling constant, is decreasing dramatically ($\alpha_s(r) \ll 1$) [DBdT16]. Hence, strong interaction becomes asymptotically weaker and asymptotic freedom is realized. In this high energy regime quarks can be treated as effectively free particles, which allows theory to treat the QCD Lagrangian perturbatively with the quarks being the relevant degrees of freedom [Sch03]. Consequently, with increasing temperature or density, one can think of deconfined quarks and gluons in a phase called Quark-Gluon-Plasma (QGP). Whereas, the linear term kr (Eq. (1.1)) is related to the color confinement, which is dominating at large distances and low energies. Due to the confinement, quarks can only exist within colorless states. If a quark anti-quark pair gets separated far enough from each other, the energy in the gluon field gets high enough, that it will become energetically favorable to generate another quark-anti-quark pair. This process leads to spontaneous hadronization and hence the suitable degrees of freedom of the QCD are the hadrons.

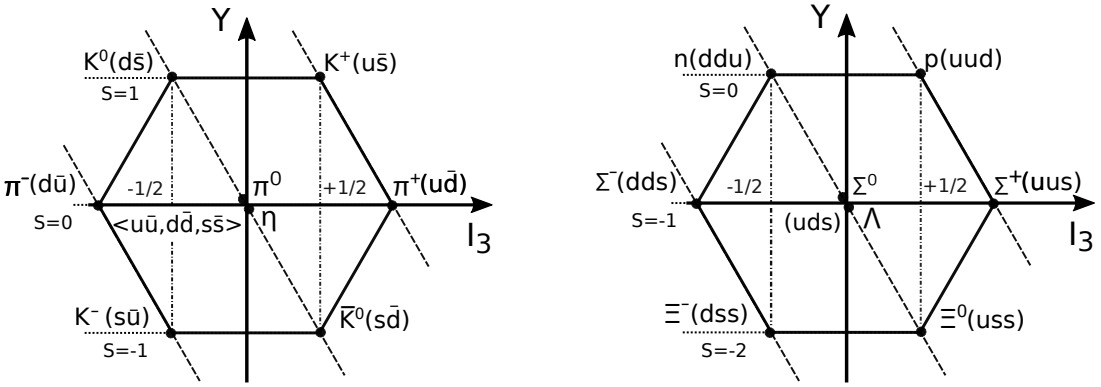

Figure 1.2: Pseudoscalar meson octet with $J^P = 0^-$ (left) and baryon octet with $J^P = 1/2^-$ (right).

Due to the attractive strong interaction, the quark exist in bound states, the hadrons. A fundamental question of nuclear physics is the origin of the hadron masses. Compared to quarks, the hadrons are notably heavier. A charged pion (π^+ ($u\bar{d}$), π^- ($d\bar{u}$)) has a mass of about 140 MeV/c^2. By adding up the quark masses of its constituents a mass of about 6.9 MeV/c^2 would be expected. Hence, the total mass of the hadron is not only the sum of its constituents. The mass of hadrons can only be explained by introducing the spontaneous breaking of chiral symmetry, which is commonly studied within the framework of chiral effective field theory (ChEFT). In this theory the degrees of freedom are hadrons or quarks depending on the energy scale. Within ChEFT the $SU(3)_{color}$ and $U(1)$ symmetries are conserved to preserve the baryon number [Sch03]. The fundamental symmetry of chiral theories is the $SU(3)_L \times SU(3)_R$ symmetry, in which the quarks mass goes to zero in the chiral limit. This symmetry preserves the chirality of the left- and right-handed hadrons in strong interaction processes. However, this symmetry is broken, if one considers the ground state, the vacuum, since the expectation value of the ground state $< 0|\bar{q}q|0 >$ is not vanishing. The latter is called quark condensate.
As the quarks interact with this quark-anti-quark pair the chirality can be changed. Hence, the chiral symmetry is broken as the chirality may changes e.g. from q_r to q_l by the annihilation of q_r with the anti-quark of $< 0|\bar{q}_r q_l|0 >$. Thus, the expectation value of the ground state does not vanish and consequently spontaneously breaks the chiral symmetry. Along with the sum of the quark masses the spontaneous breaking of the chiral symmetry generates additional hadron mass.

The eight Goldstone bosons (π, η, K) are predicted by spontaneous chiral symmetry breaking and illustrated in Fig. 1.2 (left). The explicit breaking of the chiral symmetry arises from the finite bare quark masses. The pion mass ($m_\pi \approx 140$ MeV/c^2) is described by the Gell-Mann-Oakes-Renner (GOR) relation (Eq. (1.2)) [GMOR68]. Therefore, the hadron mass consist of an explicit part, due to the non vanishing quark masses, and an spontaneous part, due to the non vanishing expectation value of the vacuum.

$$m_\pi^2 f_\pi^2 = -\frac{m_u + m_d}{2} < 0|\bar{u}u + \bar{d}d|0 > \tag{1.2}$$

with

$$\begin{aligned} f_\pi : &\quad \text{pion decay constant} \\ m_u/m_d : &\quad \text{bare masses of the first generation quarks} \\ < 0|\bar{u}u + \bar{d}d|0 > : &\quad \text{expectation value of the ground state} \end{aligned}$$

With increasing temperature and/or density the expectation value of the ground state is expected to decrease or even disappear completely. In this way the chiral symmetry can get partially restored. Figure 1.3 shows the calculations for the chiral condensate $| < \bar{q}q > |$ on the basis of the Nambu-Jona-Lasinio model [KLW90]. The expectation value is presented as a function of temperature T and nuclear density ρ/ρ_0. With increasing temperature as well as density the expectation value is decreasing. High temperatures can be reached with experiment located at high-energy accelerators like RHIC/LHC indicated in yellow. Whereas, high densities ($2 - 3\,\rho_0$) can be probed with experiments located at SIS18 or the future accelerator SIS100 of FAIR shown in red. Hence, within hot or dense matter the mass of the hadrons is predicted to change. This prediction triggered several physics programs searching for an experimental evidence of chiral restoration. With HADES located at the SIS18 in particular the in-medium modification of vector mesons, which are produced in heavy-ion collisions and decay into e^+e^- pairs, are studied. However, even though if the mass of the vector mesons is modified within matter it is still debated, if this would be a clear sign for (partial) chiral restoration [BLR$^+$98].

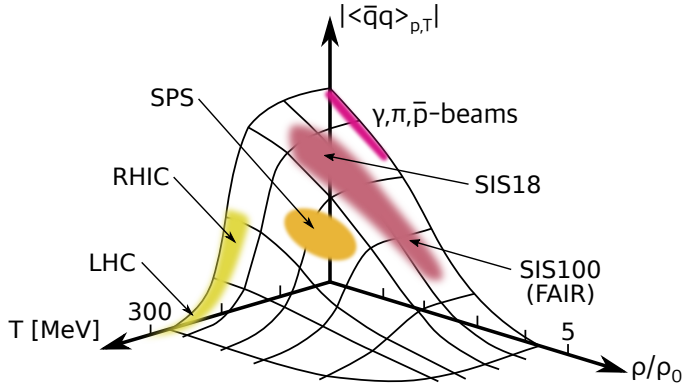

Figure 1.3: Expectation value of the chiral condensate as a function of the temperature T and nuclear density ρ/ρ_0 calculated with the Nambu-Jona-Lasinio model [KLW90]. Indicated are the experimental accessible regions. Figure adapted from [KMM09].

In the following, the in-medium modification of nearly complete set of (strange) meson ($\pi^\pm, K^\pm$ and ϕ) will be discussed. Since in hadronic reactions the strangeness is always conserved, the

connection (anti-)kaons and ϕ mesons to the hyperons, e.g. $Y = \Lambda, \Sigma$ (Fig. 1.2 (right)), will be outlined.

1.3 Pion Interaction with Nuclear Matter

The pion was predicted by Yukawa as mediator (carrier) of the nuclear force [Yuk35], while its discovery followed afterwards in observation of cosmic rays [LMOP47, OP47, Per47]. In particular, effective theories employ pions as force carriers to describe for example interaction between the constituents of a nucleus, protons and neutrons, as illustrated in Fig. 1.4. Pions can either be positively, π^+ ($u\bar{d}$), negatively, π^- ($d\bar{u}$) or neutrally charged, π^0 ($1/\sqrt{2}(u\bar{u} + d\bar{d})$).

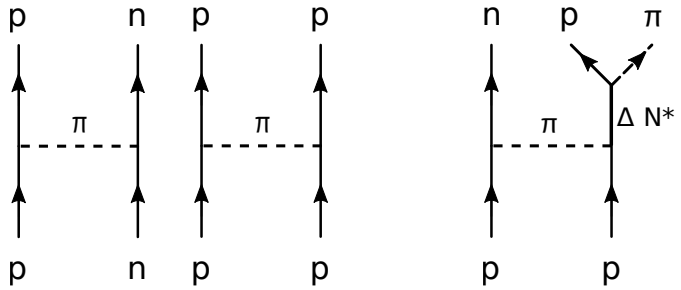

Figure 1.4: Feynman diagram of non-resonant and resonant pion exchange processes.

A final understanding of the intrinsic properties of pions is still missing. In this context, the pion atoms were intensively investigated. They can be produced by stopping π^- in a target nucleus. Once captured by the atom by replacing a electron, the pion cascades to a lower energy level by emitting x-rays with different transition energies. The π^- is primarily bound by the Coulomb force, while the strong interaction is repulsive. The strong interaction induces shifts in energy and width of energy levels with respect to electromagnetic energy levels. While, the shift in energy of any x-ray transition is proportional to the pion mass, the strong absorption of pions manifest itsself in the width of the energy level [Bac70]. In fact, pionic atoms indicate a in-medium modification of the pion mass [S$^+$04].

In addition, the pions strongly couple to short-lived baryonic resonances as shown in Fig. 1.4. In fact, pion spectra in hadron-hadron collisions at kinetic energies around a few GeV are dominated by the strong decays of short-lived baryonic resonances, $\Delta(1232)$ and N^*. To quantify the contributions of baryonic resonances, $\Delta(1232)$ and N^*, to the single and double-pion final state spectra, intensive studies were conducted in $p + p$ reaction. Either incoherent hadron cocktails [A$^+$14b] or partial wave analyses [AM$^+$17b, A$^+$15b] were employed. Fig. 1.5 show the invariant mass distribution of $p\pi^+$ (Fig. 1.5 (a)) and $n\pi^+$ (Fig. 1.5 (b)) pairs in $p + p \to np\pi^+$ reactions at 3.5 GeV measured with HADES [A$^+$14b]. Especially the $\Delta(1232)$ resonance contributes to both invariant mass distributions. In order to learn more about the interaction of the pions, it is important to study their production mechanisms in detail. In particular, elementary reactions are well suited to constrain the coupling to resonances. Whereby, pion-induced reactions are especially sensitive to the πN branching ratios (e.g. $\pi N \to \Delta$).

The properties of hadrons immersed in a strongly interacting environment can be modified. Extensive measurements of the inclusive production of pions were performed to investigate the

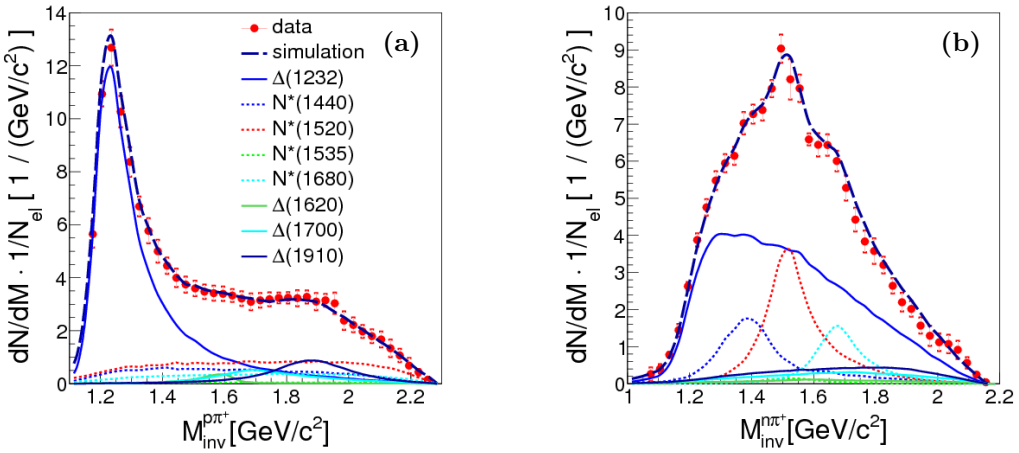

Figure 1.5: Invariant mass distribution of $p\pi^+$ (a) and $n\pi^+$ (b) pairs in $p + p \rightarrow np\pi^+$ reactions at 3.5 GeV measured with HADES [A$^+$14b]. The result of simulations (dashed curves) assuming an incoherent sum of the resonance contributions shown by separate curves, as indicated in the legend. The data are normalized to the proton-proton scattering yield N_{el} measured within the HADES acceptance. Figure taken from [A$^+$14b].

effects of nuclear matter in heavy-ion collisions (HIC) at energies of 1 GeV, at which the baryon densities ρ_B exceed the normal nuclear density [R$^+$07]. In this respect, however, heavy-ion collisions appear to be less suitable, since the strong coupling to resonances can cover in-medium properties of pions.

For astroparticle physics experiments, the precise knowledge of pion production is essential as they serve as an important ingredient for calculations of the atmospheric neutrino flux [Bat01] and accelerator neutrino flux [BG06]. Moreover pions are commonly used for the validation as well as a reference of transport model calculations, which are widely used for the interpretation of particle-physics results. In this respect, the HARP Collaboration performed extensive measurement of the inclusive double-differential charged pion production cross-sections in various pion-nucleus reactions [A$^+$09d]. However, this work provides further insights on the charged pion production off different nuclei in terms of the (double-)differential cross-sections at a lower incident pion beam momentum (1.7 GeV/c).

1.4 In-Medium Modification of (Anti-)Kaons

The (anti-)kaon production and in-medium behavior is of particular interest in the presented work. Their mass is around 500 MeV/c^2 and they differ in their strangeness content, whereby kaons have $S = 1$ and antikaons $S = -1$. One distinguishes between kaons, K^+ ($u\bar{s}$) and K^0 ($d\bar{s}$), and anti-kaons, K^- ($s\bar{u}$) and $\bar{K}^0$ ($s\bar{d}$). Moreover, they differ additionally by charge, isospin and mass. For the (anti-)kaon in-medium description an (effective) Lagrangian is formulated, in which hadrons are the degrees of freedom. Kaplan and Nelson were the first to calculated the interaction of kaons with the nuclear medium in the framework of the chiral pertubative theory (ChPT) [KN86, NK87]. The chrial effective Lagrangian for (anti-)kaon-nucleon interaction reads [Fuc06, HOL$^+$12]:

$$\mathcal{L} = \bar{N}(i\gamma^\mu\partial_\mu - m_N)N + \partial^\mu\bar{K}\partial_\mu K - \left(m_K^2 - \frac{\Sigma_{KN}}{f_\pi^2}\bar{N}N\right)\bar{K}K - \frac{3i}{8f_\pi^2}\bar{N}\gamma^\mu N\bar{K}\overleftrightarrow{\partial^\mu}K \tag{1.3}$$

with

$N(\bar{N})$ and $K(\bar{K})$: nucleon and kaon field
$N = \begin{pmatrix} p \\ n \end{pmatrix}$ $\bar{N} = (\bar{p}\ \bar{n})$, $K = \begin{pmatrix} K^+ \\ K^0 \end{pmatrix}$ $\bar{K} = \begin{pmatrix} K^- & \bar{K}^0 \end{pmatrix}$
m_N and m_K : nucleon and kaon mass
Σ_{KN} : kaon-nucleon sigma term
f_π : pion decay constant

Besides, the nucleon term the effective Lagrangian contains the kinetic (anti-)kaon term. The third term called Kaplan-Nelson term corresponds to the attractive scalar kaon-nucleon interaction, which is equal for both, kaon and antikaons. It depends on the strength of the kaon-nucleon term Σ_{KN}, which is related to the strangeness content of the nucleons. Contrary to the pion-nucleon sigma term ($\Sigma_{\pi N} \approx 45$ GeV/fm), which is well known constrained by pion-nucleon scattering, the latter is a relative uncertain quantity varying within $\Sigma_{KN} \approx 270 - 450$ GeV/fm depending on the underlying model [MNP17]. The last term is the so-called Weinberg-Tomozawa term describes the vector kaon-nucleon interaction. While for the kaons it is repulsive, for antikaons it is attractive. On the basis of the effective Lagrangian Eq. (1.3) in the mean-field approximation the dispersion relation for (anti-)kaons in nuclear matter can be deduced [HOL$^+$12]:

$$\omega^2(\vec{k}, \rho_N) = m_K^2 + \vec{k}^2 - \frac{\Sigma_{KN}}{f_\pi^2}\rho_S \pm \frac{3}{4}\frac{\omega}{f_\pi^2}\rho_N \tag{1.4}$$

with

$m_K/\vec{k}$: mass and momentum of the (anti-)kaon
Σ_{KN} : kaon-nucleon sigma term
f_π : pion decay constant
ρ_S and ρ_N : scalar and nuclear density

The last two terms correspond to self-energy $\Pi(\omega,\vec{k},\rho_N)$ which summarizes all the meson interactions in nuclear matter. Here, one distinguishes between kaons and antikaons. Whereby, the positive sign (+) of the last term represents the repulsive KN interaction for the kaons and the negative sign (−) indicates the attractive $\bar{K}N$ interaction. From the dispersion relation, the in-medium (anti-)kaon energy is given by [Fuc06, HOL$^+$12, MNP17]:

$$E(\vec{k}, \rho_N) = \left[m_K^2 + \vec{k}^2 - \frac{\Sigma_{KN}}{f_\pi^2}\rho_S + \left(\frac{3}{8}\frac{\rho_N}{f_\pi^2}\right)^2\right]^{1/2} \pm \frac{3}{8}\frac{\rho_N}{f_\pi^2} \tag{1.5}$$

As mentioned above, this so-called Weinberg-Tomozawa term is the origin for the opposite behavior of kaons and antikaons in medium. Consequently, due to the repulsive KN interaction, the effective energy of kaons in nuclear matter is increasing. Hence, the in-medium mass defined as $E(\vec{k} \to 0,\rho_N)$ is shifted to higher masses. While the antikaon behavior is vise versa. Due to the attractive nature of the $\bar{K}N$ interaction, hypotheses have been made in the past about the presence of antikaons within dense objects like neutron stars (NS) [KN86, NK87, RSBW01, BTKR92]

(Section 1.6). Figure 1.6 shows a variety of possible kaon and antikaon energies as a function of the normalized density ρ/ρ_0 for several underlying equation-of-states (Section 1.6). A variation of the kaon-sigma term influences the dependency of the kaon energy on the nuclear density, which should be kept in mind. However, several possibilities exist to study the kaon-nucleon interaction experimentally, of which some are discussed in the next sections.

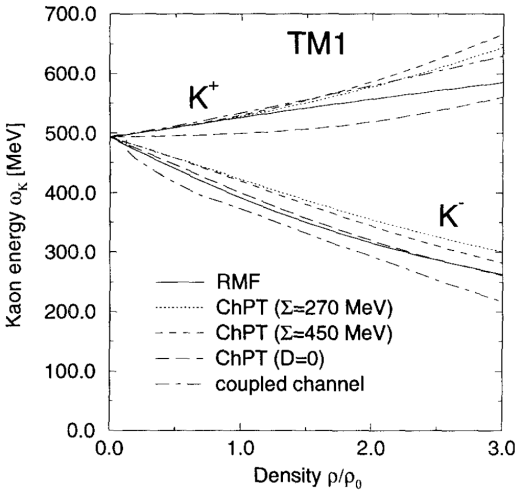

Figure 1.6: The kaon and anti-kaon energies as a function of the nuclear density ρ/ρ_0 resulting from various theoretical calculations for a soft equation-of-states (Section 1.6) [S$^+$97]. Figure taken from [S$^+$97].

1.4.1 Kaons in Nuclear Matter

In strong hadronic reactions strangeness is conserved exactly, so that kaons, K^+ ($u\bar{s}$) and K^0 ($d\bar{s}$), which were once produced, cannot be re-absorbed by the surrounding medium. This means that kaons cannot be converted to hyperons by strangeness exchange reactions. Furthermore, there are no resonance states with $S = 1$, so that they can propagate relatively freely within nuclear matter [Fuc06, P$^+$16a]. Therefore, kaons can be treated pertubatively. The real part of the KN potential in a nuclear medium can be estimated from the isospin average kaon-nucleon scattering length in free space ($\bar{a}_{KN} = -0.255$ fm), which corresponds to a potential in the order of 30 MeV at saturation density ρ_0 [MNP17]. Comparable potential depths are obtained based on the mean-field approximation to chiral Lagrangian [MNP17] (Section 1.4) as well as in the coupled-channel framework of [WKW96a]. Therefore, a slightly repulsive KN potential of $20 - 40$ MeV at saturation density ρ_0 is predicted.

The final phase space distributions of kaons are influenced by the repulsive KN potential. In particular, insight of the latter can be derived by comparing the kinematic distributions of kaons produced off heavy and light nuclei. The effect of the potential is expected to increase with the nucleus size as the kaons are on average exposed to higher densities. In Figure 1.7 shows an example of such an investigation in which the ratio of the differential K^+ cross-section in $p + \text{Au}$ to $p + \text{C}$ collisions at 1.5, 1.75 and 2.3 GeV, measured with ANKE [B$^+$04], is compared to the CBUU transport model [RCJ$^+$05]. It can be seen that at low momenta ($p < 230$ MeV/c) the production of K^+ mesons in the heavy target (Au) is suppressed with respect to the lighter target (C). This effect can be explained by the repulsive interaction caused by the Coulomb and by

the KN potential that accelerates the kaons while escaping the nucleus. The CBUU calculation, which includes a repulsive KN potential of 20 MeV at normal nuclear density ρ_0, provides a (rather) good description of the experimental data over the entire momentum range for all beam energies. Finally, it was found that the depth of the KN potential is 20 ± 5 MeV (ρ_0).

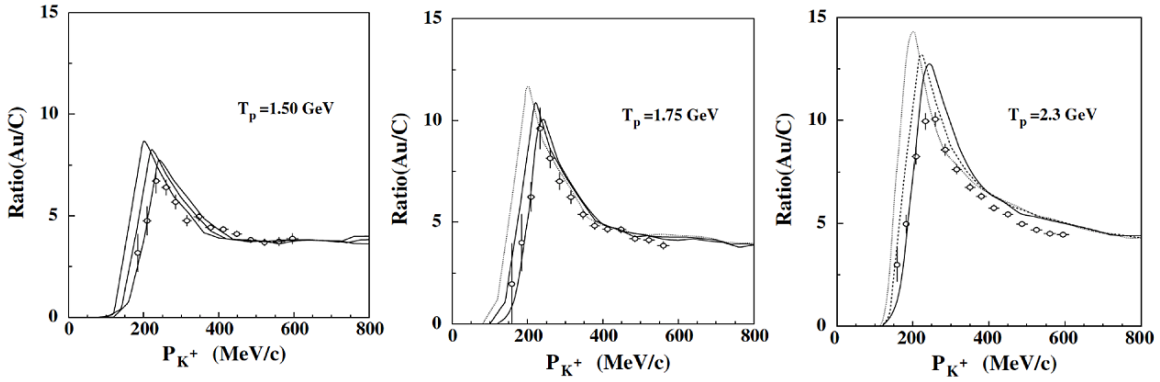

Figure 1.7: The ratio of the differential K^+ spectra in p + Au to p + C reactions at 1.5, 1.75 and 2.3 GeV (see legend) predicted by CBUU [RCJ+05] in comparison to the ANKE data [B+04]. The curves correspond to calculations with repulsive kaon potentials of 0, 10 and 20 MeV at ρ_0 (from left to right). Figure taken from [RCJ+05].

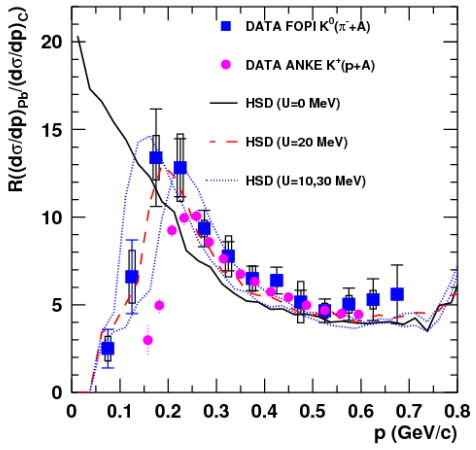

Figure 1.8: The ratio of K^0 (K^+) yields produced by pions (protons) on heavy and light targets as a function of the kaon momentum in the laboratory frame. The blue full squares depict the ratio of K_s^0 produced on Pb and C targets [B+09c]. The ratio of K^+ yields measured in proton-induced reactions on Au and C targets at 2.3 GeV is given by pink full circles [B+04]. The results of the HSD model [CB99] for different strengths of the K^0 potential are depicted by black solid (0 MeV), red dashed (20 MeV) and blue dotted (10, 30 MeV) curves. Figure taken from [B+09c].

Deeper insights into the in-medium KN potential can be gained by studying neutral kaons as they are not influenced by the Coulomb interactions that may shield the in-medium KN potential. These in-medium effects were studied in K_s^0 meson production off multiple nuclear targets in π^--induced reactions at 1.15 GeV/c by the FOPI Collaboration [B+09c]. The ratio

of the measured K_s^0 momentum distributions in $\pi^- + \mathrm{Pb}$ and $\pi^- + \mathrm{C}$ reactions is indicated by the blue squares in Fig. 1.8. Similar to the observations for K^+ in proton-induced reactions by ANKE [B$^+$04] (pink circles), a depletion is observed for low momenta. Contary to the K^+ distribution, no additional shift to higher momenta due to Coulomb interaction was observed for the K_s^0 spectra. In Figure 1.8 the experimental ratio is compared to the HSD transport model calculations [CB99]. In HSD a KN potential with a linear dependence on the nuclear density can be employed. As expected, no suppression of the momentum ratio is observed for the HSD prediction without KN potential (black solid line). While the presence of the potential (dashed and dotted curves) leads to suppression at low kaon momenta. It was found that the data best match a repulsive KN potential of 20 ± 5 MeV. The K^+ study in $p + A$ collisions of ANKE together with the CBUU transport calculations resulted in an equal value (20 ± 5 MeV).

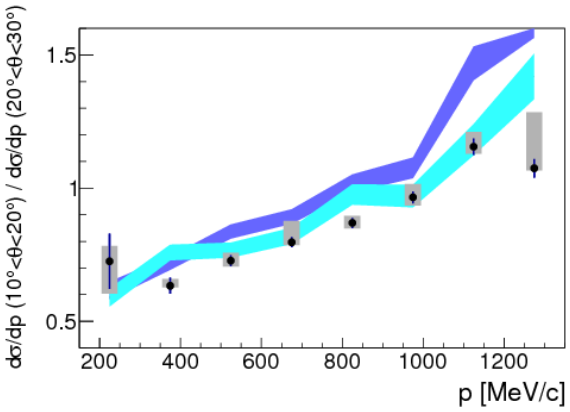

Figure 1.9: Ratio of K^0 momentum spectra measured in $p + \mathrm{Nb}$ collisions at 3.5 GeV [A$^+$14d] in two adjacent polar angle regions (black circles) and GiBUU transport model simulations [BGG$^+$12] with (cyan curve) and without (blue curve) an in-medium ChPT repulsive momentum-dependent kaon potential described in detail in [A$^+$14d] ($\approx +35$ MeV for the kaon at rest and for density ρ_0). Both the momentum and the polar angle are in the laboratory reference frame. Figure taken from [A$^+$14d]

Moreover, detailed investigations of the inclusive K_s^0 production in $p + \mathrm{Nb}$ collisions at a kinetic beam energy of 3.5 GeV were carried out by the HADES Collaboration [A$^+$14d] to study the effect of the repulsive KN potential in this sytem. Figure 1.9 shows the ratio R of K^0 momentum spectra measured in two adjacent polar angle regions. The K_s^0 data were compared with theoretical calculations using the GiBUU transport model. According to the GiBUU model [BGG$^+$12, A$^+$14d], the effect of the repulsive potential is maximal for kaons traveling in forward directions as the average paths within the nucleus are longer. While for the kaons emitted at larger polar angles ($\theta > 20°$), the influence of the potential should be much smaller. The in-medium ChPT KN potential of GiBUU features, besides a nonlinear density dependence, an explicit momentum dependence (Fig. 5.15) [A$^+$14d]. Therefore, the largest effect of the KN potential is predicted for large kaon momenta. This effect is in fact observed in Fig. 1.9, which compares the distribution with (cyan curve) and without (blue curve) the repulsive ChPT KN potential. The ratio of K^0 momentum spectra as well as transverse momentum and rapidity distributions led to an estimate of the strength of the repulsive K^0 potential of ≈ 35 MeV at saturation density ρ_0 and for kaons at rest.

Several experiments also investigated the effects of the KN potential in heavy-ion collisions (HIC),

where densities of up to $2-3\,\rho_0$ can be reached. The K_s^0 transverse momentum and rapidity distributions in Ar + KCl reactions at a kinetic energy of 1.756 AGeV, measured by the HADES Collaboration [A$^+$10a], suggest the existence of a stronger repulsive in-medium KN potential of about 40 MeV at saturation density ρ_0. However, recent studies of K_s^0 and Λ in Au + Au collisions at 1.23 AGeV by HADES [AM$^+$19c] do not lead to a conclusive picture. Due to the associated production of kaons and hyperons, it is expected that also the Λ is influenced by the in-medium KN potential. Hence, the HSD and IQMD models considered a repulsive KN potential of 40 MeV at nuclear ground state density ρ_0 together with ΛN potential of 2/3 of the NN potential strength [HOL$^+$12]. The transport model predictions including KN potentials were by far the closest to the experimental K_s^0 kinematic spectra. However, no simultaneously satisfactory description of the kinematic distributions of Λ was obtained. Especially for the interpretation of highly dynamical nuclear reaction like heavy-ion collisions, the hadron production and propagation is complex. Hence, a further model refinement is required in order to draw concrete conclusions about the KN potential in nuclear matter at $2-3\,\rho_0$.

In particular, the currently available experimental data on $K^0(K^+)$ meson production in pion-nucleus and proton-nucleus collisions support (strongly) the existence of a repulsive in-medium KN potential of about $20-40$ MeV at a density of ρ_0 for kaons at rest.

1.4.2 Antikaons in Nuclear Matter

The properties of the K^- meson ($s\bar{u}$) in nuclear matter are much less known and are still controversially discussed. K^-p scattering data [P$^+$16a] and K^- hydrogen data [B$^+$11a] allow to investigate the antikaon-nucleon interaction. Kaonic hydrogen, in which in particular the strong interaction at threshold can be probed, can be produced with stopped K^- in a light nuclear target such as hydrogen. Once captured by the atom replacing an electron, the antikaon cascades to the ground state $1s$ while emitting x-rays with specific transition energies. The strong interaction induces shifts in the energy and width of the $1s$ state in kaonic hydrogen with respect to (pure) electromagnetic energy levels. Both, kaonic hydrogen data [B$^+$11a] and low-energy K^-p scattering data [P$^+$16a], allowed to extract the free K^-p scattering length at ($a_{K^-p} = (-0.65 + i0.81)$ fm [IHW11, IHW12]) and above threshold implying that the K^-p interaction would be repulsive in free space [HJ12, MNP17]. While, the sub-threshold free K^-p interaction is attractive. Although, the scattering amplitude of K^-p is extremely model dependent in sub-threshold regime, since this range is not constrained by experimental data. The $\Lambda(1405)$ resonance plays a peculiar role above threshold, since the K^-p interaction is dominated by the presence of the $\Lambda(1405)$. The $\Lambda(1405)$ has a two-pole structure in the complex energy plane. While the lower (broader) pole at ≈ 1330 MeV mainly couples with the $\pi\Sigma$ channel, the higher pole at ≈ 1430 MeV is more coupled to the K^-N channel. Near the threshold energies, the existence of the $\Lambda(1405)$ resonance leads on the one hand to change in sign of real part of the K^-p interaction and on the other hand to a pronounced peak in the imaginary part of the free K^-p forward scattering amplitude. Therefore, the large $\bar{K}N$ coupling with $\Lambda(1405)$ resonance leads to absorption processes. Such absorption processes, strange exchange reactions, can occur on one ($K^-N \to Y\pi$) or even more nucleons ($K^-NN \to YN(\pi)$). In this context, the coupling to the $\Sigma(1385)$ is also relevant, as illustrated in Fig. 1.10.

Due to the strong coupling of the $\bar{K}N$ to the $\Lambda(1405)$, the K^- in medium properties and the $\Lambda(1405)$ in matter should be treated self-consistently. Hence, the repulsive free K^-p scattering length becomes well attractive below saturation density ρ_0 [FG07, WKW96b, HJ12], which is

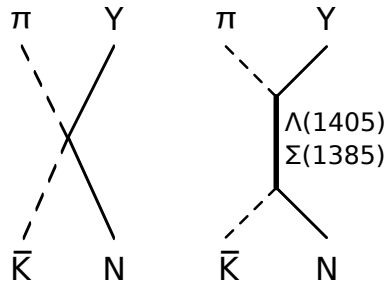

Figure 1.10: Feynman diagram of non-resonant and resonant strangeness exchange processes.

compatible with observations of kaonic atoms. On the basis of kaonic atoms also the effective in-medium density-dependent isospin-averaged K^-N scattering length could be calculated, which allowed to extract the real part of the $\bar{K}N$ potential, which is attractive with -190 MeV [FGB93]. However, it should be noted that the kaonic atom data examine the surface of the nucleus and thus do not represent strong limitations for the $\bar{K}N$ potential at normal nuclear density. Several self-consistent coupling channel calculations of K^- self-energy in nuclear matter were performed on the basis of chiral Lagrangian and mesonic exchange potentials [MNP17]. They predict a relatively shallow momentum-dependent $\bar{K}N$ potential with a depth in the order of $-(50-80)$ MeV. Also the situation with the imaginary part of the $\bar{K}N$ potential at low energies is controversial. Models based on a chiral Lagrangian or meson exchange potential predict potential depths in the order of $\approx -(25-60)$ MeV at the threshold [MNP17]. However, if multi–nucleon absorptive processes are also considered, the imaginary potential depth of $\bar{K}N$ interaction is predicted to be even smaller $(-(70-80)$ MeV).

In recent decades, several experimental efforts have been made to investigate the in-medium properties of antikaon in more detail. In addition to the (detailed) studies on kaonic atoms, recent evidence for the existence of ppK^- bound states [A$^+$19b] indicate that the $\bar{K}N$ interaction is attractive. Furthermore, an enhanced antikaon production in C+C and Ni+Ni collisions at beam energies per nucleon below the NN threshold observed by the KaoS Collaboration [B$^+$97, S$^+$96, L$^+$99] was attributed to the in-medium mass reduction of K^- and thus to an attractive $\bar{K}N$ potential in nuclear matter. Similar to the investigation of the KN potential, the experimental kinematic distributions K^- were confronted with transport model calculations with different strengths of the $\bar{K}N$ potential. For example, the analysis of inclusive K^- momentum spectra by KaoS [B$^+$97, S$^+$96, L$^+$99] and FRS [S$^+$94] compared to the CBUU transport model [CBM$^+$97, CB99] suggests an attractive effective $\bar{K}N$ potential of about $-(100-120)$ MeV at a density of ρ_0.

However, the extraction of the $\bar{K}N$ potential in heavy-ion collisions, but also in hadron-nucleus reactions, poses another difficulty. The shape of the K^- momentum spectra and the K^- yields are strongly distorted by the feeding of ϕ decays ($\phi \to K^+K^-$, $BR \approx 48.9\%$ [P$^+$16a]). Since most calculations of the transport model underestimate the yield of the ϕ meson, they do not account for these distortions correctly. The effect of the ϕ meson on the K^+ yield is negligible, since the K^+ production cross-section is much larger. The FOPI Collaboration has measured the ϕ/K^- ratio in Al+Al and Ni+Ni collisions at 1.9 AGeV, which was found to be $0.34 \pm 0.06(\text{stat}) + 0.04(\text{syst})$ [G$^+$16] and 0.36 ± 0.05 [P$^+$16b], respectively. For the deep sub-thresholds ϕ and K^- production in Au + Au collisions at 1.23 AGeV by HADES [AM$^+$18a], the ϕ/K^- ratio was even larger with 0.52 ± 0.16, which means that $\approx 25\%$ of the observed K^- mesons originate from ϕ feed-down. The effect of these (surprisingly) large ϕ/K^- ratios on the determination of the $\bar{K}N$ potential

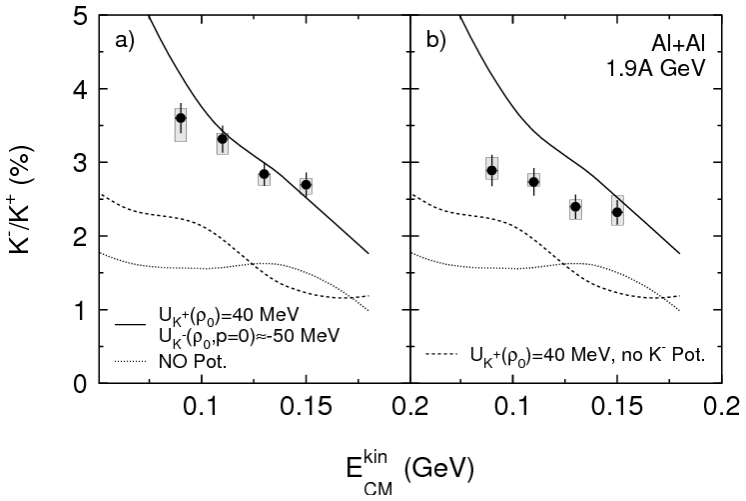

Figure 1.11: The measured K^-/K^+ ratio as a function of the kinetic energy in the center-of-mass frame for Al+Al collsions at 1.9 AGeV [G$^+$16]: (a) not-corrected and (b) corrected for the 17% contribution of K^- mesons from ϕ decays. Curves are the results of HSD transport model [CB99] predictions without any in-medium effects (dotted curves), with only a K^+ potential with a linear dependence on density with $V_{K^+}(\rho_0) = 40$ MeV (dashed curves) as well as with the in-medium effects for both kaons and antikaons $V_{K^+}(\rho_0) = 40$ MeV and $V_{K^-}(\rho_0,\vec{p} = 0) = -50$ MeV (solid curves). Figure taken from [G$^+$16].

is demonstrated in Fig. 1.11, in which the K^-/K^+ ratio is represented as a function of kinetic kaon energy. Without considering the ϕ feed-down, comparisons with HSD would indicate a $\bar{K}N$ potential of $V_{K^-}(\rho_0) = -50$ MeV. However, a much weaker $\bar{K}N$ potential is required to reproduce the experimental data corrected for the ϕ feeding. Hence, the ϕ meson decays contribute significantly to the observed K^- yield and should be considered in attempts to extract the $\bar{K}N$ potential.

To date, K^- absorption processes on light nuclei have been studied [HR62, N$^+$78]. Multi-nucleon absorption occurs in about 16.5% of events containing hyperons (Λ or Σ), without an additional pion in the final state [KBD$^+$70]. In particular, the role of two- and more-nucleon absorption for slow K^- (< 127 MeV/c) was investigated by the AMADEUS Collaboration [VD$^+$16]. It was found that about 9% of all multi-nucleon absorption processes take place on two nucleons without further interaction. While, total two-nucleon absorption amounts to 28%. This approach also considered the absorption on three (19%) or more nucleons and the final state interaction with the residual nucleons. In addition, the contribution of resonant and non-resonant processes with intermediate formation of $\Sigma(1385)$ and $\Lambda(1405)$ was extracted based on AMADEUS data [PWC16, P$^+$18]. However, an accurate measurement of absorption in (heavy) nuclei is still missing.
Moreover, strangeness exchange reactions can occur in the both directions, $K^-N \leftrightarrow Y\pi$, in heavy-ion collisions at energies around $1 - 2$ AGeV. KaoS showed that the measured K^- yield in sub-threshold Ni+Ni collisions is considerably larger with respect to nucleon-nucleon collisions near threshold [B$^+$97]. In fact, on the basis of transport model calculations it was found that the dominant K^- production channel is not $NN \rightarrow NNK^+K^-$ ($\sqrt{s_{thr}} = 2.87$ GeV) but the mesonic $\Lambda(\Sigma)\pi \rightarrow K^-N$ reaction [HOA03], since the production threshold is lower for $NN \rightarrow N\Lambda(\Sigma)K^-$ ($\sqrt{s_{thr}} = 2.55$ GeV). However, it is difficult to address the role of strangeness exchange directly as heavy-ion collisions are highly dynamic processes.

The behavior of K^- mesons in nuclear matter is complex. The ϕ meson decays in nuclear reactions contribute to the observed K^- abundance and should therefore also be considered. Scattering experiments, kaonic atomic data and evidence for the existence of ppK^- bound states [A$^+$19b] show that the K^-N interaction is attractive. However, the large K^- coupling to the $\Lambda(1405)$ resonance leads to absorption processes for the states K^-N and K^-NN. Due to the attractive nature of the $\bar{K}N$ interaction, hypotheses have been made in the past about the presence of antikaons within neutron stars (NS). This scenario neglects the imaginary part of the $\bar{K}N$ interaction, which leads to absorption processes and thus to hyperon production. A quantitative determination of the K^- absorption is therefore crucial to provide a more realistic equation-of-state of dense matter generated in heavy-ion collisions and scenarios for NS and NS merger (Section 1.6).

1.5 In-Medium Modification of ϕ Meson

The ϕ Meson ($s\bar{s}$) with a width of $\Gamma = 4.27$ MeV [P$^+$16a] is a hadron with so-called hidden strangeness. Its production is expected to be strongly suppressed according to the Okubo-Zweig-Iizuka (OZI) rule [Oku77, Zwe64, Iiz66], which hinders processes with unconnected quark lines. Therefore, in the interpretation of the ultra-relativistic heavy-ion collision data [A$^+$15a, Wad13] the ϕN cross-sections are assumed to be small [SB16]. However, the large branching ratio $\phi \to K\bar{K}$ ($BR \approx 83\%$ [P$^+$16a]) shows that the ϕ meson is strongly coupled with kaons and antikaons. In addition, chiral effective field theory models predict a significant broadening of the in-medium width ($40 - 50$ MeV) and thus a reduced life-time due to in-medium modification of kaon loop and direct ϕN coupling [GW15, CHBVV17].

The photoproduction of ϕ mesons near the threshold was studied to extract the free ϕN scattering length [TNDO07], which allowed to derive the differential cross-section at the threshold. The latter is consistent with the estimates of the ϕN scattering length ($a_{\phi N} = -(0.15 \pm 0.02)$ fm) based on QCD sum rule calculations [KH97]. While, at higher incident photon energies, the ϕN interaction is rather weak with an inelastic ϕN cross-section of about 8 mb [B$^+$75].

The inelastic ϕN interaction and therefore the ϕ meson absorption in nuclear matter is often investigated in terms of the transparency ratio. The latter compares the ϕ production cross-section off heavy and light nuclei normalized to the mass numbers, since the effect of the ϕN coupling is expected to increase with increasing nucleus size. Hence, the ϕ production off heavy nuclei (A) should be suppressed with respect to the light one (C). The normalization to carbon reduces the sensitivity of the measured cross-sections to differences in the initial state interaction of (various) hadron-induced reactions as well as the role of secondary production processes. The transparency ratio for the ϕ meson was measured in photoproduction experiments [I$^+$05, W$^+$10] and $p + A$ collisions [P$^+$11, H$^+$12]. In Figure 1.12 the ϕ transparency ratio for the latter reactions is depiced. It can be seen that the transparency ratio decreases significantly with increasing nucleus size, since the ϕ mesons are on average exposed to higher densities. While for the nucleus with intermediate atomic mass the transparency ratio is reduced by about 60%, in the heavy nucleus a reduction of almost 70% can be observed compared to carbon. To extract the inelastic ϕN cross-section and the in-medium ϕ width, the data are compared with calculations by Mühlich and Mosel [MM06], Magas et al. [MRO05], Paryev [Par09] and Cabrera et al. [CRO$^+$04]. Figure 1.12 compares the transparency ratio data obtained in $p + A$ collisions by ANKE [P$^+$11] with calculations by Magas et al. and Paryev. Taking into account the contributions from secondary production processes,

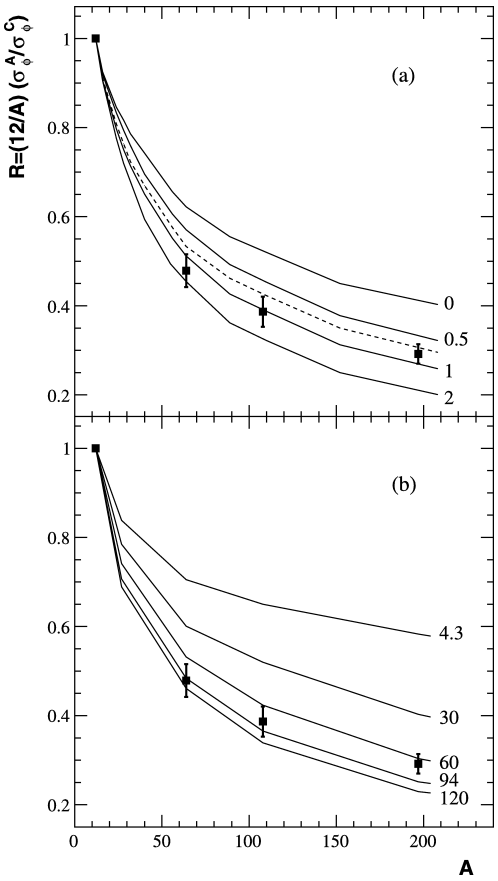

Figure 1.12: Transparency ratio for ϕ mesons obtained in $p+A$ collisions by the ANKE Collaboration [P$^+$11] compared to calculations by Magas et al. [MRO05] (a) and Paryev [Par09] (b) for different in-medium ϕ widths. Figure taken from [P$^+$11].

which increase the transparency ratio, in-medium width of $\Gamma = 45^{+17}_{-9}$ MeV and $\Gamma = 50^{+10}_{-6}$ MeV have been extracted, respectively. All these measurements consistently show that the ϕ meson is strongly broadened in the medium by about an order of magnitude as compared to its free width of 4.3 MeV [P$^+$16a]. The imaginary potential of the ϕN interaction thus lies within $-(20-30)$ MeV. Hence, the width of the ϕ mesons increases in nuclear matter due to the opening of inelastic reaction channels. Furthermore, the spectral function ϕ is further broadened due to in-medium modification of kaon loop. Both effects are predicted by chiral effective field theory models, which result in strong broadening of the in-medium width $(40-50$ MeV) [GW15, CHBVV17].

Furthermore, the momentum dependence of the transparency ratio ϕ was investigated by the ANKE Collaboration [H$^+$12]. Figure 1.13 shows the transparency ratio over the $0.6-1.6$ GeV/c momentum range, measured in proton-induced reactions with Cu, Ag, and Au targets. Again the transparency ratio was normalized to carbon. Compared to model calculations [Par09, MRO05] the in-medium ϕ width in the nuclear rest frame was derived with significant dependence on the ϕ momentum, which ranges from 20 to 60 MeV, corresponding to an imaginary part of the ϕN potential in the $-(10-30)$ MeV range. Hence, an effective ϕN absorption cross-section of $14-21$ mb [H$^+$12] was obtained. This extracted inelastic ϕN cross-section is in agreement with A-dependent transparency ratio measurements by CLAS [W$^+$10] and by LEPS [I$^+$05] Collaboration, which were analyzed within Glauber-type models yielding to $\sigma_{\phi N}$ in the range of $16-70$ mb and

35^{+17}_{-11} mb, respectively.

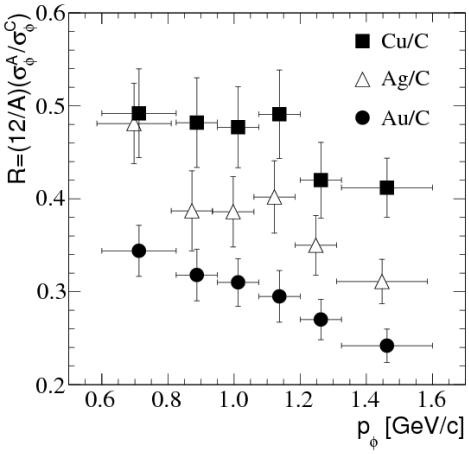

Figure 1.13: Momentum dependent transparency ratio for ϕ mesons as function of the mass number A obtained in $p + A$ collisions by the ANKE Collaboration [H$^+$12]. Figure is taken from [H$^+$12].

The properties of the ϕ meson are still controversially discussed. Mainly due to OZI suppression [Oku77, Zwe64, Iiz66] hindering processes with disconnected quark lines, in the interpretation of the ultra-relativistic heavy-ion collision data [A$^+$15a, Wad13] the ϕN cross-sections are assumed to be small [SB16]. Whereas, measurements of the modification of the ϕ production rates in proton- and photon-induced reactions do suggest a rather sizable ϕN interaction cross-section. The data on the ϕ in-medium modification are, however, interpreted in a rather model-dependent way implying the contribution of secondary processes, in-medium propagation and initial and final state interactions. Direct evidence of ϕ meson absorption would not only shed light on ϕN interaction, but would also be relevant for the description of heavy-ion collisions and structure of neutron stars (Section 1.6).

1.6 Equation-of-State and Neutron Stars

The properties of nuclear matter are described by the equation-of-state (EoS), which connects the relevant macroscopic state variables temperature T, baryonic density ρ_B and pressure p. The EoS is determined by the fundamental interactions predicted by QCD. These interactions and hence the EoS allow to describe nuclear matter under extreme conditions generated in heavy-ion collisions but also in the inner core of neutron stars. The complexity of strongly interacting nuclear matter under various conditions is represented in the QCD phase diagram shown in Fig. 1.14. In the low temperature and moderate baryo-chemical potential μ_B (low baryon density ρ_B) region the nuclear matter is characterized by hadrons (hadrons gas) indicated by yellow shaded area in Fig. 1.14. In this region, hadrons are the degrees of freedom and chiral effective theories can be used to provide a description of the hadronic interactions. Normal nuclear matter is located in this phase ($\mu_B \approx 1$ GeV, $\rho_0 = 0.16$ fm^{-3}). At very high densities (up to 8 ρ_0) and moderate temperatures ($T \approx 1$ MeV) the neutron stars (NS) are located. For higher temperatures and low baryo-chemical potential a smooth cross-over from the hadronic phase to the Quark-Gluon-Plasma (QGP) is predicted at $T_c \approx 155$ MeV [FH11, AEF$^+$06] shown by the red shaded area. In the QGP the quarks and gluons are predicted to be deconfined. Whereas, with increasing densities

a transition is expected above the critical point indicated by the solid black line. However, the order of this transition and the exact position in the (T, μ_B) plane of the so-called critical point are strongly model-dependent. Also from an experimental point of view, there is no evidence, which is able to pin down the nature of such transition and the location of the critical point. A third phase is predicted the so-called color-superconducting phase, which should be reached with increasing baryo-chemical potential at rather moderate temperature.

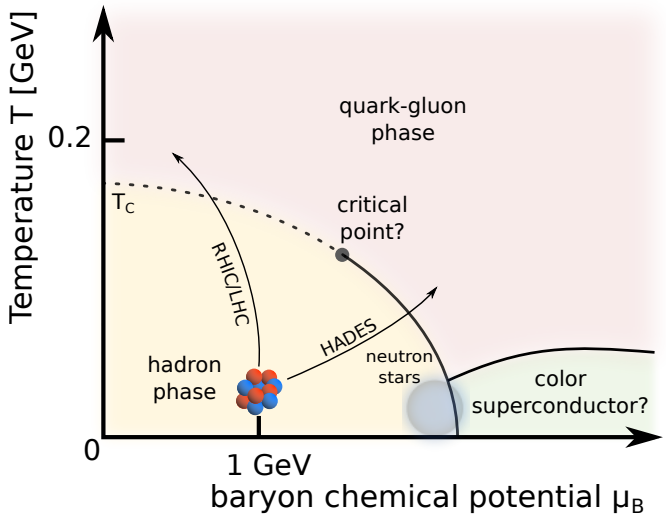

Figure 1.14: QCD phase diagramm for temperature vs. baryon-chemical potential. The yellow shaded area corresponds to the hadron phase, the red area to the quark-gluon plasma and blue to the hypothetical color superconducting phase. Figure adapted from [Mau19].

Experiments located at high-energy accelerators like LHC/RHIC allow to probe high temperatures and therefore are expected to be sensitive to the QGP phase. Whereas HADES as well as other experiments located at the future accelerator facility FAIR can study dense nuclear matter $(2-3\rho_0)$ in heavy-ion collision at moderate temperatures. In addition, hadron-hadron and hadron-nucleus reactions at at a few GeV allow to further constrain the hadron properties in vacuum and cold nuclear matter, respectively.

The study of the hadron properties and hence their interaction in nuclear reactions is of particular relevance. Since they are the key ingredient of the EoS, which describes dense matter and affects macroscopic phenomena like neutron stars and neutron star merger [HTB$^+$17, AM$^+$19a]. Neutron stars are super dense objects (up to $8\,\rho_0$) with masses around $1-2$ solar masses and radii of around 12 km. The precise and detailed structure and composition of the inner core of a NS is not known to the present. Several possibilities such as pure nuclear matter, pion or kaon condensates, color superconducting quark phases, hyperon within nuclear matter or mixed phases of quark and nuclear matter are under debate as illustrated Fig. 1.15. The fundamental interaction of particle constrain the EoS of such dense nuclear objects and hence can help to gain knowledge about constituents of neutron star inner core. The Tolman-Oppenheimer-Volkoff (TOV) equation [OV39, Tol39] can be employed to translate different EoS scenarios into the mass-radius relation, which can be directly compared to the astronomical observations of NS. The TOV equation assumes a hydrostatic equilibrium, therefore to be constant in time and a isotropic mass distribution. Moreover, it implies that the gravitational pressure is counterbalanced by the matter preventing the star from collapsing. Astrophysical observations, in particular the

discovery of the neutron stars PSR J0348+0432 and PSRJ1614-2230 [C+06, D+10], which both reached a mass of two solar masses, provide stringent constrains to the EoS. Different inner-core scenarios correspond to different EoS and hence to different inner-core constituents along with their interaction.

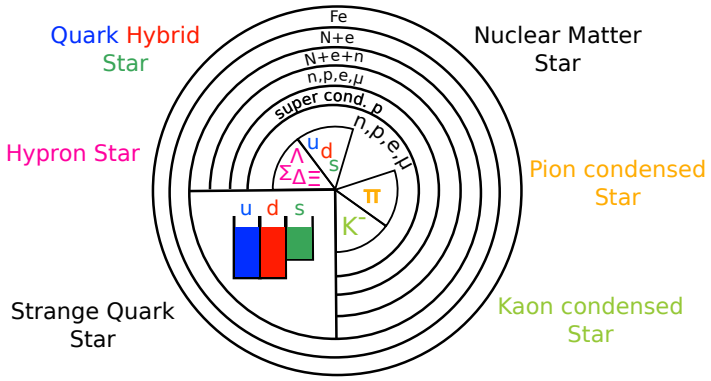

Figure 1.15: Possible structures and novel phases of matter in the inner cores of neutron stars predicted by theory.

In the following the appreance of antikaons in dense matter in terms of kaon condensed star, but also in connection to hyperon stars, will be discussed. The predicted antikaons properties have (major) impact on the nuclear EoS at higher densities and with this also on the possible properties of neutron stars. As introduced in Section 1.4.2, due to the attractive nature of the K^-N interaction, already Kaplan and Nelson [KN86, NK87] predicted that antikaons may condense at densities around $3\,\rho_0$. Even hypotheses have been made in the past about the presence of antikaons within neutron stars (NS) [BTKR92, RSBW01], since in neutron star matter (extremely) high densities can be reached easily. Within the inner core of neutron stars, neutrons, protons and electrons are in beta equilibrium via processes like $n \rightarrow p + e^- + \bar{\nu}_e$ and $p + e^- \rightarrow n + \nu_e$ [RBW05]. As these particles are fermions, they induce a Fermi pressure, which counteracts the gravitational compression. If, however, the antikaon mass drops below the chemical potential of electrons (μ_e), processes like $e^- \rightarrow K^- + \nu_e$ and $n \rightarrow p + K^-$ should become energetically favorable [RBW05]. The exact onset is determined by the $\bar{K}N$ interactions. These processes reduce the number of electrons and neutrons and thus reduce the Fermi pressure. On the other hand, the reduced Fermi pressure is not counterbalanced, since kaons are bosons and can condensate at $p = 0$. Hence, the appearance of kaon condensation softens the EoS substantially as demonstrated in Fig. 1.16 (a) [GA12] and therefore also limits the maximum mass of neutron stars. In fact, the measurement of the two solar mass neutron stars excludes most of the theoretical models assuming a very soft EoS induced by kaon condensation as shown in Fig. 1.16 (b). A very soft EoS and hence relatively low maximal mass is obtained, if the real part of the $\bar{K}N$ potential is very attractive (e.g. $U_{\bar{K}N} = -180$ MeV) (brown dashed curves in Fig. 1.16). However, it becomes rather clear that all EoS strongly depend on the underlying model assumptions as indicated by the two different parameter sets, G1 and G2, in Fig. 1.16 (b). Further constrains on the interaction of particles within dense nuclear matter are needed to reduce the allowed parameter space. Besides, all scenario of kaon condensed star neglect the imaginary part of the $\bar{K}N$ interaction, which leads to absorption processes and thus to hyperon production (e.g. $K^-N \rightarrow Y\pi$) (Section 1.4.2). Hence, considerations of strangeness exchange reactions within dense nuclear matter, will not only impact our understanding of EoS of kaon condensed star but also the one of hyperon stars. A quantitative determination of the K^- interaction and absorption in combination with hyperon is therefore

crucial to provide a more realistic EoS of dense matter and scenarios for NS and NS merger.

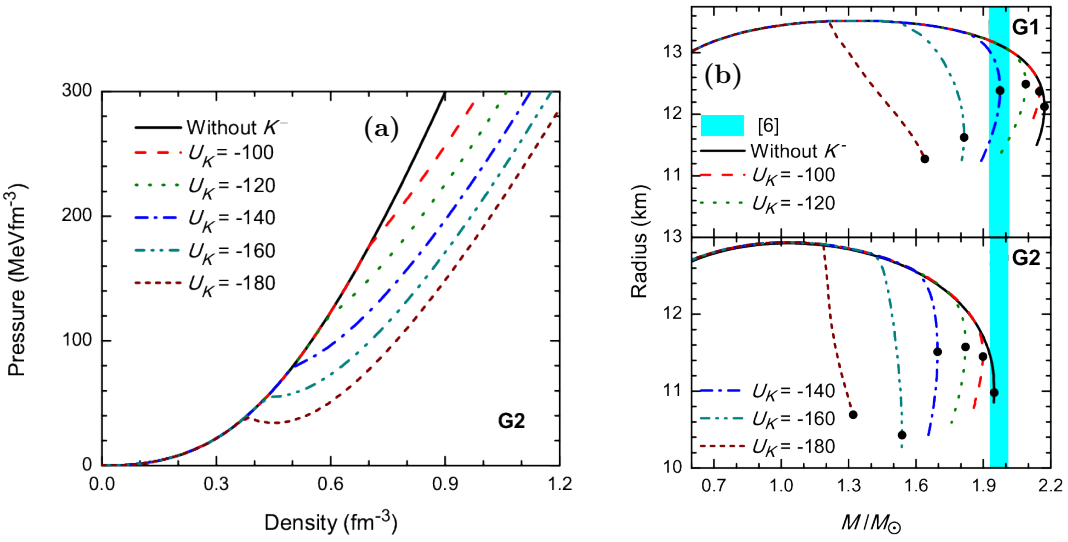

Figure 1.16: (a) Pressure in NS matter versus baryon density calculated using different optical potentials and G2 parameter set [GA12]. (b) The mass-radius relation for NS calculated using different optical potentials and with G1 and G2 parameter sets [GA12]. The different curve indicate different $\bar{K}N$ potential depths, while the solid circles represent the corresponding maximum mass. The shaded region correspond to the recent observation of $1.97 \pm 0.04\ M_\odot$. G1 and G2 correspond to different EOS. Figures taken from [GA12].

In the context of hyperon stars also the ϕ mesons have to be taken into account. The appearance of hyperons for increasing nuclear densities has been suggested in [AS60]. As matter becomes more and more compressed during the formation of a neutron star, the baryochemical potential increases as the Fermi pressure is increasing. At some point the threshold for the hyperon production is reached and hence it becomes energetically favorable to convert nucleons into hyperons (e.g. $n + e^- \to \Sigma^- + \nu_e$, $p + e^- \to \Lambda + \nu_e$) [AS60]. The onset of the hyperon appearance within dense matter strongly depends on the YN interaction. However, the details of the hyperon-nucleon (YN) interaction and even of the hyperon-hyperon (YY) interaction are known only poorly. From femtoscopy, scattering and hypernuclei data [A$^+$19a, HPK$^+$13, MDG88] the ΛN interaction is known to be attractive. The situation of the Σ hyperon is unsolved. Σ^- atomic data indicates repulsive potential [MFGJ95], which is in agreement with the absence Σ hypernuclei in a recent research of [B$^+$99a]. On the other hand the only observed Σ hypernuclei is ${}^{4}_{\Sigma}He$ [H$^+$89, N$^+$98]. The Kiso event, in which a Ξ hypernuclei has been observed, points to an attractive ΞN interaction [N$^+$15]. According to the $\Lambda\Lambda$-hypernuclear data, the $\Lambda\Lambda$ interaction is only weakly attractive [DMGD91]. For the investigation of nucleons and hyperons in neutron stars, the baryon-baryon interaction is mediated by the exchange of scalar (σ), isovector (ω) and isovector (ρ) mesons. While the YY interaction can be incorporated by strange vector mesons (ϕ) introducing a repulsive interaction, which is in accordance with the weakly attractive $\Lambda\Lambda$ interaction observed for $\Lambda\Lambda$-hypernuclei. Not only the potential depths of hyperon in nuclear matter play are role, but also mediators of the interaction, the exchange mesons, have a impact on the EoS.

In Figure 1.17 (a) the EoS is presented for a various ΣN potential depths, while the potential depth of the ΞN ($U_{\Xi N} = -28$ MeV) and ΛN ($U_{\Lambda N} = -30$ MeV) interaction is kept constant. If the interaction is repulsive ($U_{\Sigma N} \geq 0$ MeV), the Σ hyperons are not anymore bound to the nuclear matter and thus the EoS in principle stiffens. For lower branches in Fig. 1.17 (a) σ, ω and ρ were

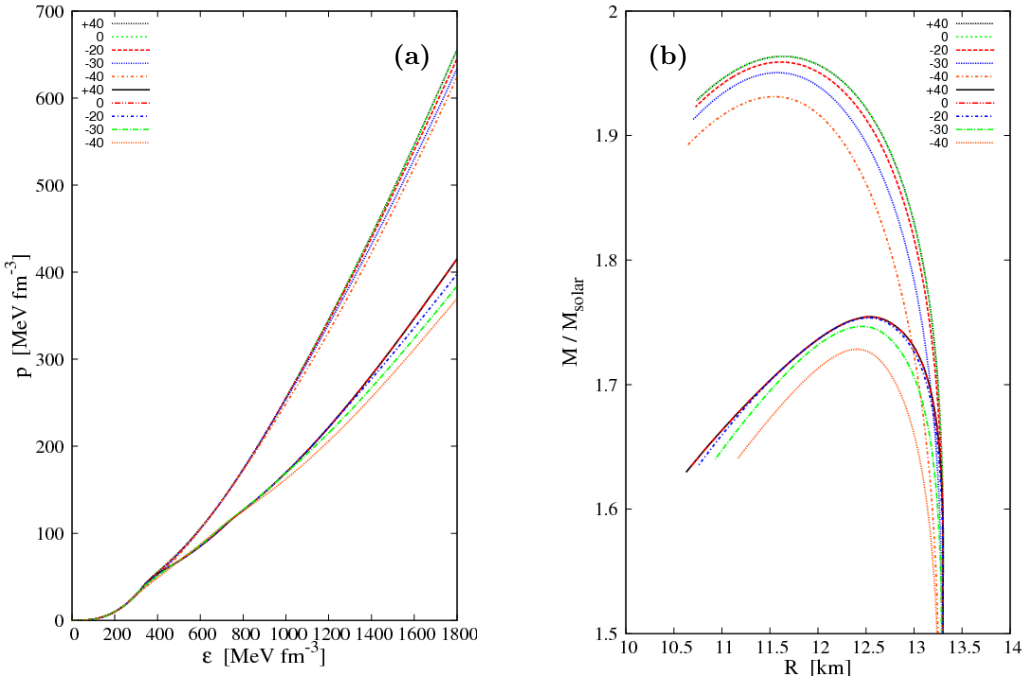

Figure 1.17: (a) EoS for different potential depths $U_{\Sigma N}$ for details see legend [WCSB12]. (b) The mass-radius relation for NS obtained with the different EoS [WCSB12]. The lower branch is obtained for "model $\sigma\omega\rho$" for the GM1 parameter set while the upper branch is obtained including additionally the ϕ meson. Figures taken from [WCSB12].

considered as exchange mesons. The upper branches were obtained including additionally the ϕ meson. The EoS depend only little on the ΣN interaction, while the inclusion of an additional exchange meson, ϕ mesons, significantly influences the EoS. The inclusion of ϕ meson stiffens the EoS and thus higher maximal neutron star masses can be reached as shown in Fig. 1.17 (b). Instead of a maximal mass of $M = 1.75\ M_{\odot}$ with a repulsive ΣN interaction, the maximal mass is increased to $M = 1.96\ M_{\odot}$. Hence, the scenarios, with a repulsive ΣN interaction in combination with YY interactions mediated by ϕ mesons, would agree within error with the observation of neutron star PSRJ1614-2230 [C^{+}06, D^{+}10] with a mass of $1.97 \pm 0.05\ M_{\odot}$. The ϕN coupling strength plays a decisive role in the description of YY interactions. If one considers the in-medium ϕ properties in this context, direct evidence of a significant ϕN coupling, hence ϕ absorption within nuclear matter (Section 1.5), would lead to more realistic EoS of dense nuclear matter with hyperon content, in heavy-ion collisions, but possibly also in NS [WCSB12].

The different inner core scenarios often treat the inner-core constituents along with their interaction separately. However, in nuclear physics the interrelation between the several hadrons species is observed. Strangeness exchange reactions (e.g. $K^{-}N \rightarrow Y\pi$) couple the hyperons with antikaons. The ϕ meson plays a decisive role in the description of hyperon-hyperon interactions. Hence, in-medium modification of each hadron species will affect the other. To provide a realistic EoS of dense matter and possibly also NS, the $\bar{K}N$, ϕN and YN interactions have to be simultaneous considered.

2 Pion Beam Facility for HADES

In 2014 the versatile HADES setup at the GSI pion beam facility [AM$^+$17a] provided a worldwide unique opportunity to study pion-induced nuclear reactions and therefore extended its existing experimental campaigns with proton and heavy ion beams. A broad physics program was addressed investigating elementary reactions ($\pi^- + p$) at several incident pion beam momenta varying from 0.656 GeV/c to 800 GeV/c as well as pion-nucleus collisions ($\pi^- + A$, with A = C or A = W) at 1.7 GeV/c.

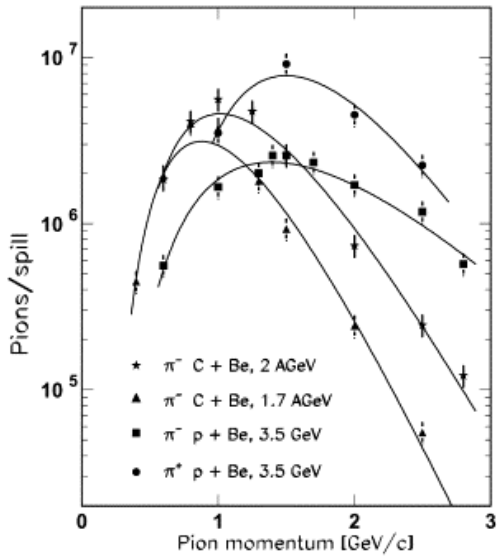

Figure 2.1: Pion intensity at the HADES target position for different primary beams, p and ^{12}C, as a function of central beam momentum of the pion beam chicane [D$^+$02].

Secondary pion beams are created at GSI pion beam facility by impinging high intensity proton or ion beams on a 1.84 g/cm^2 dense Beryllium target with a pencil shape along the first 3 cm with a diameter of 7 cm tapering to a final diameter of 4 cm. A previous study [D$^+$02] showed that fully stripped ^{12}C or ^{14}N ions close to the SIS18 space charge limit ($0.8 - 1.0 \times 10^{11}$ ions/s) at an energy of 2 AGeV lead to maximal pion currents at the HADES target covering the anticipated central beam momentum range from 0.656 GeV/c to 1.7 GeV/c (see Fig. 2.1). For technical reasons a primary ^{14}N ion beam was chosen. During the collision process various particle species are produced including positively and negatively charged pions. Since for positively charged pions the proton contamination is quite huge, negatively charged particles including π^- are chosen by the ion optic settings. Afterwards the π^- are transported along the pion beam chicane to the HADES detector, depicted in Fig. 2.2.

Due to the production kinematics at these relatively low beam energies, the outgoing pion spectrum is wide in momentum ($\Delta p/p \approx 8\,\%$) and angle, only limited by the ion optical properties and

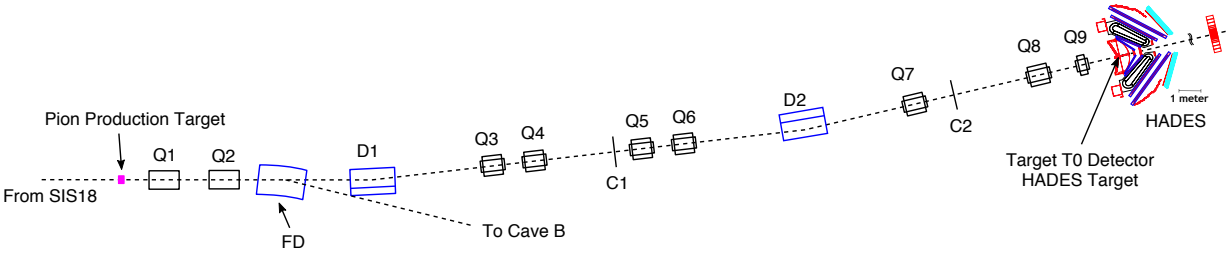

Figure 2.2: Schematic overview of the pion beam chicane between the pion production target and the HADES detector. The dipole magnets (D), quadrupoles (Q), tracking detectors (C1,C2) and the target T0 detector are included indicated. The FD dipole used to direct the beam to cave B is shown as well.

geometrical acceptances of the beam line components. The electron as well as muon contamination at the HADES target position was found to stay well below 1% for the pion beam momentum setting of 1.7 GeV/c [AM$^+$17a, D$^+$02]. The intensities of secondary negatively charged pion beam on the HADES reaction target inside the accepted momentum range amounted to $\approx 3 \times 10^5$ π^-/s.

2.1 CERBEROS

Since the outgoing spectrum of secondary pion beams is wide in momentum and angle ($\Delta p/p \approx 8\,\%$), only restricted by intrinsic properties and geometrical acceptance of the ion optics, CERBEROS (**Ce**ntr**a**l **Be**am T**r**acker for Pi**o**n**s**), a secondary beam diagnostic system, was developed. It allows for online beam monitoring at high beam rates ($> 10^6$ part./s) as well as the momentum reconstruction of each individual pion with a resolution of $\Delta p/p < 0.5\%$ mandatory for exclusive measurements of various final states. For example in the reactions like $\pi^- + p \rightarrow ne^+e^-$ the knowledge of the precise pion momentum on a per-mill level is important to disentangle the contributions of the different baryonic resonances.

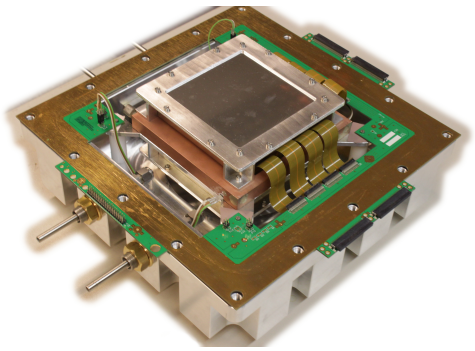

Figure 2.3: Top view of one assembled tracking detector with a silicon sensor in the center.

The momentum is evaluated using the beam optics transport code [AM$^+$17a] and the position information of each hit detected by the double sided silicon sensor located along the pion beam chicane at two different positions indicated with C1 and C2 in Fig. 2.2. Both silicon sensor have an active detection area of $10 \times 10\,\mathrm{cm}^2$ to cover most of the area inside the beamline. The multiple scattering is kept minimal with a thickness of 300 ± 10 μm. Each side is segmented into 128 parallel strips of length $L = 97.22$ mm with a single strip width of 700 μm and a pitch of

$\Delta = 760$ μm. Hence, a position measurement resolution of at least $\Delta/\sqrt{12} = 219$ μm can be reached for both directions. The strips on the front and back side are oriented perpendicularly to each other. The radiation hardness is realized with a p-bulk and therefore no type-inversion is generated. In addition, the silicon sensors are operated at temperature of around $-5\,^{\circ}$C to not only reduce the effects from radiation damages, but also to lower the reverse current at operational bias voltage, which contributes to electronic noise generation and hence affects the achievable detector energy resolution. A photograph of the assembled detector setup is presented in Fig. 2.3. To guarantee fast tracking, each silicon sensors is readout with n-XYTER chips. Due to its self-triggering architecture and local storage capability, the n-XYTER enables on-line tracking of each individual pion. Moreover, it provides time information which enables the possibility to correlate the events in the first and second detector as well as with the whole HADES detector. The read-out rate amounts to 32 MHz with on average 160 kHz per channel. The readout chain is completed by the TRB3, allowing the integration of the secondary beam tracker into the HADES data acquisition system and the operation as a stand alone system. The timing signals from the CERBEROS beam tracking detector layers (resolution $\sigma = 8.0$ ns) coincident within a 400 ns broad time window with respect to the T0 signal (Section 2.2.1) allowed to suppress pile-up and multi hit events in the tracking stations. In the experimental pion-nucleus campaign ($p_{\pi^-} = 1.7$ GeV/c) the first tracking station (C1) close to the pion production target experienced an average particle hit rate of 7 MHz, while hit rates on the second tracking station (C2) were about an order of magnitude smaller (800 kHz). With that detection efficiencies of $\varepsilon = 92.5\%$ for the upstream tracking station (C1) and $\varepsilon = 93.2\%$ for the downstream detector (C2) were achieved. The resulting track identification efficiency was $\varepsilon = 87.0\%$. Further details can be found in [AM$^+$17a].

2.2 HADES experiment

The **H**igh **A**ceptance **Di**-**E**lectron **S**pectrometer (HADES) [A$^+$09c] is a fixed target experiment currently located at the SIS18 [1] of the GSI Helmoltzzentrum für Schwerionenforschung GmbH in Darmstadt (Germany). With a magnetic rigidity of 18 mT, the SIS18 can deliver protons with a maximum kinetic energy of 4.5 GeV and heavy ions with up to 2 AGeV. In combination with the pion beam facility located at SIS18, which provides a secondary pion beam in the momentum range of $0.4 - 2.0$ GeV/c, it enables a broad lepton and hadron physics program with elementary, hadron-nucleus and heavy-ion collisions with HADES.
The properties of mesons, their width and/or mass, immersed in a strongly interacting environment are of great interest. HADES explores the effects of nuclear matter in heavy-ion collisions in which baryon densities exceed the normal nuclear density ($\rho = 2 - 3\,\rho_0$) at moderate temperatures. While elementary processes, $p + p$ and $\pi^- + p$ ($\rho = 0$), are studied to serve as a reference, modifications of meson properties are already expected in cold nuclear matter ($\rho = \rho_0$), which is studied in hadron-nucleus reactions, where dynamics are less complex and fundamental aspects can be addressed more directly. Especially for the light vector mesons ρ, ω and ϕ their rare decay channel into e^+e^- pairs is of special interest, since their decay products are not distorted by the strong interaction. Results on the vector meson based on the di-electron spectra in various colliding systems like $p + p$, $d + p$, p + Nb, C + C, Ar + KCl and Au + Au can be found in [A$^+$12d, A$^+$12e, A$^+$10c, A$^+$12c, A$^+$07, A$^+$08, A$^+$11a, AM$^+$19a]

1 Schwerionen Synchrotron

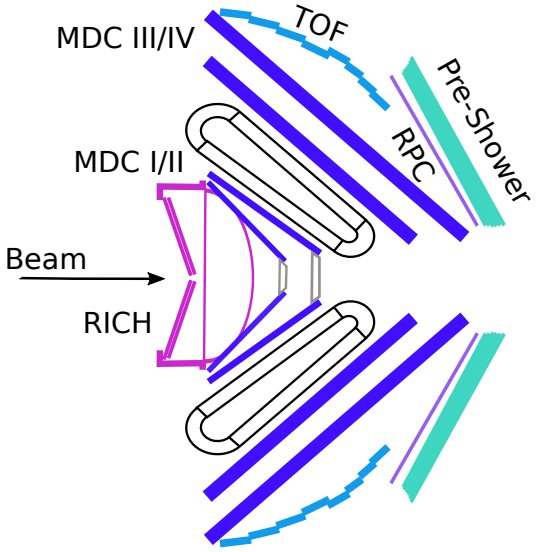

Figure 2.4: Schematic view of HADES with an angular coverage from $18° \leq \theta \leq 85°$. The beam is impinging on the target-T_0 detector, which is located in front of the target inside the beampipe surrounded by the RICH detector. The MDCs, two in front and two behind the superconducting magnet are by the the time-of-flight detectors (TOF and RPC).

Besides, HADES has also covered various aspects in the field of strange hadron physics. The production of Λ [AM$^+$17c] as well as $\Lambda(1405)$ [A$^+$13a] and $\Sigma(1385)$ [A$^+$12b] resonances amongst the associate K^0 [A$^+$14a] and $K^*(892)^+$ [A$^+$15c] production were studied in $p+p$ reactions at 3.5 GeV. In the same collision system also the existence of kaonic clusters (ppK^-) [A$^+$15d] were addressed. In $p+$Nb reactions at 3.5 GeV the Λ production and Λ polarization [A$^+$14c] as well as the Λp interaction via femtoscopy [AM$^+$16] was studied. In addition the production of another hyperon, namely the Σ^0, was determined, which allowed to extract the Λ/Σ^0 ratio. Also in Ar + KCl collisions at 1.76 AGeV the Λ production [A$^+$11b] and Λp interaction via femtoscopy [A$^+$10b] was investigated. Besides the (deep) sub-threshold production of Ξ in $p+$Nb [A$^+$15e] and Ar + KCl collisions [A$^+$09a], also the deep sub-threshold $K^*(892)^0$ production was studied in latter collision system [A$^+$13b]. The ϕ meson as relevant source for the K^- production was discussed not only in Ar + KCl reactions [A$^+$09b] but also Au + Au collisions at 1.23 AGeV [AM$^+$18a]. Moreover serveral studies were devoted to the presence of the repulsive KN potential in $p+$Nb [A$^+$14d], Ar + KCl [A$^+$10a] and Au + Au collisions [AM$^+$19c].
HADES is composed several subsystems for hadron identification, which is based on time-of-flight and on specific energy loss (dE/dx) in combination with the momentum measurement. A schematic layout of the spectrometer is shown in Fig. 2.4. It consists of six identical sectors surrounding the beam axis with a large azimuthal acceptance of about 85% covering polar angles from $15° \leq \theta \leq 85°$.

2.2.1 Target-T_0 detector

The target-T_0 detector is employed to allow for beam profile determination and generation of fast timing signals for trigger purposes as well as time-of-flight particle identification. The detector was

particularly designed for the pion beam champaign to achiev excelent timing presison ($\leq 100\,\mathrm{ps}$). However, due to pick-up noise only time resolutions of $\sigma_t \simeq 250\,\mathrm{ps}$ [AM+17a] were obtained. The detector consists in total of 9 metallized sc-CVD[1] diamond sensors arranged on two support boards with 5 and 4 sensors (Fig. 2.5). Each of the diamond elements has an active area of $4.3 \times 4.3\,\mathrm{cm}^2$ with fourfold segmentation. A thickness of 300 μm was chosen as a compromise between multiple scattering and reasonable signal-to-noise ratio.

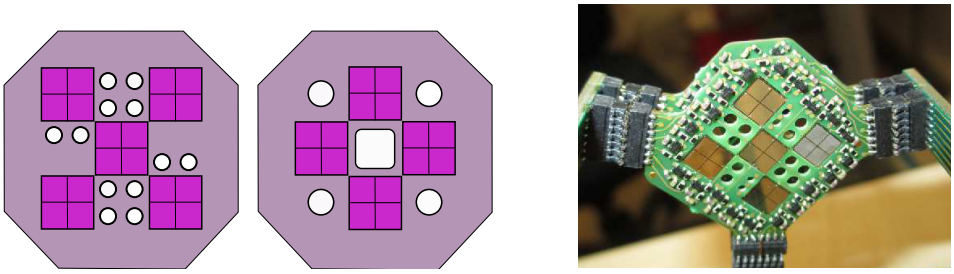

Figure 2.5: Left: Top view of the diamond support PCBs (Printed Circuit Board) containing five and four diamond sensor plates with fourfold segmentation, indicated in magenta. Right: Photograph of the assambeled target-T_0 detector taken from [AM+17a].

2.2.2 Target

The fixed target is located inside the beamline surrounded by the RICH detector. Drawings of the carbon and tungsten targets each composed of three segments are depicted in Fig. 2.6, with the different features listed in Table 2.1.

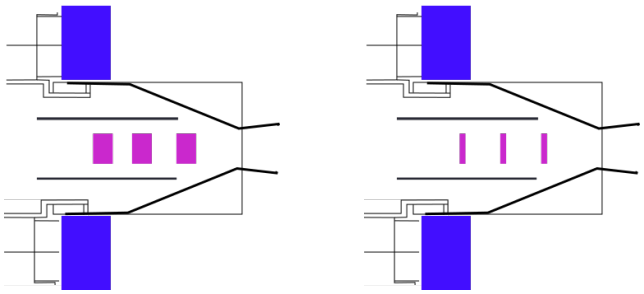

Figure 2.6: Drawing of the targets employed during the pion-nucleus production run: carbon (left) and tungsten (right)

Table 2.1: Properties of all target stacks that were employed during the pion-nucleus campaign.

Target	$N_{Segment}$	∅ [mm]	d [mm]	ρ [g/cm]	A
W	3	12	2.4	19.3	183.84
C	3	12	7.2	1.85	12.011

1 Chemical Vapor Deposition

2.2.3 RICH detector

The **R**ing **I**maging **Ch**erenkov detector is the innermost part of the spectrometer and was developed for electron and positron identification in the momentum range of 0.1 GeV/$c < p_{e^\pm} < 1.5$ GeV/c. Charged particles passing through the detector gas polarize the molecules that afterwards relax by radiation emission. If the velocity of the particles is larger than the radiator specific Cherenkov threshold γ_{thr}, a coherent wave front builds up and Cherenkov light is generated. While electrons and positrons travel at almost speed-of light, muons and hadrons are in the range of $\beta < 0.95$ at SIS18 energies. By using the radiator gas C_4F_{10} with a proper refractive index and thus a Cherenkov threshold of $\gamma_{thr} = 18$, the detector is hadron blind.
As illustrated in Fig. 2.7, the Cherekov light generated is reflected by a spherical carbon shell mirror through the CaF_2 window and focused to a ring. Finally, the photons hit the CSI cathode knocking out electrons, which are further amplified in the CH_4 filled Multi-Wire Proportional Chamber (MWPC) in front of the readout pad plane.

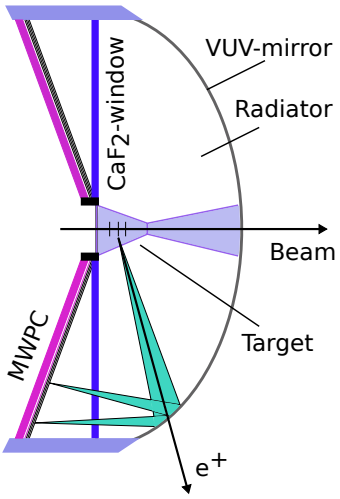

Figure 2.7: Schematic view of the RICH detector. The Cherenkov light produced by the traversing positron is reflected on the mirror and focused to a ring on the MWPC.

2.2.4 Mini-Drift Chambers (MDCs)

The tracking is done with four **M**ini-**D**rift **C**hamber (MDC) planes (I-IV), two in front (I-II) and two behind (III-IV) the toroidal magnetic field. Each MDC plane surrounding the beam axis is divided into six identical trapezoidal detection sections, each with six drift cell layers. All six drift cell layers have sense/field wires that are aligned at different stereo angles ($\pm 0°, \pm 20°, \pm 40°$) as shown in Fig. 2.8. To ensure constant drift cell granularity, the module sizes is increasing from 88 cm × 80 cm to 280 cm × 230 cm for the outermost MDC plane.
The most inner MDC plane and MDC II was filled with gas mixture of Ar:$O_2 = 70 : 30$, whereas the gas mixture of the other planes was Ar:$C_4H_{10} = 84 : 16$ [Sch16]. As they pass through the drift chambers, charged particles ionize the gas molecules and form electrons among ions along their trajectory. While the electrons are accelerated in the electric field generated between the cathode and anode wires and cause an electron cloud (avalanche effect). This drifting electron

cloud introduces an electrical signal into the field wire, which is then read out. As shown in Fig. 2.9 (left), a hit position is measured in each individual MDC plane, whereby the two almost straight hit points in the first two planes (MDC I-II) are combined to form an inner track segment and the other two, which are deflected by the magnetic field, form an outer track segment. On the basis of the Runge-Kutta method and the exact knowledge of the toroidal field map, which is (eventually) combined with a hit point in the META system (Section 2.2.6), the equation of motion is solved numerically using the MDC hit positions as a starting condition. In this way, the particle track points, the path length and the momentum are obtained with a resolution of $1-4\%$. In addition the MDCs provide the energy loss information (dE/dx), which is retrieved from the correlation of the energy loss to the Time-over-Threshold (ToT). The ToT is the duration in which the electric signal exceeds a certain threshold of the readout electronics and depends on distance from the field wire, the impact angle and the momentum of the particle. With the help of a rather complicated procedure to entangle dependencies on e.g. the reduced electric field, on the track geometry, on the drift cell size the energy loss was calibrated [Sch16].

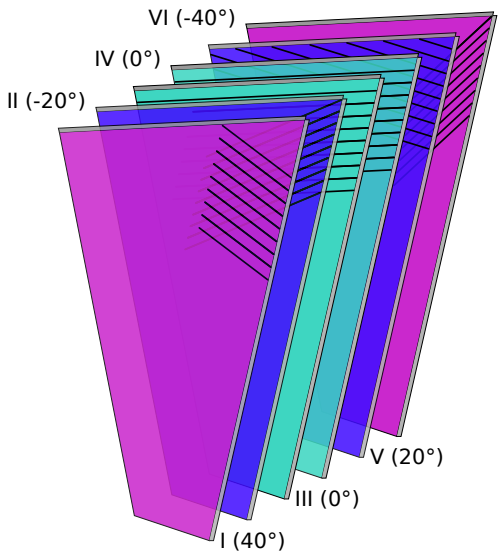

Figure 2.8: Schematic layout of a Mini-Drift Chamber module consiting of six drift cell layers with different orientation of the field wires as indicated. Figure adapted from [Mau19].

2.2.5 Magnet

The **I**ron **L**ess **S**uperconducting **E**lectromagnet consists of six NbTi-coils surrounding the beam axis. Each coil is cooled down to temperatures of 4.7 K with liquid He at 2.6 bar. The toroidal field has a maximal strength of 3.6 T, which is reached inside the coils. While in the region of the MDCs a magnetic field of around 0.8 T is provided, the area around the target and active volume of the RICH is kept nearly field-free. Charged particles traversing the toroidal field are deflected according to the Lorentz force. By measuring the bending of the particles in the two MDC planes in front and behind the magnet in combination with their charge given by their bending direction one can directly derive the momentum.

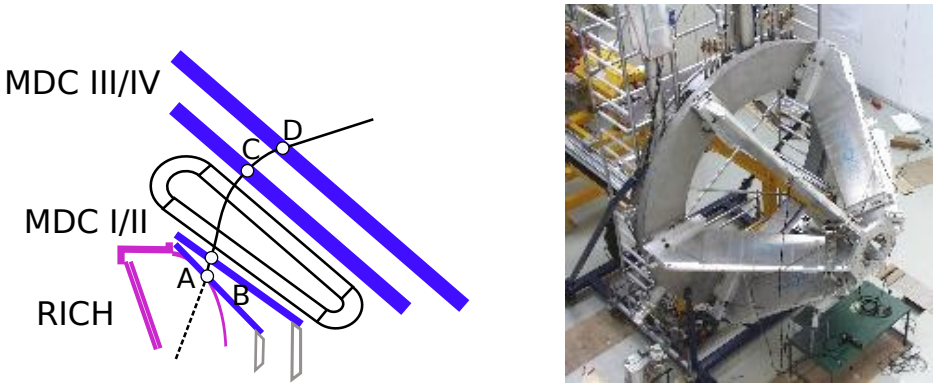

Figure 2.9: Left: Schematic view of the magnet spectrometer equipped with four planes of Mini-Drift Chambers (MDC I-IV) and the superconducting toroidal magnet (ILSE). The trajectory and momentum of traversing particles is reconstructed by measuring the hit points in each MDC and the deflection caused by the magnetic field. Right: Photograph of the superconducting toroidal magnet of HADES taken from [HADa].

2.2.6 META System

Multiplicity **E**lectron **T**rigger **A**rray (META) consists of the two time-of-flight detectors **TOF** and **RPC** accompanied by the electromagnetic shower detector **Pre-Shower**. All three detector systems are located behind MDC IV. Their main tasks are the provision of the charged particle multiplicity for the trigger decision, the time-of-flight measurement in combination with the target-T_0 detector for particle identification as well as the improvement of the reconstructed track purity by spatial correlation of the track in the MDCs with the hits in the META.

- **Time-of-Flight (TOF)**:
  The TOF wall is divided into the six hexagonal structure, like the entire spectrometer array. It covers polar angles of $44° < \theta < 85°$. Each of the six sectors consists of 8 modules with 8 plastic scintillation rods, with a total of 384 rods. Charged particles passing through the BC408 plastic scintillator excite the material that emits photons when it returns to the ground level. The photons are then captured by the PMTs[1] at both ends of each scintillation rod. The measured pulse arrival time with a resolution of $\sigma_t \approx 150\,\text{ps}$ [A$^+$02, A$^+$09c] and pulse height is related to the time-of-flight and energy loss (dE/dx) information that can be used for particle identification.

- **Resistive Plate Chamber (RPC)**:
  The RPC wall covers the low polar angle region of $18° < \theta < 45°$. The six identical sectors feature in total 187 cells. All cells are composed alternatively of aluminum electrodes and float-glass layers with a gas gap ($C_2H_2F_4$:SF_6 = 90:10) in-between, as shown in Fig. 2.10 right. Charged particles ionizes the gas triggering an electron avalanche due to the high electric field between the aluminum electrodes, which leads to a discharge. The anticipated time resolution is below $\sigma_t \approx 100\,\text{ps}$ [B$^+$09b] for improved particle identification.

- **Pre-Shower**:
  The Pre-Shower detector is mounted behind the RPC wall (see Fig. 2.4) having the same

1 Photo-Multiplier Tubes

polar and azimuthal coverage. As shown in Fig. 2.10, each pre-shower sector is composed of three wire chambers (pre-chamber, post1-chamber, post2-chamber) filled with an isobutane-based gas mixture separated by two lead converter layers. When passing through the lead converters, electrons and positrons generate Bremsstrahlung ($\propto \gamma^4$), which annihilate further via pair-production resulting in the build-up of an electromagnetic shower. Due to the significantly lower γ of hadrons, the effect of Bremsstrahlung is suppressed. The different measured charge patterns help to separate electrons and positrons from hadrons and thus complete the capability of the RICH detector.

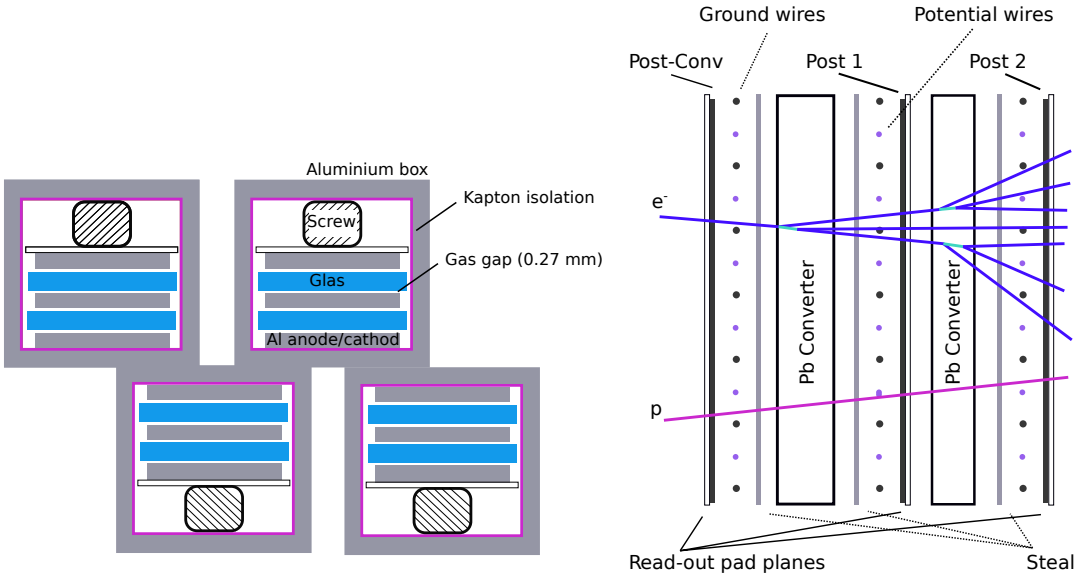

Figure 2.10: Cross-section of the RPC cells (left) and of the Pre-Shower cell (right) showing the internal structure.

2.2.7 Forward Wall

The **F**orward **W**all (FW) is 7 m downstream of the target and covers low polar angles of $0.33° < \theta < 7.17°$ with full azimuthal coverage. It is a scintillation hodoscope with a total size of $180 \times 180\,\mathrm{cm}^2$ and comprises three different module sizes increasing from the inner to the outer region: $4 \times 4\,\mathrm{cm}^2$ (small), $8 \times 8\,\mathrm{cm}^2$ (medium), $16 \times 16\,\mathrm{cm}^2$ (big) (Fig. 2.11). A total of 287 scintillator modules with a thickness of 2.54 cm are installed, which are read out by individual PMTs. It provides position and time-of-flight information, while main purpose is event plane reconstruction and spectator tagging.

2.2.8 Hodoscope

The Hodoscope, which is located at the end of the detector array, covers polar angles outside the spectrometer and Forward Wall acceptance and is used to monitor the y-position of the secondary pion beam. A total of 16 plastic rods are horizontally aligned and are read on each side by a PMT (0.75 inch Hamamatsu R3478 PMT), resulting in 32 readout channels.

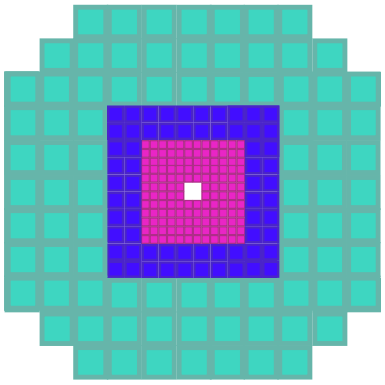

Figure 2.11: Schematic view of the Forward Wall consisting out of 287 scintillator modules with the three different cell regions: magenta ($4 \times 4\,\mathrm{cm}^2$), blue ($8 \times 8\,\mathrm{cm}^2$) and cyan ($16 \times 16\,\mathrm{cm}^2$).

2.2.9 Trigger decision

HADES is a triggered experimental setup. If the incoming beam particles interact with the target nucleons, the reaction products may be registered by the sub-detectors leaving a signal, that can be used as an input for the Central Trigger System (CTS). Afterwards the CTS transmits a trigger signal to all detectors. The CTS is based on a trigger-busy-release architecture, so that it is only possible to generate a new trigger signal after all sub-detectors are able to process the next event. In general, the trigger decision is divided into two stages:

- **LV1 trigger**:
  The first level trigger (LVL1) selects only events with a minimal charged particle multiplicity, which is supposed to minimize the contamination from random noise events in the data. For the pion-nucleus campaign a charged particle multiplicity $M \geq 2$ in the META system (TOF/RPC) (Section 2.2.6) in combination with a hit in the target-T_0 detector (Section 2.2.1) required by the so called PT1-trigger. Only if the LVL1 trigger condition is fulfilled, the event is further processed by transmitting the trigger signal to all sub-detector systems.
- **LV2 Trigger**:
  The LVL2 trigger is supposed to enhance events containing e^+/e^- pairs. Therefore the online Imaging Units (IPUs) is searching Although this trigger has not been employed in the experimental pion beam campaigns.

3 Data and Event Selection

3.1 Event Selection

To ensure that only pion-nucleus collisions ($\pi^- + A$, with A = C or A = W) are selected in the following analysis, the events must meet certain criteria regarding the quality and coincidence of multiple sub-detector measurements as well as restrictions of the reconstructed event vertex. Due to the large width ($\delta x = 1$ cm (rms)) of the secondary pion beam [AM$^+$17a], the pions can interact not only with the target material, but also with surrounding structures like the beam tube. In addition, it can happen that multiple pions interact with the target within the time window of the data acquisition, a so-called pile-up event, which leads to an incorrect determination of the reaction time t_0 and thus also to an incorrect time-of-flight measurement. This can lead even more to a incorrect absolute normalization. The following criteria have been applied:

- The trigger decision with a minimum charged particle multiplicity $M \geq 2$ in the META system has to be fulfilled (mandatory in the simulation).
- **GoodTrigger:** All events have to fulfill the physical trigger condition PT1 (Section 2.2.9).
- **GoodStart:** The target-T_0 detector must have registered a hit in the detector layers.
- **NoPileUpStart:** The multiplicity registered in the target-T_0 detector has to be one in a certain time interval (-5 ns $< t_0 <$ 15 ns) around the reaction time.
- **GoodClustVert:** A criteria is applied on the event vertex reconstructed requiring at least one track in the inner MDCs (ClusterVertex). The criteria is only fulfilled, if the χ^2 of the vertex reconstruction is greater than zero and if the reconstructed vertex position in z-direction is $z > -160$ mm.

3.2 Primary Vertex Reconstruction

The primary vertex was used to ensure that only particles originating from the target region are selected. The current analysis framework of the HADES experiment, HYDRA2, provides three different types of primary vertex reconstruction methods. The Low-Level-Vertex method (ClusterVertex) requires at least one track in the inner MDC chambers. However, this method provides only the primary vertex information in the z-direction. While the more advanced method (Vertex), which is reconstructed on the basis of at least two tracks in all MDC chambers, also provides the x- and y-coordinates of the primary vertex. The last method (RecVertex) requires at least two fully tracked particles in all MDC chambers in combination with a matching hit in the META. Single track events were also considered in the analysis and in these cases the primary vertex was reconstructed by the distance of closest approach (DCA). This allowed to reduce the bias for the inclusive hadron analysis, as otherwise reactions with at least two fully-tracked

particles (within HADES) are favored. Figure 3.1 shows the primary vertex distributions in z-direction (left) and in the x-y plane (right) for at least one fully reconstructed charged particle. The global primary vertex resolution in z-direction was found to be $\sigma_{z_{PV}} \approx 4.7$ mm, while the one in x-(y-)direction is in the order of $\sigma_{x_{PV}} \approx 3.1$ mm ($\sigma_{y_{PV}} \approx 2.6$ mm). A strong dependence on the primary vertex reconstruction method is observed in x- and y-direction. Here the resolution roughly doubles (halves) compared to the global resolution for at least two fully tracked particles (single track events). Whereas in z-direction the difference is rather small with $\sigma_{z_{PV}} \approx 5.4$ mm for the single track events and $\sigma_{z_{PV}} \approx 4.5$ mm for at least two fully tracked particles. For details see Appendix A. Only events in the primary vertex range of $-80\,\text{mm} < z_{PV} < 5\,\text{mm}$ and $\sqrt{x_{PV}^2 + y_{PV}^2} \leq 20\,\text{mm}$ were considered for further analysis.

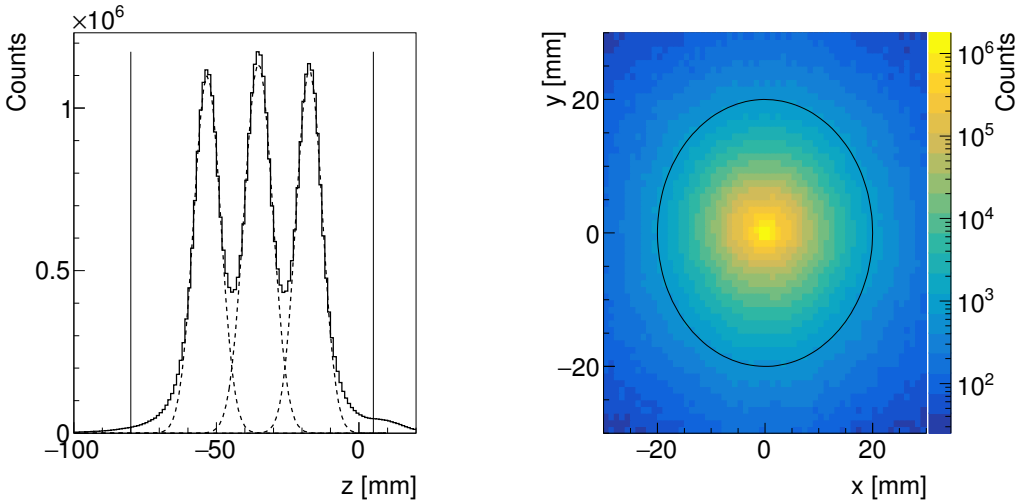

Figure 3.1: Primary vertex distribution in z-direction (left) and in the x-y plane (right) for at least one fully reconstructed charged particle. The black lines (circle) indicate the selected region raging from $-80\,\text{mm} < z_{PV} < 5\,\text{mm}$ ($\sqrt{x_{PV}^2 + y_{PV}^2} \leq 20\,\text{mm}$).

3.3 Particle Identification

The HADES detector offers an excellent charged particle identification capability by means of either the time-of-flight (β) information or the specific energy loss (dE/dx) measurement combined with the determination of the particle's momentum. Neutral particles can be reconstructed by their charged decay products with the invariant mass method, if they decay before reaching the active detector elements. Stable neutral particles cannot be measured with HADES.

3.3.1 Time-of-Flight Reconstruction

For the particle identification the particle's velocity β in combination with its momentum is commonly exploited. While the reaction time t_0 is provided by the target-T_0 detector (Section 2.2.1), the META detectors (RPC/TOF) (Section 2.2.6) deliver the second time signal t_{META} when the charged particles passed HADES. By combining both the time-of-flight $\Delta t = t_{META} - t_0$ can be

derived. Together with the traveled path length l_{META} from the event vertex to the hit in the META detectors the velocity β can be determined by the following formula:

$$\beta = \frac{v}{c} = \frac{\frac{l_{META}}{\Delta t}}{c} \tag{3.1}$$

As the theoretical velocity β_{theo} (Eq. (3.2)) can be derived from the momentum information and nominal mass (m_0), this information can be exploited to perform the identification of charged particles. Figure 3.2 shows the characteristic velocity β vs. charge q times momentum p distribution in the RPC (left) and TOF (right) detector accounting for the different time resolutions of both time-of-flight detectors. For both detectors, pronounced bands are visible indicating the different particle species ($e^{\pm}, \pi^{\pm}, K^{+}, p, d, t$). Most of the bands are well separated from each other resembling the high purity of this identification method and a rather low contamination from miss-identification. The theoretical curves calculated based on Eq. (3.2) are presented as black dashed curves in the β distributions (Fig. 3.2) for different particles.

$$\beta_{theo} = \frac{p}{\sqrt{p^2 + m_0^2}} \tag{3.2}$$

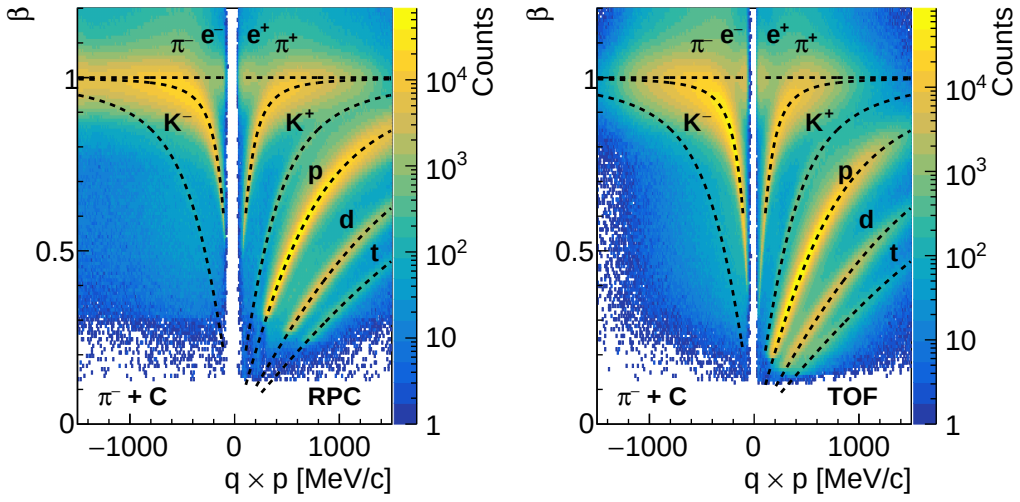

Figure 3.2: Velocity β as a function of the momentum times charge q separately for the two time-of-flight detectors RPC (left) and TOF (right) in $\pi^- + \mathrm{C}$ reactions. Indicated by the black dashed lines are the theoretically curves calculated for each particle species.

Charged Pion Identification

In the following the particle identification for the charged pions is described. Due to the similar kinematics and the high purity of the negatively charged pions, the particle identification criteria extracted for the negatively charged pions were also applied for the positively charged pions. The two-dimensional selections were calculated separately for the two time-of-flight detector systems, RPC and TOF. As presented in detail in Appendix D.1, for each detector system the distribution was projected in momentum intervals of 36 MeV/c on the velocity axis (Fig. D.1). The projections

were adapted with a Gaussian distribution to extract the mean μ and resolution σ of distribution. The so obtained mean μ follows with high accuracy the expected theoretical values according to Eq. (3.2). In Figure 3.3 (a) the dependence of the resolution σ on the momentum is depicted. As expected, it can be seen that the resolution of the RPC is better compared to the one of the TOF ($(\bar{\sigma}_{TOF} - \bar{\sigma}_{RPC})/\bar{\sigma}_{RPC} \approx 28\%$).

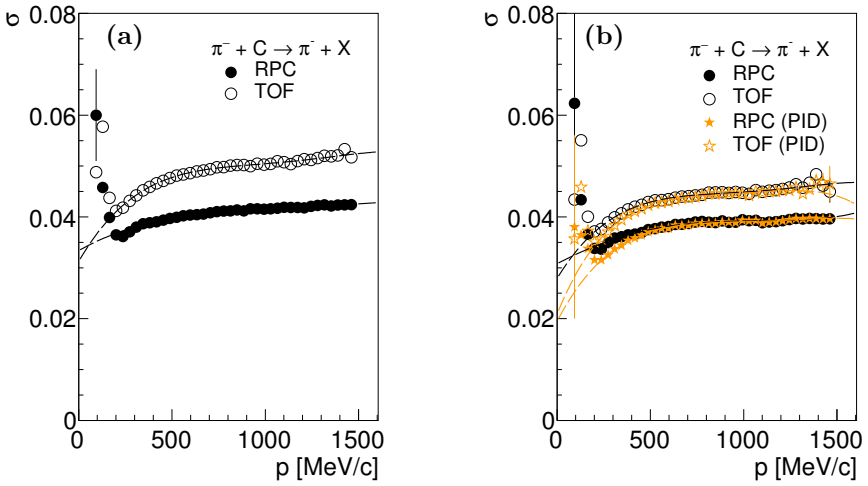

Figure 3.3: Velocity β resolution as a function of the momentum for negatively charged pions in the two time-of-flight detectors RPC (filed points) and TOF (open points) in $\pi^- + \mathrm{C}$ reactions for experimental data (a) and simulation (b). The stars correspond to the simulation containing only real pions (GEANT PID). The black (yellow) dashed lines correspond to a fourth-order polynomial fit.

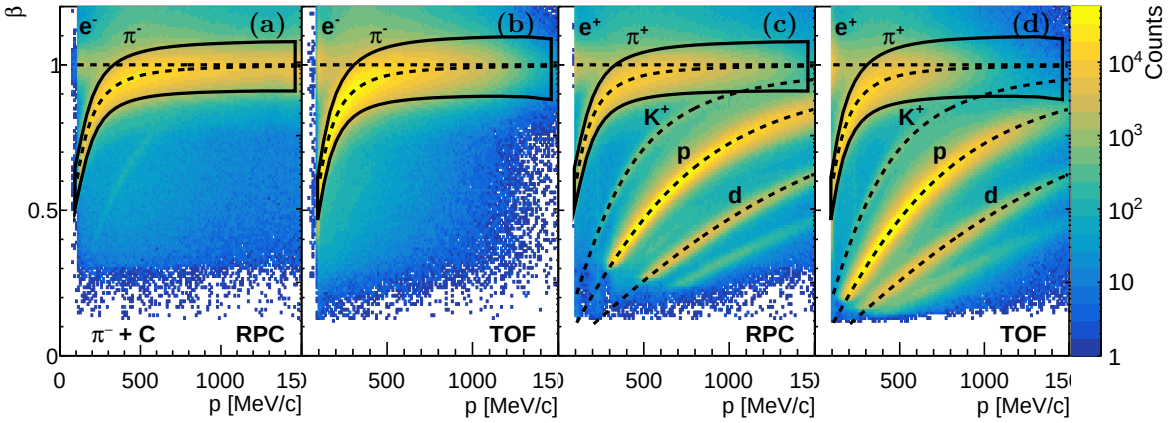

Figure 3.4: Correlation between β and momentum for negatively (a,b) and positively (c,d) charged pions for RPC (a,c) and TOF (b,d) in $\pi^- + \mathrm{C}$ reaction. The black dashed lines correspond to the theoretical velocity β_{theo}. The black curves resemble the applied two-dimensional selection.

However, the assumption of an underlying Gaussian distribution is not fully justified in the region of low momenta as the distribution has a non-linear relation between β and p. As the mean μ value is rapidly increasing within the momentum interval the projection is distorted. This is the reason for the deviation from the monotonic behavior of the resolution σ. Following the prescription already adopted in [Sch16, Sch17] to overcome this issue the distribution was

fitted with a fourth-order polynomial function to extrapolate the low momentum region. The resolution σ based on the fits indicated by the dashed line in Fig. 3.3 were further taken. The graphical selections were constructed as 2σ wide bands around the mean values. Fig. 3.4 shows the correlation between the velocity and momentum together with the resulting graphical selections used for both charged pions for RPC and TOF, respectively. In order to guarantee that simulations can be used to correct for the reconstruction efficiency (Section 3.6.4), it is mandatory that both, experimental and simulated data, are treated in the same manner. Since the velocity resolution is not fully reproduced by the simulation (Fig. 3.3 (b)), the same procedure was performed for the simulated data, such that small differences between the resolution of velocity measurement in simulation and experimental data are taken care of and thus the same pion fraction is selected. As the velocity resolution obtained in $\pi^- + \mathrm{C}$ reactions sightly deviates from those in $\pi^- + \mathrm{W}$ reactions, the two-dimensional selections was extracted for both collision systems (Appendix D.1) separately.

Another particle identification method is based on the reconstructed mass of the particles, which is related to its momentum and velocity via:

$$m = \frac{p}{\gamma\,\beta\,c} \tag{3.3}$$

with

$$\gamma: \quad \text{Lorentz factor } (\gamma = 1/\sqrt{1-\beta^2})$$

The reconstructed mass spectra of the both time-of-flight detector, RPC (left) and TOF (right), are displayed in Fig. 3.5 for $\pi^- + \mathrm{C}$ collisions. All particles are distributed around their nominal mass. In both mass distributions both charged pions are clearly visible, while the leptons are hardly seen. Since the antikaons are scare the distribution shows only a small peak corresponding to the positively charged kaons. Besides, heavier particles like protons, deuterons and tritons can be observed.

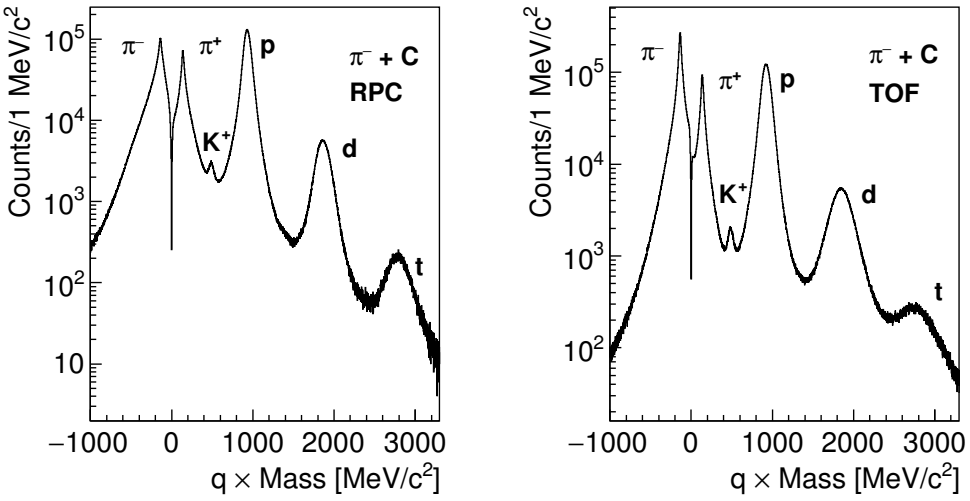

Figure 3.5: Mass spectra of charged particles separately for the two time-of-flight detectors, RPC (left) and TOF (right), in $\pi^- + \mathrm{C}$ reactions.

3.3.2 Specific Energy Loss Measurement

Besides the time-of-flight information, HADES offers the possibility to perform particle identification by means of the specific energy loss (dE/dx) measurement in the MDC chambers combined with the determination of the particle's momentum. This identification technique exploits the energy transfer of charged particles traversing through a medium to the shell electrons of the atoms. This effect is described by the relativistic Bethe-Bloch formula:

$$-\left\langle \frac{dE}{dx} \right\rangle = 4\pi N_A r_e^2 m_e c^2 z^2 \frac{Z}{A}\frac{1}{\beta^2}\left[\frac{1}{2}\ln\left(\frac{2m_e c^2\beta^2\gamma^2 T_{max}}{I^2}\right) - \beta^2 - \frac{\delta(\gamma)}{2} - \frac{C}{Z}\right] \tag{3.4}$$

with

ze :	charge of the traversing particle
Z, A :	atomic and mass number of the material
m_e :	mass of the electron
r_e :	Bohr electron radius
N_A :	Avogardo constant
I :	mean excitation energy of the material
$\delta(\gamma)$:	density correction (shielding of the particle's electric field by the atomic electrons)
C :	shell correction (low E: assumption atomic electrons are static not valid)
T_{max} :	maximal transferred kinetic energy $T_{max} = \frac{2m_e c^2\beta^2\gamma^2}{1+2\gamma m_e/M+(m_e/M)}$, were M denotes the particle mass

In the limit of $M \gg m_e$ the energy loss of a particle in a certain medium, defined by Z, A and I, depends only on its velocity β and charge ze. Since its velocity is related to its momentum and its mass ($p = \gamma m \beta c$), the energy loss as a function of the momentum is specific to each type of hadron.

Figure 3.6 shows the correlation between the specific energy loss in the MDC and the momentum in $\pi^- + \mathrm{W}$ reactions separate for the two time-of-flight detectors, RPC (left) and TOF (right), covering different areas in phase space. Although the MDC energy loss is measured independently, it shows a dependency on the selected time-of-flight system (RPC/TOF), indicating that the dE/dx is not perfectly calibrated. For both distributions, however, three distinct band are visible corresponding to the charged pions and protons as indicated by the theoretical Bethe-Bloch curves (dashed black curves). On the one hand both differ from the theoretical curve at low momenta, which can be attributed to the stopping of the slow particles in the detector material. On the other hand, while for the RPC selection the theoretical Bethe-Bloch curves are quite consistent with the experimental distribution, the distribution for the TOF shows indications of a slight deviation from the theoretical distribution for all hadrons types also at higher momenta.

Charged Kaon Identification

In the following the particle identification for the reconstruction of the charged kaons is outlined. As the antikaons are rare the extraction of the two-dimensional selection was performed using the positively charged kaons. However, due to the much smaller amount of kaons compared to

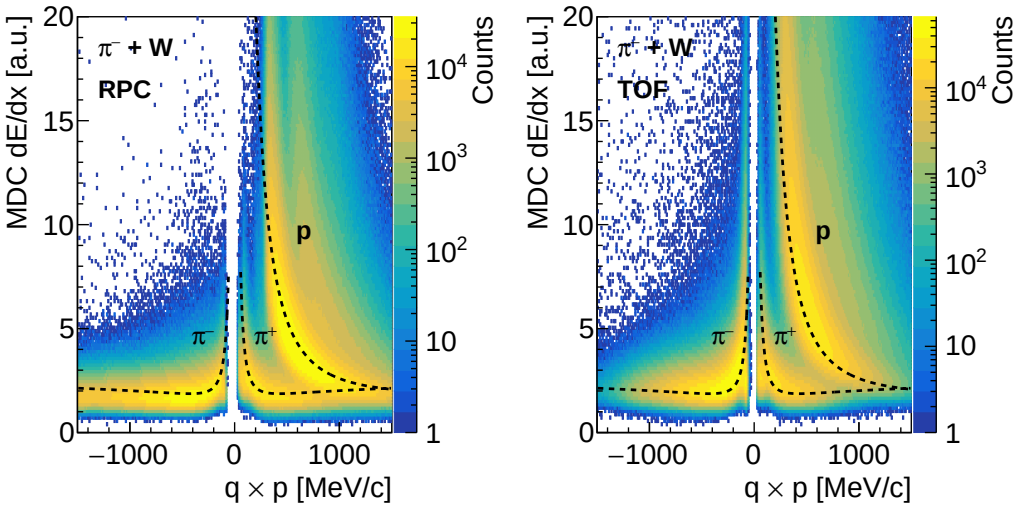

Figure 3.6: Correlation between the specific energy loss in the drift chambers and the momentum measured for the two time-of-flight detectors, RPC (left) and TOF (right), in $\pi^- + \mathrm{W}$ reactions. Indicated by the black dashed curve are the theoretical values calculated for each particle species according to the Bethe-Bloch formula.

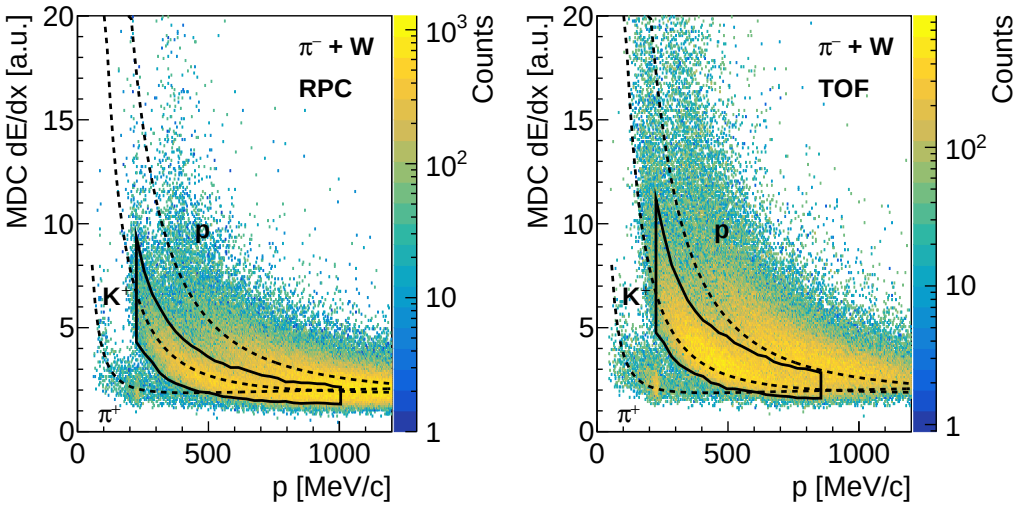

Figure 3.7: Energy loss in the MDCs as a function of the momentum for the reconstructed positively charged kaon candidates separately for the two time-of-flight detectors, RPC (left) and TOF (right), in $\pi^- + \mathrm{W}$ reactions. The contamination from other particle species has been reduced (for details see text). The dashed black lines correspond to the specific energy loss according to the theoretical Bethe-Bloch curves. The solid black line indicates the applied graphical cuts for the kaon selection.

pions and protons (Fig. 3.6), the K^+ have been pre-selected based on the correlation between β and momentum[1] (Fig. 3.2). The resulting MDC dE/dx distributions are represented in Fig. 3.7

1 $p/\sqrt{p^2 + m_0^2} \pm 0.05 \gtrless \beta_{RPC/TOF}$

separated for the two different time-of-flight detectors (RPC/TOF) with the theoretical Bethe-Bloch curves (dashed black lines) for different particles (π^+, K^+, p). In Figure 3.7 the deviation of the distribution from the theoretical values for the TOF detector is even better visible.

In general, the energy loss distribution of all hadrons can be described by a Landau (μ_L, σ_L) that is convoluted with a Gaussian (σ_G) distribution. While the Landau function considers the specific energy loss in the MDC chambers, the Gaussian function represents the finite detector resolution. As follows, the energy loss spectra were divided into momentum slices of 30 MeV/c and projected onto the energy loss axis to obtain two-dimensional sections for the identification of charged kaons based on the extracted mean and sigma of the convoluted Landau-Gaussian function.
Due to the non-negligible contamination of remaining pions and protons in the pre-selected and projected dE/dx spectra, dedicated background samples based on the correlation between β and momentum for each background particle species were produced and fitted with a convoluted Landau-Gaussian function as well. In this way, initial values for the simultaneous fitting procedure of all three particle species were derived to extract the mean value ($\mu_{K^+} = \mu_{L,K^+}$) and the sigma ($\sigma_{K^+} = \sqrt{\sigma^2_{L,K^+} + \sigma^2_{G,K^+}}$) of the kaon energy loss for each momentum slice individually (see Fig. D.8). The so obtained mean μ deviates from the theoretical values, whereas the deviation is more pronounced for the TOF detector (Fig. D.9). In Figure 3.8 (a) the σ of the kaon energy loss as function of the momentum is depicted. A dependence on the RPC and TOF selection is clearly visible. The two-dimensional selections of K^+ indicated by the solid black curves in Fig. 3.7 were constructed around μ_{K^+} with $+4\sigma_{K^+}$ and $-3\sigma_{K^+}$ to take into account the underlying asymmetric distributions.

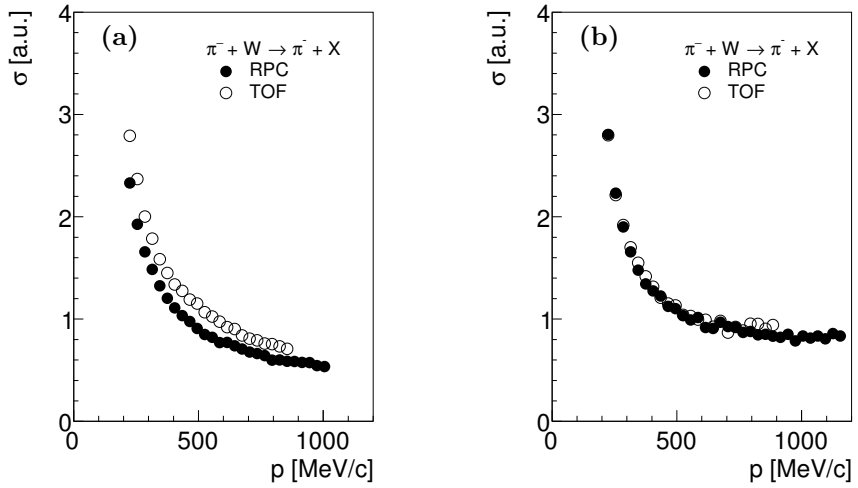

Figure 3.8: Specific energy loss dE/dx sigma as a function of the momentum for positively charged kaons for the two time-of-flight detectors RPC (filed points) and TOF (open points) in $\pi^- + \mathrm{W}$ reactions for experimental data (a) and simulation (b).

For the subsequent detector response/efficiency correction (Section 3.6.4), it is imperative that the simulated data is treated in the same way as the experimental data. Therefore, the selection power of the two-dimensional cuts must be the same for both. Since the energy loss resolution as a function of the momentum is not fully reproduced by the simulation (Fig. 3.8 (b)), the two-dimensional selections could not be applied to the simulation. Therefore, the same technique of extracting the two-dimensional selections was also applied to the simulation to ensure that the same kaon fraction is selected both in simulation and experiment. Further, details on the

extraction of the two-dimensional selection based on the specific energy loss (dE/dx) can be found in Appendix D.2.

3.3.3 Invariant Mass Technique

So far, only (direct) identification methods of charged particles leaving a trace in the detectors have been introduced. However, an additional method is particularly relevant for the reconstruction of neutral short-lived hadrons.
Neutral particles that decay before reaching the active sub-detectors of HADES can be still reconstructed via their charged decay products. The 4-momentum of the reconstructed mother particle can be determined by the sum of the 4-momentum of the daughter particles. Therefore, the mass of the mother particle can be calculated as shown in Eq. (3.5). For the invariant mass technique all n decay products have to be detected.

$$M_{inv} = \frac{1}{c^2}\sqrt{E^2 - \vec{p}^{\,2}c^2} = \frac{1}{c^2}\sqrt{\left(\sum_{i=0}^{n} E_i\right)^2 - \left(\sum_{i=0}^{n} \vec{p}_i\right)^2}, \tag{3.5}$$

with

$E/\vec{p}$: energy and momentum of the mother particle
$E_i/\vec{p}_i$: energy and momentum of the daughter particles

This procedure is applied to reconstructed the ϕ meson decaying into a charged kaon and antikaon ($BR \approx 48.9\%$ [P$^+$16a]). After attributing the nominal mass of daughter particles, the invariant mass $M_{K^+K^-}$ should be distributed around the nominal mass of the ϕ meson ($m = 1019.5$ MeV/c^2 [P$^+$16a]). For details refer to Section 6.1.

3.4 Absolute Normalization

The production cross-section of reconstructed particles is evaluated on the basis of the particle multiplicity, the total number of beam particles and the density of target atoms employing the following formula:

$$\sigma = \frac{N}{(N_{beam}\ \rho/A\ N_A\ d_{target})}, \tag{3.6}$$

with

N : number of reconstructed particles
N_{beam} : the number of incident pions
ρ/d_{target} : density and thickness of the solid target
A : mass number of the target nucleus
N_A : Avogadro constant

All relevant properties of the solid targets are listed in Table 2.1. The number of incident pions (N_{beam}) is deduced based on the hits in the target-T$_0$ detector (N_{T_0}), which have to be

corrected for the dead-time (T_{dead}) of the data acquisition system (DAQ) and the geometrical acceptance of the smaller solid target, indicated by the black circle in Fig. 3.9. The latter correction factor was deduced from dedicated beam transport calculations [AM$^+$17a]. This results in $N_{beam} = N_{T_0}\,(1 - T_{dead})\,(0.81 \pm 0.1)$. The uncertainty is due to the systematic uncertainty of the beam transport simulation. Another 10% uncertainty on the number of beam particles arises from investigations of elastic scattering in a subsquent experimental campaign with negatively charged pions with momenta of $0.656\,\mathrm{GeV/c} \leq p_{\pi^-} \leq 0.800\,\mathrm{GeV/c}$ impinging on a polyethylene (C_2H_4) target, in which day-by-day fluctuations of the hits in the target-T_0 detector (N_{T_0}) with respect to number of reconstructed elastic scattering events ($N_{elastic}$) have been observed [Sal18]. Another normalization method based on the total production cross-section in pion-induced reactions at 1.7 GeV/c was introduced (Appendix B). Within errors both methods are equivalent. In the following the normalization method based on Eq. (3.6) was used.

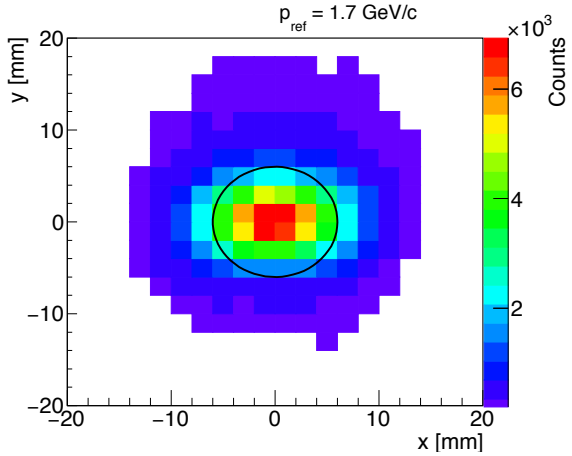

Figure 3.9: Pion beam spot in x-y plane at the position of the HADES target for central beam momentum of $p_{\pi^-} = 1.7$ GeV/c based on transport simulations. The circle indicates the effective target area. Figure taken from [AM$^+$17a].

Table 3.1: Total number of hits in the target-T_0 detector (N_{T_0}), number of events that fulfill the physical trigger PT1 (N_{PT1}) and the event selection (N_{evt}) as well as the dead-time of the data acquisition (T_{dead}) in both experimental campaigns.

Target	N_{T_0}	N_{PT1}	N_{evt}	T_{dead} [%]
W	4.08 10^9	2.00 10^8	1.69 10^8	0.154
C	4.31 10^9	1.58 10^8	1.33 10^8	0.156

3.5 (Double-)Differential Kinematic Anaylsis

A double-differential analysis in two independent kinematic variables offers the possibility to investigate the kinematic distribution of particles and thus should give insights into the particle interaction with nuclear matter. It is also important for reconstruction efficiency corrections within the geometrical acceptance of HADES, as explained in Section 3.6.4. On the one hand kinematic distributions in different momentum and polar angle ranges ($p - \theta$) are investigated, on the other hand spectra in different transverse momentum and rapidity ranges ($p_T - y$) are discussed. Both sets of kinematic variables are in the laboratory frame. Since the transverse

momentum reflects the momentum perpendicular to the beam direction ($p_T^2 = p_x^2 + p_y^2$), it is decoupled from the boost of the beam. Hence, the transverse momentum is supposed to carry the information of the interaction itself and therefore it should be particularly sensitive to medium effects of particles, e.g. KN potential. Contrary, the rapidity y, similar to the polar angle θ, indicates the direction of a particle with respect to the beam direction (z-axis) ($c = 1$):

$$y = \frac{1}{2} ln \frac{E + p_L}{E - p_L} = \frac{1}{2} ln \frac{1 + \beta \cos\theta}{1 - \beta \cos\theta}, \tag{3.7}$$

with

E : energy of the particle
p_L : momentum component parallel to the beam direction
β : velocity of the particle

Based on (double-)differential analysis in the $p_T - y$ phase space, the rapidity density distribution dN/dy can be extracted. In the laboratory frame, $y = 0$ is called target rapidity and $y \to \infty$ beam rapidity, while the rapidity of the πN center-of-mass system corresponds to $y_{\pi N} = 0.76$. By studying the rapidity density distribution dN/dy the particle emission can be ivestigated. Target rapidities indicate backward emission, while beam rapidities resemble forward emission. Scattering processes with the target nucleons can lead to a shift to backward rapidity. However, due to the limited acceptance of HADES, a method for extrapolating the yield to unmeasured regions must be employed. Following the prescription already adapted in [A$^+$13c, A$^+$14c, AM$^+$18b] a Boltzmann fit Eq. (3.8) can be applied to the measured p_T spectra and the yield in the uncovered regions can be estimated by integrating the Boltzmann distribution over this range ($c = 1$).

$$\frac{d^2N}{dp_T dy} = C(y) \cdot p_T \cdot \sqrt{p_T^2 + m_0^2} \cdot e^{\frac{-\sqrt{p_T^2 + m_0^2}}{T_{\mathrm{B}}(y)}} \tag{3.8}$$

with

$C(y)$: scaling factor
p_T/y : transverse momentum/rapidity
m_0 : nominal mass
$T_B(y)$: inverse-slope parameter

Although a priori the p_T spectra of the particles generated in $\pi^- + A$ collisions are not expected to follow a Boltzmann distribution. However, the comparison of K^+ p_T spectra in the exclusive production channels of $\pi^- + p \to K^+K^-n$ and $\pi^- + p(\mathrm{C}) \to K^+K^-n(\mathrm{B})$ based on Pluto simulations [F$^+$07, FGH$^+$10] (Section 3.6.1) implies that the Fermi momentum of the nucleons leads to the Boltzmann-like behavior of transverse momentum spectra (Appendix E.1). The total yield measured in a given rapidity range can then be extracted by summing all measured p_T points and the integral in the uncovered p_T range, extrapolated by the Boltzmann fit.

3.6 Simulation Procedure

Simulations are of great importance not only for the interpretation of experimental results, but they are also used for the correction of the data, to compensate losses and detector effects. In the

following, the framework to perform a full-scale simulation is presented. This involves complete chain of event (particle) generation (Section 3.6.1), processing it through the detector acceptance (Section 3.6.2), detector response procedure (Section 3.6.3) and the applied analysis. With this whole procedure the acceptance and efficiency correction (Section 3.6.4) can be deduced, which then corrects for all detector effects. The finally applied analysis and extracted acceptance and efficiency correction will be addressed in detail for each particle species individually in the corresponding Chapters 4 to 6.

3.6.1 Event Generators

Event generators are the tools to model the particle production on the basis of physical assumptions. They are the input for a full-scale simulation. While event generators like Pluto produces particles according to either a user-defined final state, following phase space distribution of user-defied angular correlations or it is possible to produce particles according to a Boltzmann distribution with a certain temperature parameter. Transport model calculation simulate not only the particle production, but also the propagation meaning the whole time evolution of the collision process from the initial to the final state. The later will be discussed in Section 3.7.

Pluto
Pluto is a Monte Carlo based event generator, which was developed for hadronic interactions at SIS18 and FAIR energy regimes [F$^+$07, FGH$^+$10]. Particle production in heavy-ion collisions can be modeled by a thermal source ("fireball") based on a Boltzmann distribution ($dN/dE \propto p\,E\,e^{-E/T}$). Besides, exclusive reactions like elastic events as well as a multi-reaction channel cocktail can be simulated by adding up the different elementary reactions to an incoherent sum. Pluto is also capable to serve as an event generator for hadron-nucleus reactions, in which the Fermi-momentum of the nucleons inside the nucleus is modeled.
Pluto includes several adjustable input parameters like cross-sections, decay branching ratios, spectral functions of resonances and angular distributions. Particles as well as resonances together with their properties (mass, width, decay channel) can be added. The particle production is performed according to the available phase space.

3.6.2 Detector Acceptance (HGeant)

HGeant is a simulation tool based on the CERN software Geant 3.21 [HADb]. In this framework, detector geometries can be defined, particles originating from an event generator can be propagated through a detector system and hits in the active detector material can be simulated by modeling the underlying physical processes such as multiple scattering, deflection in a magnetic field and energy loss in the detectors according to the Bethe-Bloch formula. In the used version HGeant 4.9k the GCalor package [ZG96] is used and the detailed geometry of HADES was implemented.

3.6.3 Detector Response (SimDST)

For complete modeling of detector effects, the detector response must be simulated accurately. The event/particle information provided by HGeant serves as input for the digitization process. In this way, the simulated particle hits are treated in the same way as the measured hits of passing particles. This means that the same track fitting algorithms and the same track criteria are

applied. All reconstructed particle/track properties such as the particle momentum are stored in the SimDST (Simulated Data Summary Table), which has the same structure as the stored experimental data.

3.6.4 Acceptance and Efficiency Correction

All experimentally measured particle distributions are always hampered by inefficiencies of the detector systems. The HADES spectrometer with six identical detection sections has a limited geometrical acceptance not only along the azimuthal angle but also in forward ($15^\circ > \theta$) and backward ($85^\circ < \theta$) direction. Hence, particles which are not bend into the active region of the detectors by the magnetic field or which traverse the supporting structures are not measured. Moreover the produced particles are distorted by multiple scattering occurring within the detector material and in the mechanical structures.
Besides that, the detector electronics as well as the analysis procedure can cause inefficiencies. The detector response, trigger decision and also the tracking algorithm influence the final spectra. Especially, by investigating the inclusive particle production the trigger decision can introduce a bias. Further, in every analysis the selection procedure e.g. particle identification method or event criteria has impact on the reconstructed particle distributions. Thus, to extract the undistorted physical information, and thus be able to perform an interpretation of physics and comparison to theoretical models, a correction of reconstruction efficiency within the geometrical acceptance is crucial.
The particle production in the whole available phase space is commonly modeled by an event generator (Section 3.6.1). The influence of the spectrometer acceptance and various inefficiencies are modeled by means of several simulations tools, which were discussed above. The detector acceptance is treated with the HGeant framework (Section 3.6.2). Efficiency effects caused by the detector response and tracking algorithm are considered in the SimDST step (Section 3.6.3). In addition, the particle identification method for the simulation is adjusted such to select the same particle fraction as in the experimental case (sSection 3.3). Besides, the effect of the trigger decision is implemented requiring a minimum charged particle multiplicity $M \geq 2$ in the META system. It has been demonstrated in Appendix C that this implementation can be used to correct for any trigger bias. All other efficiency are taken into account by processing the simulation through the same analysis chain as the experimental data. In such way, a reconstructed full-scale simulation is generated suffering similar losses.
To avoid any model-dependence of the correction method and thus to avoid the need for perfect phase space description in simulation, the correction method is carried out in two independent kinematic variables (e.g. $p_T - y$). Hence, by knowing the kinematical distributions of the initial unfiltered simulation and reconstructed full-scale simulation it is possible to extract the correction matrix for the experimental spectra according to:

$$\varepsilon_{corr}(v_1, v_2) = \frac{N_{out}(v_1,v_2)}{N_{in}(v_1,v_2)} \tag{3.9}$$

with

$\varepsilon_{corr}(v_1, v_2)$: geometrical acceptance and efficiency correction matrix
$N_{out}(v_1, v_2)$: distribution of the reconstructed full-scale simulation
$N_{in}(v_1, v_2)$: distribution of the initial unfiltered simulation
v_1 and v_2 : two independent kinematic variables

The correction uncertainty corresponds to 3% for each reconstructed charged particle obtained from investigations of elastic scattering in a subsequent experimental campaign with negatively charged pions with momentum of 0.690 GeV/c impinging on a polyethylene (C_2H_2) target [Mau19].

3.7 Transport Model Calculations

Microscopic transport models are often used to describe the interaction dynamics covering a wide range of nuclear reactions, including hadron-, photon-, electron- and neutrino-induced reactions and heavy ion collisions. A variety of particle production mechanisms have to be considered such as resonance production at intermediate energies as well as string excitation and fragmentation at relativistic energies. Particularly heavy-ion collisions, but also e.g. hadron-nucleus reactions, are dominated by multi-body effects that develop dynamically. Hence, the whole reaction must be described in time-dependent frameworks in which the particles are simulated including sequential propagation, collisions and decays. As illustrated in Fig. 3.10, transport models take care of scattering processes, production and absorption of the particles. Since the (experimental) final state particle spectra contain only time-integrated information, such microscopic transport models are suitable for the interpretation of experimental results. Heavy-ion collisions undergo a large density and temperature evolution that make it in particular difficult to address fundamental aspects directly. Moreover, microscopic transport models can be used for predictions as different interactions can be included and their impact on the final state tested.

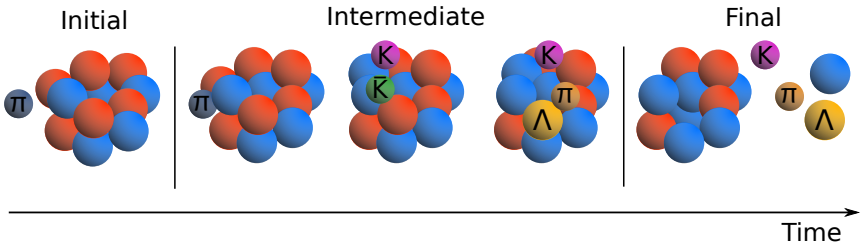

Figure 3.10: Illustrative representation of the time evolution of the transport calculations from the intial to the final state.

Common Transport Approach

All microscopic transport models are based on the assumption of time-dependent propagation of N particles through space-time in combination with their interaction with each other. Their fundamental degrees of freedom are strings, partons or hadrons depending on the kinetic beam energy. Nuclear reactions in the SIS energy regime are most successfully described by hadronic degrees of freedom due to the dominant role of resonance production.

The classical derivation of transport equation [Aic91] is based on Liouville theorem (Eq. (3.10)) for single-particle phase space distribution $f(\vec{r},\vec{p},t)$. The latter gives the probability to find a particle at time t at certain position $\vec{r}$ with momentum $\vec{p}$.

$$df = \frac{\partial f(\vec{r},\vec{p},t)}{\partial t}dt + \frac{\partial f(\vec{r},\vec{p},t)}{\partial \vec{r}}d\vec{r} + \frac{\partial f(\vec{r},\vec{p},t)}{\partial \vec{p}}d\vec{p} = 0 \tag{3.10}$$

By including an external force $\vec{F}$, the Vlasov equation (Eq. (3.11)) can be derive [BG88]. This equation incorporates the propagation of stable, non-interacting particles under the influence of an external field.

$$\begin{aligned}\frac{df}{dt} &= \frac{\partial f(\vec{r},\vec{p},t)}{\partial t} + \frac{\partial \vec{r}}{\partial t}\frac{\partial f(\vec{r},\vec{p},t)}{\partial \vec{r}} + \frac{\partial \vec{p}}{\partial t}\frac{\partial f(\vec{r},\vec{p},t)}{\partial \vec{p}} = 0 \\ &= \frac{\partial f(\vec{r},\vec{p},t)}{\partial t} + \frac{\vec{p}}{m}\frac{f(\vec{r},\vec{p},t)}{\partial \vec{r}} + \vec{F}\frac{\partial f(\vec{r},\vec{p},t)}{\partial \vec{p}} = 0 \end{aligned} \tag{3.11}$$

The non-relativistic Boltzmann equation (Eq. (3.12)), which is based on the Vlasov equation (Eq. (3.11)), is the underlying transport equation [B$^+$99b] on which the models are based on. In this equation, collisions will change the phase space density, as the collision term includes gain and loss terms, which take care about scattering and decay processes as well as hadron production and absorption rates.

$$\frac{df}{dt} = \frac{\partial f(\vec{r},\vec{p},t)}{\partial t} + \frac{\vec{p}}{m}\frac{f(\vec{r},\vec{p},t)}{\partial \vec{r}} + \vec{F}\frac{\partial f(\vec{r},\vec{p},t)}{\partial \vec{p}} = I_{coll} \tag{3.12}$$

with

$f(\vec{r},\vec{p},t)$: single-particle phase space distribution
$\vec{F}$: external force experienced by single particle
I_{coll} : collision term

An exact solution of the Boltzmann equation is complicated, hence various simplified descriptions valid under certain assumptions have to be used to solve the equation. An example for a specific implementation in transport models is the test-particle method used in BUU (Boltzmann-Ueling-Uhlenbeck) or HSD (Hadron String Dynamics) codes. While in the Quantum Molecular Model (QMD) approach [B$^+$98] is based on many-body assumption.

Test-Particle Method

The underlying transport equation implemented in models based on the test-particle ansatz is the non-relativistic Boltzmann-Uehling-Uhlenbeck (BUU) equation:

$$\frac{df}{dt} = \frac{\partial f(\vec{r},\vec{p},t)}{\partial t} + \frac{\vec{p}}{m}\nabla_{\vec{r}} f(\vec{r},\vec{p},t) - \nabla_{\vec{r}} U(\vec{r},t)\nabla_{\vec{p}} f(\vec{r},\vec{p},t) = I_{coll} \tag{3.13}$$

with

$f(\vec{r},\vec{p},t)$: single-particle phase space distribution
m : mass of the test-particle
$U(\vec{r},t)$: mean-field potential ($\vec{F} = -\nabla_{\vec{r}} U(\vec{r},t)$)
I_{coll} : collision term

Here, the complicated many-body interactions are approximated by an mean-field $U(\vec{r},t)$. This mean-field influences all particles in exactly the same way independent of local fluctuations caused by each individual particle itself. Thus external fields are still treating as one-body problem. Pauli

blocking is considered in the collision term suppressing the collision in a already occupied phase space cell.
In this test-particle ansatz, the phase space distribution $f(\vec{r},\vec{p},t)$ are represented by a large number N of point-like test-particles each represented by a δ-function in coordinate and momentum space:

$$f(\vec{r},\vec{p},t) \to \sum_{r}^{N} \delta(\vec{r} - \vec{r}_i(t))\delta(\vec{p} - \vec{p}_i(t)) \tag{3.14}$$

The latter are propagated classically with Hamiltonian equation of motion ($\frac{\partial \vec{r}}{\partial t} = \frac{\vec{p}}{m}$, $\frac{\partial \vec{p}}{\partial t} = -\nabla_{\vec{r}} U$) yielding a solution of the Vlasov part of Eq. (3.13). If the distance is at that point is smaller than $\sqrt{\sigma_{tot}/\pi}$ a scattering process is performed. The final scattering state and angle is determined according to cross-section and angular distribution.
With increasing beam energy, the non-relativistic transport is not any more applicable. Here, the underlying transport equation commonly implemented in the model is the relativistic Boltzmann equation:

$$p^{\mu}\partial_{\mu} f_i(r,p) + m_i F^{\alpha} \partial^{p}_{\alpha} f_i(r,p) = C^{i}_{coll} \tag{3.15}$$

with

$f_i(r,p)$: single-particle phase space distribution
F^{α} : force experienced by single particle
($F^{\alpha} = -\partial^{\alpha} U(\vec{r})$, with mean-field potential $U(\vec{r})$)
C^{i}_{coll} : collision term

The following transport model calculations are based on the test-particle method: GiBUU (Giessen BUU) [BGG$^+$12], SMASH (Simulating Many Accelarated Strongly-Interacting Hadrons) [W$^+$16] and HSD (Hadron String Dynamics) [CB99].

Quantum Molecular Model (QMD)
The QMD approach [Aic91, B$^+$98] is a many-body theory, which translates the mean-field into a classical but density and momentum dependent two-body interaction. Instead of a point-like treatment in terms of test-particles, the particles are considered as Gaussian wave packages with finite size in phase space ($\hbar, c = 1$) [B$^+$98]:

$$\phi_i(\vec{r},\vec{r}_i,\vec{p}_i) = \left(\frac{2}{L\pi}\right)^{\frac{3}{4}} \exp\{-\frac{2}{L}(\vec{r} - \vec{r}_i(t))^2\} - i\vec{p}_i(t)\vec{r}\} \tag{3.16}$$

with

$\vec{r}_i/\vec{p}_i$: space and momentum coordinates
L : extension of the wave package in phase space

Collision partners such as the nucleus is represented as a product of single particle wave functions (Eq. (3.17)), thus a direct product of coherent states. This ansatz can account for particle states with different widths and smooths at the same time the boundaries of the spectral function.

$$\Phi = \prod_i \phi_i(\vec{r},\vec{r}_i,\vec{p}_i) \tag{3.17}$$

The equation of motion ($\frac{\partial \vec{r}}{\partial t} = \frac{\partial \langle H \rangle}{\partial \vec{p}_i}$, $\frac{\partial \vec{p}}{\partial t} = -\frac{\partial \langle H \rangle}{\partial \vec{r}_i}$) is obtained based on the coherent states and a Hamiltonian of the form $H = \sum_i T_i + \frac{1}{2}\sum_{i,j} V_{ij}$ (T_i= kinetic energy, V_{ij}= potential energy), which represent the same structure as the classical Hamilton equations [Aic91, B$^+$98]. QMD simulations are typically restricted to binary collisions (two-body processes), which are treated similar to BUU models. Two particles collide, if $d \leq d_0 = \sqrt{\sigma_{tot}/\pi}$ is fulfilled. The minimal relative distance d resembles the centroid of the Gaussian and σ_{tot} denotes the vacuum cross-section.
The following transport model calculations are based on the QMD approach: IQMD (Isospin Quantum Molecular Dynamics), RQMD (Relativistic Quantum Molecular Dynamics) and UrQMD (Ultra-Relativistic Quantum Molecular Dynamics) [B$^+$99b].

GiBUU (Giessen BUU)
The GiBUU model [BGG$^+$12] based on the BUU equation (Eq. (3.13)) is applicable in the energy range of tens of MeV to tens of GeV. Low (intermediate) energies reactions are described by hadrons and resonances. Usually, in transport models only two-body collisions are implemented, so that an intermediate step is needed to obtain the final three-body state (e.g. $BB \to BR \to BYK$). However, in the GiBUU also three-body collisions (e.g. $BB \to BYK$) are included.

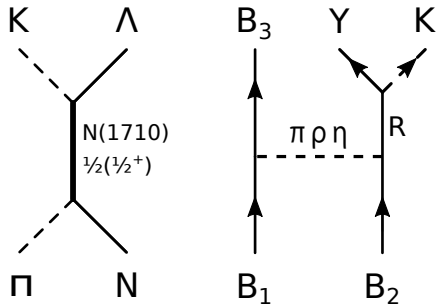

Figure 3.11: Feynman diagram used in the Tsushima model [TSTL99, THF94] for cross-section calculation of strange hadron production channels.

The GiBUU model does not explicitly propagate resonances. Only the final non-resonant reaction channels, when the resonances have already decayed, are implemented. The resonance influence is therefore only taken into account indirectly via the cross-section parametrizations. Most of strange hadron production channels are based on the parametrization of elementary reaction cross-sections according to the Tsushima resonance model [TSTL99, THF94, THF97]. The Tsushima model treats mesons π, η, ρ as exchange bosons and considers e.g. the following resonances $N(1650)$, $N(1710)$, $N(1720)$, $\Delta(1920)$, $K^\star(892)$. In this model it is assumed that each hyperon-kaon (YK) pair stems from a resonance decays $R \to Y + K$ as shown in Fig. 3.11. While other production channels are parameterized by expressions from [SCK97, SCM97]. The energy-dependent cross-section parametrizations (Eq. (3.18)), that are implemented in GiBUU for pion-induced reactions, are constrained by available experimental data. The relevant (anti-)kaon and ϕ production cross-sections in pion-nucleus collisions at incident beam momentum of 1.7 GeV/c employed in GIBUU are listed in Table 5.4. In addition, the experimental cross-section together with parametrizations

of GiBUU as function of the incident beam momentum are depicted in Fig. 5.23 and Fig. F.1.

$$
\begin{aligned}
\sigma(\pi p \to pK^0K^-) &= 1.121\left(1-\frac{s_0}{s}\right)^{1.86}\left(\frac{s_0}{s}\right)^2 \\
\sigma(\pi p \to nK^+K^-) &= 2\sigma(\pi p \to pK^0K^-) \\
\sigma(\pi B \to YK\pi) &= a\left(\frac{s}{s_0}-1\right)^b\left(\frac{s}{s_0}\right)^{-c} \\
\sigma(\pi^- p \to \Sigma^- K^+) &= \frac{0.009803(\sqrt{s}-1.688)^{0.6021}}{(\sqrt{s}-1.742)^2+0.006583}+\frac{0.006521(\sqrt{s}-\sqrt{s_0})^{1.4728}}{(\sqrt{s}-1.940)^2+0.006248} \\
\sigma(\pi^- p \to n\phi) &= \frac{0.00588}{2}\frac{0.99^2}{\left(\sqrt{s}-1.8\right)^2+\frac{0.99^2}{4}}\frac{\sqrt{(s-(m_n+m_\phi)^2)(s-(m_n-m_\phi)^2)/(4s)}}{(s-(m_\pi+m_p)^2)(s-(m_\pi-m_p)^2)/(4s)}
\end{aligned}
\tag{3.18}
$$

with

σ :	cross-section of a specific channel [mb]
a,b,c :	individual fit parameters
s_0,$\sqrt{s}$:	channel dependent threshold and center-of-mass energy

At higher energies GiBUU uses the string model PYTHIA [SMS06, SMS08], so quarks and gluons become the degrees of freedom. The standard transition occurs at $\sqrt{s} = 2.6\,\text{GeV}$ for baryon-baryon collisions and at $\sqrt{s} = 2.2\,\text{GeV}$ for meson-baryon collisions.

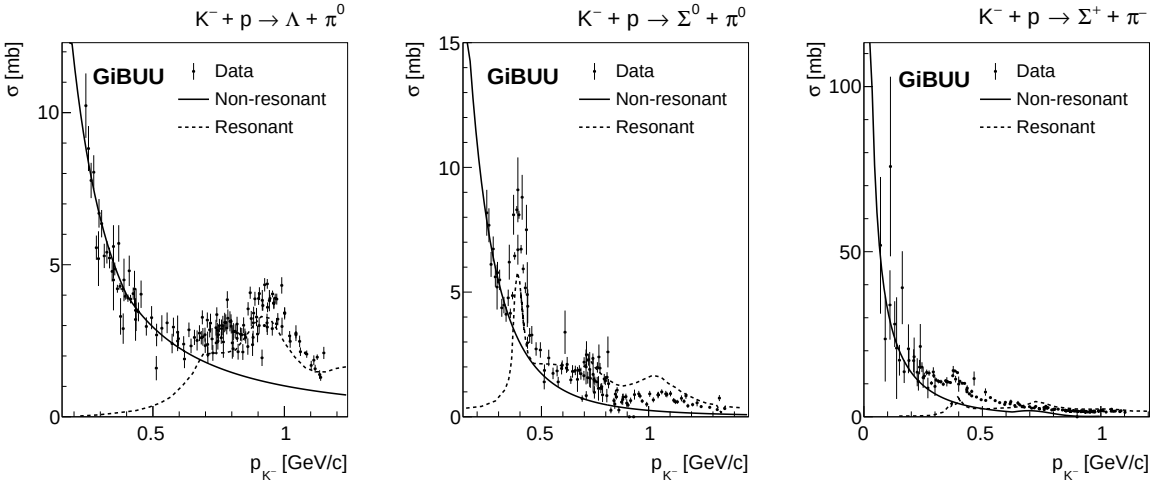

Figure 3.12: Cross-sections of strangeness exchange reactions in $K^- + p$ reactions implemented in GiBUU [Eff99, BGG+12] together with experimental data taken from Landolt-Börnstein [MS88]. The dashed line corresponds to the resonance contribution and the solid line to the non-resonant contribution.

The elastic and inelastic scattering of (anti-)kaons is included based on analytical functions constrained by available experimental data. Inelastic interactions in particular play an important role in the description of antikaon dynamics in nuclear matter. The antikaon-nucleon interaction is particularly complex since large $\bar{K}N$ coupling to resonances leads to absorption processes. The resonance contribution of such absorption processes, which are implemented in GiBUU, are shown

for certain channels(see legend) in Fig. 3.12 . Since the resonances (dashed curves) themselves are not sufficient to describe the experimental data in the low momentum range, the so-called non-resonant background cross-section (solid curve) has to be considered as well. This is partly due to the presence of the $\Lambda(1405)$ with a pole mass of about 30 MeV below the $\bar{K}N$ threshold. The coupling to $\Lambda(1405)$ is not directly included in GiBUU and hence the effect of the $\Lambda(1405)$ is modeled by cross-section parametrizations [Eff99].
The particle properties can change significantly in the presence of nuclear matter. In-medium potentials contained in transport models can shift production thresholds and thus total yields. Moreover, the vector field part in the relativistic mean-field (RMF) potential can affect the kinematic distributions of the particles, e.g. momentum spectrum. In the specific case of kaon production, the inclusion of in-medium potentials will effectively enhance the kaon and lower the antikaon production threshold. The in-medium ChPT KN potential implemented in GiBUU features a nonlinear density dependence in combination with a momentum-dependence (Fig. 5.15) [A$^+$14d]. Due to the associated production of strange particles, the hyperon-nucleon (YN) potential is also of importance. Motivated by the additive quark model the YN potential is a factor 2/3 of the nucleon-nucleon mean-field [HOL$^+$12], which is also considered in GiBUU.

UrQMD (Ultra-relativistic Quantum Molecular Dynamics)
UrQMD [B$^+$98, B$^+$99b] is based on the QMD approach [B$^+$98]. It is a microscopic many-body simulation that includes hadron-hadron, hadron-nucleus and nucleus-nucleus collisions in the energy range from SIS to RHIC ($\sqrt{s} = 200\,\text{GeV}$). Below $\sqrt{s} = 5\,\text{GeV}$ for baryon-baryon collisions and $\sqrt{s} = 3\,\text{GeV}$ for meson-baryon and meson-meson, nuclear reactions are modeled by interactions of hadrons and their associated resonances. At high energies quarks and gluons cannot be neglected as degrees of freedom, therefore the concept of color string excitation with subsequent fragmentation in hadrons is introduced.
In total UrQMD contains 32 different meson species and 55 different baryon species like N, Δ and Y resonances with masses up to 2.25 GeV. The implemented heavy baryon resonances comprise $N(1650)$, $N(1720)$, $N(1990)$, $N(2080)$, $N(2200)$, $N(2250)$. The latter were introduced into the model to describe the abundance of ϕ and Ξ in sub-threshold heavy-ion collisions [SB16]. To fulfill the baryon symmetry, the corresponding antiparticles are also included. Besides, UrQMD also contains mesonic resonances (e.g. ρ, K^*, ϕ). All particles can be generated and propagated in this model, hence resonances including their decays are explicitly treated in the model. At low (intermediate) energies, final three-body state containing kaons and hyperons are produced via decays of N and Δ resonances (e.g. $BB \to BR \to BYK$). Pion-induced reactions are especially relevant for the resonance approach, because they are more sensitive to the πN branching ratios ($\pi N \to R$) than nucleon-nucleon collisions ($NN \to NR$).

$$\sigma(K^- p \to Y\pi) = \frac{a}{(\sqrt{s} - b)^2}, \tag{3.19}$$

with

σ : cross-section of a specific channel [mb]
a,b : individual fit parameters
s : invariant collision energy for the reaction

Strangeness exchange processes such as the exchange of the strange quark from a strange meson to

nucleon, i.e. $\bar{K} + N \to Y + \pi$, are an important component and are included in the UrQMD model using parameterizations (Eq. (3.19)) [GSLB14] based on experimental data. All other possible isospin channels and the (necessary) back reaction result from isospin symmetry and detailed balance relations. The implemented strangeness exchange cross-section for certain channels (see legend) together with experimental data are visualized in Fig. 3.13. Since resonances are explicitly treated in UrQMD, hyperon resonances (e.g. $\Lambda(1405)$, $\Lambda(1520)$, $\Sigma(1385)$) can be directly formed and hence contribute to the antikaon absorption ($\bar{K} + N \to Y^* \to Y + \pi$) as well.

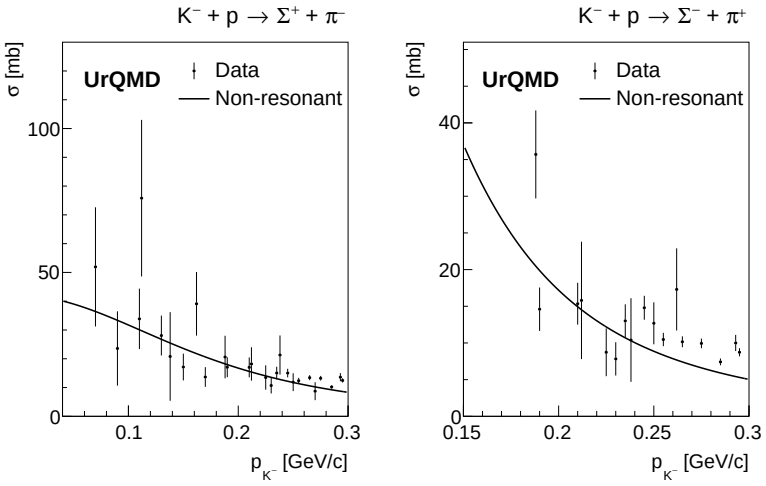

Figure 3.13: Non-resonant cross-sections of strangeness exchange reactions in $K^- + p$ reactions implemented in UrQMD [GSLB14] compared to experimental data taken from Landolt-Börnstein [MS88].

Unlike GiBUU, UrQMD contains neither mean-field NN potentials nor explicit KN potentials. UrQMD follows the approach of including high-mass nucleon resonances [SB16] to describe the strangeness production in nuclear reactions at SIS18 energies.

SMASH (Simulating Many Accelarated Strongly-Interacting Hadrons)

SMASH [W$^+$16] comprises in total 106 hadron species (excluding charge/antiparticles), thus over 10000 types of 2-body collisions have been implemented. Each of this collisions can end-up in several possible final states. Three-body interactions are not implemented. For most of these reactions, the energy-dependent cross-sections have not been measured, thus this cross-sections have to be modeled. In SMASH, most of the cross-sections are implemented via resonances comparable to UrQMD. Whereas, some cross-sections, that are parametrized similar to GiBUU, are not resonant. Off-shell propagation is not taken into account. The test-particle ansatz is applied.

For the charge exchange reactions $K^- p \leftrightarrow \bar{K}^0 n$ the non-resonant contribution is similarly expressed to GiBUU. While, the non-resonant contribution of strangeness exchange processes, $\bar{K} + N \to Y + \pi$, are implemented based on the same formula as used in UrQMD (Eq. (3.19)). Although the free parameters for the channel $K^- p \to \Sigma^0 \pi^0$ and $K^- p \to \Lambda \pi^0$ slightly differs from the ones of UrQMD. However, most of the strangeness exchange reaction channels are modeled via hyperon resonances ($\bar{K} + N \to Y^* \to Y + \pi$). [SSO$^+$19]

Similar to UrQMD, SMASH follows the approach of including high-mass nucleon resonances [SSO$^+$19], which is complementary to introducing KN potentials, that are so far not included.

HSD (Hadron String Dynamics)
HSD [CB99] is a transport approach developed for the description of nuclear reaction from proton-proton to heavy-ion collisions covering a wide energy range form SIS18 to SPS ($1 - 200$ AGeV). This approach uses the test-particle ansatz of a coupled set of relativistic transport equations for particles with in-medium self-energies. For the hadronic description the baryonoctet and decuplet, the pseudoscalar and vector meson nonets and selected higher resonances together with their antiparticles are included. Contrary to other transport models, hadrons are explicitly propagated with momentum-dependent scalar and vector self-energies. Moreover in-medium elastic and inelastic cross-sections for all hadrons are taken into account. The dominant production mechanism for baryon-baryon and meson-baryon collisons above $\sqrt{s} > 2.65$ GeV and $\sqrt{s} > 2.3$ GeV is string fragmentation based on the FRITIOF model [NAS87].
In-medium potentials can be added to the propagation of all hadrons. In HSD, a repulsive KN potential of 40 MeV at nuclear saturation density ρ_0 can be included, which increases linearly with density, and the strength of the YN mean-field is assumed to be 2/3 of the NN mean-field. In addition, HSD allows the propagation of off-shell particles, which is more relevant for antikaon production. The phenomenology of kaonic atoms [B$^+$11a, B$^+$09a, B$^+$11b] requires an attractive potential for K^- mesons, whereas the K^-N scattering amplitude in vacuum is repulsive at low energies due to the presence of the $\Lambda(1405)$ resonance, which is located just below the $\bar{K}N$ threshold. Hence, in work of [CTAB14], the chiral effective scheme in dense matter developed in Refs. [TRO06, TCR08] was improved by incorporating the full self-consistent s- and p-waves at finite density and temperature. In this way, in-medium meson-baryon cross-sections (amplitudes) for the strangeness sector ($S = -1$) were deduced containing the single-particle properties of hyperons, for example $\Lambda(1115)$, $\Sigma(1195)$, and $\Sigma(1385)$. In the model, the following channels are considered:

$$\begin{aligned} &K^-p \to K^-p, \bar{K}^0n, \Lambda\pi^0, \Sigma^0\pi^0, \Lambda\eta, \Sigma^0\eta, \Sigma^-\pi^+, \Sigma^+\pi^-, K^+\Xi^-, K^0\Xi^0 \\ &K^-n \to K^-n, \Sigma^-\pi^0, \Sigma^0\pi^-, \Lambda\pi^-, \Sigma^-\eta, K^0\Xi^- \end{aligned} \tag{3.20}$$

In general, the calculation of dynamical quantities in transport theory will require an appropriate folding of reaction rates or transition probabilities with the spectral functions of the particles in the initial and final states. The integrated and differential transition probability (P_{ij}) from initial i to final j channel are based on Eq. (3.21).

$$\begin{aligned} P_{ij}(P_0, \vec{P}, \rho, T, \cos(\theta)) &= |f_{ij}^{(s)} + (2f_{ij}^{+} + f_{ij}^{-})\cos^2(\theta)|^2 + |f_{ij}^{+} - f_{ij}^{-})|^2 \sin^2(\theta) \\ P_{ij}(P_0, \vec{P}, \rho, T) &= \int_{-1}^{1} du\{|f_{ij}^{(s)} + (2f_{ij}^{+} + f_{ij}^{-}u)|^2 + |f_{ij}^{+} - f_{ij}^{-})|^2(1-u^2)\} \end{aligned} \tag{3.21}$$

with

$P_0/\vec{P}$:	total energy and momentum of meson-baryon pair
θ ($u \equiv cos(\theta)$) :	scattering angle in the c.m. frame of the meson-baryon pair
$f_{ij}^{(s)}$:	s-wave scattering amplitude
f_{ij}^{+}/f_{ij}^{-} :	spin-flip and spin-nonflip p-wave scattering amplitude

Various temperatures ($T = 0 - 150$ MeV) and densities ($\rho = 1/8 - 11/4\ \rho_0$) as well as a wide range of total energy ($P_0 = 900 - 1854$ MeV) and momentum ($\vec{P} = 0 - 800$ MeV/c) of the meson-pair have been considered. The transition rates depend separately on the total energy P_0 and momentum $\vec{P}$ of the meson-baryon pair.
In the following selected results are presented for $\vec{P} = 0$, as a function of $\sqrt{s} = P_0$ for several nuclear densities and temperatures and refer to the transition probability as $P(s)$. In Figure 3.14 the transition probability for elastic $K^-p \to K^-p$ and inelastic $K^-p \to \Sigma^0\pi^0$ strangeness exchange reactions are presented. The K^-p state is an admixture of $I = 0{,}1$ and hence the two isoscalar Λ resonances and the isovector $\Sigma(1195)$ are clearly visible. Contrary, the $\Sigma(1385)$ couples weakly to the $\bar{K}N$ system and cannot be seen. The $K^-p \to \Sigma^0\pi^0$ reaction selects the $I = 0$ component of the $\bar{K}N$ amplitude and consequently only the isoscalar hyperons contribute. With increasing density the structure of the $\Lambda(1405)$ is practically washed out.

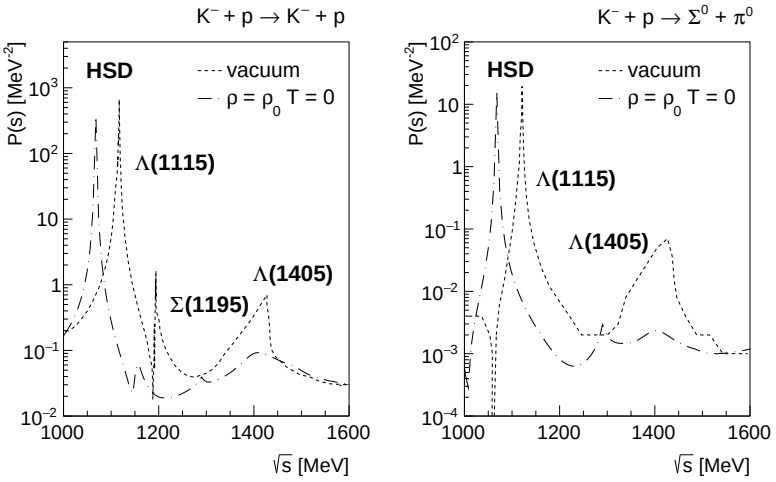

Figure 3.14: In-medium transition probability $P(s)$ based on [CTAB14] at zero total three-momentum for the elastic $K^-p \to K^-p$ and inelastic $K^-p \to \Sigma^0\pi^0$ reactions. The peaks associated to the $\Lambda(1115)$, $\Sigma(1195)$ and $\Lambda(1405)$ resonances are clearly visible in the vacuum case.

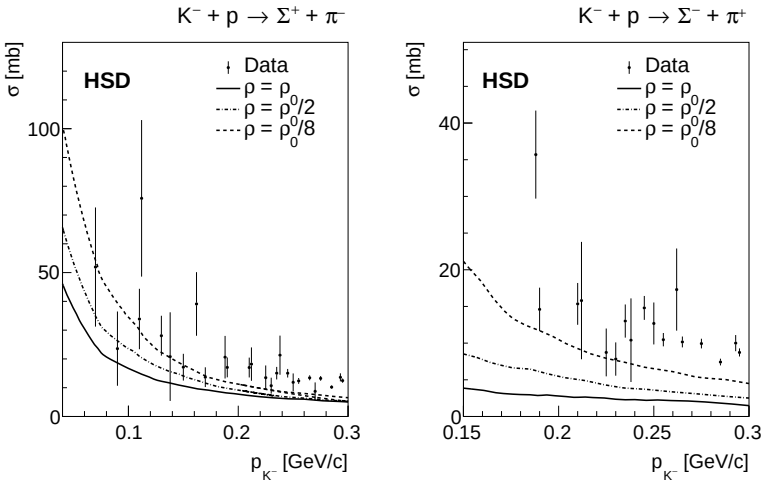

Figure 3.15: Cross-sections of strangeness exchange reactions in $K^- + p$ reactions [BCTS19] based on [CTAB14] compared to experimental data taken from Landolt-Börnstein [MS88].

Based on the transition probabilities the differential and integrated in-medium cross-sections of the meson-baryon pair for the process $i \rightarrow j$ can be figured out (Eq. (3.22)). The corresponding in-medium strangeness exchange cross-section for certain channels (see legend) together with experimental data are depicted in Fig. 3.15. The implementation of density and temperature dependent cross-sections in the HSD model is currently ongoing.

$$\frac{d\sigma_{i,j}}{d\Omega} = \frac{1}{16\pi^2}\frac{M_i M_j}{s}\frac{\tilde{q}_j}{\tilde{q}_i}\{|f_{ij}^{(s)} + (2f_{ij}^{+} + f_{ij}^{-})\cos^2(\theta)|^2 + |f_{ij}^{+} - f_{ij}^{-})|^2 \sin^2(\theta)\}$$

$$\sigma_{tot} = \int d\Omega \frac{d\sigma_{i,j}}{d\Omega} = 2\pi \int_{-1}^{1} du \frac{d\sigma_{i,j}}{d\Omega}(u) \tag{3.22}$$

with

M_i/M_j :	invariant mass of the meson-baryon pair
s :	invariant collision energy of the reaction
θ $(u \equiv cos(\theta))$:	scattering angle in the c.m. frame of the meson-baryon pair
$f_{ij}^{(s)}$:	s-wave scattering amplitude
f_{ij}^{+}/f_{ij}^{-} :	spin-flip and spin-nonflip p-wave scattering amplitude

4 Inclusive Pion Production

Since the charged pions, π^+ ($u\bar{d}$) and π^- ($d\bar{u}$), are produced with high abundance in nuclear collisions at kinetic energies of few GeV, their properties have been studied to great extend in the last decades. A comprehensive experimental campaign was carried out by the HARP Collaboration measuring the inclusive double-differential charged pion production cross-sections for various pion-nucleus reactions with beam momenta ranging from $3 - 12$ GeV/c [A$^+$09d]. For astroparticle physics experiments, the precise knowledge of pion production is essential as they serve as an important ingriendient for calculations of the atmospheric neutrino flux [Bat01] and of the accelerator neutrino flux [BG06]. However, a conclusive understanding of the intrinsic properties of pions is still missing, besides in-medium modification of the pion mass indicated by pionic atoms [S$^+$04]. Indeed, pion spectra in hadron-hadron collisions at kinetic energies around few GeV are dominated by the strong decays of short-lived baryonic resonances as $\Delta(1232)$ and N^*. Nevertheless, charged pions are commonly used as a reference for the comparison to transport model calculations.
The inclusive π^+ and π^- production in π^- + C and π^- + W reactions at an incident beam momentum of 1.7 GeV/c is presented in the following chapter. The investigation will provide further insights to the production, but also about their behavior within nuclear matter. Moreover, due to their high abundance, charged pions are especially suited to estimate the systematic uncertainties concerning the reconstruction procedure as the statistical uncertainties are small. Besides, charged pions can be reconstructed with high purity.
In the following the complete analysis procedure is discussed. All distribution are corrected for acceptance and efficiency effects. In order to verify that the applied correction method introduces no model-dependence, a self-consistency check was performed. The obtained kinematical distribution are not only compared to state-of-the-art transport calculations, but also to the inclusive double-differential charged pion production cross-sections measured by the HARP experiment.

4.1 Analysis Procedure

A double-differential analyses was performed for both charged pions for the two collision systems in two sets of kinematic variables ($p_T - y$, $p - \theta$) in the laboratory frame. The kinematic ranges are summarized in Table 4.1.

Table 4.1: Analyzed phase space ranges of π^+ and π^- for both sets of kinematic variables, $p_T - y$ and $p - \theta$, in the laboratory frame.

Particle	y	Δy	p_T [MeV/c]	Δp_T [MeV/c]
π^+/π^-	$0.0 - 1.9$	0.1	$30 - 870$	60

Particle	θ [°]	$\Delta\theta$ [°]	p [MeV/c]	Δp [MeV/c]
π^+/π^-	$15 - 90$	6.25	$150 - 990$	70

4.1.1 Pion Reconstruction

Both charged pions were identified by means of two-dimensional selections on the correlation between β and momentum of the particle candidates (Section 3.3.1.) The two-dimensional selections were systematically calculated for the two time-of-flight detectors, RPC and TOF, as well as for experimental data and simulation separately, to account for the different resolution. In the following analysis, simulations based on GiBUU [BGG+12] (Section 3.7) were employed. As all simulations contain the information of GEANT PID, one can verify whether the reconstructed particle is a real or mis-identified pion. Besides, momentum corrections were applied accounting for the energy loss e.g in the beam tube and systematic re-calibration of the HADES magnetic field. While, the latter correction was only applied to the experimental data. In addition, to reduce systematic uncertainties of the momentum reconstruction, the momentum of the pions was restricted to be $p_\pi < 1000$ MeV/c.

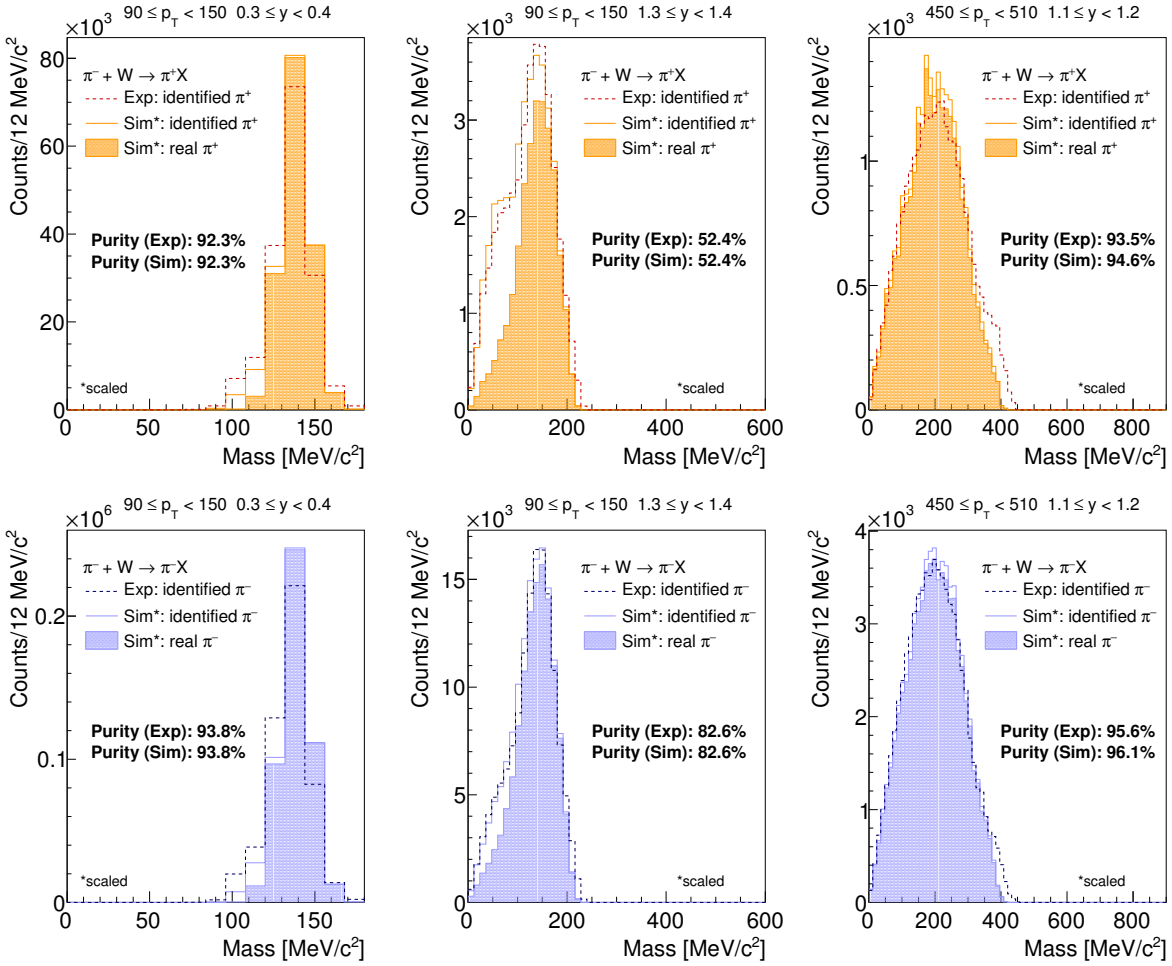

Figure 4.1: Mass distribution of π^+ (orange) and π^- (blue) in different transverse momentum and rapidity regions (see legend) for experimental data (dark dashed curve) and simulation with (light filled area) and without (light solid curve) GEANT PID information in π^- + W collisions.

The final charged pion yield was extracted on the basis of the measured mass distributions. Figure 4.1 shows experimental mass spectra (dark dashed curve) of π^+ (orange) and π^- (blue)

in different transverse momentum and rapidity regions (see legend) for $\pi^- + \mathrm{W}$ collisions. For comparison the corresponding mass spectra of the simulation without GEANT PID information (light solid curve) have been scaled to the integral of the experimental mass spectra (dark dashed curve) in the region of $0 - 400$ MeV/c^2. The same scaling factor has been also applied to the one with GEANT PID information (light filled area). With increasing transverse momentum as well as rapidity all mass spectra get broader. Moreover, one can observe that the shape of experimental and simulated mass spectra selected by means of the two-dimensional selections agree rather well for both charged pions.

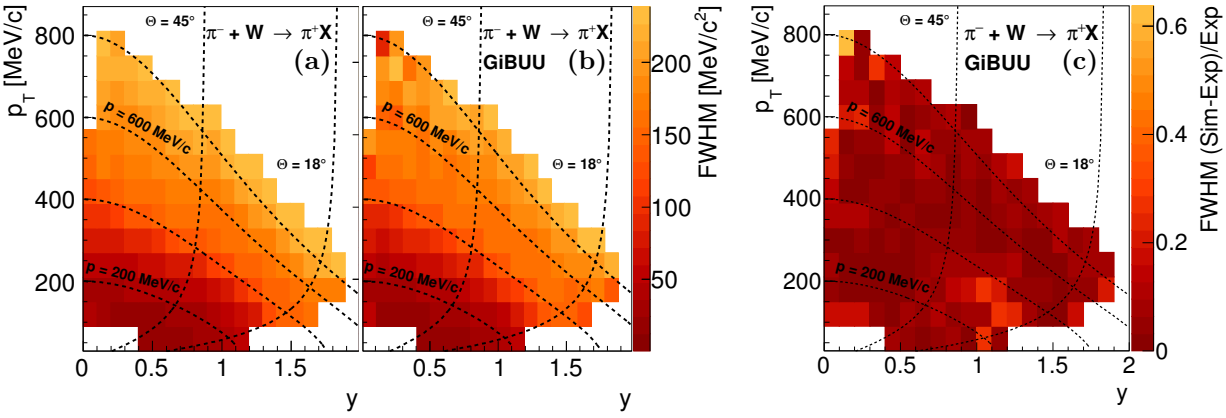

Figure 4.2: FWHM of the mass distribution of π^+ as a function of transverse momentum and rapidity inside the HADES acceptance for experimental data (a) and simulation (b) with corresponding FWHM deviation between experiment and simulation (c) in $\pi^- + \mathrm{W}$ reactions. The vertical lines indicate different polar angle regions, while the horizontal lines indicate different regions of constant momentum in the laboratory frame.

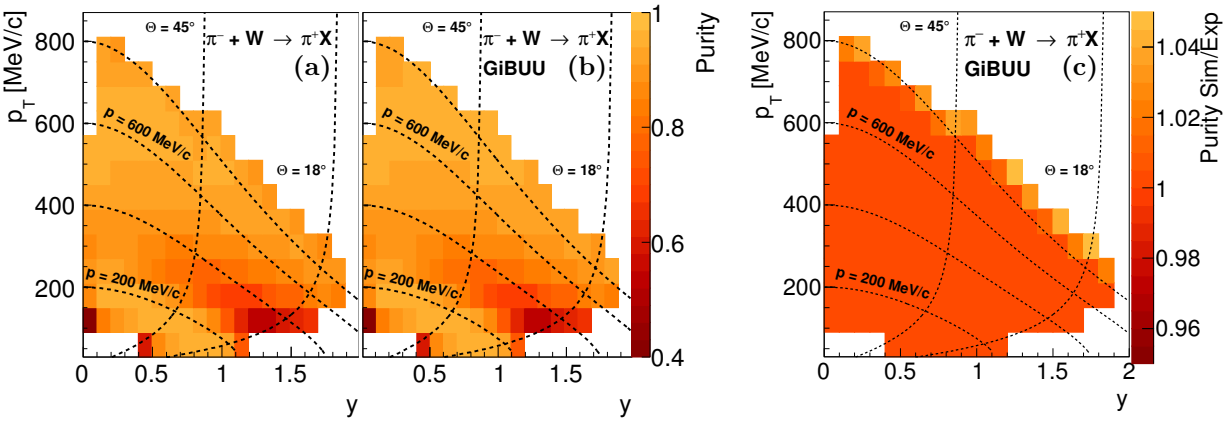

Figure 4.3: Purity of π^+ as a function of transverse momentum and rapidity inside the HADES acceptance for experimental data (a) and simulation (b) with corresponding purity ratio between experiment and simulation (c) in $\pi^- + \mathrm{W}$ reactions. The black dotted horizontal lines indicate the momentum at 200, 400, 600 and 800 MeV/c. The back dotted vertical lines denote the polar angle regions between $\theta = 18 - 45°$.

To quantify the agreement of the mass resolutions in experiment and simulation, the full width at half maximum (FWHM) of the mass spectra were investigated. As presented in Fig. 4.2 the FWHM for π^+ extracted in experiment (Fig. 4.2 (a)) and simulation (Fig. 4.2 (b)) is increasing

with increasing transverse momentum and rapidity. Similar behavior is observed for π^-. All in all, the mass resolution deviation of π^+ between experiment and simulation was found to be on average within 7.7 % in $\pi^- + \mathrm{W}$ collisions (Fig. 4.2 (c)) and 7.2 % in $\pi^- + \mathrm{C}$ collisions, respectively. While, the mass resolution deviation between experiment and simulation for π^- was found to be slightly smaller, on average within 5.7 % in $\pi^- + \mathrm{W}$ collisions and 6.5 % in $\pi^- + \mathrm{C}$ collisions.

As the charged pions correspond to the most abundant particles, they can be reconstructed with high purity in a wide phase space range within the HADES acceptance. However, it can happen that due to e.g. mis-matches of the tracking algorithm also other tracks are identified as being a pion, if they lie by chance within the two-dimensional selection based on correlation between β and momentum (Fig. 3.4). Electrons and muons can be mis-identfied. Here, especially muons play a role, due to the finite detector resolution as muons and pions are close in mass. However, some fraction of muons stem from charged pions, which decay into a muon - neutrino pairs ($BR = 99.99\,\%$ [P+16a]). Although, with a mean decay length of 7.8 m most of the pions decay outside the HADES detector.

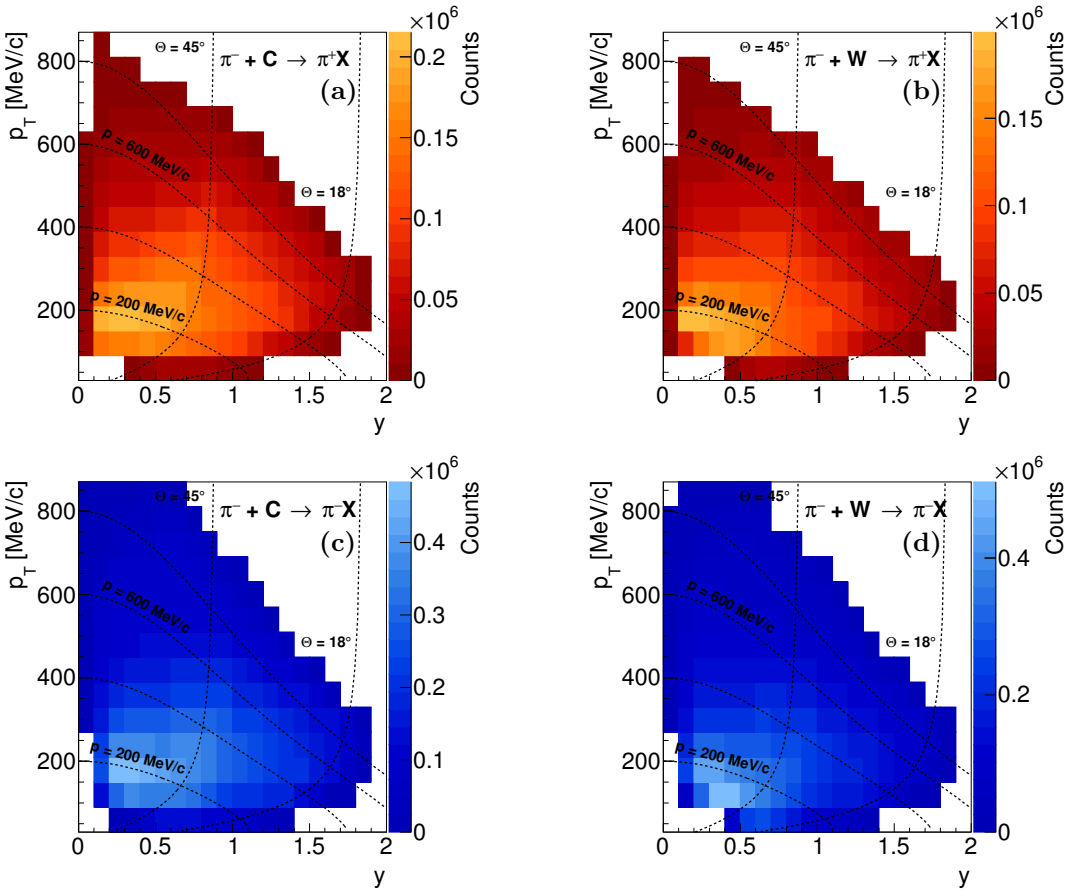

Figure 4.4: Reconstructed yield of π^+ (a,b) and π^- (c,d) as a function of transverse momentum and rapidity inside the HADES acceptance for $\pi^- + \mathrm{C}$ (a,c) and $\pi^- + \mathrm{W}$ (c,d) reactions. The dotted black vertical lines indicate different polar angle regions, while the dotted black horizontal lines indicate different regions of constant momentum in the laboratory frame.

In simulation the purity of the charged pions is obtained by identifying them not only based on the correlation between β and momentum of the particles, but additionally checking for the

GEANT PID information in order to distinguish between real and mis-identified pions. While in the experimental data the purity can be estimated by comparing the yields of the integrated mass spectra in the experiment and scaled simulation with GEANT PID information as the mass resolution in experiment and simulation agree rather well. The mass distributions presented in Fig. 4.1 reveal that the π^+ purity in the experimental data as well as in simulation is worse as the mass distributions significantly deviate from the one with GEANT PID information for certain transverse momentum and rapidity regions (see legend) in $\pi^- + \mathrm{W}$ reactions. Figure 4.3 depicts the purity for π^+ in experimental data (Fig. 4.3 (a)) and simulation (Fig. 4.3 (b)) together with the ratios of the corresponding purities (Fig. 4.3 (c)) in $\pi^- + \mathrm{W}$ reactions. The average purity of experiment and simulation in $\pi^- + \mathrm{W}$ reactions are equal to 88.0% and 88.4%, while in $\pi^- + \mathrm{C}$ reactions are equal to 94.5% and 94.9%. Purity ratios deviating by more than ±5% have been excluded. However, as the residual impurities from the particle mis-identification are not only present in the experimental data but also in simulation, they are corrected for in the later on performed acceptance and efficiency correction, which will be explained in Section 4.1.2.

Without the subtraction of residual impurities, the double-differential charged pion yields are obtained by integrating over the mass distributions. The resulting phase space distributions of the extracted raw yield are displayed in Fig. 4.4 for π^+ (upper panel) and for π^- (lower panel) in $\pi^- + \mathrm{C}$ and $\pi^- + \mathrm{W}$ reactions, respectively. The total number of reconstructed π^+ and π^- for the $p_T - y$ analysis within the HADES acceptance in $\pi^- + \mathrm{C}$ reactions are equal to $N_C^{\pi^+} = 11442638 \pm 3383$ and $N_C^{\pi^-} = 27584824 \pm 5252$ and in $\pi^- + \mathrm{W}$ reactions are equal to $N_W^{\pi^+} = 9004770 \pm 3001$ and $N_W^{\pi^-} = 23334256 \pm 4831$.

4.1.2 Acceptance and Efficiency Correction

The measurement itself, but also all applied analysis steps such as the particle identification method or event selection have influence on the reconstructed double-differential distributions of the charged pions. In order to obtain information about the production or interaction with the nuclear matter, all spectra must be corrected for acceptance and efficiency effects (Section 3.6.4). In the following, full-scale simulations based on GiBUU were used. All effects on acceptance, detector response and tracking algorithm were considered (Section 3.6).

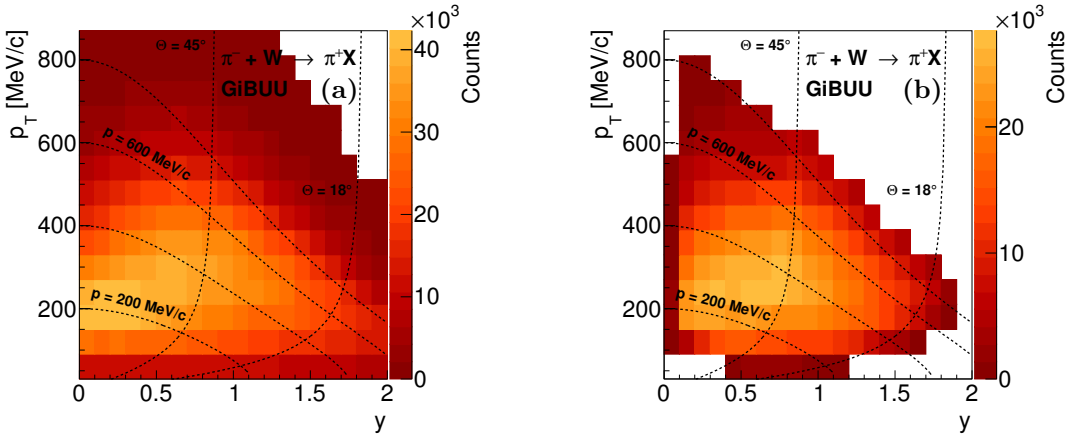

Figure 4.5: π^+ distribution as a function of transverse momentum and rapidity for initial unfiltered (a) and reconstructed (b) full-scale simulation of $\pi^- + \mathrm{W}$ reactions based on GiBUU.

Since pion spectra are studied in this analysis, the trigger condition of the minimally charged particle multiplicity $M \geq 2$ was taken into account. In addition, the particle identification method for the simulation was adapted to take into account small differences between the resolution of the velocity measurement in the simulation and the experimental data (Fig. 3.3). In this way it is ensured that the contamination by incorrectly identified pions is treated equally in simulation and experiment. In this way, the correction of the reconstruction efficiency directly addresses possible contamination of the particle identification in the experiment. This is also true for muons originating from charged pion decays, since they occur in the same range of two-dimensional selection for particle identification in the experiment as well as in the simulation. The correction thus also takes into account possible losses due to pion decay. Purity ratios deviating by more than ±5% were excluded. All in all, the charged pions of the simulation were treated exactly the same as the experimental ones. And the correction method was applied in both sets of two independent observations ($p_T - y$, $p - \theta$).

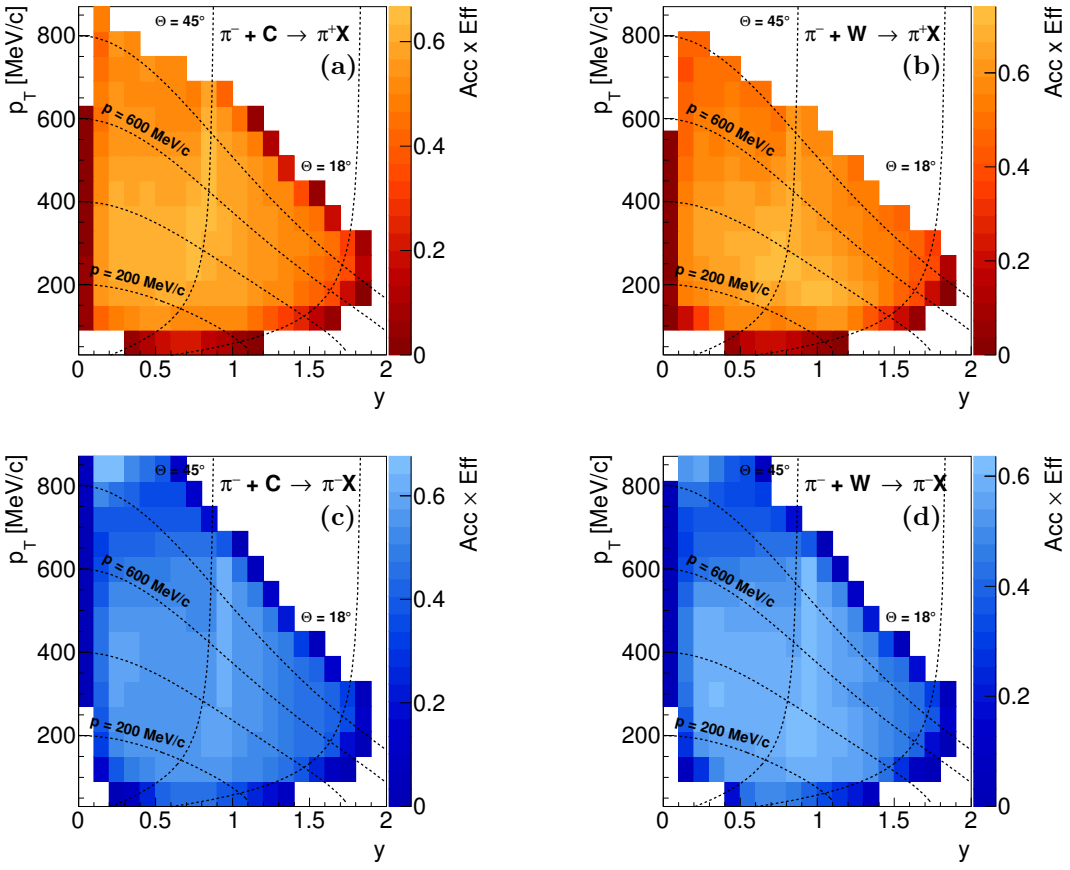

Figure 4.6: Acceptance and efficiency matrix for π^+ (a,b) and π^- (lc,d) as a function of transverse momentum p_T vs. rapidity y inside the HADES acceptance for π^- + C (a,c) and π^- + W (b,d) reactions.

The double-differential distribution for positively charged pions of the corresponding full-scale based on GiBUU for π^- + W reactions are shown in Fig. 4.5 (a) for the unfiltered simulation and in Fig. 4.5 (b) after the complete analysis chain. While the range and binning is similar to that of the experimental distribution (Fig. 4.4), the unfiltered simulated distribution is not hindered by geometrical acceptance effects of HADES. The extracted reconstruction efficiency matrix is given

in Fig. 4.6 for both charged pions and collision systems. The average efficiency of π^+ is 50% and the average efficiency of π^- is 40% for both collision systems. In all cases, non-negligible phase space dependencies are observed. After dividing the reconstructed experimental distribution with the corresponding corrections, unbiased corrected spectra were obtained.

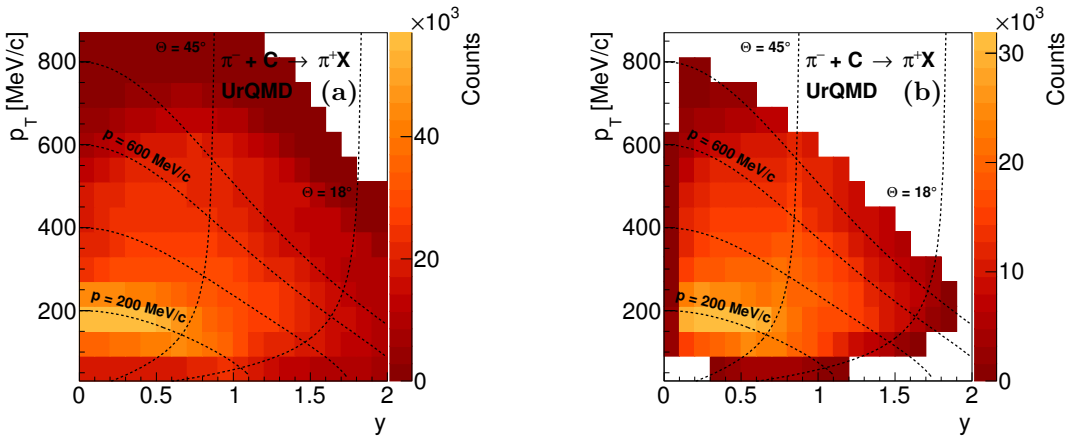

Figure 4.7: (Double-)differential yield of π^+ as a function of transverse momentum and rapidity for initial unfiltered (left) and reconstructed full-scale simulation of $\pi^- + \mathrm{C}$ reactions based on UrQMD.

In order to confirm the independence of the correction from the underlying simulation and thus to ensure the reliability of the correction procedure, a self-consistency check was carried out on the basis of two different models. Here, the correction matrices obtained separately for each model can be directly compared with each other. For this purpose, the correction matrix obtained with GiBUU simulations was used, since this is the model used for the correction of the experimental data. As a second model, UrQMD [B+99b] (Section 3.7) was employed to validate the correction method. The same ranges and binning were applied as for the experimental data. By comparing the π^+ double-differential distribution for $\pi^- + \mathrm{W}$ reactions based on an unfiltered GiBUU simulation shown in Fig. 4.5 (a) with the one based on UrQMD depicted in Fig. 4.7 (a), it can be seen that both models differ slightly. After a full simulation with HGeant to consider the acceptance of the spectrometer, the digitization procedure and all analysis steps, the corresponding reconstructed simulations are presented in Fig. 4.5 (b) and Fig. 4.7 (b).

Finally, the acceptance and efficiency correction on the basis of GiBUU (orange open circles) and UrQMD (light red triangles) as a function of the transverse momentum in different rapidity intervals (see legend) is compared as presented in Fig. 4.8. Deviations in acceptance and efficiency correction between both models are observed. However, this is primarily due to the difference in contamination by incorrectly identified pions in both models, which directly affects the correction itself. In Figure 4.8 the orange solid curve represents the contamination in GiBUU and the light red solid curve represents the contamination in UrQMD. While the trend of the contamination is reproduced as a function of the transverse momentum, the contamination for UrQMD is (sightly) less in the low p_T range $(0 - 200\ \mathrm{MeV}/c)$ for $y \leq 1.2$ and much more in the intermediate p_T range $(200 - 500\ \mathrm{MeV}/c)$. The contamination difference indicated by the bright red area goes up to 13%. Besides, the errors of acceptance and efficiency correction for UrQMD resembles the difference in contamination of GiBUU compared to UrQMD. For comparison, the estimated contamination in the experimental data is also represented by the dark dashed red curve in Fig. 4.8. It can be seen that the contamination in the experimental data and GiBUU is almost the same over the entire kinematic range. Thus the relative difference in the contamination of GiBUU compared to the

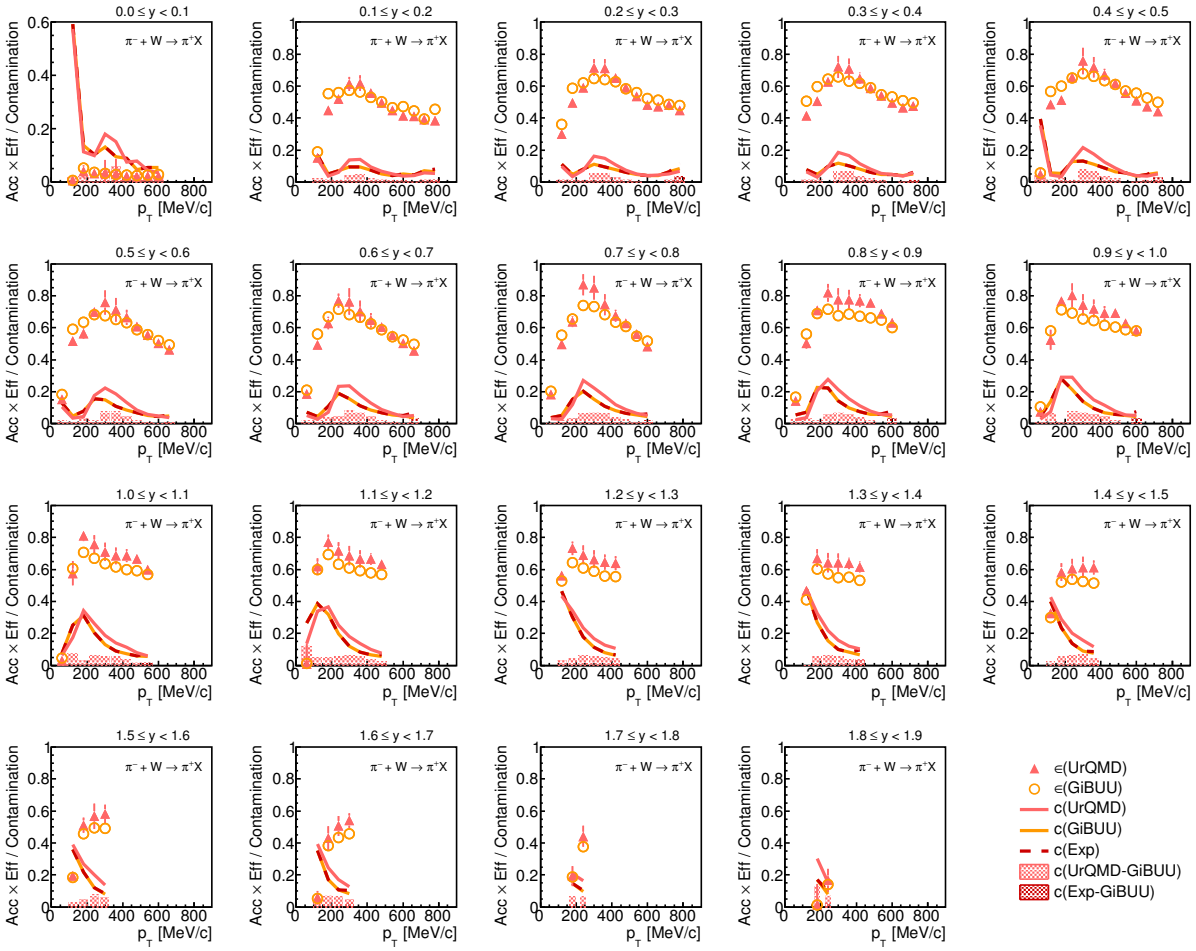

Figure 4.8: Comparison of the π^+ acceptance and efficiency correction matrices as a function of transverse momentum in different rapidity regions (see legend) for $\pi^- + \mathrm{W}$ reactions. The orange open circles depict the correction obtained with GiBUU and the light red triangles correspond to UrQMD. The solid curves represent the contamination originating from impurities in GiBUU (orange curve) and UrQMD (light red curve), respectively. The estimated contamination in the experimental data is shown by the dark red dashed curve. The filled areas indicated the relative difference in contamination of GiBUU compared UrQMD (light red filled area) and experimental data (dark red filled area). The errors of the acceptance and efficiency correction in UrQMD indicated the relative difference in contamination of GiBUU compared UrQMD.

experimental data (dark red filled area) is rather small, up to the values limited by the analysis.

Although deviations of the correction from GiBUU and UrQMD are observed, the reliability of the correction procedure based on GiBUU is still fulfilled. Since the deviations of the correction are mainly due to deviations of the contamination in both models, while the contamination in the experimental data is (almost) completely reproduced by GiBUU. Besides, by comparing the π^+ acceptance and efficiency correction based on GiBUU and UrQMD in $\pi^- + \mathrm{C}$ collisions (Fig. 4.9) an extremely good agreement between both models is observed. Here, the comparison is not hampered by the contamination by misidentified pions. Similar agreement was found for negatively charged pions. This confirms the reliability of the correction method for both collisions systems. The extracted spectra of the inclusive charged pion analysis can be used for the comparison with

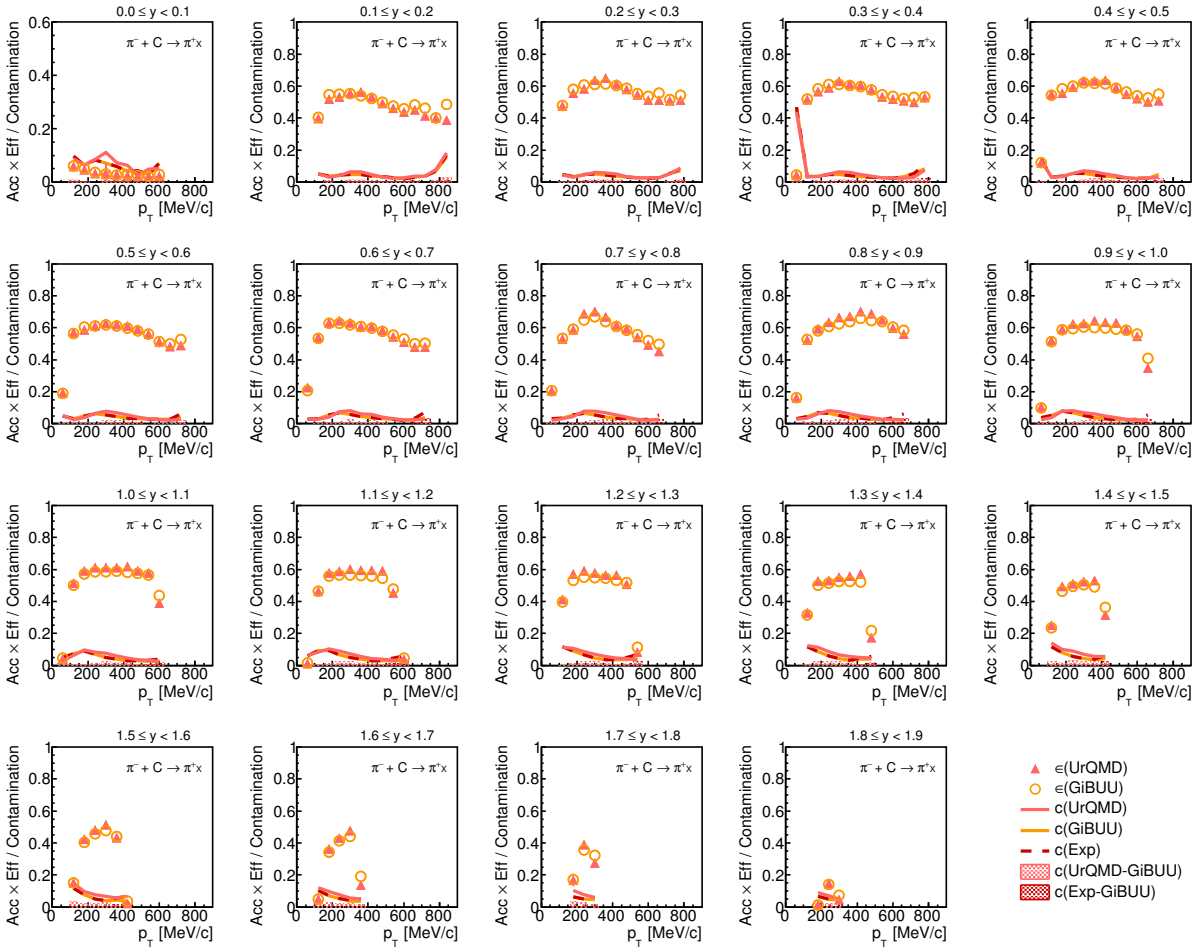

Figure 4.9: Comparison of the π^+ acceptance and efficiency correction matrices as a function of transverse momentum in different rapidity regions (see legend) for $\pi^- + \mathrm{C}$ collisions. The orange open circles depict the correction obtained with GiBUU and the light red triangles correspond to UrQMD. The solid curves represent the contamination originating from impurities in GiBUU (orange curve) and UrQMD (light red curve), respectively. The estimated contamination in the experimental data is shown by the dark red dashed curve. The filled areas indicated the relative difference in contamination of GiBUU compared UrQMD (light red filled area) and experimental data (dark red filled area). The errors of the acceptance and efficiency correction in UrQMD indicated the relative difference in contamination of GiBUU compared UrQMD.

state-of-the-art transport model calculations.

4.1.3 Systematic Uncertainties

In the following, the systematic uncertainties that are caused by the measurement itself or by the applied analysis method were evaluated. An important analysis step is the particle identification which was introduced by the two-dimensional cut corresponding to 2σ -selection, around the expected β-value of pions in the correlation in β-momentum plane, which was applied to select a high purity charged pion sample. Any removal of true charged pions or impurities due to this cut should be accounted for by the efficiency correction. In order to investigate if there are some

residual differences between the experimental data and simulation, the analysis was repeated with a broader (smaller) selection of 2.5σ (1.5σ) (Appendix D.1). The systematic uncertainties based on the above discussed variations was estimated with help of the minimal and maximal systematic uncertainties. The correction uncertainty corresponds to 3% and was evaluated from investigations of elastic scattering negatively charged pions in a subsequent experimental campaign (Section 3.6.4). In case of the rapidity density distribution, the extrapolation error corresponding to the uncertainty of the Boltzmann fit (Section 4.2.2) is the dominant contribution to the systematic uncertainty.

4.2 Results and Discussion

4.2.1 Pt-y Distribution

The (double-)differential yields (Fig. 4.4) obtained in Section 4.1.1 were corrected for the reconstruction efficiency, as explained in Section 4.1.2. These corrected spectra are shown in Fig. 4.10. For π^+ the corrected (double-)differential distributions in $\pi^- + \mathrm{C}$ and $\pi^- + \mathrm{W}$ reactions look quite similar, but the spectrum is shifted more to backward rapidity and the absolute yield is higher for the latter collision system. Similar behavior is seen for π^-.

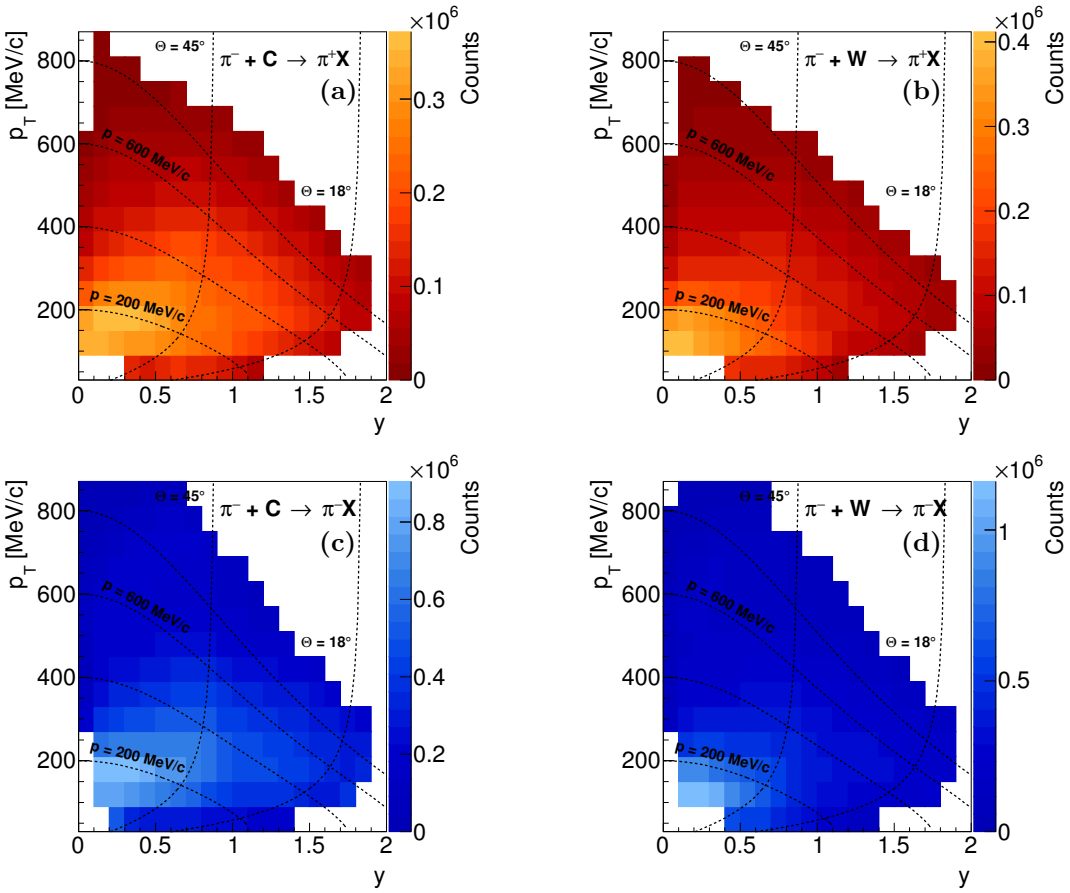

Figure 4.10: Corrected π^+ (a,b) and π^- (c,d) yield as a function of transverse momentum and rapidity inside the HADES acceptance for $\pi^- + \mathrm{C}$ (a,c) and $\pi^- + \mathrm{W}$ (b,d) collisions.

The total number of corrected π^+ and π^- for the $p_T - y$ analysis within the HADES acceptance in $\pi^- + \mathrm{C}$ reactions are equal to $N_C^{\pi^+} = 23139260 \pm 6840(\mathrm{stat})^{+694655}_{-694407}(\mathrm{syst})$ and $N_C^{\pi^-} = 58380168 \pm 11116(\mathrm{stat})^{+1752275}_{-1751581}(\mathrm{syst})$ and in $\pi^- + \mathrm{W}$ reactions are equal to $N_W^{\pi^+} = 17173510 \pm 5723(\mathrm{stat})^{+519629}_{-515913}(\mathrm{syst})$ and $N_W^{\pi^-} = 48760716 \pm 10094(\mathrm{stat})^{+1472625}_{-1465026}(\mathrm{syst})$.

4.2.2 Rapidity Distribution

Based on corrected $p_T - y$ distributions of charged pions extracted in Section 4.1, the rapidity density distribution (dN/dy) can be obtained. For both charged pions, the p_T spectra reflect the yield within the acceptance, which depend on the selected rapidity interval. Figure 4.11 shows the p_T distributions of π^+ in different rapidity regions (see legend) for $\pi^- + \mathrm{W}$ reactions. As presented in Section 3.5 a Boltzmann fit (Eq. (3.8)) can be applied to the p_T spectra and then the resulting Boltzmann distribution can be consulted to extrapolate the yield in the uncovered kinematic regions. For the π^+ in $\pi^- + \mathrm{W}$ collisions, the Boltzmann distribution (orange curve) reproduces the shape of the experimental distribution reasonably well, as shown in Fig. 4.11. Although small deviations between the experimental data and the Boltzmann fit for $y < 0.4$ at intermediate p_T are observed in the heavier collision system. However, this is not a problem since the coverage of the experimental data is quite large and therefore the Boltzmann is only used for the extrapolation of the very low (high) p_T range. A similar agreement is observed for the entire measured rapidity range for $\pi^- + \mathrm{C}$ collisions (Fig. E.2) as well as for $\pi^- + \mathrm{W}$ reaction (Fig. E.3). The total yield in a given rapidity range was then extracted by summing all measured data points and the integral in the low and high p_T range, extrapolated by the Boltzmann fit.

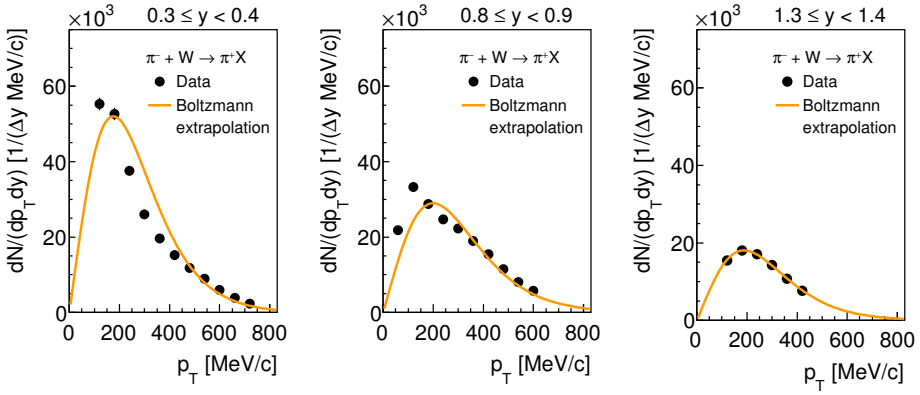

Figure 4.11: Transverse momentum spectra of π^+ corrected for reconstruction efficiency within the geometrical acceptance in different rapidity regions (see legend) for $\pi^- + \mathrm{W}$ reactions. The orange solid curve indicate Boltzmann fits. The errors represent the combined, statistical and systematic uncertainties.

For the π^- the extrapolation in the unmeasured kinematic regions is more complex, since here (quasi-)elastic scattering events have to be considered as well. Figure 4.12 shows the p_T distributions for different rapidity regions (see legend) in $\pi^- + \mathrm{W}$ collisions. For the rapidity $0.3 \leq y < 0.4$ two contributions in the p_T spectra are visible. Negatively charged pions, which were either produced in inelastic reactions (low p_T) or (quasi-)elastically scattered (high p_T). Thus, for the π^- produced in inelastic reactions a Boltzmann fit (Eq. (3.8)) was applied similar to the extrapolation procedure for the π^+. While for (quasi-)elastic scattered π^- a Gaussian fit was introduced to extrapolate the yield in the tail of the p_T distribution. In Figure 4.12 (a) the resulting total fit

is represented by the solid dark blue line, while the Boltzmann and Gaussian contribution are indicated by the dark blue dashed curve and the light blue dashed curve, respectively. A good description of the experimental distribution with the combined, Boltzmann and Gaussian, fit was achieved. With increasing rapidity the p_T coverage within the HADES acceptance gets less. For $y \approx 0.8$, the part of the p_T distribution corresponding to (quasi-)elastically scattered π^- is outside the acceptance and thus only the inelastic part can be extrapolated. Here, the Boltzmann fit is consistent with the shape of the experimental distributions, as shown in Fig. 4.12 (b) and Fig. 4.12 (c). For the entire measured rapidity range and for $\pi^- + \mathrm{C}$ collisions the employed fit, either combined Boltzmann and Gaussian or Boltzmann, reproduces the experimental data well (Fig. E.4 and Fig. E.5).

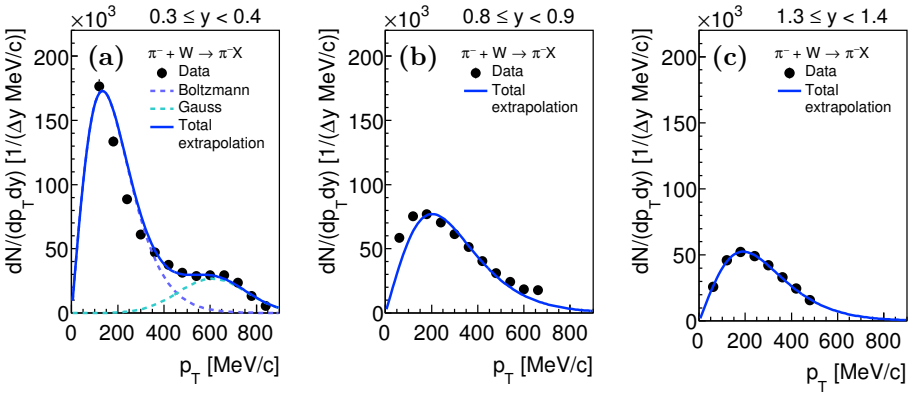

Figure 4.12: Transverse momentum spectra of π^- corrected for reconstruction efficiency within the geometrical acceptance in different rapidity regions (see legend) in $\pi^- + \mathrm{W}$ reactions. The solid lines indicate the total fits. For the rapidity range $0.3 \leq y < 0.4$ dark blue dashed curve resembles the Boltzmann distribution for the π^- produced in inelastic reactions and light blue dashed curve the Gaussian distribution for (quasi-)elastic scattered π^-. The errors represent the combined, statistical and systematic, uncertainties.

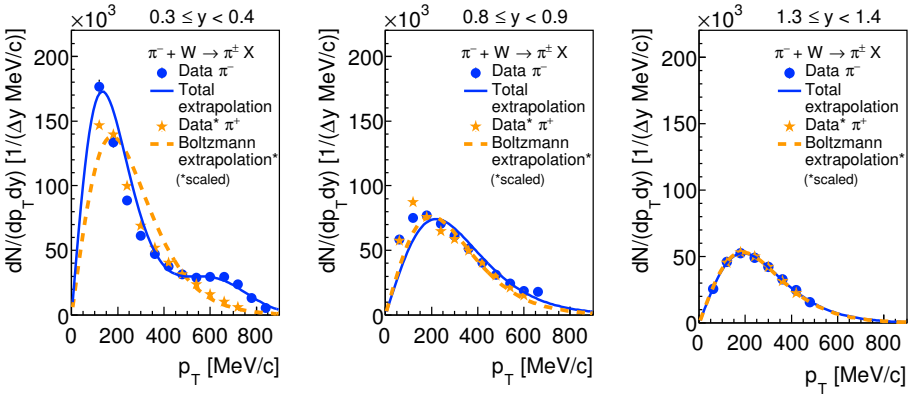

Figure 4.13: Transverse momentum spectra of π^- (blue points) in different rapidity regions (see legend) in $\pi^- + \mathrm{W}$ reactions. The blue solid curves represent the total extrapolations of π^-. The corresponding scaled transverse momentum spectra of π^+ are resembled by the orange stars together with Boltzmann extrapolations (orange dashed curve).

Further, one can compare the shape of the inelastic scattering peak for both charged pions. Thus, the p_T spectra of π^+ were scaled to the integral of the p_T distributions of π^- in the range upto $p_T = 400$ MeV/c. Figure 4.13 depicts the comparison of p_T distributions for π^- (orange stars)

and π^+ (blue points) in the same rapidity regions as shown above for in $\pi^- + \mathrm{W}$ reactions. For backward rapidities deviations between the inelastic scattering peak of π^- and π^+ are seen, however for forward rapidities the agreement is almost perfect. The comparison for all rapidity regions is presented in Fig. E.7. In $\pi^- + \mathrm{C}$ reactions the shapes of inelastic scattering peak for π^- and π^+ are (nearly) similar over the entire rapidity range (Fig. 4.14, Fig. E.6)).

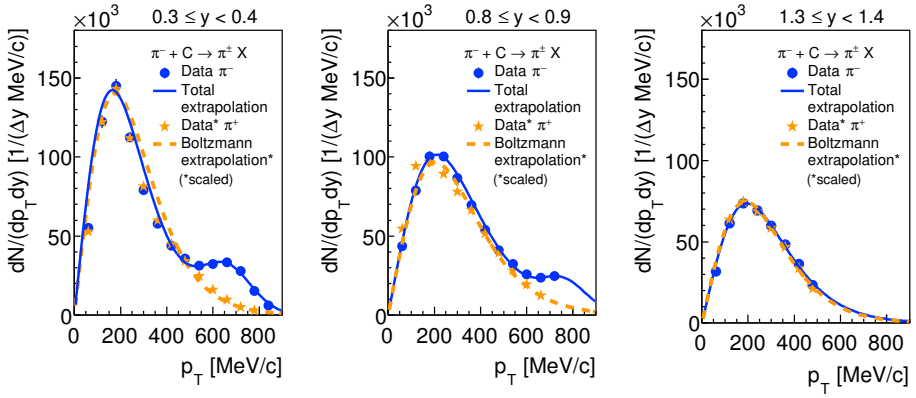

Figure 4.14: Transverse momentum spectra of π^- (blue points) in different rapidity regions (see legend) in $\pi^- + \mathrm{C}$ reactions. The blue solid curves represent the total extrapolations of π^-. The corresponding scaled transverse momentum spectra of π^+ are resembled by the orange stars together with Boltzmann extrapolations (orange dashed curve).

By summing all measured data points and the integral in the low and high p_T range based on the total fit, the total yield of the π^- in a given rapidity range can be obtained. For $y \lesssim 0.8$, the total yield ((quasi-)elastic and inelastic yield) was extracted with help of the total fit, while the inelastic yield was obtained for the entire covered rapidity range. Thus, to extract the inelastic yield in the rapidity range $y \lesssim 0.8$ all measured data points were summed up in the inelastic range until $p_T = 390$ MeV/c and the Boltzmann contribution of the total fit was integrated in the remaining regions. As for the higher rapidities the experimental distributions contain only the inelastic part, the total fits are consistent with Boltzmann functions, which were used for the extrapolation.

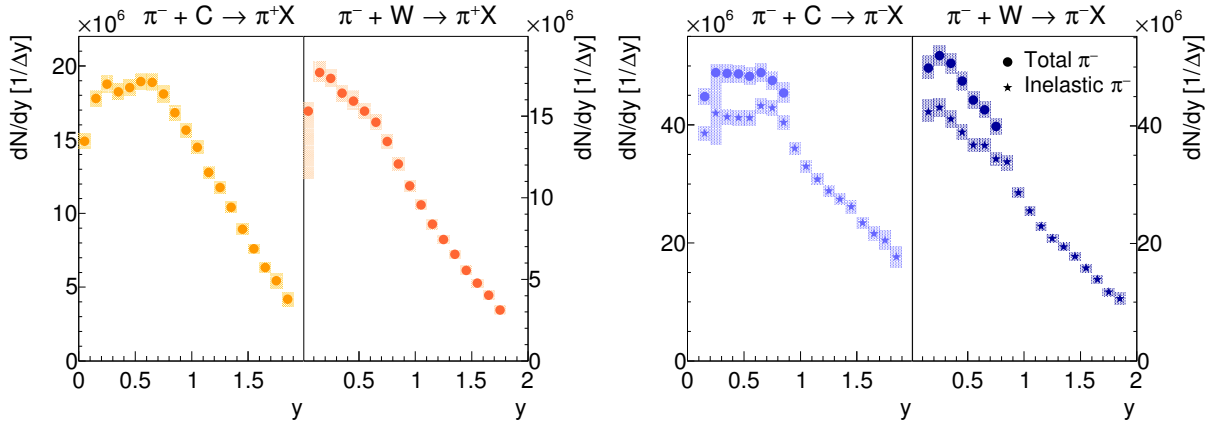

Figure 4.15: Rapidity density distribution of π^+ (orange) and π^- (blue) in $\pi^- + \mathrm{C}$ and $\pi^- + \mathrm{W}$ collisions (see legend). The statistical uncertainty is smaller than the symbol size, while the bands denote the systematic uncertainty. For π^- the total distribution originating from (quasi-)elastic and inelastic reactions is represented by the circles, while the inelastic part of the distribution indicated by the stars.

The resulting rapidity density spectra for π^+ and π^- in both collision systems are depicted in Fig. 4.15. The shapes of the rapidity distribution for the inelastic π^+ (orange points) and π^- (blue stars) look comparable for $\pi^- + \mathrm{C}$ and $\pi^- + \mathrm{W}$ collisions, respectively. Moreover, concerning the shape of π^- rapidity distributions for the total, (quasi-)elastic and inelastic, and inelastic reactions no difference is observed. However, in the heavier target (W) the distribution of the charged pions is shifted to backward rapidity, the ones in the lighter target (C) are rather symmetric. Thus scattering processes are dominant in the heavier system (W).

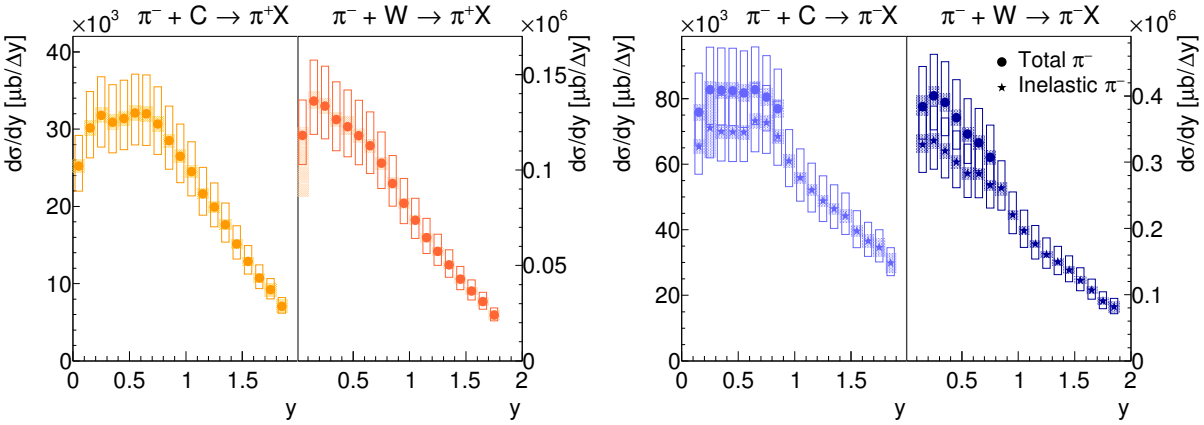

Figure 4.16: Cross-section of π^+ (orange) and π^- (blue) as function of rapidity in $\pi^- + \mathrm{C}$ and $\pi^- + \mathrm{W}$ collisions (see legend). The statistical uncertainty is smaller than the symbol size, while the bands denote the systematic uncertainty. The open boxes represent the normalization error. For π^- the total distribution originating from (quasi-)elastic and inelastic reactions is represented by the circles, while the inelastic part of the distribution indicated by the stars.

Furthermore, obtained (double-)differential yields of π^+ and π^- were normalized to the total number of beam particles and the target thickness to obtain absolute cross-sections. The normalization error is dominated by the uncertainty on the beam intensity, which amounts to 15%. For details see Section 3.4. The π^+ and π^- production cross-section as function of rapidity is presented in Fig. 4.16. The integrated differential production cross-section ($\Delta\sigma$) for π^+ ($0 \leq y < 1.9(1.8)$) and π^- ($0.1 \leq y < 1.9$) inside the HADES acceptance are listed in inelastic $\pi^- + \mathrm{C}$ and $\pi^- + \mathrm{W}$ reactions in Table 4.2. Moreover, the integrated differential cross-section ($\Delta\sigma$) for (quasi-)elastic and inelastic π^- ($0.1 \leq y < 0.9(0.8)$) inside the HADES acceptance are summarized in Table 4.3.

Table 4.2: Target, particle species and cross-section for π^+ ($0 \leq y < 1.9(1.8)$) and π^- ($0.1 \leq y < 1.9$) for inelastic $\pi^- + \mathrm{C}$ and $\pi^- + \mathrm{W}$ reactions (see text for details). Error values shown are statistic (first), systematic (second) and normalization (third).

Target	Particle	$\Delta\sigma$ [μb]
C	π^+	$43787 \pm 13\ ^{+1323}_{-1322}\ ^{+6880}_{-5629}$
C	π^-	$94398 \pm 20\ ^{+2872}_{-2997}\ ^{+14833}_{-12136}$
W	π^+	$152711 \pm 51\ ^{+4637}_{-5600}\ ^{+23996}_{-19633}$
W	π^-	$348240 \pm 79\ ^{+10564}_{-10578}\ ^{+54721}_{-44771}$

Table 4.3: Target, particle species and total cross-section for π^- $(0.1 \leq y < 0.9(0.8))$ (quasi-)elastic and inelastic $\pi^- + \mathrm{C}$ and $\pi^- + \mathrm{W}$ reactions (see text for details). Error values shown are statistic (first), systematic (second) and normalization (third).

Target	Particle	$\Delta\sigma$ [μb]
C	π^-	$56961 \pm 13\ ^{+1723}_{-1925}\ ^{+8951}_{-7323}$
W	π^-	$213699 \pm 57\ ^{+6517}_{-6515}\ ^{+33584}_{-27478}$

4.2.3 P-θ Distribution

The same analysis procedure as explained for $p_T - y$ phase space (Section 4.1), was applied to the $p - \theta$ phase space. For the $p - \theta$ analysis the total number of reconstructed π^+ and π^- within the HADES acceptance in $\pi^- + \mathrm{C}$ reactions are equal to $N_C^{\pi^+} = 10832343 \pm 3291$ and $N_C^{\pi^-} = 26186070 \pm 5117$ and in $\pi^- + \mathrm{W}$ reactions are equal to $N_W^{\pi^+} = 8446896 \pm 2906$ and $N_W^{\pi^-} = 21486628 \pm 4635$.

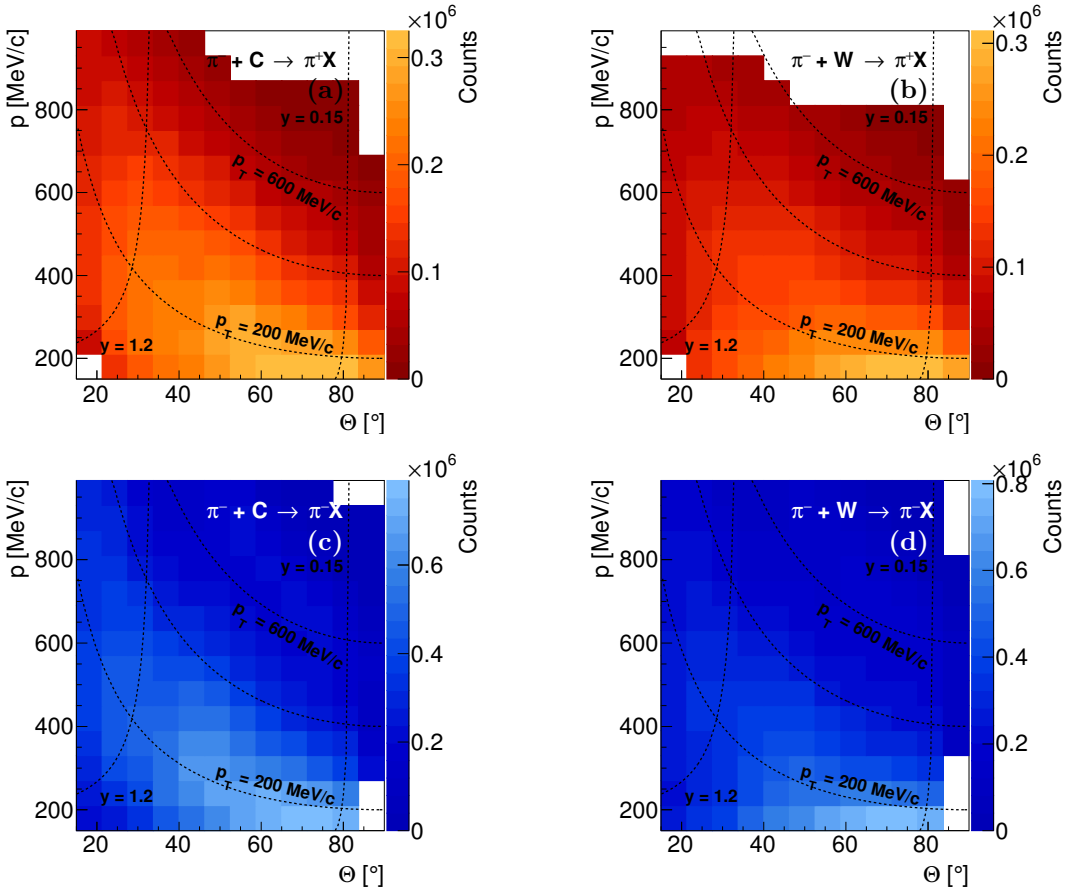

Figure 4.17: Corrected π^+ (a,b) and π^- (c,d) yield as a function of momentum p and polar angle θ inside the HADES acceptance for $\pi^- + \mathrm{C}$ (a,c) and $\pi^- + \mathrm{W}$ (b,d) collisions.

After the application of corrections for the reconstruction efficiency, corrected double-differential spectra are obtained as depicted in Fig. 4.17. The total number of corrected π^+ and π^- for the $p - \theta$ analysis within the HADES acceptance in $\pi^- + \mathrm{C}$ reactions are equal to $N_C^{\pi^+} =$

$20568304 \pm 6249(\text{stat})^{+617430}_{-617067}(\text{syst})$ and $N_C^{\pi^-} = 52058096 \pm 10173(\text{stat})^{+1562551}_{-1561881}(\text{syst})$ and in $\pi^- +$ W reactions are equal to $N_W^{\pi^+} = 15072563 \pm 5186(\text{stat})^{+452708}_{-452343}(\text{syst})$ and $N_W^{\pi^-} = 41611060 \pm 8977(\text{stat})^{+1248935}_{-1248346}(\text{syst})$.

4.2.4 Comparison to HARP Data

The HARP Collabortaion performed a systematic study of the inclusive double-differentail cross-section of $\pi^\pm$ with incident charged pions beams ($\pi^\pm$) with a momentum of 3, 5, 8 and 12 GeV/c impinging on beryllium, carbon, aluminium, copper, tin, tantalum and lead targets [A$^+$09d]. The obtained results allowed to investigate the dependence of charged pion production on the atomic number A and incoming beam momentum. From this data, a weak beam momentum dependence of pion production by incoming pions was observed, particularly striking for low A targets and enhanced for same-charge pion production. Besides, it was found that the momentum dependence is larger for the more forward angles, while backward production shows little beam momentum dependence over the whole range in A.

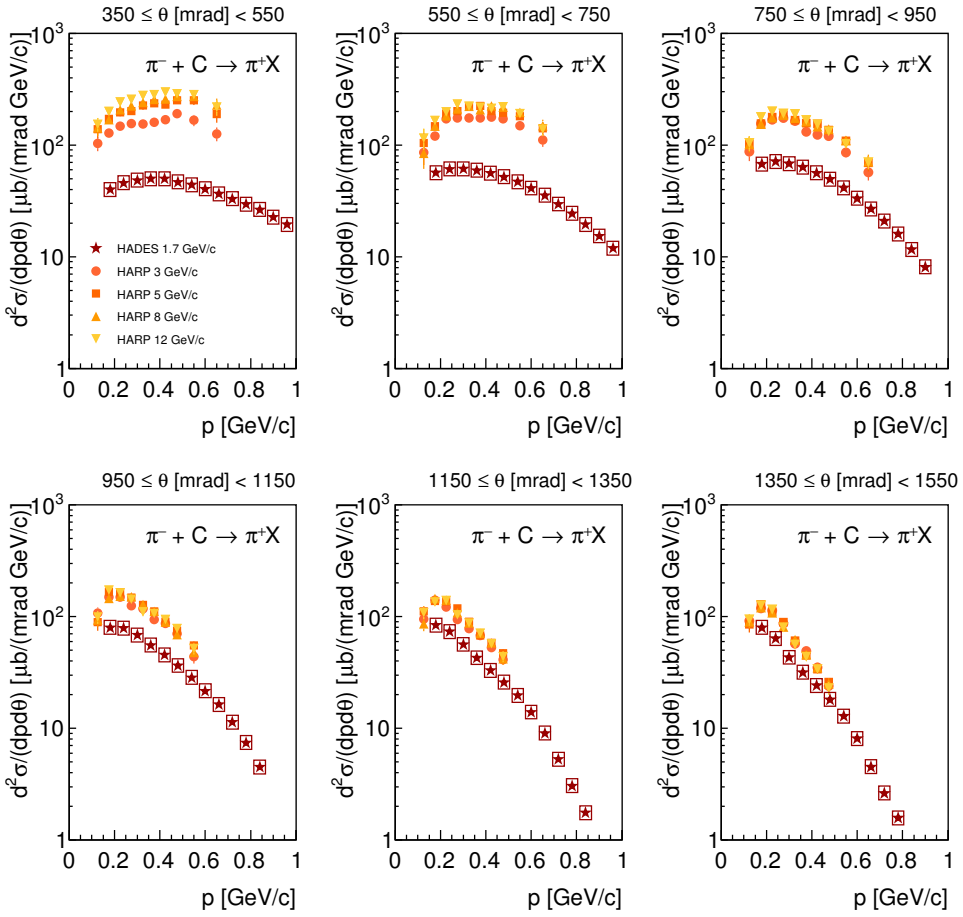

Figure 4.18: Double-differential cross-section for π^+ as a function of momentum in $\pi^- + \text{C}$ reactions displayed in different angular regions (see legend). The stars resemble the cross-sections of π^- in this work. The combination of statistical and systematic uncertainty is smaller than the symbol size, while the normalization error is represented by the open box. The circles, squares and triangles depict the results by HARP [A$^+$09d] at a beam momentum of 3, 5, 8 and 12 GeV/c, respectively.

With the $\pi^- + \mathrm{C}$ reactions at a beam momentum of 1.7 GeV/c measured by HADES the dependence on the incoming beam momentum can be extended to an unmeasured regime. Figure 4.18 presents the comparison of the π^+ double-differential cross-section for different angular regions ranging from 0.35 mrad $\leq \theta <$ 1.55 mrad, while HADES features a larger momentum coverage than HARP. For the lowest angular range a clear dependence of inclusive double-differential cross-section on the incoming beam momentum can be seen as the cross-section is increasing with increasing incoming beam momentum. The difference between the measured cross-sections corresponding to different beam momenta is decreasing with increasing angular range. However, for the HARP measurements the deviations for the different beam momenta $(3 - 12$ GeV/$c)$ is rather shallow, while the measurement of HADES for the lowest beam momentum (1.7 GeV/c) is clearly separated from the other measurements.

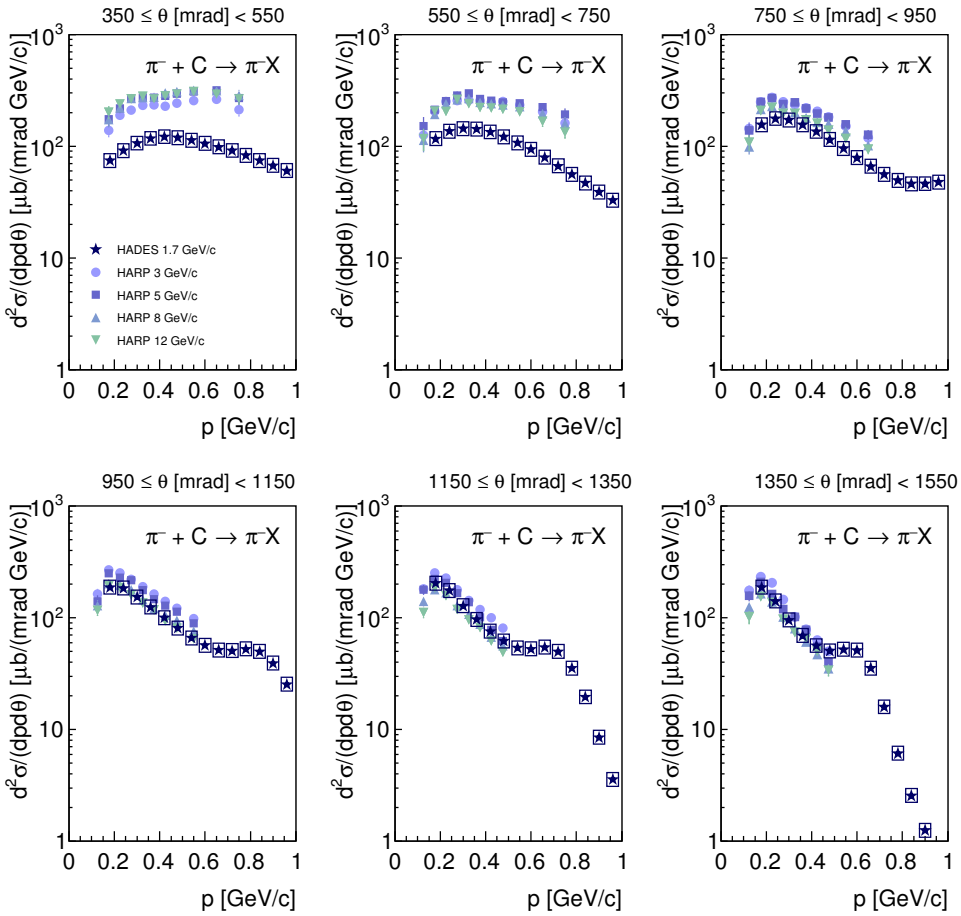

Figure 4.19: Double-differential cross-section for π^- as a function of momentum in $\pi^- + \mathrm{C}$ reactions displayed in different angular regions (see legend). The stars resemble the cross-sections of π^- in this work. The combination of statistical and systematic uncertainty is smaller than the symbol size, while the normalization error is represented by the open box. The circles, squares and triangles depict the results by HARP [A$^+$09d] at a beam momentum of 3, 5, 8 and 12 GeV/c, respectively.

Further, comparisons of the π^- double-differential cross-section in $\pi^- + \mathrm{C}$ collisions are presented in Fig. 4.19. Also for the same sign-pion production, the dependence on the beam momentum is best seen for the smallest angular region. However, the dependence on the beam momentum is less pronounced as the measurement of this work (1.7 GeV/c) comes close the HARP measurement

starting from $\theta > 750$ mrad.

The dependence of the averaged cross-sections on the incident beam momentum is shown in Fig. 4.20 (a) for π^+ and in Fig. 4.20 (b) for π^-. The cross-sections are averaged over the forward angular region 0.350 rad $\leq \theta <$ 1.550 rad and momentum region 200 MeV/$c \leq p <$ 700 MeV/c. Results for the light nucleus C ($A = 6$) are presented together with the data for heavy nuclei, W ($A = 184$) and Ta ($A = 181$). The beam momentum dependence of the cross-section for the light nucleus differs clearly from the dependence in the heavy nuclei as the dependence in the C data is much more flat. Moreover, the momentum dependence is larger for opposite-charge pion production than for equal-charge production.

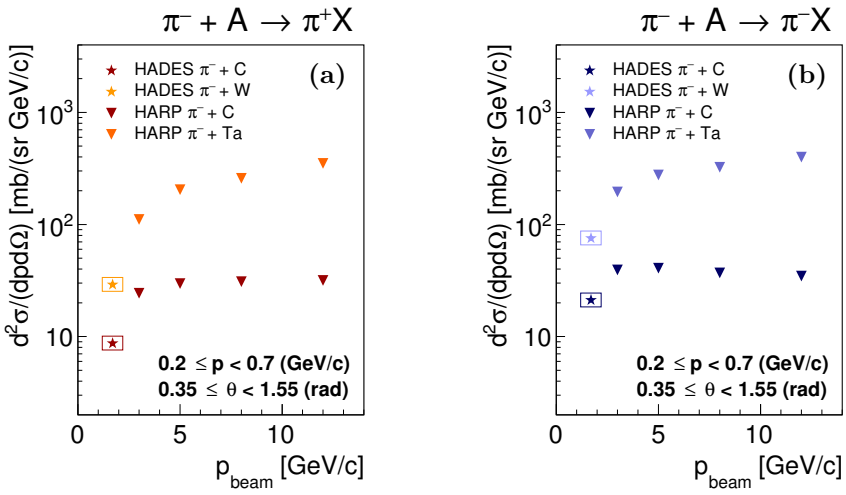

Figure 4.20: Dependence on the beam momentum of the π^- (b) and π^- (b) production cross-section in $\pi^- + \mathrm{C}$, $\pi^- + \mathrm{Ta}$ and $\pi^- + \mathrm{W}$ reactions averaged over the forward angular region (0.350 rad $\leq \theta <$ 1.550 rad) and momentum region (200 MeV/$c \leq p <$ 700 MeV/c). The combination of statistical and systematic uncertainty is smaller than the symbol size, while the normalization error is represented by the open box. The data by HARP is taken from [A$^+$09d].

In summary, the presented data provide an additional measurements at a low beam momentum. The strongest dependence on the incoming beam momentum is observed for small polar angles. Contrary to the conclusion by HARP, the additional data point to a sizable beam momentum dependence of the pion production. Further, this dependence seems to be more striking for π^+.

4.2.5 Comparison to Transport Calculations

In the following section, comparisons between the measured charged pion (double-)differential cross-sections as a function of p_T and rapidity to three state-of-the-art hadronic transport models, GiBUU (version 2017) [BGG$^+$12], UrQMD (UrQMD v3.4) [B$^+$99b] and SMASH (SMASH 1.6) [W$^+$16], are presented. The production mechanisms implemented in these transport models differ strongly. Since in UrQMD and SMASH (most) final state originate from the strong decays of intermediate resonances (e.g. Δ, N^*) with differences masses and widths. GiBUU mediates the hadron production channels via (final) cross-section parametrizations and does do not explicitly produce and propagate intermediate resonances. In the following, the predictions of GiBUU are represented by solid curves, while the ones of UrQMD are indicated by the dotted curves and the ones of SMASH are resembled by the dashed curves. While the upper panels present the (direct)

comparison of the experimental data to the predictions, the lower panels in each figure show the deviation between the measured and simulated distributions expressed as the relative difference normalized to experimental cross-section ((Sim-Exp)/Exp).

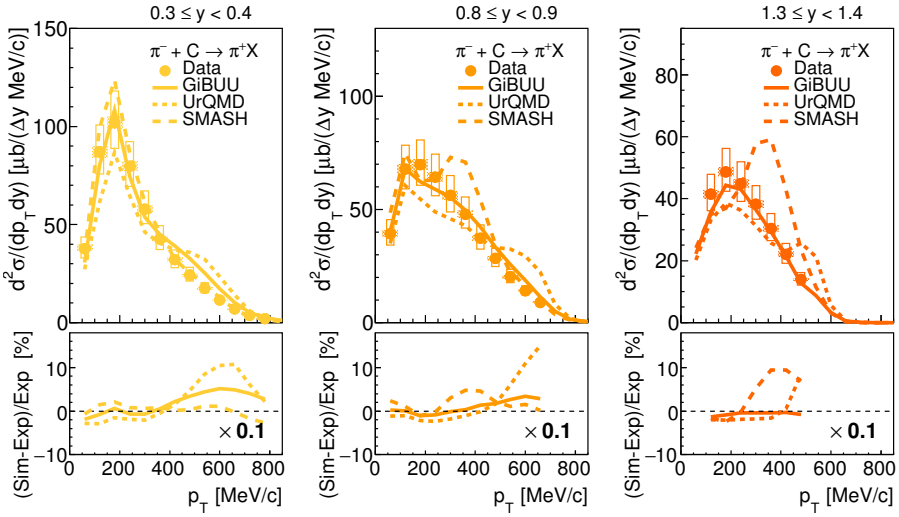

Figure 4.21: Comparison of the experimental π^+ $p_T - y$ distribution to the GiBUU (solid curve), UrQMD (dotted curve) and SMASH (dashed curve) transport model on an absolute scale in $\pi^- + \mathrm{C}$ reactions for different rapidity regions (see legend). The statistical errors are smaller than the symbol size. The systematic (hashed areas) and normalization (open boxes) uncertainties are indicated.

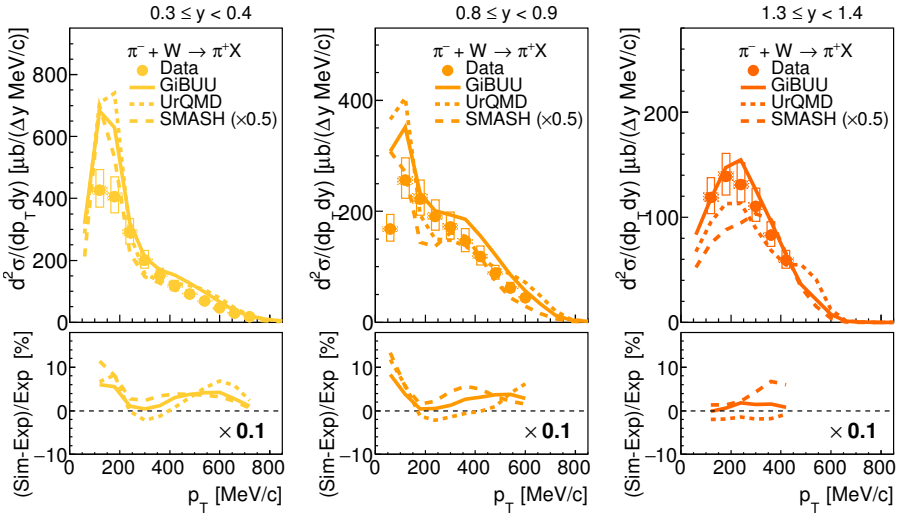

Figure 4.22: Comparison of the experimental π^+ $p_T - y$ distribution to the GiBUU (solid curve) and UrQMD (dotted curve) and SMASH (dashed curve) transport model on an absolute scale in $\pi^- + \mathrm{W}$ reactions for different rapidity regions (see legend). The statistical errors are smaller than the symbol size. The systematic (hashed areas) and normalization (open boxes) uncertainties are indicated.

Figure 4.21 shows the comparison between the measured π^+ differential cross-sections as a function of p_T with GiBUU (solid curve), UrQMD (dotted curve) and SMASH (dashed curve) calculations for backward $(0.3 - 0.4)$, mid- $(0.8 - 0.9)$ and forward $(1.3 - 1.4)$ rapidity regions in $\pi^- + \mathrm{C}$ reactions. In the low p_T range, both transport models, GiBUU and UrQMD, deliver p_T distribution shapes for π^+ almost comparable to each other. While for high transverse momenta

and increasing rapidity deviations become visible. SMASH, except for the lowest rapidity, predicts completely different shapes. With respect to the experimental distributions, GiBUU agrees within errors quantitatively over almost the entire p_T range. UrQMD predicts in intermediate p_T range ($p_T < 400$ MeV/c) comparable shapes indicated by rather flat distributions in the difference plots, while for higher p_T the deviations are striking. The peak in UrQMD at higher transverse momenta ($p_T > 300$MeV/c) grows with increasing rapidity. It was found in Appendix H.2 that this peak is caused by the $\Delta(1232)$ resonance. For low rapidities the experimental distributions is best described by SMASH. Although with increasing rapidity the distributions of SMASH significantly differs from the experimental ones. Figure 4.22 presents the comparison in $\pi^- + \mathrm{W}$ reactions analogous to $\pi^- + \mathrm{C}$ collisions. The shapes of the p_T distributions predicted by GiBUU, UrQMD and SMASH are (rather) comparable for almost the entire p_T and rapidity range. Although, with increasing rapidity the remaining difference become more obvious. The peaky structure at high p_T caused by heavy resonances in UrQMD is less visible. Especially for the backward and mid-rapidity at low transverse momenta ($p_T < 200$ MeV/c) all three models deviate strongly from the experimental distribution in shape and absolute cross-section. Differences are also observed for $p_T > 500$ MeV/c. Besides, the cross-sections predicted by SMASH in $\pi^- + \mathrm{W}$ reactions are overestimated by far as it had to be reduced by a factor of 0.5 for the representation.

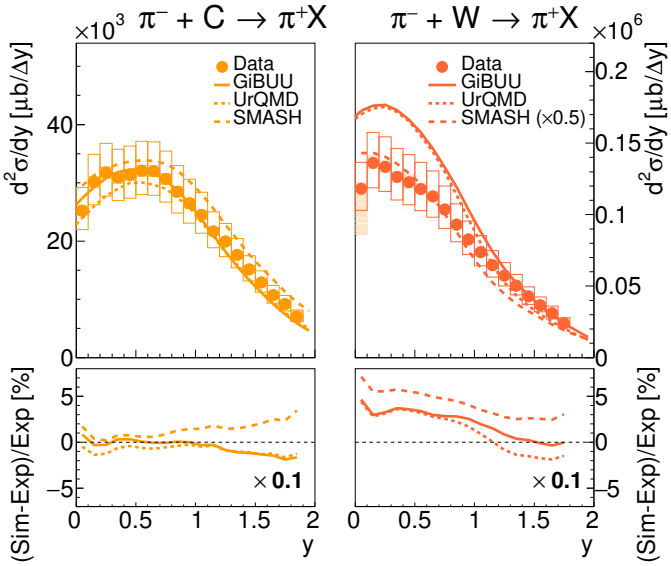

Figure 4.23: Comparison of the experimental π^+ rapidity distribution to GiBUU (solid curve) and UrQMD (dotted curve) and SMASH (dashed curve) on an absolute scale in $\pi^- + \mathrm{C}$ and $\pi^- + \mathrm{W}$ reactions (see legend). The statistical errors are smaller than the symbol size. The systematic (hashed areas) and normalization (open boxes) uncertainties are indicated.

In addition, the experimental π^+ cross-section is represented as a function of rapidity in Fig. 4.23. As already discussed in Section 4.2.2, the shape of the rapidity distribution differs slightly for the light (C) and the heavy (W) target, the latter being shifted to backward rapidity. GiBUU, UrQMD and SMASH predict almost the same behavior as the function of rapidity. Only minor differences between GIBUU and UrQMD are observed for backward rapidity in $\pi^- + \mathrm{C}$ reactions and for forward rapidity in $\pi^- + \mathrm{W}$ reactions. Nevertheless, the experimental π^+ cross-section is (slightly) better reproduced by GiBUU in lighter collision system. However, both models, GiBUU and UrQMD, agree within errors with the experimental distribution (almost) over the whole range. Whereas, SMASH differs from both other models also in forward rapidity region and hence

agrees less with the experimental data. In the heavier collision system the π^+ cross-sections is significantly over-predicted by GiBUU and UrQMD for backward rapidity, although not significant within errors. Contrary, SMASH strikingly overestimates the experimental cross-section over the entire rapidity range. Due to the observed ambiguities, a refinement of all three models is necessary. As the π^+ cross-section is more or less under control in the lighter nucleus (C), the elementary πN cross-section for the π^+ production channels seem to be rather under control. While the observed deviations in the heavy nucleus point to an incomplete description of in-medium effects such as secondary processes and scattering effects. Besides, in the case of UrQMD and SMASH the contribution of the (heavy) resonances decaying into π^+ and thus the branching ratios have to be re-tuned.

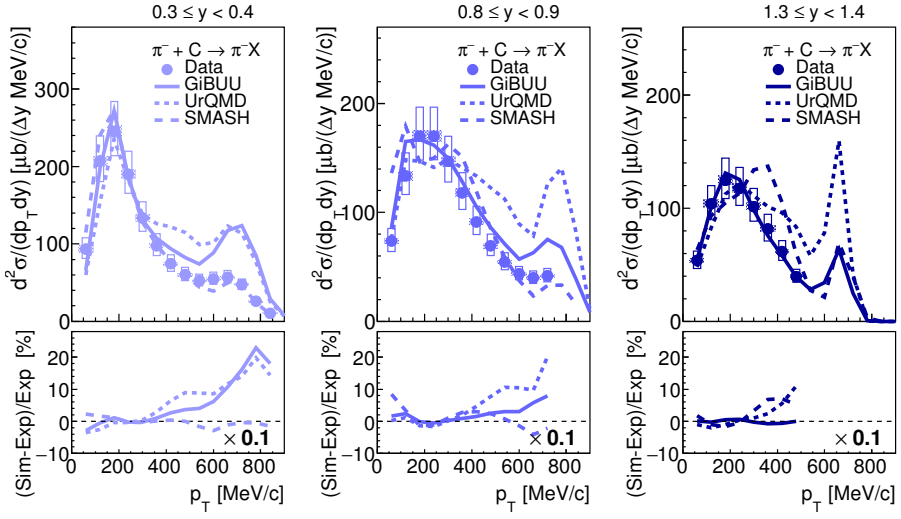

Figure 4.24: Comparison of the experimental π^- $p_T - y$ distribution to the GiBUU (solid curve), UrQMD (dotted curve) and SMASH (dashed curve) transport model on an absolute scale in $\pi^- + \mathrm{C}$ reactions for different rapidity regions (see legend). The statistical errors are smaller than the symbol size. The systematic (hashed areas) and normalization (open boxes) uncertainties are indicated.

With regard to the negatively charged mesons, the π^- is examined below. Not only the inclusive production, but also (quasi-)elastic scattering has to be considered. Analogous to the comparisons for π^+, the GiBUU (solid curve), UrQMD (dotted curve) and SMASH (dashed curve) model is confronted with the measured π^- difference cross-sections as a function of p_T in $\pi^- + \mathrm{C}$ (Fig. 4.24) and $\pi^- + \mathrm{W}$ (Fig. 4.25) collisions. Similar to π^+, the two models, GiBUU and UrQMD, predict an (almost) similar shape for low p_T ($p_T < 250$ MeV/c). SMASH, except for the forward rapidity, slightly differs. The inclusive π^- production off carbon seems to be reproduced for GiBUU, but for high p_T, the expected region of (quasi-)elastic events, the deviations are striking. For the heavier target, the predicted absolute cross-section of GiBUU is higher than for experimental data, although the agreement becomes better at forward rapidity. UrQMD is not able to reproduce the shapes nor the absolute cross-sections in the mid and high transverse momentum ranges, while the prediction is consistent with the experimental π^- production off carbon for very low p_T. Hence, also for UrQMD the (quasi-)elastic scattering seem to be over-estimated. Since in UrQMD (most) final states originate from the strong decay of intermediate resonances (e.g. Δ, N^*), elastic meson-baryon cross-sections are determined by resonance excitation and decay (e.g. $\pi N \rightarrow \Delta \rightarrow \pi N$). Detailed investigations (Appendix H.2) revealed the main resonance contributions arise from the $\Delta(1232)$ and $\Delta(1950)$ resonances. For backward and mid-rapidity the experimental distribution in $\pi^- + \mathrm{C}$ reactions is best described by SMASH. For the heavy

nucleus (W), SMASH overestimates the experimental cross-section over the entire rapidity range. Although the overestimation is less significant as compared to the π^+.

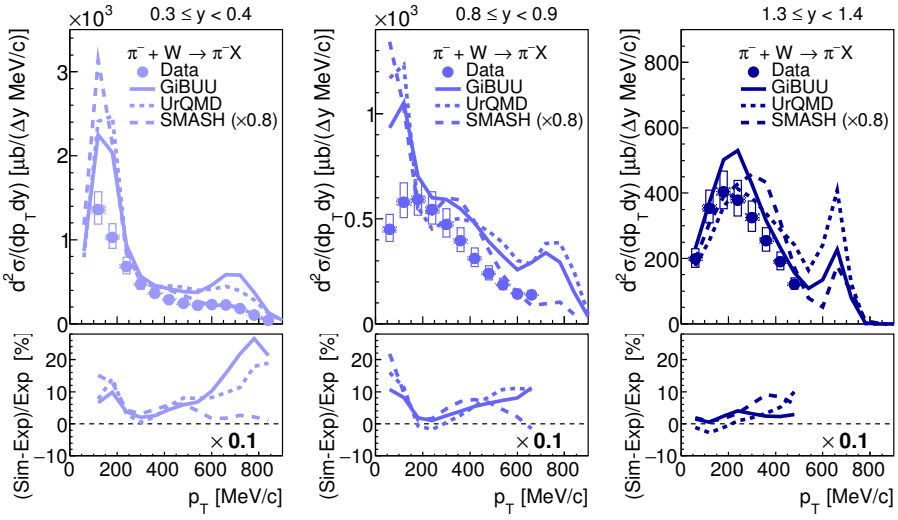

Figure 4.25: Comparison of the experimental π^- $p_T - y$ distribution to the GiBUU (solid curve), UrQMD (dotted curve) and SMASH (dashed curve) transport model on an absolute scale in $\pi^- + \mathrm{W}$ reactions for different rapidity regions (see legend). The statistical errors are smaller than the symbol size. The systematic (hashed areas) and normalization (open boxes) uncertainties are indicated.

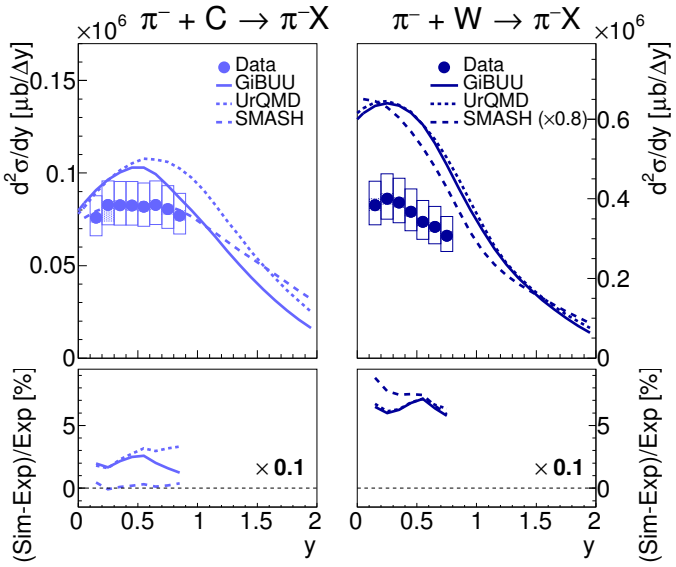

Figure 4.26: Comparison of the experimental π^- rapidity distribution to the GiBUU (solid curve), UrQMD (dotted curve) and SMASH (dashed curve) transport model on an absolute scale in $\pi^- + \mathrm{C}$ and $\pi^- + \mathrm{W}$ reactions (see legend). The statistical errors are smaller than the symbol size. The systematic (hashed areas) and normalization (open boxes) uncertainties are indicated.

The comparison of the absolutely normalized π^- rapidity distributions with the three models, GiBUU, UrQMD and SMASH, is shown in Fig. 4.26. GiBUU and UrQMD differ from each other by the forward rapidity in $\pi^- + \mathrm{C}$ reactions. The backward scattering in the heavier nucleus (W) is predicted by all three models. GiBUU and UrQMD overestimate the absolute π^-

cross-section of carbon and tungsten, while SMASH is in good agreement with the experimental distribution for the lighter nucleus. The prediction of both models, GiBUU and UrQMD is similar for $\pi^- + \mathrm{W}$ collisions, both overestimate the experimental cross-sections by far. For SMASH the overestimation is even bigger. All in all, there is no conclusive theoretical description of the (double-)differential π^- cross-sections. Comparable with π^+, the inelastic π^- cross-sections in the lighter nucleus (C) (almost) agrees with GiBUU predictions. Thus, also the elementary πN cross-section for the π^- production channels seems to be implemented correctly. But the description of (especially) scattering effects is insufficient. Looking at the π^- cross-section in the heavy nucleus (W), this becomes even clearer. Furthermore, in UrQMD and SMASH the branching ratios and thus the contribution of the resonances must be better restricted.

4.3 Summary of the Inclusive Pion Production

The inclusive charged pion analysis was performed to determine the production cross-sections in $\pi^- + \mathrm{C}$ and $\pi^- + \mathrm{W}$ reactions at an incident beam momentum of 1.7 GeV/c. For many-particle and astroparticle physics experiments the precise knowledge of hadron production is essential. Pion yields are not only important for calculations of the atmospheric neutrino flux [Bat01] and the accelerator neutrino flux [BG06], but also for the validation as well as a reference of transport model calculations, which are widely used for the interpretation of particle-physics results. Therefore, the charged pions were reconstructed and corrected for the reconstruction efficiency within the geometrical acceptance of HADES in two sets of kinematical variables $p_T - y$ and $p - \theta$ in the laboratory frame. Besides, the (double-)differential distributions shown in Fig. 4.10 and Fig. 4.17, the data allowed to extract the rapidity density (dN/dy) distribution presented in Fig. 4.15. The shapes of the rapidity density distribution for the inelastic π^+ and π^- look comparable for $\pi^- + \mathrm{C}$ and $\pi^- + \mathrm{W}$ collisions, respectively. However, in the heavier target (W) the distribution of the charged pions is shifted to backward rapidity, the ones in the lighter target (C) are rather symmetric. Moreover, the integrated differential inelastic production cross-section ($\Delta\sigma$) for π^+ ($0 \leq y < 1.9(1.8)$) and π^- ($0.1 \leq y < 1.9$) inside the HADES acceptance in both collision systems was obtained (Table 4.2).
In Figure 4.2.4 the double-differential cross-sections of charged pions were compared to comprehensive experimental campaign performed by the HARP Collaboration [A$^+$09d]. With the presented measurement at the lowest incident pion beam momentum of 1.7 GeV/c the existing data could be extended to an unmeasured regime and revealed a striking dependence on the incoming beam momentum, which is stronger for the positively charged pions.
Moreover, comparisons to state-of-the-art transport model calculations, GiBUU [BGG$^+$12], UrQMD [B$^+$99b] and SMASH [W$^+$16], were presented. For both charged pions, inclusive cross-section agrees with GiBUU predictions in the lighter nucleus (C) pointing to correctly implemented elementary inelastic πN cross-section for the charged pion production channels. However, the description of (especially) scattering effects seems insufficient as the predictions deviate for the heavier target (W) as well as for the (quasi-)elastically scattered π^-. The backward scattering in the heavier nucleus (W) is reproduced by all three models. But, for UrQMD and SMASH the contribution of the resonances decaying into charged pions and thus the branching ratios have to be re-tuned. All in all, there is no conclusive theoretical description of the (double-)differential charged pion cross-sections in pion-nucleus reactions.

5 Inclusive (Anti-)Kaon Production

The following section deals with the investigation of inclusive K^+ ($u\bar{s}$) and K^- ($s\bar{u}$) production in $\pi^- + \mathrm{C}$ and $\pi^- + \mathrm{W}$ collisions. The extracted (double-)differential cross-section within the HADES acceptance can give insights in the behavior of the (anti-)kaons in cold nuclear matter such as scattering and absorption processes. Of particular interest are the modification of the (anti-)kaon spectral function in nuclear matter which should already occure at finite baryon densities. For the kaon (K^+, K^0), kaon-nucleon scattering data [P$^+$16a] revealed that the KN interaction is repuslive. Extensive investigations of kaon (transverse) momentum distribution led as well to the conclusion that the real part of KN potential is repulsive within $20 - 40$ MeV [A$^+$10a, A$^+$14d, B$^+$09c, B$^+$04]. While, the existing data on in-medium effects of the antikaon produced off nuclear targets are very scare. On the one hand scattering experiments [P$^+$16a] as well as the observation of kaonic atoms [B$^+$11a, B$^+$09a, B$^+$11b] point to an attractive $\bar{K}N$ interaction. On the other hand the large coupling of the $\bar{K}N$ channel to baryonic resonances [Fuc06] introduces a large imaginary part of the potential and hence leds to strong absorption processes for K^-. The present results quantify the absorption effects in π-induced reactions. Hence, they are an important reference for in-medium effects for more complicated system like heavy-ion collisions as well as for the understanding of the equation-of-state for neutron stars [BTKR92, RSBW01]. Moreover they can be used to constrain theoretical calculations and serve as input for transport model calculations.
The analysis procedure to obtain kinematical distribution is described in detail. The distributions were corrected for the reconstruction efficiency within the geometrical acceptance and a self-consistency check was performed to exclude any model-dependence of this correction procedure. A comparison to state-of-the-art transport model calculations (GiBUU [BGG$^+$12], UrQMD [B$^+$99b] and SMASH [W$^+$16]) is presented. The in-medium behavior of the (anti-)kaons in terms of kaon scattering and antikaon absorption is discussed as well. Concerning the KN potential the obtained data is compared to observation by FOPI and ANKE.

5.1 Analysis Procedure

A double-differential analyses was performed for both charged kaons in $\pi^- + \mathrm{C}$ and $\pi^- + \mathrm{W}$ reactions in two sets of kinematic variables ($p_T - y$, $p - \theta$) in the laboratory frame. The kinematic regions are summarized in Table 5.1 and Table 5.2.

Table 5.1: Analyzed phase space region for K^+ and K^- in $p_T - y$ in the laboratory frame.

Particle	y	Δy	p_T [MeV/c]	Δp_T [MeV/c]
K^+	$0.0 - 1.1$	0.1	$30 - 750$	60
K^-	$0.2 - 1.0$	0.3/0.2/0.3	$90 - 330$	60

Table 5.2: Analyzed phase space region for K^+ and K^- in $p - \theta$ in the laboratory frame.

Particle	θ [°]	$\Delta\theta$ [°]	p [MeV/c]	Δp [MeV/c]
K^+	$15 - 90$	6.25	$150 - 990$	70
K^-	$15 - 65$	6.25/9.375/9.375	$220 - 570$	70

5.1.1 (Anti-)Kaon Reconstruction

Both charged kaons were pre-identified on the basis of the specific energy loss measured in the MDCs as a function of momentum (Section 3.3.2). Additional momentum corrections for the (anti-)kaon were applied, partly resulting from a systematic re-calibration of the HADES magnetic field values (of order $6 \cdot 10^{-3}$) and the energy loss in the beam tube, RICH radiator and target materials. The final (anti-)kaon yield was extracted by fitting the measured mass distribution in the corresponding phase space interval. To account for the different resolutions of the two time-of-flight detectors RPC and TOF, the procedure was performed separately for both detector systems. The mass spectrum for the K^+ corresponding to an interval in the RPC (Fig. 5.1 (a)) and TOF (Fig. 5.1 (b)) of 210 MeV/$c \leq p_T <$ 270 MeV/c and $0.4 \leq y < 0.5$ is shown in Fig. 5.1. The K^- abundance is two orders of magnitude lower compared to the K^+. The corresponding mass spectrum for the K^- in the RPC (Fig. 5.2 (a)) and TOF (Fig. 5.2 (b)) interval of 150 MeV/$c \leq p_T <$ 210 MeV/c and $0.2 \leq y < 0.5$ is depicted in Fig. 5.2.

The signal can be described by a Gaussian on top of a background consisting of a polynomial combined with an exponential function for each background particle species (p and π^+ or π^-). An iterative fitting procedure was employed to take into account the momentum-dependent mass distribution and background contamination. For each background particle species an exponential function was adapted to the experimental mass spectrum outside the signal range. Furthermore, full-scale GiBUU simulations [BGG+12] (Section 3.7) for events containing only (anti-)kaons were used to extract starting values for the mean μ and sigma σ of the Gaussian used to fit the signal.

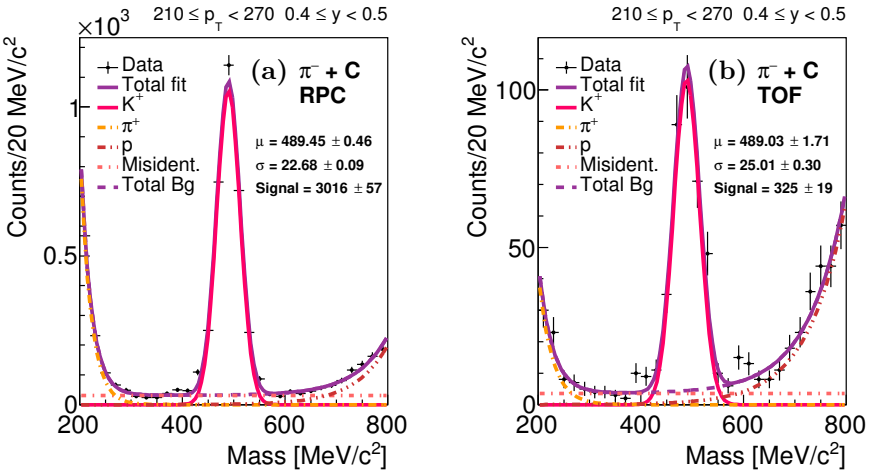

Figure 5.1: Mass distribution of K^+ in a certain $p_T - y$ interval (see legend) for the RPC (a) and TOF (b) in $\pi^- + \mathrm{C}$ reactions. The K^+ mass spectra is fitted with a composed function of a Gaussian for the signal (pink solid curve) and exponential function for the pions (orange dashed-dotted curve) and protons (red dashed-dotted curve) combined with a polynomial (magenta dashed-dotted curve).

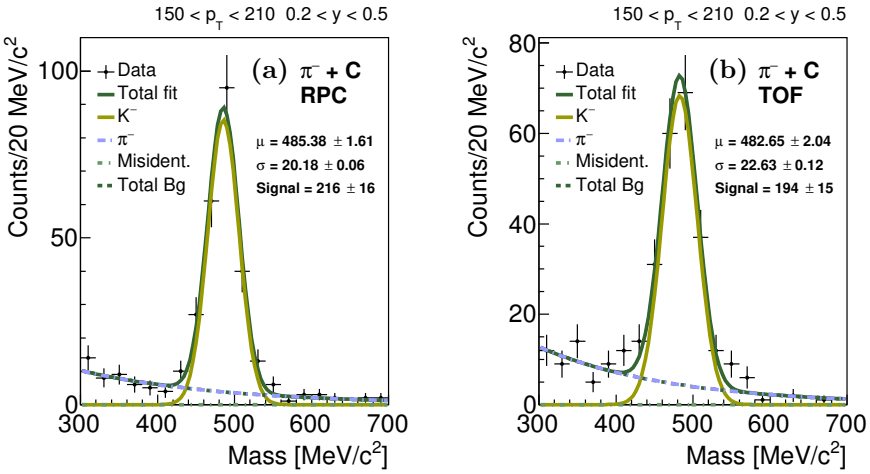

Figure 5.2: Mass distribution of K^- in a certain $p_T - y$ interval (see legend) for the RPC (a) and TOF (b) in $\pi^- + \mathrm{C}$ reactions. The K^- mass spectra are fitted with a composed function of a Gaussian for the signal (light green solid curve) and an exponential function for the pions (blue dashed-dotted curve) combined with a polynomial (green dashed-dotted curve)

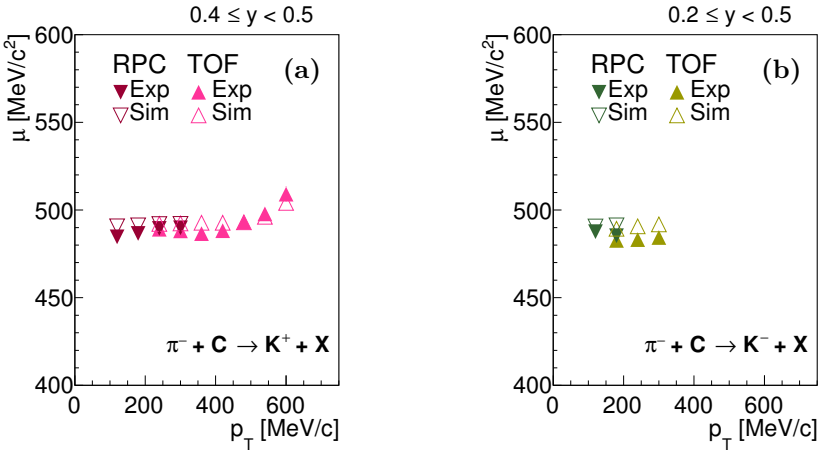

Figure 5.3: Mean (μ) of the Gaussian parametrization used for signal extraction as a function of transverse momentum for the rapidity region of $0.4 \leq y < 0.5$ for K^+ (a) and of $0.2 \leq y < 0.5$ for K^- (b) in experiment (closed symbols) and simulation (open symbols). For both detectors, RPC (dark symbols) and TOF (light symbols), the parameter μ is expected to increase with momentum.

Additionally, the width of the Gaussian was limited to vary around to the mean value of the width obtained from the simulation ($\sigma_{exp} = \sigma_{sim} \pm 0.5 \cdot \sigma_{sim,err}$). Around the (anti-)kaon signal area, a Gaussian together with a polynomial function for the background was added in the next step. All parameters thus obtained were used as input parameters for the combined fit shown by the violet spectra (K^+) in Fig. 5.1 and dark green (K^-) distributions in Fig. 5.2. To demonstrate the stability of the signal extraction, the mean value of the final Gaussian distribution of (anti-)kaon as a function of the transverse momentum in each rapidity interval was investigated (examples in Fig. 5.3). Due to momentum resolution effects, the mean μ of the Gaussian is monotonously increasing with increasing momentum in experiment and simulation, respectively. The agreement between experiment and simulation is reasonably good for both time-of-flight detectors, RPC and TOF. However the residual deviations can be attributed to the background underneath

the (anti-)kaon peak, which is (almost) negligible in simulation. Especially, K^- is affected by background in experimental data.

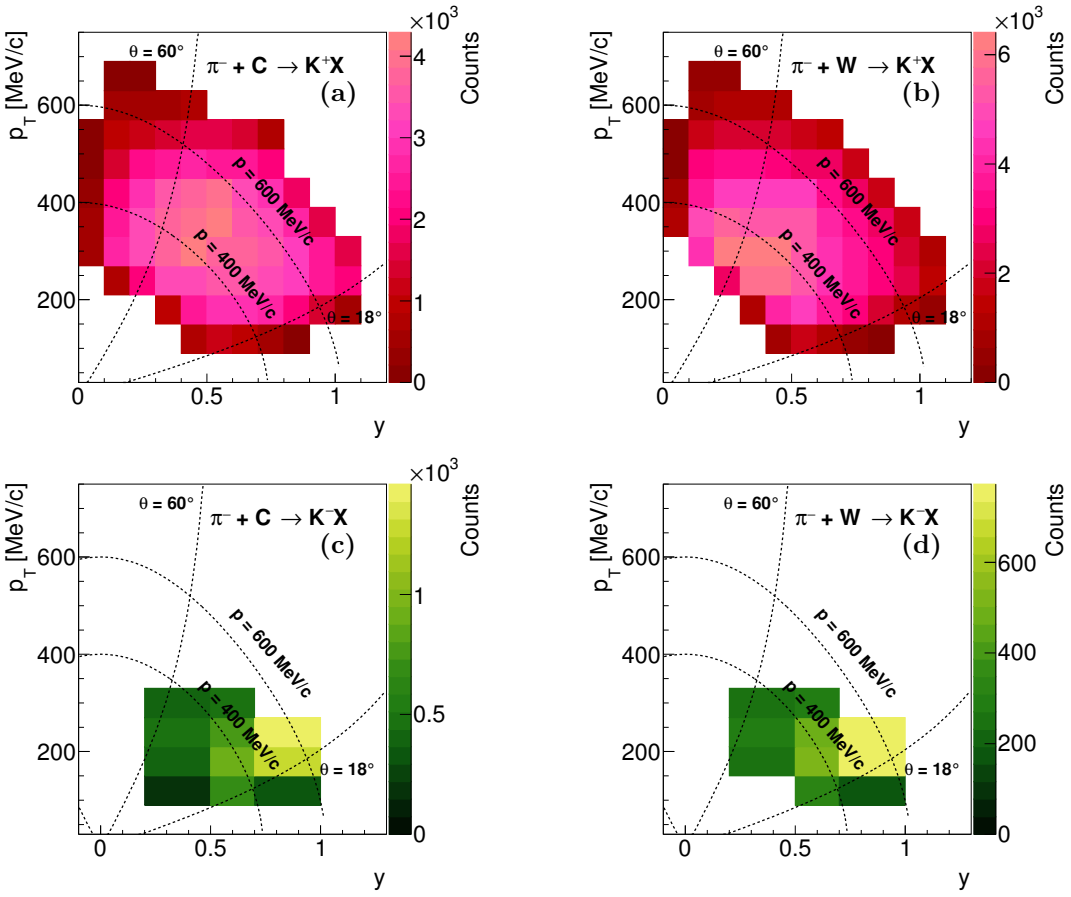

Figure 5.4: Reconstructed K^+ (a,b) and K^- (c,d) yield as a function of transverse momentum p_T vs. rapidity y inside the HADES acceptance for $\pi^- + \mathrm{C}$ (a,c) and $\pi^- + \mathrm{W}$ (b,d) reactions. The upper panel corresponds to K^+, while the lower one to K^-. The dotted black vertical lines indicate different polar angle regions, while the dotted black horizontal lines indicate different regions of constant momentum in the laboratory frame.

To obtain the (anti-)kaon yield, Gaussian parameterizations indicated by the pink distributions (K^+) in Fig. 5.1 and light green (K^-) distributions in Fig. 5.2 were integrated within a 3σ region around the mean μ. The signal-to-background ratio of the identified K^+ varies between $0.2\,(0.3) \leq S/B < 165.2\,(67.0)$ with an average of 9.0 (8.1) for $\pi^- + \mathrm{C}$ ($\pi^- + \mathrm{W}$) reactions. While, the K^- is reconstructed with lower signal-to-background ratios of $0.5\,(0.3) \leq S/B < 22\,(10.4)$ with an average of 5.2 (2.4) for $\pi^- + \mathrm{C}$ ($\pi^- + \mathrm{W}$) collisions. The resulting phase space distributions of the extracted raw yield within the HADES acceptance in $\pi^- + \mathrm{C}$ and $\pi^- + \mathrm{W}$ reactions are displayed in Fig. 5.4 for K^+ (upper panel) and for K^- (lower panel). In the range of the πN rapidity ($y_{\pi N} = 0.78$) both kaon types can be reconstructed down to low transverse momenta. However, due to the higher abundance and signal-to-background ratio, the K^+ has a larger phase space coverage within HADES than the K^-. The total number of reconstructed K^+ and K^- for the $p_T - y$ analysis within the HADES acceptance in $\pi^- + \mathrm{C}$ reactions are equal to $N_C^{K^+} = 160820 \pm 561$ and $N_C^{K^-} = 7310 \pm 138$ and in $\pi^- + \mathrm{W}$ reactions are equal to $N_W^{K^+} = 208783 \pm 602$ and $N_W^{K^-} = 4106 \pm 123$.

5.1.2 Acceptance and Efficiency Correction

As explain in detail in Section 3.6.4, not only all detector but also the applied analysis methods features inefficiencies and thus experimentally measured (anti-)kaon distributions are always hampered by those effects. However, to interpret the underlying physics of (anti-)kaons, a correction of the finite efficiency within the geometrical acceptance is mandatory. For this purpose, dedicated full-scale simulations based on GiBUU [BGG+12] (Section 3.7) were employed modeling the influence of the spectrometer acceptance and various inefficiencies (Section 3.6). While with the HGeant framework the detector acceptance is treated, effects of the detector response and tracking is performed on the SimDST level. The latter provides the same data format as for the experimental data.

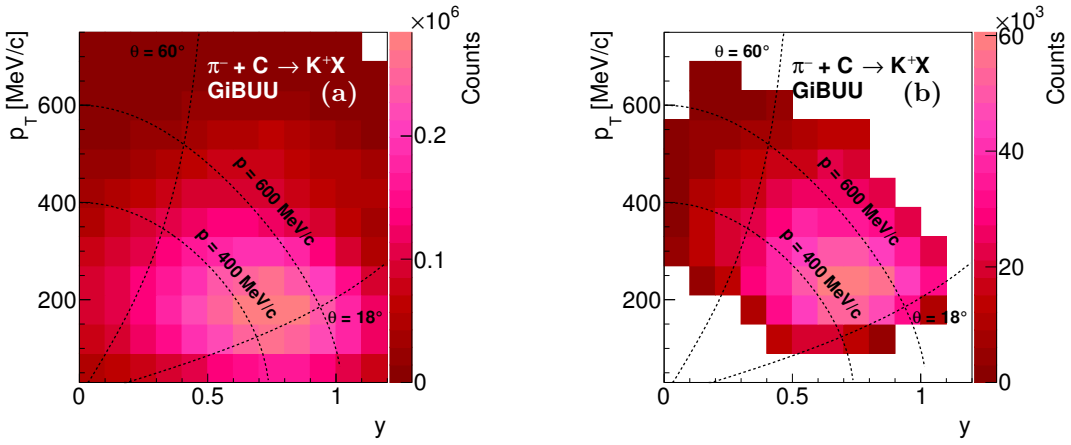

Figure 5.5: K^+ distribution as a function of transverse momentum p_T vs. rapidity y for initial unfiltered (a) and reconstructed (b) full-scale simulation of $\pi^- + \mathrm{C}$ reactions based on GiBUU. The black dotted horizontal lines indicate the momentum at 400 and 600 MeV/c. The back dotted vertical lines denote the polar angle regions between $\theta = 18 - 60°$.

For both charged kaons, in addition, the particle identification method for the simulation was adjusted such to select the same fraction of kaons as in the experimental data (see Section 3.3.2). Also the trigger condition was considered by requiring minimum charged particle multiplicity $M \geq 2$ in the META system. By processing the simulation through the same analysis chain as the experimental data, all other efficiency originating from the (anti-)kaon reconstruction method were taken into account. The correction was carried out in both sets of two independent kinematic variables ($p_T - y$, $p - \theta$) in the laboratory frame as listed in Table 5.1 and Table 5.2.

An example of kinematic distribution for K^+ in $\pi^- + \mathrm{C}$ reactions based on GiBUU is shown in Fig. 5.5. Figure 5.5 (a) shows the initial unfiltered distribution, while Fig. 5.5 (b) depicts the spectrum of the reconstructed full-scale simulation. The binning is equal to the experimental spectra (Fig. 5.4). The reconstructed full-scale simulation spectra is limited by the geometrical HADES acceptance, which can be seen by the empty spots in Fig. 5.5 (b). By comparing the initial with the reconstructed spectra one observes a drop of around one orders of magnitude in yield. The obtained reconstruction efficiency matrices within the geometrical acceptance of HADES are shown in Fig. 5.6. The efficiencies measured of K^+ in both reactions is comparable ranging from typically $12 - 30\%$. The same holds true for the K^- with typical values around $10 - 26\%$. One can see that the correction has a large phase space dependence. By dividing the experimental distribution by the correction matrix, unbiased experimental spectra were obtained.

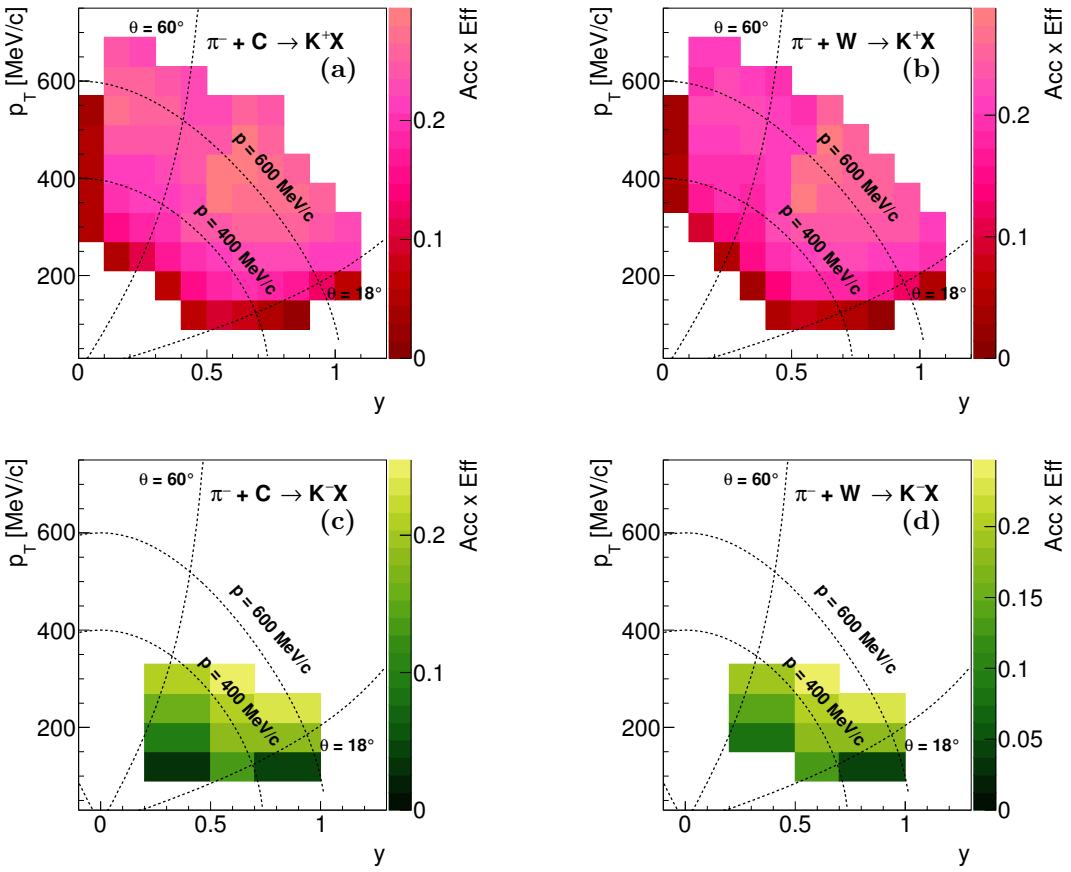

Figure 5.6: Acceptance and efficiency matrix for K^+ (a,b) and K^- (c,d) as a function of transverse momentum p_T vs. rapidity y inside the HADES acceptance for $\pi^- + \mathrm{C}$ (a,c) and $\pi^- + \mathrm{W}$ (b,d) reactions. The dotted black vertical lines indicate different polar angle regions, while the dotted black horizontal lines indicate different regions of constant momentum in the laboratory frame.

To validate the reliability and model independence of the correction method, a self-consistency check was performed. Two different models are used for the self-consistency check, which can be done in two ways. One can either correct the reconstructed spectra of the second model with the correction matrix determined with first model and check if the corrected spectra of the second model is equal to its initial distribution, or can directly compare the correction matrices from both models. The conclusion, that can be drawn from both methods, are equivalent. In the following, the first method was applied.

For this purpose the correction matrix based on GiBUU simulation was used, since this model was employed to obtain the correction of the experimental data, while for the cross-check UrQMD [B$^+$99b] (Section 3.7) was utilized. As shown in Fig. 5.5 (a) and Fig. 5.7 (a) both transport models feature quite different kinematical distributions and thus are well suited for the self-consistency check. Both models were processed through the whole analysis chain using HGeant simulating the detector acceptance, the digitization procedure taking into account detector efficiency and tracking algorithm as well as all analysis steps.

A double-differential correction (Fig. 5.6 (a)) was chosen to do not introduce any model dependence.

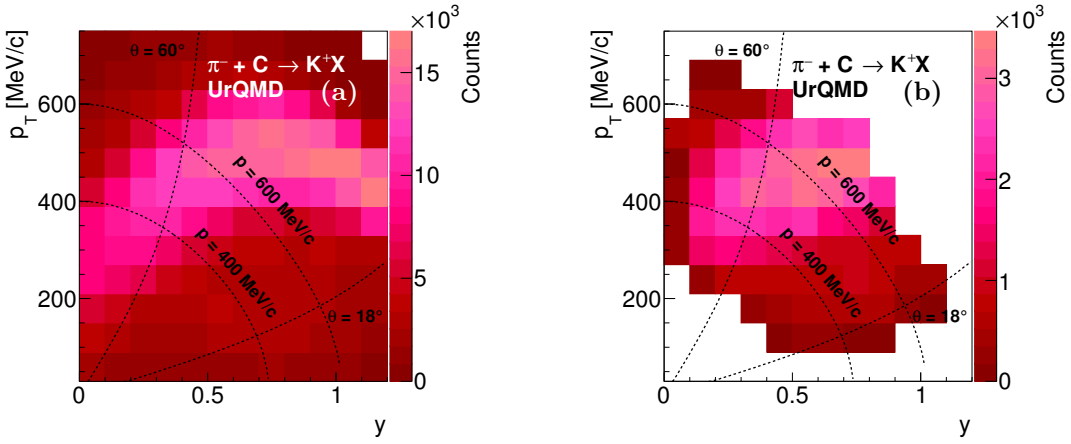

Figure 5.7: (Double-)differential yield of K^+ as a function of transverse momentum p_T and rapidity y for initial unfiltered (a) and reconstructed (b) full-scale simulation of $\pi^- + \mathrm{C}$ reactions based on UrQMD. The black dotted horizontal lines indicate the momentum at 400 and 600 MeV/c. The back dotted vertical lines denote the polar angle regions between $\theta = 18 - 60°$.

Finally, the reconstructed spectra based on UrQMD simulations (Fig. 5.7 (b)) was corrected with the correction matrix based on the GiBUU model and compared to the initial UrQMD distribution as shown in Fig. 5.8. Except for the first rapidity bin, the same range as in the experimental analysis (Section 5.1) was investigated. Both, the initial and corrected UrQMD spectra, are in reasonable agreement over the entire kinematic range. Small deviations can be attributed to the fit quality of the mass distributions for the UrQMD simulations. This confirms the reliability of the correction method implying that it can be applied to the experimental distribution without introducing any bias. Indeed, one can conclude that the extracted spectra of the inclusive (anti-)kaon analysis can be used to carry out comparison to state-of-the-art transport model calculations.

5.1.3 Systematic Uncertainties

Every experimental results comes along with systematic uncertainties, caused by the measurement itself or by the applied analysis method. A major step of the (anti-)kaon analysis is the two-dimensional identification based on the correlation of the specific energy loss and momentum, which was constructed around mean energy loss of the charged kaons with $+4\sigma$ and -3σ to take into account the underlying asymmetric distributions (Section 3.3.2, Appendix D.2). To evaluate the systematic uncertainty introduced by the two-dimensional (anti-)kaon identification, it was varied by $+4.5\sigma$ ($+3.5\sigma$) and -3.5σ (-2.5σ) corresponding to (typical) average signal-to-background ratios in $\pi^- + \mathrm{C}$ reactions equal to $S/B_C^{K^+} = 6.8 - 25.8$ and $S/B_C^{K^-} = 4.3 - 9.1$ and in $\pi^- + \mathrm{W}$ reactions equal to $S/B_W^{K^+} = 6.9 - 8.6$ and $S/B_W^{K^-} = 1.8 - 3.1$. Furthermore, the width of the Gaussian function used to fit the experimental (anti-)kaon mass distribution was fixed to the maximum allowed limits obtained from simulations (Section 5.1.1). The systematic uncertainties based on the above discussed variations was estimated with help of the minimal and maximal systematic uncertainties. The correction uncertainty corresponds to 3% and was evaluated from investigations of elastic scattering negatively charged pions in a subsequent experimental campaign (Section 3.6.4). In case of the rapidity density distribution, the extrapolation error corresponding

to the uncertainty of the Boltzmann fit (Section 5.2.2) is the dominant contribution to the systematic uncertainty.

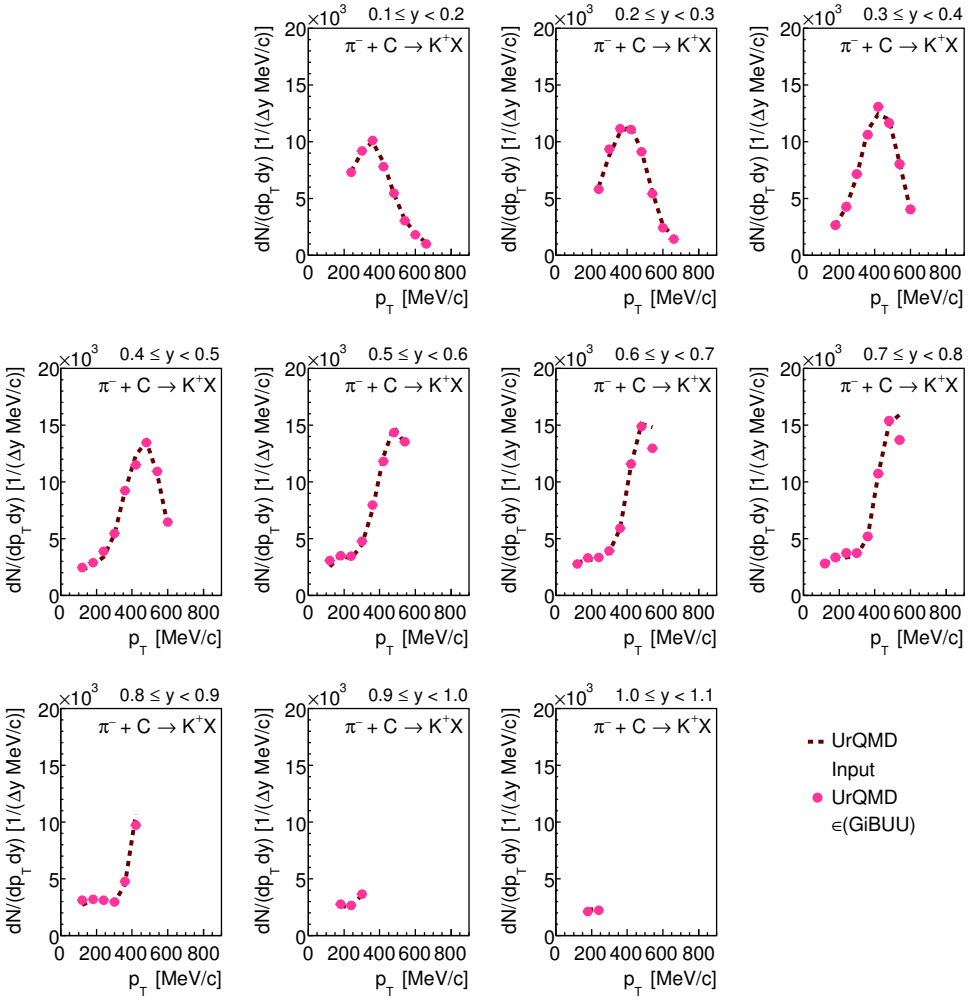

Figure 5.8: Comparison of the unfiltered (dark red dashed line) and corrected (pink points) transverse momentum spectra based on UrQMD simulation for K^+ in $\pi^- + \mathrm{C}$ reactions in different rapidity intervals (see legend). The correction was performed using the correction matrix based on GiBUU.

5.2 Results and Discussion

5.2.1 Pt-y Distribution

The in Section 5.1.1 obtained (double-)differential yields (Fig. 5.4) were corrected for the reconstruction efficiency as explained in Section 5.1.2. These corrected spectra are shown in Fig. 5.9. The (double-)differential distribution of K^+ look very different for the two collision systems, since the distribution is shifted to backward rapidity in the heavier target (W). For the K^- the distributions look rather similar. The K^+ is way more abundant than the K^- in both collision systems. The maximum of the K^+ $p_T - y$ distribution differs by an order of magnitude from the

one of the K^- in $\pi^- + \mathrm{W}$ reactions. Whereas for the light nucleus (C) only roughly a factor of 2 is observed.

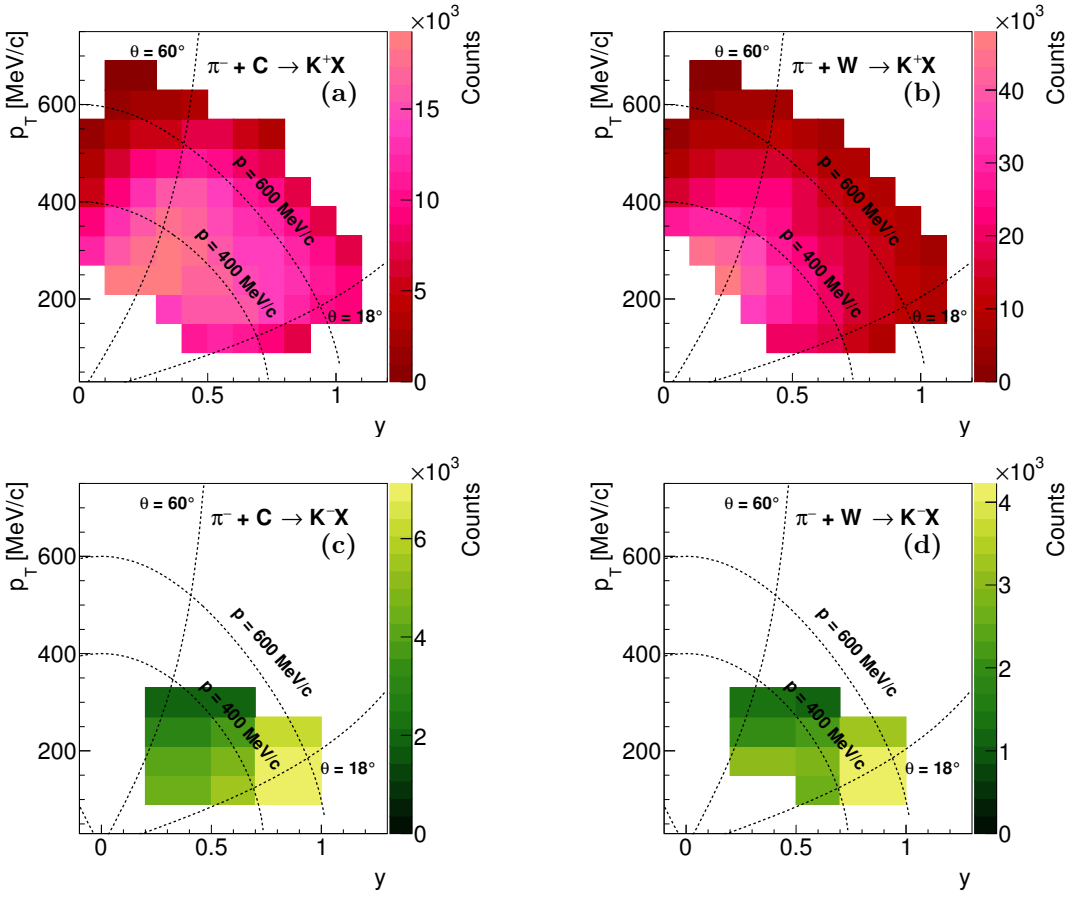

Figure 5.9: Corrected K^+ (a,b) and K^- (c,d) yield as a function of transverse momentum p_T vs. rapidity y inside the HADES acceptance for $\pi^- + \mathrm{C}$ (a,c) and $\pi^- + \mathrm{W}$ (b,d) reactions. The dotted black vertical lines indicate different polar angle regions, while the dotted black horizontal lines indicate different regions of constant momentum in the laboratory frame.

The total number of corrected K^+ and K^- for the $p_T - y$ analysis within the HADES acceptance in $\pi^- + \mathrm{C}$ reactions are equal to $N_C^{K^+} = 811742 \pm 2832(\mathrm{stat})^{+24388}_{-24404}(\mathrm{syst})$ and $N_C^{K^-} = 49615 \pm 939(\mathrm{stat})^{+1588}_{-1628}(\mathrm{syst})$ and in $\pi^- + \mathrm{W}$ reactions are equal to $N_W^{K^+} = 1222663 \pm 3528(\mathrm{stat})^{+36730}_{-36802}(\mathrm{syst})$ and $N_W^{K^-} = 27212 \pm 813(\mathrm{stat})^{+1070}_{-861}(\mathrm{syst})$.

5.2.2 Rapidity Density Distribution

Based on the double-differential analysis the rapidity density distribution $\mathrm{d}N/dy$ of (anti-)kaons can be extracted. As explained in Section 3.5 a Boltzmann fit (Eq. (3.8)) can be applied to the measured p_T spectra and the yield in the uncovered regions can be estimated by integrating the Boltzmann distribution over the corresponding range. As already mentioned, the comparison of K^+ transverse momentum spectra in the exclusive production channels of $\pi^- + p \to K^+K^-n$ and $\pi^- + p(\mathrm{C}) \to K^+K^-n(\mathrm{B})$ based on Pluto simulations [F$^+$07, FGH$^+$10] (Section 3.6.1) implied

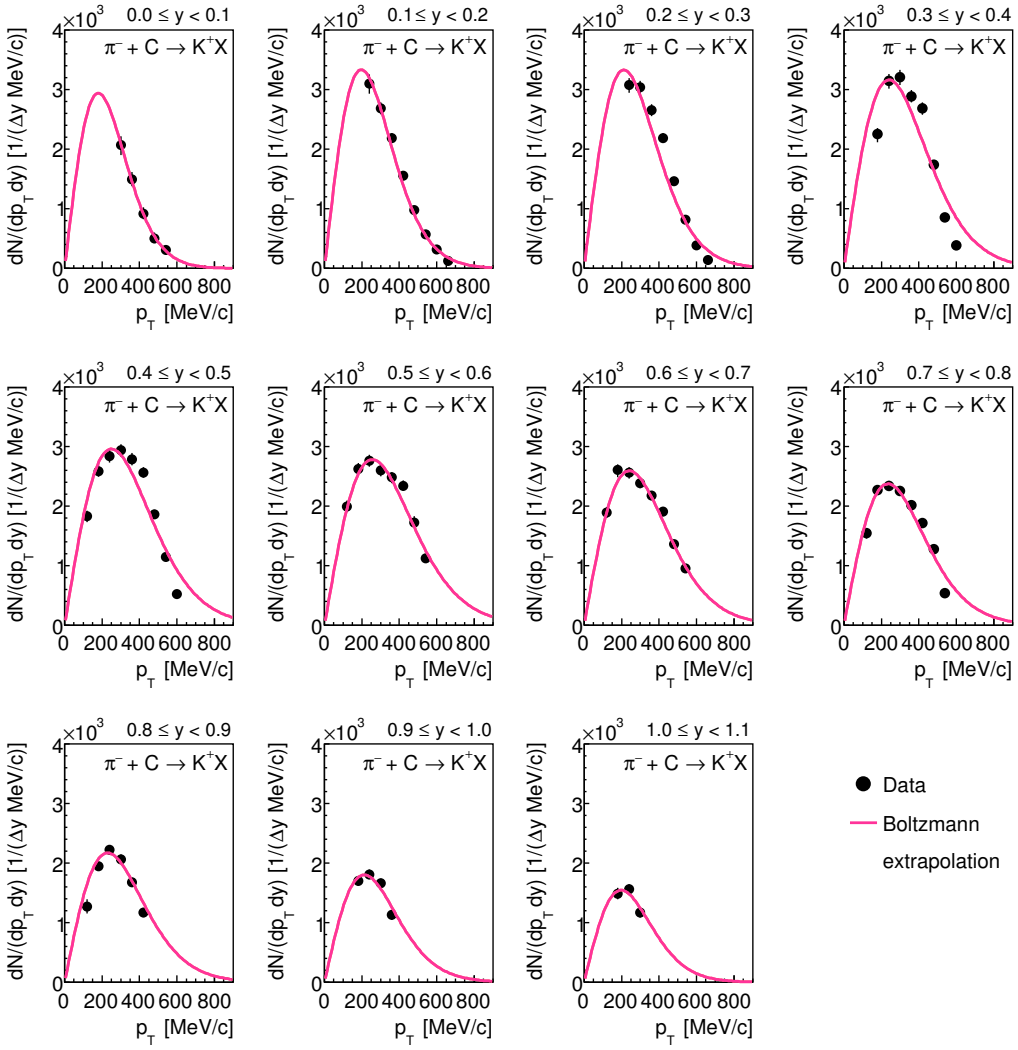

Figure 5.10: Transverse momentum spectra of K^+ in $\pi^- + \mathrm{C}$ collisions corrected for reconstruction efficiency within the geometrical acceptance in different rapidity regions (see legend). The pink solid curves indicate Boltzmann fits.

that the Fermi momentum of the nucleons leads to the Boltzmann-like behavior of transverse momentum spectra (Appendix E.1).

The Boltzmann distribution (pink solid curve) reproduces the shape of the experimental distribution for K^+ well over the entire rapidity range as demonstrated for $\pi^- + \mathrm{C}$ collisions in Fig. 5.10. The total yield measured in a certain rapidity region was then extracted by summing up all measured p_T points and the integral in the low and high p_T range extrapolated by the Boltzmann fit. Since also the K^- transverse momentum spectra for $\pi^- + \mathrm{C}$ reaction are well described by the Boltzmann fit indicated by the green solid curve in Fig. 5.11, the same procedure was also applied to the antikaons. A similar agreement is observed for the entire measured rapidity range for K^+ (Fig. E.8) and K^- (Fig. E.9) in $\pi^- + \mathrm{W}$ collisions.

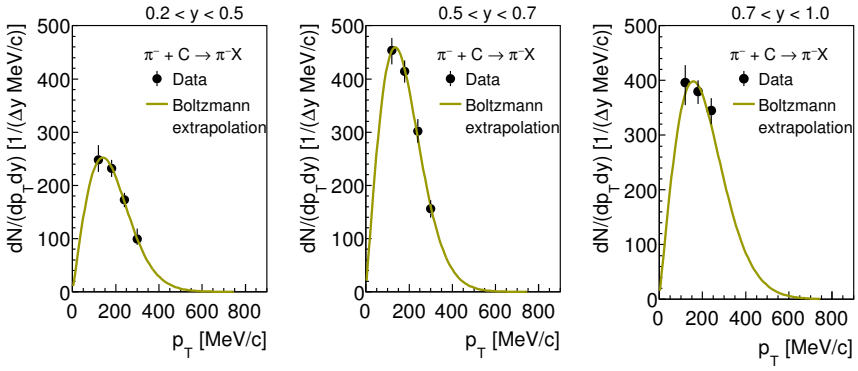

Figure 5.11: Transverse momentum spectra of K^- in $\pi^- + \mathrm{C}$ collisions corrected for reconstruction efficiency within the geometrical acceptance in different rapidity regions (see legend). The green solid curves indicate Boltzmann fits.

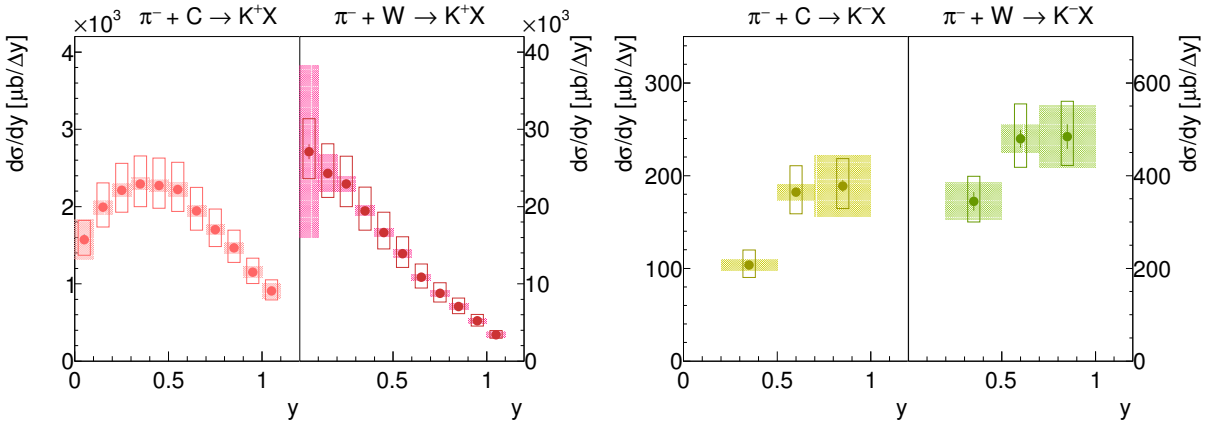

Figure 5.12: Cross-section of K^+ (pink) and K^- (green) as function of rapidity in $\pi^- + \mathrm{C}$ and $\pi^- + \mathrm{W}$ collisions (see legend). The error bars indicate the statistical uncertainty, while the bands denote the systematic uncertainty. The open boxes are the normalization error.

The resulting rapidity density spectra with the absolute normalization applied (Section 3.4) are depicted in Fig. 5.12. The shapes of the rapidity distribution for K^+ look very different for the two collision systems. While the distribution is shifted to backward rapidity in the heavier target (W), the one in the lighter target (C) is rather symmetric, thus scattering processes are dominant. The effect of kaon scattering will be discussed in detail in Section 5.2.4. Between both targets roughly an order of magnitude difference in cross-section is observed. The shape of the K^- rapidity distribution look similar with a factor two in cross-section comparing both nuclear environments. Here absorption processes (e.g. $K^- N \to Y N$) are dominating since only a factor two in cross-section is observed. In Section 5.2.5 a detailed investigation of the antikaon absorption can be found. The integrated differential production cross-section ($\Delta\sigma$) for K^+ ($0 \leq y < 1.1$) and K^- ($0.2 \leq y < 1.0$) in $\pi^- + \mathrm{C}$ and $\pi^- + \mathrm{W}$ reactions inside the HADES acceptance are listed in Tab. 5.3.

Table 5.3: Target, particle species and cross-section for K^+ ($0 \leq y < 1.1$) and K^- ($0.2 \leq y < 1.0$). Error values shown are statistic (first), systematic (second) and normalization (third).

Target	Particle	$\Delta\sigma$ [μb]
C	K^+	$1974 \pm 7^{+67}_{-69} \pm 310$
C	K^-	$124 \pm 2 \pm 11 \pm 20$
W	K^+	$15965 \pm 46^{+1236}_{-1247} \pm 2509$
W	K^-	$345 \pm 10 \pm 26 \pm 54$

5.2.3 P-θ Distribution

The same analysis procedure as explained for $p_T - y$ phase space (Section 5.1), was applied to the $p - \theta$ variables. For the $p - \theta$ analysis the total number of reconstructed K^+ and K^- within the HADES acceptance in $\pi^- + \mathrm{C}$ reactions are equal to $N_C^{K^+} = 153022 \pm 537$ and $N_C^{K^-} = 6793 \pm 134$ and in $\pi^- + \mathrm{W}$ reactions are equal to $N_W^{K^+} = 200399 \pm 589$ and $N_W^{K^-} = 3770 \pm 117$.

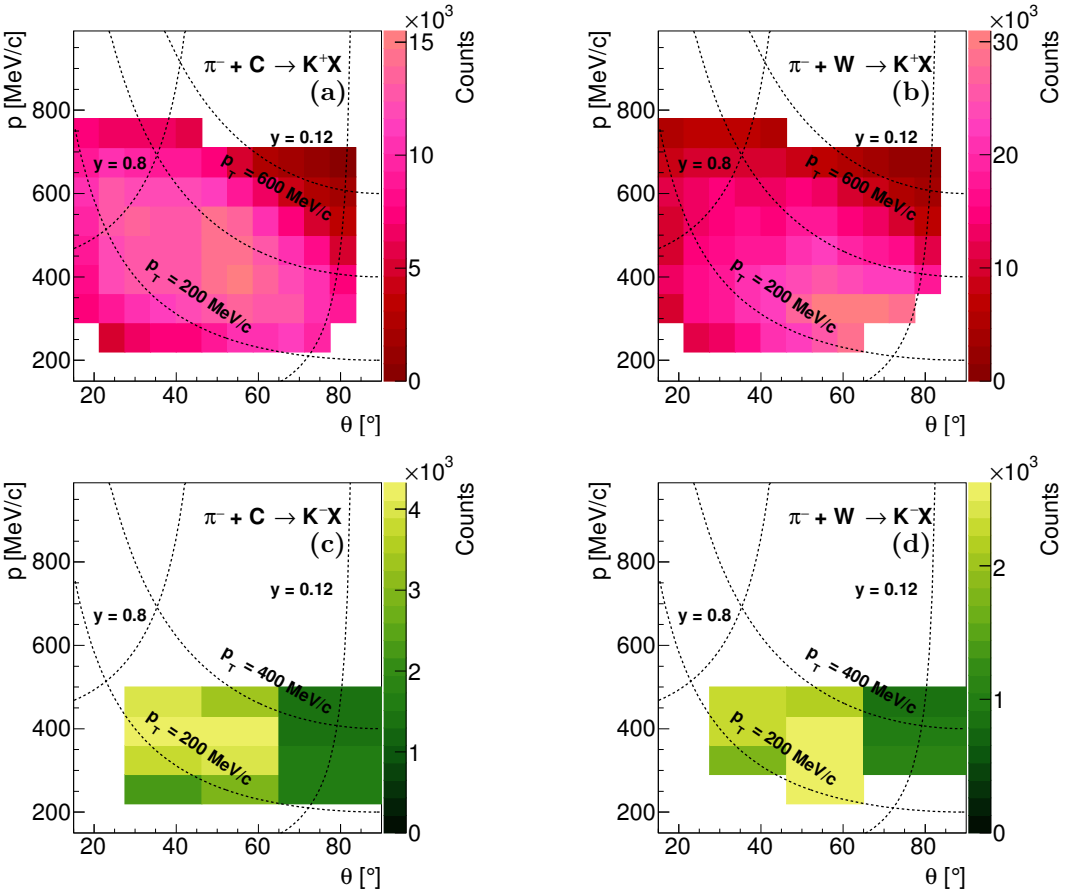

Figure 5.13: Corrected K^+ (a,b) and K^- (c,d) yield as a function of momentum p vs. polar angle θ inside the HADES acceptance for $\pi^- + \mathrm{C}$ (a,c) and $\pi^- + \mathrm{W}$ (b,d) reactions. The dotted black vertical lines indicate different polar angle regions, while the dotted black horizontal lines indicate different regions of constant momentum in the laboratory frame.

Deviations in the total reconstructed (anti-)kaon yields compared to $p_T - y$ analysis may be attributed to variations in the mass distributions with corresponding changes of the background in the (double-)differential analysis. Especially, the antikaons are affected by background in the experimental data. The observed difference stays below 10%.

After the application of corrections for the reconstruction efficiency, corrected (double-)differential spectra are obtained as depicted in Fig. 5.13. The total number of corrected K^+ and K^- for the $p - \theta$ analysis within the HADES acceptance in $\pi^- + \mathrm{C}$ reactions are equal to $N_C^{K^+} = 763183 \pm 2676(\mathrm{stat})^{+22965}_{-22929}(\mathrm{syst})$ and $N_C^{K^-} = 40601 \pm 800(\mathrm{stat})^{+1266}_{-1296}(\mathrm{syst})$ and in $\pi^- + \mathrm{W}$ reactions are equal to $N_W^{K^+} = 1160460 \pm 3{,}408(\mathrm{stat})^{+34872}_{-34943}(\mathrm{syst})$ and $N_W^{K^-} = 22614 \pm 701(\mathrm{stat})^{+768}_{-866}(\mathrm{syst})$.

5.2.4 Kaon Scattering

Both in-medium kaon-nucleon scattering and the repulsive KN potential affect the final state phase space distribution of the kaons. As observed in kaon rapidity distribution (Fig. 5.12) strong scattering effects shifted the distribution to backward rapidity in the heavier target (W).

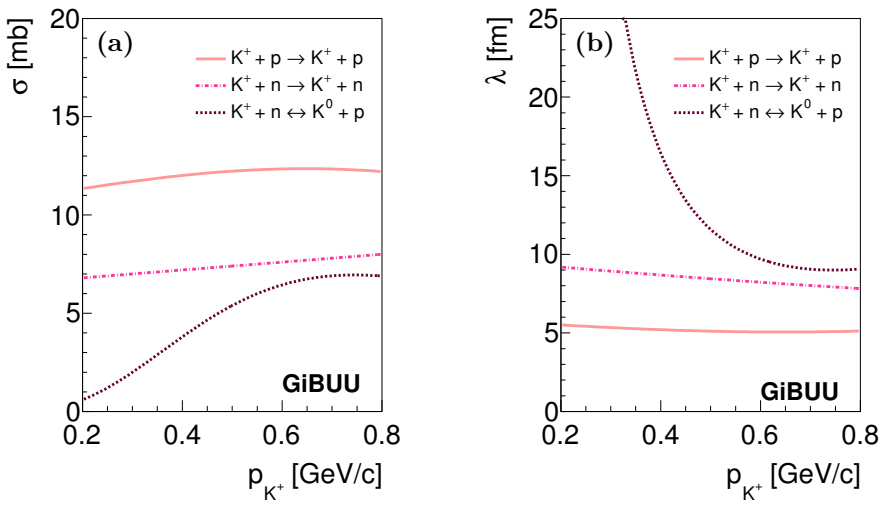

Figure 5.14: Elastic and inelastic scattering cross-section (a) and mean free path (b) parametriztaions for K^+ implemented in GiBUU.

Since kaons contain a $\bar{s}$ valence quark, due to strangeness conservation they cannot turn to hyperons via strangeness exchange and hence are not absorbed. Besides, no resonance states with strangeness $S = 1$ are located close to the KN threshold. Thus, they propagate rather freely in nuclear matter with a mean free path of $\lambda \approx 5$ fm for $p_{K^+} < 800$ MeV/c as indicated by the light pink solid curve in Fig. 5.14. The cross-section for charge exchange is rather low ($\sigma < 7$ mb [D$^+$75]) compared to elastic scattering. However, by taking into account geometrical assumptions one finds that the remaining maximal path length of the K^+ within the tungsten nucleus is $l < 12$ fm, due to the mean free path of the incident pion of ≈ 2 fm (ρ_0, $p_\pi = 1.7$ GeV/c) in combination with the diameter of a tungsten nucleus of $d_W = 14$ fm. The cross-section for charge exchange translate to rather large mean free path $\lambda > 10$ fm (purple dotted curve in Fig. 5.14). Moreover one has to consider that the nucleus has a density profile with a maximal density up to normal nuclear density ρ_0, thus charge exchange reactions do not play a dominant role.

Also the presence of the repulsive in-medium KN potential can influence the observed kinematic distribution, since it is expected to accelerate the kaons while escaping the nucleus. As the in-medium KN potential is dependent on density, the effect of such a potential should increase with increasing nucleus size [B$^+$04] as the kaons are exposed to higher densities on average. Several experiments intensively studied the presence of the KN potential by investigating the kaon production off different nuclei in pion- and proton-induced reactions like FOPI ($\pi^- + A$ [B$^+$09c]) and ANKE ($p + A$ [B$^+$04]). Comparisons to transport models yield to an on average repulsive potential of 20 ± 5 MeV. Whereas, measurements of heavy-ion collisions (Ar + KCl [A$^+$10a]) and proton-nucleus (p + Nb [A$^+$14d]) reactions by HADES are consistent with a sightly higher repulsive potential of ≈ 40 MeV (ρ_0, $p_K \approx 0$). Comparisons to three state-of-the art transport model calculations are provided in Section 5.2.4.1 and Section 5.2.4.2. Special emphasis is put to the investigation of the KN potential.

5.2.4.1 Comparison to Transport Calculations

Since the produced K^+ were analyzed over a large phase space and corrections for the efficiency effects of the reconstruction were applied, the data are suited to for a comparison to transport model calculations. Comparisons with the GiBUU (version 2017) [BGG$^+$12] transport model with and without in-medium ChPT KN potential are presented. The implemented in-medium ChPT KN potential features in addition to the non-linear density dependence also an explicit momentum dependence (Fig. 5.15) [A$^+$14d]. A second and third transport model was consulted for comparisons, namely the UrQMD (UrQMD v3.4) [B$^+$99b] and the SMASH (SMASH 1.6) [W$^+$16] model without inclusion of potentials. Details on the corresponding transport models can be found in Section 3.7. While the upper panels present the (direct) comparison of the experimental data to the predictions, the lower panels in each figure show the deviation between the measured and simulated distributions expressed as the relative difference normalized to experimental cross-section ((Sim-Exp)/Exp).
Since the transverse momentum reflects the momentum component perpendicular to the beam axis, it is decoupled from the boost transferred by the beam. Therefore, it is particularly important for the investigation of possible in-medium effects.

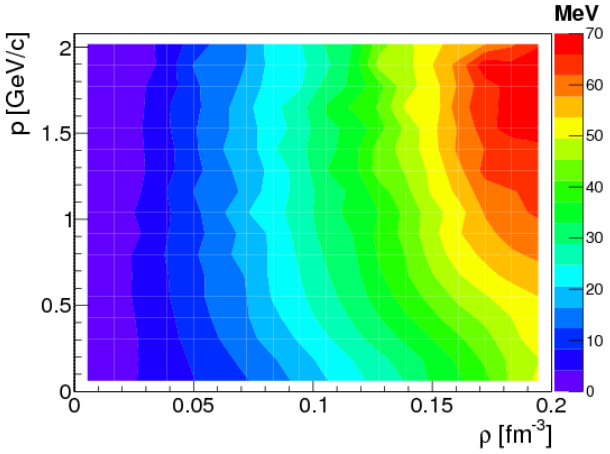

Figure 5.15: In-medium ChPT KN potential ($U = E^* - E$ [MeV]) as a function of the baryon density and kaon momentum implemented in GiBUU [A$^+$14d]. Figure taken from [A$^+$14d].

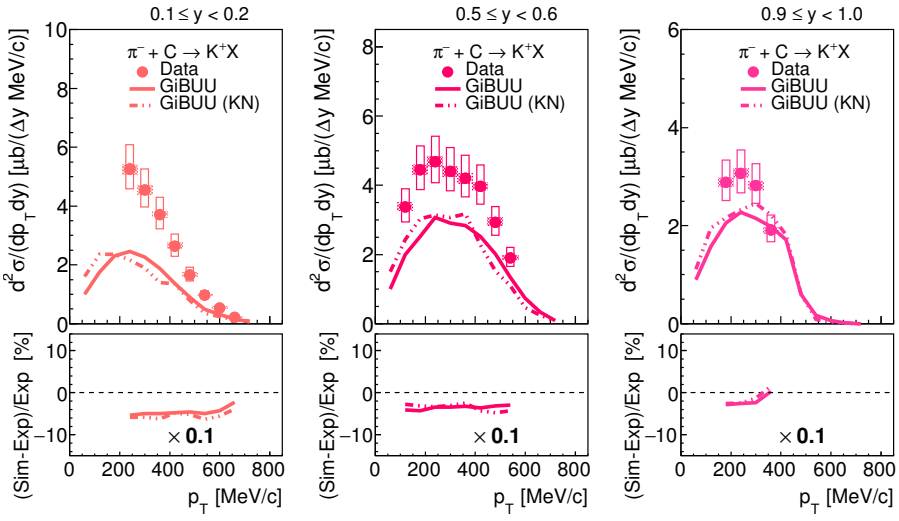

Figure 5.16: K^+ $p_T - y$ distribution compared to the GiBUU without (solid curve) and with (dashed-dotted curve) the in-medium ChPT KN potential on an absolute scale in $\pi^- + \mathrm{C}$ reactions for different rapidity regions (see legend). The statistical errors are smaller than the symbol size. The systematic (hashed areas) and normalization (open boxes) uncertainties are indicated.

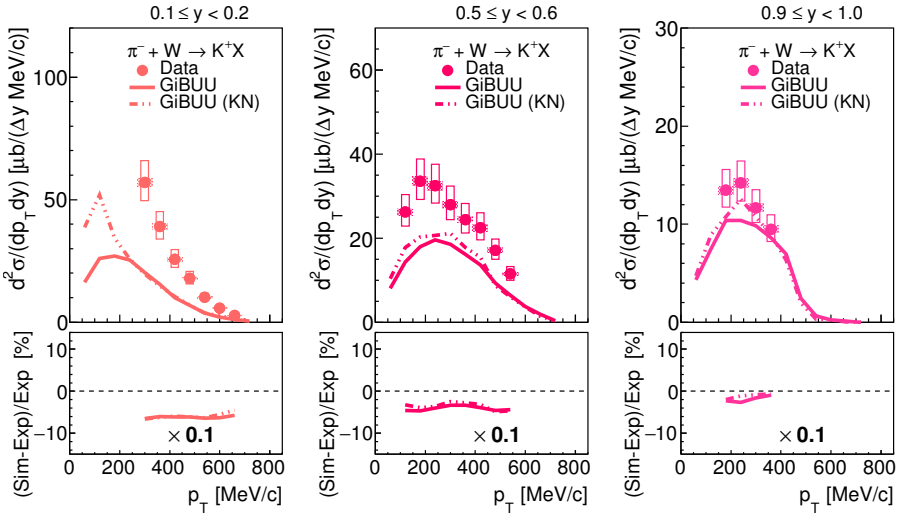

Figure 5.17: K^+ $p_T - y$ distribution compared to the GiBUU without (solid curve) and with (dashed-dotted curve) the in-medium ChPT KN potential on an absolute scale in $\pi^- + \mathrm{W}$ reactions for different rapidity regions (see legend). The statistical errors are smaller than the symbol size. The systematic (hashed areas) and normalization (open boxes) uncertainties are indicated.

Transverse momentum spectra of K^+ produced in $\pi^- + \mathrm{C}$ and $\pi^- + \mathrm{W}$ collisions are shown in Fig. 5.16 and Fig. 5.17, respectively. Here, the GiBUU model calculations without (solid curve) and with (dashed-dotted curve) the in-medium ChPT KN potential are absolutely normalized like the experimental data points. Both, the data and the model calculations, show a strong rapidity dependence. The comparison reveals that the GiBUU model generally underestimates the experimental cross-section. It seems that the underestimation is less significant with increasing rapidity. However, it can be noted that the shape of the transverse momentum spectra is fairly

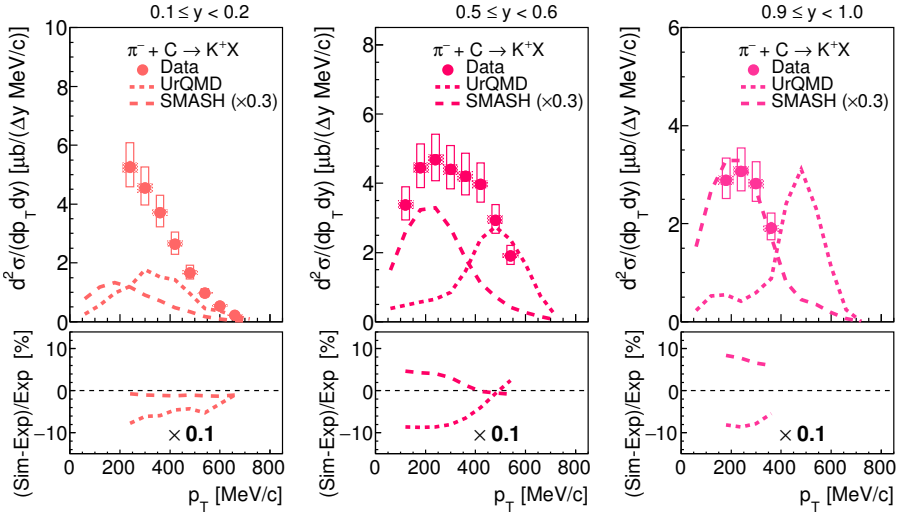

Figure 5.18: K^+ $p_T - y$ distribution compared to the UrQMD (dotted curve) and the SMASH transport model (dashed curve) on an absolute scale in $\pi^- + \mathrm{C}$ reactions for different rapidity regions (see legend). The statistical errors are smaller than the symbol size. The systematic (hashed areas) and normalization (open boxes) uncertainties are indicated.

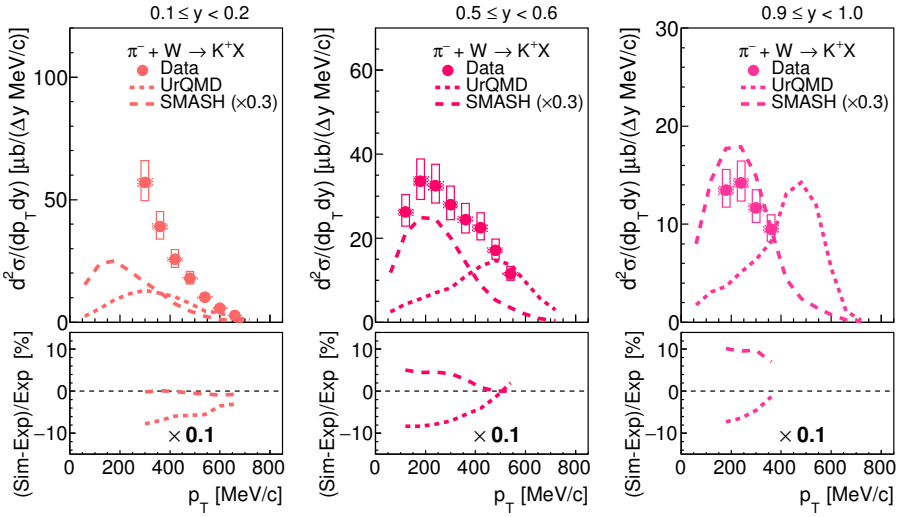

Figure 5.19: K^+ $p_T - y$ distribution compared to the UrQMD (dotted curve) and the SMASH transport model (dashed curve) on an absolute scale in $\pi^- + \mathrm{W}$ reactions for different rapidity regions (see legend). The statistical errors are smaller than the symbol size. The systematic (hashed areas) and normalization (open boxes) uncertainties are indicated.

well reproduced. While for $\pi^- + \mathrm{C}$ collisions the difference of the GiBUU model without and with the in-medium ChPT KN potential is rather small, the deviation is more obvious for $\pi^- + \mathrm{W}$ collisions as the kaons are exposed to higher densities on average. For the latter the deviation with and without repulsive KN potential is more pronounced, both for low transverse momenta and backward rapidities. This most sensitive region, however, lies outside the HADES acceptance. In addition, the absolutely normalized rapidity distribution is compared to both GiBUU calculations shown in Fig. 5.20. As already observed in the transverse momentum spectra the absolute

cross-section for $\pi^- + \mathrm{C}$ as well as $\pi^- + \mathrm{W}$ collisions is underestimated. As expected the difference between the transport calculation with and without ChPT KN potential is also almost negligible for the lighter target nucleus (C). Whereas, the repulsive KN potential shifts the K^+ in the direction of backward rapidity, thus the agreement between the experimental distribution with the in-medium ChPT KN potential seems to be better. Although, the shape of the spectrum is not completely reproduced. However, it must be mentioned that the cross-sections for the K^+ production channels have not been verified. To draw conclusions about the presence of the KN potential, a subsequent experimental campaign of $\pi + p$ collisions at an incident moment of 1.7 GeV/c must be conducted and a detailed tuning of the kaon production cross-sections implemented in the model must be performed to reproduce these experimental data. Similar to the approach presented in [A$^+$14d].

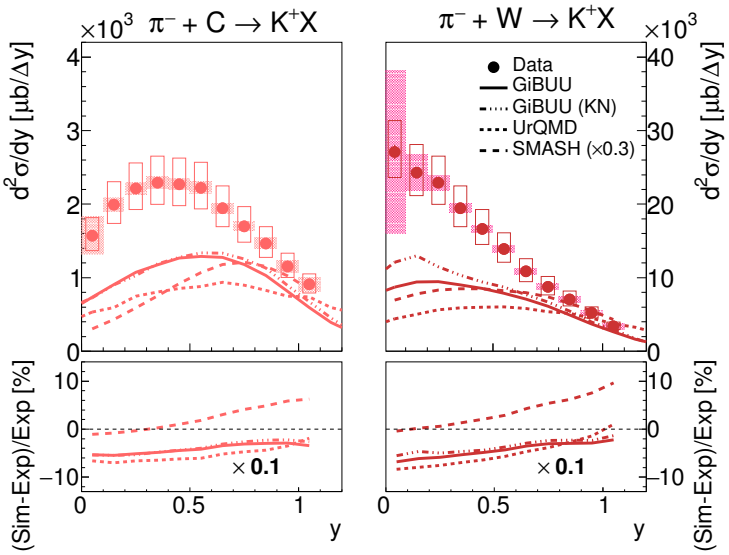

Figure 5.20: K^+ rapidity spectra compared to the GiBUU without (solid curve) and with (dashed-dotted curve) the in-medium ChPT KN potential, the UrQMD (dotted curve) and the SMASH transport model (dashed curve) on an absolute scale in $\pi^- + \mathrm{C}$ and $\pi^- + \mathrm{W}$ reactions (see legend). The statistical errors are smaller than the symbol size, while systematic (hashed areas) and normalization uncertainties (open boxes) are indicated.

Furthermore, the UrQMD transport model is represented by the dotted curves in Fig. 5.18 and Fig. 5.19. One observes that UrQMD underestimates the experimental cross-section. In contrast to the GiBUU model, particle production is always realized by a two-body absorption of resonances. It can be seen that the shape of the experimental data and UrQMD differ completely from each other. While the peak position for the experimental data is at low transverse momenta, the UrQMD distribution peaks at higher transverse momenta ($p_T > 300\mathrm{MeV}/c$). This peak becomes even more pronounced with increasing rapidity. It was found that these peaks are caused by heavy Δ and N^* resonance decays introduced into the model to describe the abundance of ϕ and Ξ in sub-threshold heavy-ion collisions [SB16]. A detailed summary of the various resonance decays contributing to the transverse momentum spectra is contained in Appendix H.2. Especially, the $\Delta(1930)$ and $\Delta(1950)$ resonances contribute to the second peak at high transverse momenta.
The absolutely normalized rapidity spectrum is also compared with UrQMD calculations presented by the dotted curve in Fig. 5.20. Similar to the transverse momentum spectra, the absolute cross-section for both reactions is underestimated. In addition, the shape of the distribution is

not reproduced. This is even clearer for the heavier target nucleus (W). The rapidity distribution is not shifted towards the target rapidity as the shapes of the rapidity distribution for the light (C) and heavy (W) target nucleus look quite similar.

A third transport model was used for comparison, namely the SMASH model. It is represented by the dashed curves in Fig. 5.18 and Fig. 5.19 showing the K^+ p_T distributions. Contrary to the observation presented in [SSO+19], SMASH 1.6 no longer exhibits the unusual two-peak structure at higher rapidities, which was due to Δ (e.g. $\Delta(1910)$, $\Delta(1920)$) and N^* (e.g. $N^*(1710)$, $N^*(1875)$) resonance decays. Although both, the cross-sections and shape, predicted by SMASH agree well with the experimental data for backward rapidity ($y < 0.4$), SMASH overestimates the cross-section with increasing rapidity. It had to be reduced by a factor of 0.3 for the representation. The over-prediction is strongest for both the forward rapidity and the heavier nucleus (W).
Besides, the experimental absolutely normalized rapidity spectrum is compared to SMASH predictions presented by the dashed curves in Fig. 5.20. While the backward rapidity is reproduced, the deviations are striking for forward rapidity. Hence, the shape of the rapidity distribution is not well described in both collisions systems. A revision of the resonance branching ratios becomes mandatory in order to obtain a better description of the experimental data.

It is although clear that the K^+ production cross-sections currently assumed in all three transport models, GiBUU, UrQMD and SMASH, are inadequate to describe the experimental data. The K^+ cross-section is under-estimated by far in both collision systems for GiBUU and UrQMD. While, SMASH significantly over-predicts the cross-section. The agreement between the experimental distribution with the in-medium ChPT KN potential implemented in GiBUU is best. However, to conclude about the KN potential, a subsequent experimental campaign of $\pi + p$ collisions at an incident momentum of 1.7 GeV/c must be performed and a detailed tuning of the kaon production cross-sections implemented in the model must be performed to reproduce these experimental data.

5.2.4.2 Kaon Nuclear Modification Factor

Another insight on the in-medium KN potential can be deduced by comparing phase space distributions of kaons produced off heavy and light nuclei. Commonly, the ratio $R(\sigma_A^K/\sigma_C^K)$ as a function of the kaon momentum is employed to study in-medium effects of the KN potential:

$$R(\sigma_A^K/\sigma_C^K) := \frac{\sigma_A^K}{\sigma_C^K}, \tag{5.1}$$

with

$$\sigma_A^K/\sigma_C^K : \quad \text{kaon production cross-section off nuclei } (A) \text{ and carbon (C)}$$

The effect of the KN potential is increasing with increasing the nucleus size [B+04], since the kaons are exposed to higher densities on average. The presence of a repulsive KN potential accelerates the kaons while escaping the nucleus leading to a suppression of the kaon production in the heavy target with respect to the light one (C) at low kaon momenta. However, according to the effective Lagrangian the largest effect of the KN potential should be seen for large kaon momenta, which is confirmed by detailed investigations of K^0 production in $p + \text{Nb}$ reactions measured with HADES [A+14d] (Fig. 1.9). In addition, the propagation of charged kaons is affected by the (repulsive) Coulomb interaction. The depletion at low kaon momenta is followed by an excess in the intermediate range for heavier targets with respect to lighter ones.

The ratio of the inclusive K^+ (K^0) production cross-section $R(\sigma_A^K/\sigma_C^K)$ measured in collisions with heavy targets (W) with respect to lighter one (C) as a function of the kaon momentum is shown in Fig. 5.21. The ratio of this work (full dark red circles) is extracted in the overlap regions of the $p-\theta$ spectra for both collision systems (Fig. 5.13 (a,b)) within the HADES acceptance. The presented normalization uncertainty is a conservative estimate as most contributions to error are expected to cancel in the ratio. Indeed, it was found in Appendix B that one obtains a comparable ratio on the basis of another normalization method. A decrease of the ratio is observed with increasing kaon momenta for kaon momenta $p > 0.2$ GeV/c. However, due to the geometrical acceptance of HADES, one sensitive part of the distribution, the low kaon momentum region, to test the presence of the KN potential is outside the acceptance.

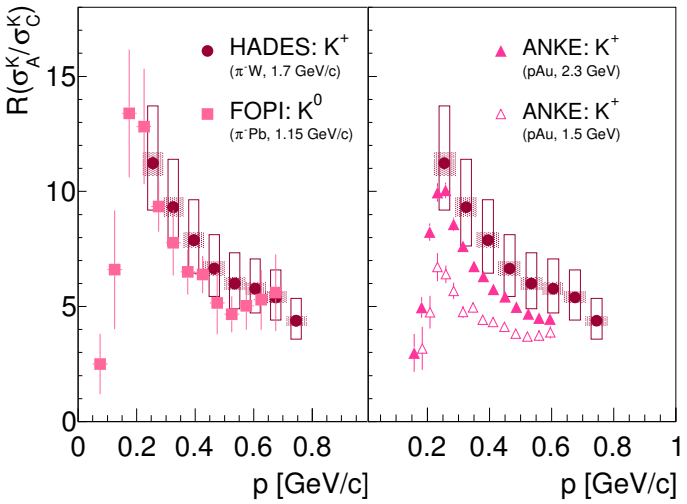

Figure 5.21: Ratio of inclusive K^+ (K^0) cross-sections produced by pions/protons on heavy and light targets as a function of the kaon momentum. The full dark red circle resembles the ratio of K^+ in this work. The statistical errors are smaller than the symbol size. The systematic and normalization uncertainties are given by the hashed areas and open boxes, respectively. The filled pinkish squares depict the ratio of K_s^0 produced on Pb and C targets measured by FOPI at an beam momentum of 1.15 GeV/c [B$^+$09c]. While, the full (open) pink triangle show the ratio of K^+ produced on Au and C targets of proton-induced reactions at 2.3 (1.5) GeV (ANKE) [B$^+$04].

Although, the suppression at low momenta is outside the HADES acceptance, we observe a similar trend at the intermediate kaon momenta compared to observations by FOPI for the K_s^0 production at lower pion beam momentum of 1.15 GeV/c (filled pinkish squares). By comparing the K^+ results from ANKE in p-induced reactions at 1.5 GeV (open pink triangles) and 2.3 GeV (full pink triangles) in Fig. 5.21, one can see that with increasing beam energy the suppression at low kaon momenta as well as the excess at intermediate kaon momenta is more pronounced. The more pronounced enhancement at intermediate kaon momenta with increasing beam energy is not observed comparing the results of HADES and FOPI. However, a one-to-one comparison is not possible since K^+ are additionally to KN interaction hampered by the Coulomb force. Moreover, the heavy target nucleus (Pb) employed by FOPI is sightly larger compared to the one of HADES.

Nevertheless, with this observations one is able to test in influence of the repulsive KN potential with help of transport model calculations. Figure 5.22 shows the ratio in comparison with GiBUU calculations. The GiBUU model calculation is shown without (solid curve) and with (dashed-dotted curve) the in-medium ChPT KN potential. Both simulations deviated from each other,

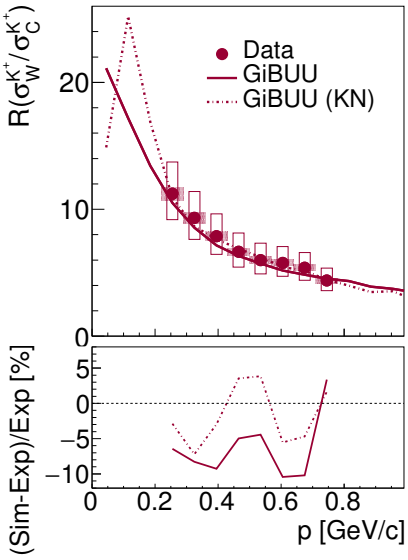

Figure 5.22: Ratio of inclusive K^+ cross-sections produced by pions on heavy (W) and light (C) targets as a function of the kaon momentum. The full circle resembles the ratio of K^+ in this experiment in comparison to GiBUU without (solid curve) and with (dashed-dotted curve) the in-medium ChPT KN potential. The statistical errors are smaller than the symbol size. The systematic and normalization uncertainties are given by the hashed areas and open boxes, respectively.

but the strongest deviation is observed as expected for very low kaon momenta $p > 0.2$ GeV/c. Within errors both calculations agree with the experimental data. However, by investigating in detail the deviation from the experimental data one observes that the data agrees better with the calculation including a repulsive KN potential.

5.2.5 Antikaon Absorption

The interaction of antikaons, K^- ($s\bar{u}$), with nuclear matter is complex as several effects compete. Antikaons can be re-scattered or be absorbed by nucleons and form baryonic resonances that lead to the modification of their in-medium properties [Fuc06, EYHK15]. The $\Lambda(1405)$ plays a peculiar role since the large $\bar{K}N$ coupling with $\Lambda(1405)$ resonance leads to absorption processes. Such absorption processes, strangeness exchange reactions, can occur on one ($K^-N \rightarrow Y\pi$) or even more nucleons ($K^-NN \rightarrow YN(\pi)$). A direct indication of absorption can be derived from the comparison of the K^-/K^+ ratio measured in collisions with the heavy target (W) and the lighter target (C). In the double ratio $(K^-/K^+)_\mathrm{W}/(K^-/K^+)_\mathrm{C}$ the K^+ acts as a reference particle for the strange hadron production due to its very small absorption cross-section [D$^+$75] (Section 5.2.4). The evidence of strong K^- absorption based on the double ratio is discussed in Section 5.2.5.1 and Section 5.2.5.2.
Hence, transport model calculations do not only have to take care about the production channels, but also have to take into account several absorption processes. The comparison to state-of-the-art transport model calculations is provided in Section 5.2.5.3.

5.2.5.1 Cross-Section based Antikaon-to-Kaon Ratio

In order to interpret the extracted double ratio $(K^-/K^+)_{\mathrm{W}}/(K^-/K^+)_{\mathrm{C}}$ in terms of the K^- absorption, the influence on the double ratio caused by the different number of neutrons and protons in tungsten ($A = 184, Z = 74, N = 110$) compared to carbon ($A = 12, Z = 6, N = 6$) with the assumption of pure (anti-)kaon production without absorption was taken into account. For this purpose all K^+ and K^- production channels that can be accessed are listed in Table 5.4.

As not all cross-sections have been measured at the presented beam momentum, a cross-section parametrization proposed by Sibirtsev *et al.* [SCK97, CBM$^+$97] has been adapted to extracted the cross-section for each individual channel at $p_{\pi^-} = 1.7$ GeV/c. It reads as follows:

$$\sigma = a\left(1 - \frac{s_0}{s}\right)^b \left(\frac{s_0}{s}\right)^c, \tag{5.2}$$

with

σ : cross-section of a specific channel
a,b,c : individual fit parameters
s_0,$\sqrt{s}$: channel dependent threshold and center-of -mass energy

Table 5.4: Production channels of K^+ and K^- in pion-induced reactions with corresponding threshold momentum for the incident pions. The cross-section σ_{fit} at $p_{\pi^-} = 1.7$ GeV/c corresponding to a fit with a cross-section parametrization to experimental cross-sections measured at several energies compared to the cross-section parametrization implemented in GiBUU.

$\pi^- + p$	$p_{\pi^-,thr}$ [GeV/c]	σ_{fit} [mb]	σ_{GiBUU} [mb]
$\Lambda\pi^-K^+$	1.144	0.0793	0.0908 [BGG$^+$12]
$\Lambda\pi^0\pi^-K^+$	1.407	0.0015	
$\Sigma^+\pi^-\pi^-K^+$	1.568	0.0003	
$\Sigma^0\pi^-K^+$	1.290	0.0220	0.0212 [BGG$^+$12]
$\Sigma^-\pi^+\pi^-K^+$	1.585	≈ 0	
$\Sigma^-\pi^0K^+$	1.290	0.0190	0.0152 [BGG$^+$12]
Σ^-K^+	1.035	0.1498	0.1564 [THF94]
$\Sigma(1385)^0\pi^-K^+$	1.680	≈ 0	
$\Sigma(1385)^-\pi^0K^+$	1.680	≈ 0	
$\Sigma(1385)^-K^+$	1.399	< 0.0693	
nK^+K^-	1.495	0.0231	0.0224 [SCK97]
$n\phi$	1.559	0.0274	0.0196 [SCM97]
($\phi \to K^+K^-$, $BR \approx 50\%$ [P$^+$16a])			
pK^0K^-	1.497	0.0071	0.0110 [SCK97]
$\pi^- + n$			
$\Sigma^-\pi^-K^+$	1.296	< 0.0697	0.0247 [BGG$^+$12]

The parametrization has been fitted to the available experimental measurements taken form Landolt-Börnstein [MS88] as shown for four example channel in Fig. 5.23. All measured cross-sections are shown as black points, whereas the fit function is represented as red solid curve together with the cross-section parametrization implemented in GiBUU [BGG$^+$12] given by the yellow solid curve. Moreover, the blue dashed lines depicted the estimated cross-section for the

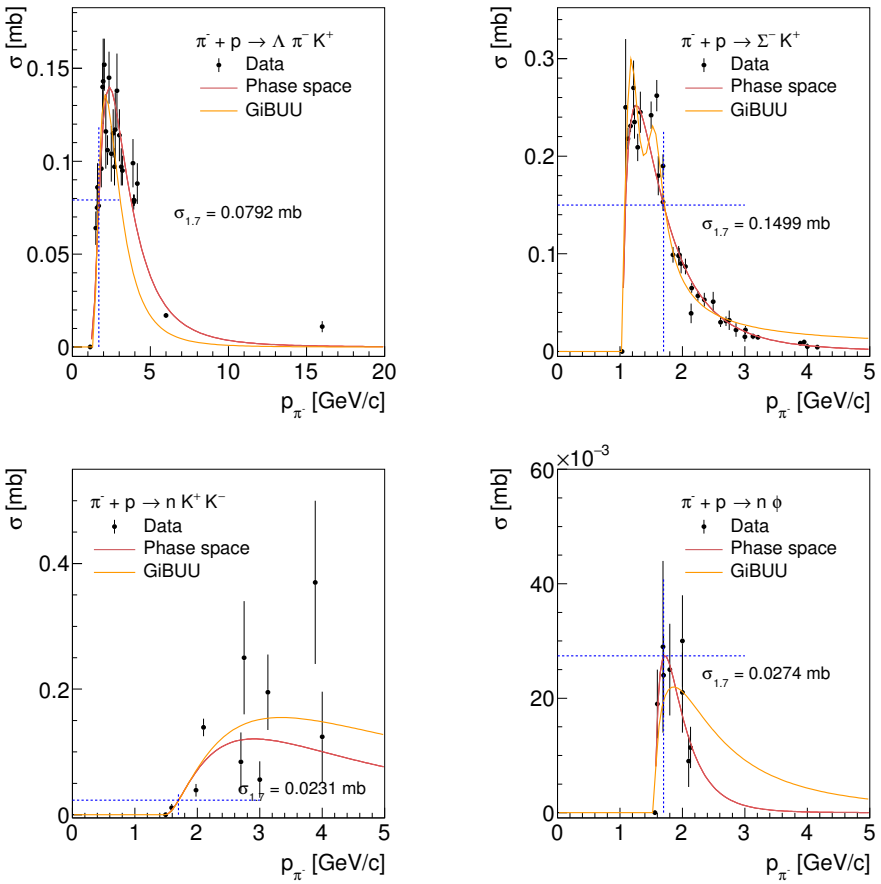

Figure 5.23: Cross-sections measured by different experiments taken from the Landolt-Börnstein compilation [MS88] as a function of the incident pion momentum p_{π^-}. The red solid curve indicates the fit corresponding to a cross-section parametrization adapted from Sibirtsev *et al.* [SCK97, CBM+97], while the yellow solid curve pictures the parametrization employed in GiBUU [BGG+12]. The blue dashed lines represent the suggested cross-section by the fit at $p_{\pi^-} = 1.7$ GeV/c

incident pion beam momentum $p_{\pi^-} = 1.7$ GeV/c. It has to be mentioned that the experimental data for the channels $\pi^- + p \to \Sigma(1385)^- K^+$ and $\pi^- + n \to \Sigma^- \pi^- K^+$ is scarce, thus the extracted cross-sections are rather an upper limit. For all remaining channels listed in Table 5.4 the corresponding experimental cross-sections as a function of incident pion momentum together with the phase space extrapolations can be found in Appendix F.

The reference double ratio based on the pure production has been obtained by summing all elementary cross-sections (σ_{fit} listed in Table 5.4) weighted with the relative neutron and proton contents. The scaling by $A^{2/3}$ [B+09c] corresponding the effective number of nucleons on the surface of the nucleus cancels out. A double ratio based on the pure production of $(K^-/K^+)_{\mathrm{W}}/(K^-/K^+)_{\mathrm{C}} = 0.930 \pm 0.09$ has been extracted. For comparison also the double ratio has been deduced on the basis of the cross-sections (σ_{GiBUU} listed in Table 5.4) implemented in GiBUU with an value of $(K^-/K^+)_{\mathrm{W}}/(K^-/K^+)_{\mathrm{C}} = 0.966$.

Besides, also the channel $\pi^- + n \to nK^0K^-$ can contribute. Although, this channel has up to now not been measured, based on [SCK97] exploring the isospin symmetry of the Feynman

diagram the following relation can be found: $\sigma(\pi^- + p \rightarrow pK^0K^-) = \sigma(\pi^- + n \rightarrow nK^0K^-)$. The inclusion of this channel would lead to a double ratio based on the pure production of $(K^-/K^+)_\mathrm{W}/(K^-/K^+)_\mathrm{C} = 1.04 \pm 0.09$. Since both reference double ratios agree within errors, the double ratio of $(K^-/K^+)_\mathrm{W}/(K^-/K^+)_\mathrm{C} = 0.930 \pm 0.09$ was taken as lower limit for further comparisons.

5.2.5.2 Extracted Antikaon-to-Kaon Ratio

The comparison of the K^-/K^+ ratio measured in collisions with the heavy target (W) and the lighter target (C) can give a direct indication of K^- absorption inside the nuclear medium. Therefore, the measured K^- distribution was normalized to the integrated K^+ yield ($0 \leq y < 1.1$).

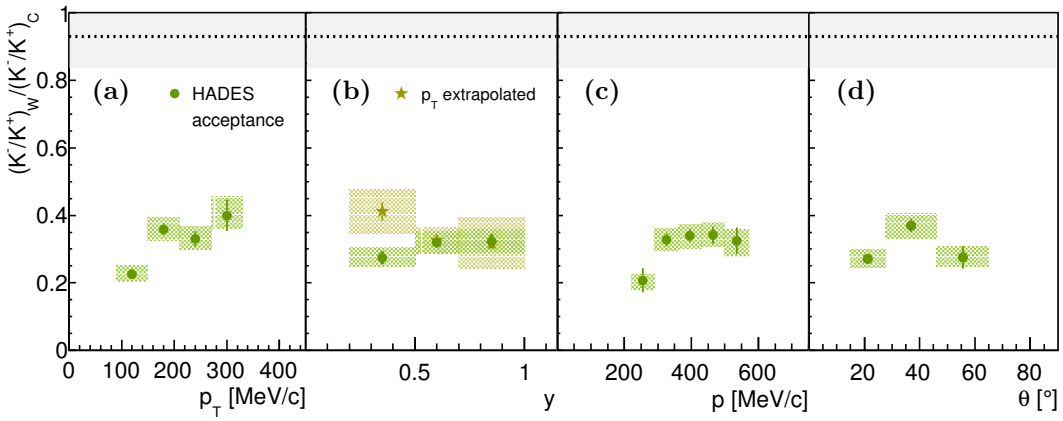

Figure 5.24: Double ratio $(K^-/K^+)_\mathrm{W}/(K^-/K^+)_\mathrm{C}$ as a function of p_T (a), rapidity y (b), momentum p (c) and polar angle θ (d) without (green circles) and with p_T extrapolation (light green stars) inside the HADES acceptance. The experimental data include statistical (error bars) and systematic (hashed areas) uncertainties. The black dotted line resembles reference double ratio with the corresponding error shown by the grey box (Section 5.2.5.1). For details see text.

The extracted double ratio $(K^-/K^+)_\mathrm{W}/(K^-/K^+)_\mathrm{C}$ inside the HADES acceptance is moderately increasing with increasing p_T as shown in Fig. 5.24 (a). Within errors, no significant dependence on the rapidity y (Fig. 5.24 (b)), with and without p_T extrapolation, is observed with an average value of $(K^-/K^+)_\mathrm{W}/(K^-/K^+)_\mathrm{C} = 0.319 \pm 0.009(\mathrm{stat})^{+0.014}_{-0.012}(\mathrm{syst})$ in the latter case. Comparably to the p_T dependence the double ratio is also increasing moderately as function of momentum (Fig. 5.24 (c)), whereas no strong dependence on the polar angle θ is observed (Fig. 5.24 (d)). In order to define a reference value in which no nuclear absorption is present, a double ratio $(K^-/K^+)_\mathrm{W}/(K^-/K^+)_\mathrm{C}$ was constructed considering $\pi^- N$ reactions and scaling the elementary cross-sections by the number of participating nucleons in each target. This procedure results in a value of 0.93 ± 0.09 (Section 5.2.5.1) indicated by the black dotted line in Fig. 5.24. The fact that the measured double ratios are well below this reference demonstrates the K^- absorption.

5.2.5.3 Comparison to Transport Calculations

The interaction of antikaons with nuclear matter is complex. It has been shown before that absorption effects within nuclear matter play a dominant role by comparing the K^-/K^+ ratio measured in collisions with the heavy target (W) and the lighter target (C). Hence, transport

model calculations do not only have to take care about the production channels, but also have to take into account several absorption processes. Comparisons with the GiBUU (version 2017) [BGG+12] model, the UrQMD (UrQMD v3.4) [B+99b] model and the SMASH (SMASH 1.6) [W+16] are presented. Details on the corresponding transport models can be found in Section 3.7. Antikaon-nucleon cross-section parametrizations of strangeness exchange reactions implemented in GiBUU (Fig. 5.25 (a)) and UrQMD (Fig. 5.25 (b)) without resonance contribution are depicted in Fig. 5.25. The expression of the antikaon-nucleon cross-section for SMASH [SSO+19] is comparable to the one employed in UrQMD. Besides, all other possible isospin channels follow from isospin symmetry relations. The comparisons will be presented analogue to the K^+, the upper panels present the (direct) comparison of the experimental data to the transport model predictions, the lower panels show the deviation between the measured and simulated distributions expressed as the relative difference normalized to experimental cross-section ((Sim-Exp)/Exp).

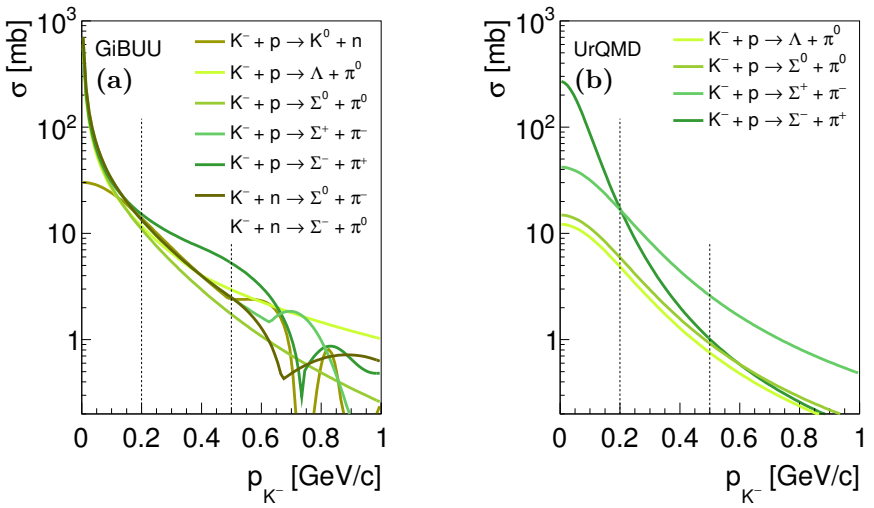

Figure 5.25: Antikaon-nucleon cross-section parametriztaions of strangeness exchange reactions implemented in GiBUU ([Eff99]) (a) and UrQMD ([GSLB14]) (b) without resonance contribution. The black dotted lines indicate the measured K^- momentum coverage within HADES.

The cross-sections as function of the transverse momentum for K^- produced in $\pi^- + \mathrm{C}$ and $\pi^- + \mathrm{W}$ collisions are shown in Fig. 5.26 and Fig. 5.27, respectively. The GiBUU model calculation (solid curve) is absolutely normalized as the experimental data points. While in the case of $\pi^- + \mathrm{W}$ reaction, the cross-sections of GiBUU and the experimental data are almost cosistent with sightly increasing deviations with decreasing rapidity, the agreement is somewhat worse for $\pi^- + \mathrm{C}$ reactions. In the latter reaction, the deviation increases with decreasing p_T as well as rapidity.
In addition, the absolutely normalized rapidity distribution is compared to both GiBUU calculations shown in Fig. 5.28. As already observed in the transverse momentum spectra the absolute cross-section for $\pi^- + \mathrm{C}$ reactions is slightly underestimated and in $\pi^- + \mathrm{W}$ collisions slightly overestimated. Although within errors the GiBUU predictions agrees with the experimental distribution. Both shapes are rather good reproduced by GiBUU. All in all, the experimental data and GiBUU are almost consistent.

Furthermore, the experimental cross-sections are compared to UrQMD transport model represented by the dotted curve in Fig. 5.26 and Fig. 5.27. Contrary to the K^+ production (Section 5.2.4.1), UrQMD overestimates the experimental K^- cross-section. The over-prediction is more striking

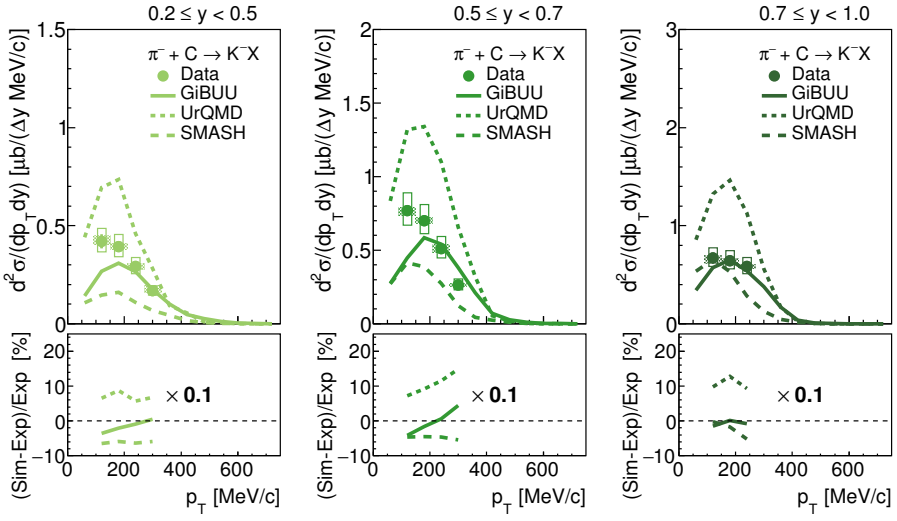

Figure 5.26: Comparison of the experimental K^- $p_T - y$ distribution to the GiBUU (solid curve), UrQMD (dotted curve) and SMASH (dashed curve) transport model on an absolute scale in $\pi^- + \mathrm{C}$ reactions for different rapidity regions (see legend). The experimental data include statistical (error bars), systematic (hashed areas) and normalization uncertainties (open boxes).

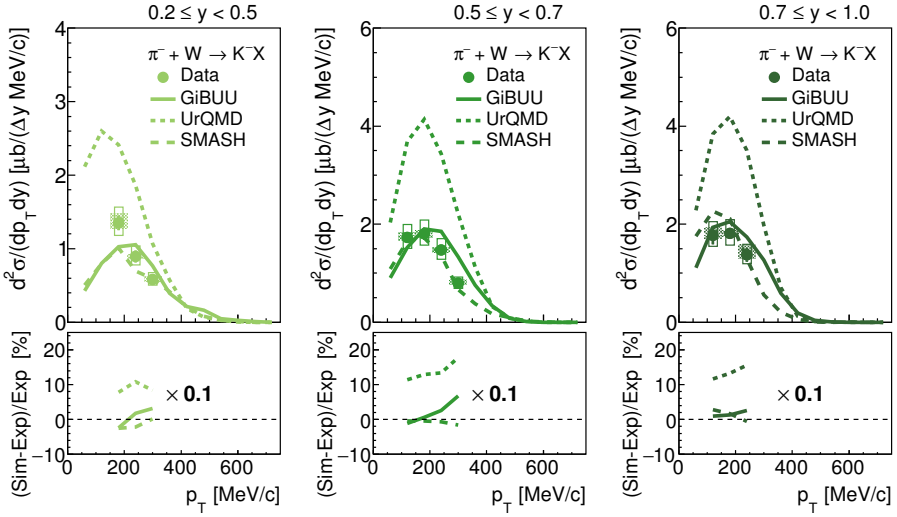

Figure 5.27: Comparison of the experimental K^- $p_T - y$ distribution to the GiBUU (solid curve), UrQMD (dotted curve) and SMASH (dashed curve) transport model on an absolute scale in $\pi^- + \mathrm{W}$ reactions for different rapidity regions (see legend). The experimental data include statistical (error bars), systematic (hashed areas) and normalization uncertainties (open boxes).

for the heavier target nucleus (W). Besides one can see that the shape of the distributions is sightly better reproduced in UrQMD compared to GiBUU.
As already observed for the transverse momentum spectra, for UrQMD (dotted curve) over-predicts the cross-section as function of rapidity (Fig. 5.28) in both collision systems, although the overestimation is decreasing with decreasing rapidity. Heavy N^* resonance decays (e.g. $N^*(1990)$, $N^*(2080)$, $N^*(2190)$, $N^*(2220)$, $N^*(2250)$) introduced into the model to describe the abundance of ϕ in sub-threshold heavy-ion collisions [SB16] may lead an enhanced abundance of ϕ mesons,

which decay predominantly in charged kaon pair and thus contribute significantly to the K^- yield. Therefore, a revision of the K^- and ϕ meson production channels is necessary in order to draw conclusions about the K^- absorption in nuclear matter.

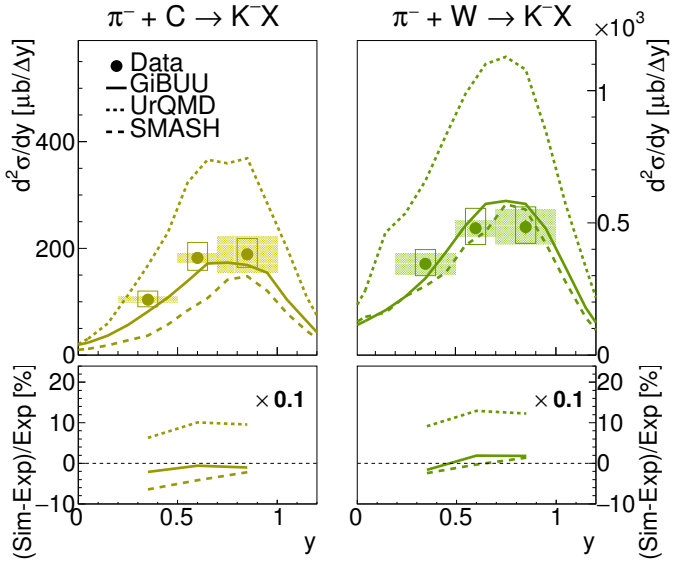

Figure 5.28: Comparison of the experimental K^- y distribution to the GiBUU (solid curve), UrQMD (dotted curve) and SMASH (dashed curve) transport model on an absolute scale in $\pi^- + \mathrm{C}$ and $\pi^- + \mathrm{W}$ reactions (see legend). The statistical errors are smaller than the symbol size, while systematic (hashed areas) and normalization uncertainties (open boxes) are indicated.

In Figure 5.26 and Figure 5.27 also a comparison to the predictions of SMASH (dashed curves) are presented. SMASH underestimates the experimental cross-section almost for all rapidities in $\pi^- + \mathrm{C}$ reactions. Nevertheless, the shape is best described. For the heavier target nucleus (W), SMASH agrees well with the experimental data in terms of the shape and absolute cross-section. Only minor deviations are observed for low transverse momenta and rapidity.
Comparable to the observations for the transverse momentum also the rapidity distribution (Fig. 5.28) reveals that the absolute cross-section is underestimated for the light nucleus (C). While for the heavy nucleus (W) the experimental distribution is best described by SMASH. It seems that less K^- are produced, which is compensated by a smaller K^- absorption.

While the predictions of GiBUU for K^- are rather promising, the cross-sections of K^- in UrQMD are significantly over-predicted. No consistent picture is observed for the K^- prediction of SMASH as the production off carbon is under-estimated. The shape of the experimental distribution are best described by SMASH. Yet, the predictions of GiBUU show the least deviations.

5.2.5.4 Comparison to First Collision Model

In the following also the inclusive K^- production in $\pi^- + \mathrm{C}$ collisions is compared to the first collision model [EP95]. In this model various forms of the nucleon momentum distribution within the nucleus can be accounted for such as Fermi motion and high-momentum components of the nuclear wave function. Besides, the free elementary production processes are described by phase space calculations normalized to the corresponding total experimental cross-sections. The following production processes have been considered: $\pi^- + p \to K^+ K^- n$, $\pi^- + p \to K^0 K^- p$ and

$\pi^- + n \rightarrow K^0 K^- n$. For the last reaction channel two different parametrizations were examined. For the light carbon nucleus absorption processes are not dominant. Figure 5.29 presents the total K^- cross-section as function of the incident pion beam momentum in $\pi^- + \mathrm{C}$ collisions. The long-dashed curve corresponds to the first cross-section parametrization, while the dotted curve to the second parametrization. The study demonstrated that total K^- cross-section off carbon in the sub-threshold regime ($p < 1.5$ GeV/c) is sensitive to the internal nucleon distribution resembled by the different curve in Fig. 5.29. Only a slight dependence on the cross-section parametrization is observed.

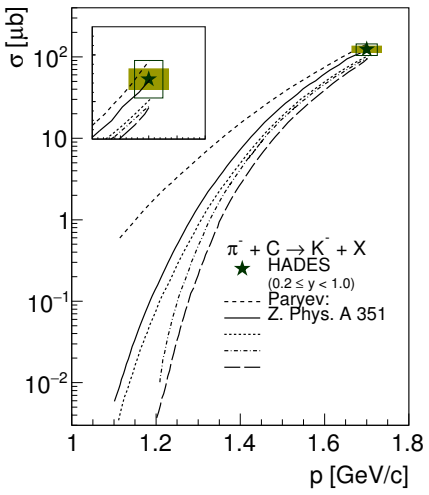

Figure 5.29: Total cross-section for K^- in $\pi^- + C$ reactions as a function of the incident pion beam momentum. The different curve taken from [EP95] correspond to different parametrizations of the elementary cross-sections. The experimental data point corresponds to the cross-section in the rapidity interval $0.2 < y < 1.0$. The statistical error is small than the symbol size. The systematic uncertainty is indicated by the hashed band and the normalization uncertainty is represented by the open box.

For the incident pion beam momentum of 1.7 GeV/c the cross-section of K^- is less sensitive to the internal nucleon distribution. Nevertheless, this measurement can serve as further constrain. In Figure 5.29 it can be seen, that the extracted K^- cross-section (green star) is compatible with the calculations based on the shell-model momentum distribution with the assumption of on-shell target nucleons. However, one must be aware that the experimentally integrated differential production cross-section for K^- corresponds to the rapidity range of $0.2 \leq y < 1.0$ and thus does not resemble the total cross-section. However, since most of the yield is within the HADES acceptance, the total cross-section should not differ significantly from the integrated differential cross-section. In order to draw a conclusion, the contribution of the predominately decaying meson ϕ to the charged kaons must also be considered, which is not the case in the current version of the first collision model. Since the contribution of the ϕ meson is not negligible based on the elementary cross-sections listed in Table 5.4.

5.3 Summary of the Inclusive (Anti-)Kaon Production

In summary, the inclusive (double-)differential production cross-sections of charged kaons in $\pi^- + \mathrm{C}$ and $\pi^- + \mathrm{W}$ collisions at an incident beam momentum of 1.7 GeV/c within the HADES

acceptance were measured. Since they give insights in the behavior of the (anti-)kaons in cold nuclear matter such as scattering and absorption processes. Therefore, the charged kaons were reconstructed and corrected for the reconstruction efficiency within the geometrical acceptance of HADES in two sets of kinematic variables $p_T - y$ and $p - \theta$ in the laboratory frame. The corresponding corrected (double-)differential distribution are presented in Fig. 5.9 and Fig. 5.13. The rapidity density distributions for K^+ and K^- (Fig. 5.12) produced on heavy (W) and light (C) nuclei were compared. Strong scattering effects are observed shifting the maximum of the K^+ distribution to backward rapidity in the heavier target, while the shape of the K^- distribution is comparable in both targets. Besides for the K^+ roughly an order of magnitude difference in cross-section between both target is observed, the cross-section for K^- differs only by a factor two. Hence for the antikaons not scattering effects, but absorption processes (e.g. $K^- N \to Y\pi$) are dominant. Furthermore, the integrated differential production cross-section ($\Delta\sigma$) for K^+ ($0 \leq y < 1.1$) and K^- ($0.2 \leq y < 1.0$) in $\pi^- + \mathrm{C}$ and $\pi^- + \mathrm{W}$ reactions inside the HADES acceptance was extracted (Table 5.3).

The final phase distributions of kaons can be influenced not only by the (in-medium) kaon-nucleon scattering, but also by the repulsive KN potential. While charge exchange reactions based on geometric assumptions play a subordinate role in $\pi^- + A$ reactions (Section 5.2.4), several experiments studying the kinematic distributions of kaons in different nuclear collisions showed that the KN potential is repulsive within $20 - 40$ MeV [B$^+$09c, B$^+$04, A$^+$10a, A$^+$14d]. Therefore the extracted (double-)differential K^+ cross-sections were compared with state-of-the-art hadronic transport model. In contrast to GiBUU [BGG$^+$12], the presented versions of UrQMD [B$^+$99b] and SMASH [W$^+$16] contain neither mean-field NN potential nor in-medium KN potentials. Since none of the three transport models can describe the experimental data, no conclusion could be drawn about the presence of the KN potential. Furthermore, the momentum distributions of K^+ mesons produced off heavy (W) and light (C) nuclei were compared in Section 5.2.4.2. The ratio of the inclusive kaon production cross-section $R(\sigma_A^K/\sigma_C^K)$ is expected to be particularly sensitive to the effects of the KN potential. A similar trend of the ratio can be observed in comparison to the K^0 ratio of FOPI in $\pi^- + A$ collisions at 1.5 GeV/c [B$^+$09c] as well as the K^+ ratios of ANKE in $p + A$ collisions at 1.15 GeV/c and 2.3 GeV/c [B$^+$04]. Although the one sensitive parts of the ratio in the low momentum range are outside HADES acceptance, comparisons with GiBUU including a in-medium ChPT KN potential are more consistent with the experimental data.

A direct indication of absorption was derived from the comparison of the K^-/K^+ ratio measured in collisions with the heavy target (W) and the lighter target (C). In the double ratio $(K^-/K^+)_\mathrm{W}/(K^-/K^+)_\mathrm{C}$ the K^+ serves as reference particle for the strange hadron production due to its very small absorption cross-section [D$^+$75]. The measured double ratio of $(K^-/K^+)_\mathrm{W}/(K^-/K^+)_\mathrm{C} = 0.319 \pm 0.009(\mathrm{stat})^{+0.014}_{-0.012}(\mathrm{syst})$ is far below the expected (anti-)kaon production reference based on elementary πN reactions, directly indicating a considerable K^- absorption in heavy nuclei (W) with respect to light nuclei (C). With respect to antikaon in-medium behavior, comparisons with state-of-the-art transport models, GiBUU [BGG$^+$12], UrQMD [B$^+$99b] and SMASH [W$^+$16], were also presented. In order to predict the correct K^- cross-sections in $\pi^- + A$ reactions, the transport model calculations have to consider the production channels on the one hand and several absorption processes on the other hand. Not only the K^- production is implemented differently in these models, but also the absorption processes (Section 3.7). The predictions for K^- in GiBUU are promising, while UrQMD clearly overestimates the experimental cross-sections. SMASH is able to reproduce the K^- cross-section in the heavier system (W), although it underestimates the production off carbon.

6 Inclusive ϕ Meson Production

The ϕ meson ($s\bar{s}$) is a hadron with hidden strangeness and a narrow width of $\Gamma = 4.27$ MeV [P$^+$16a]. Its production in $\pi + N$ and $N + N$ collisions is expected to be strongly suppressed according to the Okubo-Zweig-Iizuka (OZI) rule [Oku77, Zwe64, Iiz66], which hinders processes with unconnected quark lines.
The large branching ratio $\phi \to K\bar{K}$ ($BR \approx 83\%$ [P$^+$16a]) couples the ϕ properties with the kaon and antikaon properties. On that account, chiral effective field theory models predict a considerable broadening of the in-medium width ($40 - 50$ MeV) and thus a reduced life-time due to in-medium modification of kaon loop and direct ϕN coupling [GW15, CHBVV17]. This circumstance makes the properties of the ϕ meson sensitive to the medium. On the other hand, the ϕ meson candidates observed in the final state are influenced by the in-medium behavior of their decay products, the K^+ and K^- mesons.
The ϕN coupling strength plays a decisive role in the description of hyperon-hyperon interactions [WCSB12], since the ϕ meson can act as mediator of hyperon-hyperon interactions. This means that direct evidence of significant ϕN coupling would lead to a more realistic equation-of-state (EoS) of dense nuclear matter with hyperon content in heavy-ion collisions, but possibly also in neutron stars (NS) [DSW10].
In the investigated $\pi^- + A$ reactions, the ϕ mesons are generated (exclusively) by $\pi^- + p \to \phi + n$ processes. The incident pion beam momentum of 1.7 GeV/c is just above the reaction threshold ($p = 1.56$ GeV/c), which ensures that the ϕ mesons exhibit only a small momentum transfer and hence the probability that the ϕ mesons decay within the target nucleus is higher according to the decay length. However, if one considers that the ϕN cross-section would be small, and the life-time of the ϕ meson fixed to the vacuum life-time ($\tau_{vac} = 46.5$ fm/c), only few ϕ meson would decay inside the target nucleus.
The inclusive ϕ meson production in π^- + C and π^- + W reactions at an incident beam momentum of 1.7 GeV/c is presented in the following chapter. The study will provide further insights into its production, but also into its behavior in nuclear matter. In the following, the analysis procedure is explained. The measured ϕ meson yields are corrected for acceptance and efficiency effects. To ensure that the correction method used does not introduce a model-dependence, a self-consistency check was performed. The ϕ meson in-medium absorption is discussed not only in terms of the transparency ratio with a comparison to the results of ANKE [P$^+$11, H$^+$12] and CLAS [W$^+$10], but also based on the ϕ/K^- ratio. Furthermore, the ϕ decay probability within the heavy nucleus (W) and the influence of the final state interactions of the decay products, K^+ and K^-, on the observed ϕ absorption is discussed.

6.1 Analysis Procedure

The inclusive analysis of the ϕ meson ($\pi^- + A \to \phi X$) exploits its nature as a short-lived hadron, since HADES is not able to detect neutral hadrons. This property enabled the reconstruction of

the ϕ meson via its dominant charged decay channel ($\phi \to K^+K^-$ with $BR \approx 48.9\%$ [P$^+$16a]) using the invariant mass technique (Section 3.3.3). The analyzed kinematic ranges are summarized in Table 6.1.

Table 6.1: Analyzed phase space ranges of ϕ meson for both sets of kinematic variables, $p_T - y$ and $p - \theta$, in the laboratory frame.

Particle	y	p_T [MeV/c]
ϕ	$0.4 - 1.0$	$150 - 650$

Particle	θ [°]	p [MeV/c]
ϕ	$10 - 45$	$500 - 1500$

6.1.1 ϕ Meson Reconstruction

The ϕ mesons were identified via their dominant charged decay channel into K^+K^- pairs ($BR = 48.9 \pm 0.5\%$ [P$^+$16a]). Both charged kaons were selected based on the correlation between β and momentum ($p/\sqrt{p^2 + m_0^2} \pm 0.5 \gtrless \beta$, $m_0 = 493.677$ MeV/c^2 [P$^+$16a]). Similar to the inclusive charged kaon analysis an additional momentum corrections for the (anti-)kaon were applied (Section 5.1.1), partly resulting from a systematic re-calibration of the HADES magnetic field (of order $6 \cdot 10^{-3}$) and the energy loss in the beam tube, RICH radiator and target material. The contamination from other particle species was further reduced by selecting a reconstructed (anti-)kaon mass interval of 400 MeV/c^2 $< m <$ 600 MeV/c^2. The nominal mass m_0 was attributed to the identified (anti-)kaon candidates.

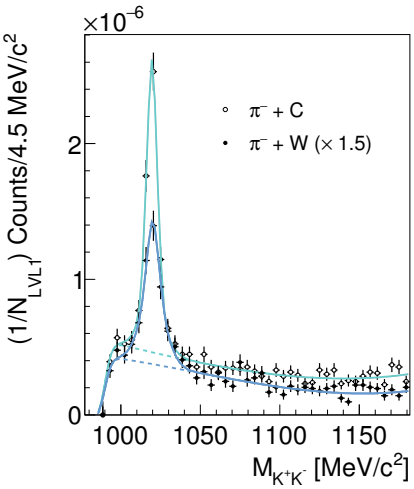

Figure 6.1: Invariant mass distributions of K^+K^- pairs normalized to the number of LVL1 events produced in $\pi^- + \mathrm{C}$ (open points) and $\pi^- + \mathrm{W}$ (full points) reactions. The fit to the uncorrected experimental data consists of two Gaussian for the ϕ signal together with the background described by a thrid-order polynomial and Gaussian function (dashed curve).

The resulting K^+K^- invariant mass distribution for $\pi^- + \mathrm{C}$ and $\pi^- + \mathrm{W}$ reactions normalized to the number of LVL1 events is presented in Fig. 6.1. A clear ϕ peak is visible and the signal can be described by the sum of two Gaussian distributions to account for finite resolution effects as well as for the re-scattering of the K^+ and K^- inside the target. The background is modeled by

a third-order polynomial together with a Gaussian to account for the mass threshold ($2 \times m_0$). In Figure 6.1 it can be seen that less ϕ mesons are produced off the heavier target (W) with respect to the lighter target (C). The precision of the ϕ mass measurement is better than 1 MeV and the ϕ mass resolutions are $\sigma_{\phi,\mathrm{C}} = 4.0 \pm 0.8$ MeV/c^2 and $\sigma_{\phi,\mathrm{W}} = 5.5 \pm 2.4$ MeV/c^2 for the C and W target, respectively. While the reconstructed mass of the ϕ is consistent within errors in both nuclear systems, an increase of the width in $\pi^- + \mathrm{W}$ reactions compared to $\pi^- + \mathrm{C}$ is observed. Even though not significant, it hints to multiple scattering effects of the K^+ and K^- inside the heavier nuclear target (W). Anyhow, an extraction of the in-medium width based on the invariant mass distribution of charged kaons poses some difficulties. Since the final-state interactions of the charged kaons, e.g. Coulomb interaction, in heavy nuclei covers the change in width of the K^+K^- invariant mass distribution that is expected from an increase of the ϕ width in nuclear matter [MFG$^+$03]. Furthermore, the ϕ mesons are to some extent expected, depending on the in-medium width, to leave the nucleus before decaying, if no selection is applied to low ϕ momenta. Therefore, the observed width is dominantly the free width. To obtain the ϕ yield, double Gaussian parameterizations were integrated within a 3σ region around the mean μ. In total $N_{\mathrm{C}}^{\phi} = 578 \pm 35$ and $N_{\mathrm{W}}^{\phi} = 341 \pm 32$ ϕ mesons are reconstructed.

6.1.2 Acceptance and Efficiency Correction

In order to gain insights into the production and interaction of ϕ mesons in nuclear matter, the raw yield must be corrected for acceptance and efficiency effects (Section 3.6.4). In the following, full-scale simulations based on Pluto [F$^+$07, FGH$^+$10] were used. All effects on acceptance, detector response and tracking algorithm were considered (Section 3.6).

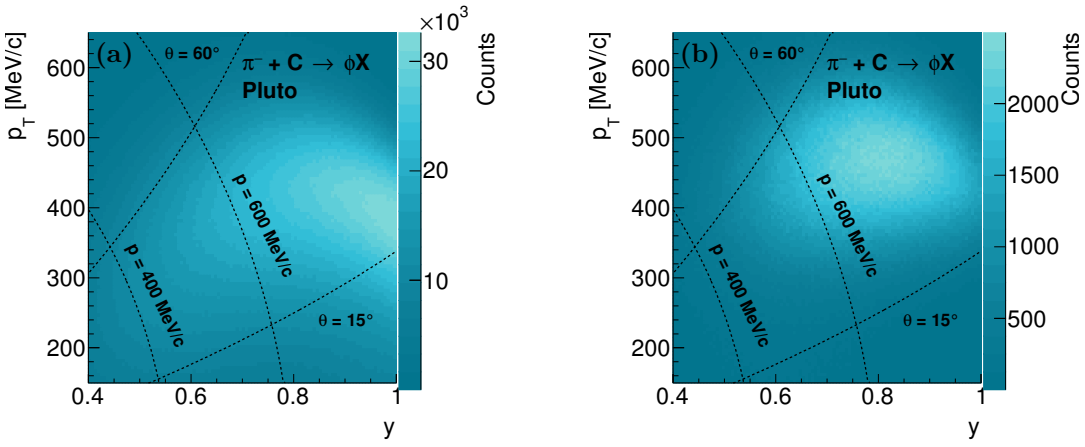

Figure 6.2: ϕ meson distribution as a function of transverse momentum p_T vs. rapidity y for initial unfiltered (a) and reconstructed (b) full-scale simulation of $\pi^- + \mathrm{C}$ reactions based on Pluto. The black dotted horizontal lines indicate the momentum at 400 and 600 MeV/c. The black dotted vertical lines denote the polar angle regions between $\theta = 15 - 60°$.

The acceptance and efficiency correction was determined by simulating the exclusive reaction $\pi^- + p(^{12}\mathrm{C}) \rightarrow \phi[\rightarrow K^+K^-] + n(^{11}\mathrm{B})$. In this reaction, the Fermi motion of the proton in the carbon nucleus (^{12}C) was taken into account. Since in Pluto the Fermi motion for tungsten is not implemented, the same reaction was used for the event generation to evaluate the acceptance and efficiency in $\pi^- + \mathrm{W}$ reactions. An example for a corresponding kinematic distribution of

the ϕ meson in $\pi^- + \mathrm{C}$ reactions is shown in Fig. 6.2. Fig. 6.2 (a) shows the initial unfiltered distribution, while Fig. 6.2 (b) depicts the spectrum of the reconstructed full-scale simulation. When comparing the initial spectra with the reconstructed one, a decrease of more than one order of magnitude of the yield is observed. The obtained efficiency of the ϕ mesons typically ranges from $(2-15)\%$. Since these corrections strongly depend on the ϕ kinematics shown in Fig. 6.3, a double-differential correction was evaluated as a function of $p_T - y$ $(p - \theta)$. Since the limited statistics do not allow for a double-differential analysis, each ϕ candidate is weighted event-by-event with the corresponding correction factor (Fig. 6.3) and an integrated K^+K^- invariant mass spectrum is built, as shown in Fig. 6.4 (a) for $\pi^- + \mathrm{C}$ and in Fig. 6.4 (b) for $\pi^- + \mathrm{W}$ collisions. The same fitting procedure used for the uncorrected K^+K^- invariant mass distribution to extract the raw yield of ϕ meson was also applied to the corrected spectra.

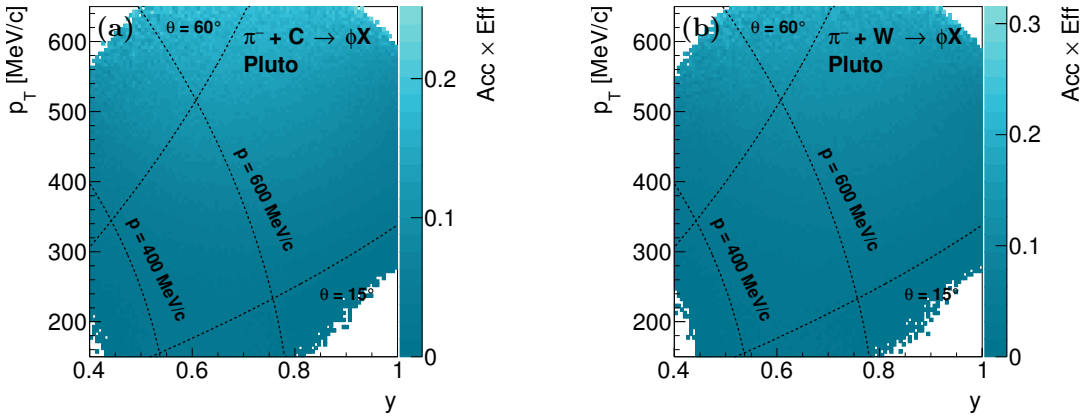

Figure 6.3: Acceptance and efficiency matrix for the ϕ meson as a function of transverse momentum p_T vs. rapidity y inside the HADES acceptance for $\pi^- + \mathrm{C}$ (a) and $\pi^- + \mathrm{W}$ (b) reactions. The dotted black vertical lines indicate different polar angle regions, while the dotted black horizontal lines indicate different regions of constant momentum in the laboratory frame.

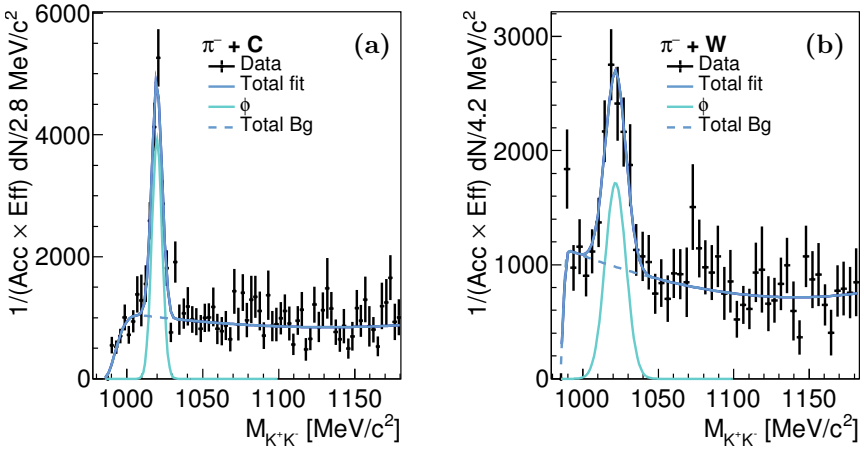

Figure 6.4: Invariant mass distributions of K^+K^- pairs with event-by-event reconstruction efficiency correction produced in $\pi^- + \mathrm{C}$ (a) and $\pi^- + \mathrm{W}$ (b) collisions. The fit to the corrected experimental data consists of two Gaussian for the ϕ signal (cyan solid curve) together with the background described by a polynomial and Gaussian function (blue dashed curve).

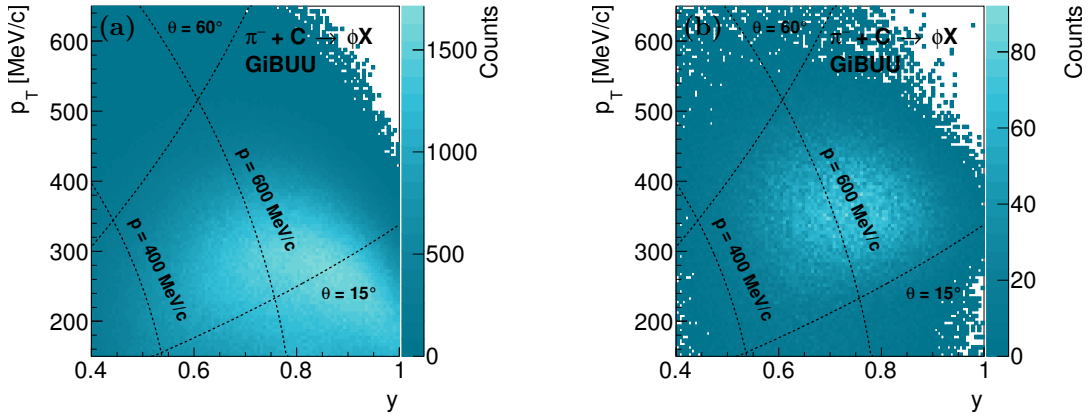

Figure 6.5: ϕ meson distribution as a function of transverse momentum p_T vs. rapidity y for initial unfiltered (a) and reconstructed (b) full-scale simulation of $\pi^- + \mathrm{C}$ reactions based on GiBUU. The black dotted horizontal lines indicate the momentum at 400 and 600 MeV/c. The back dotted vertical lines denote the polar angle regions between $\theta = 15 - 60°$.

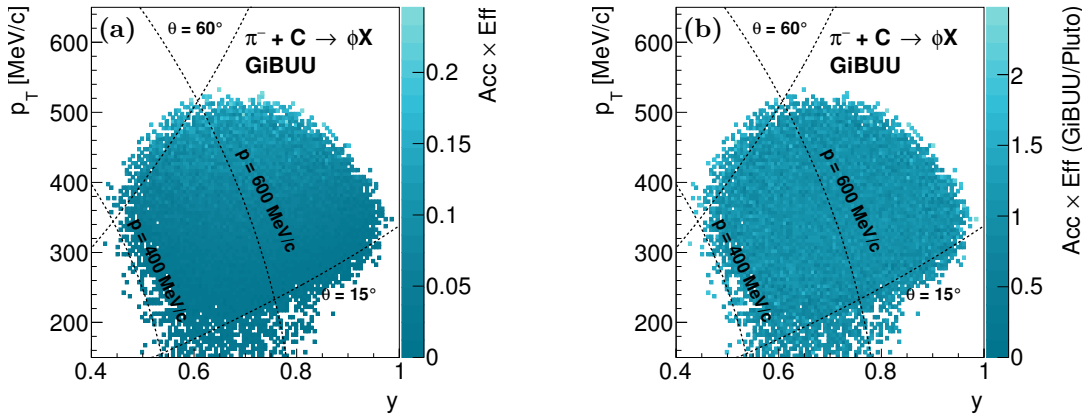

Figure 6.6: Acceptance and efficiency matrix for the ϕ meson as a function of transverse momentum p_T vs. rapidity y inside the HADES acceptance for $\pi^- + \mathrm{C}$ reactions based on GiBUU (a) with the corresponding ratio between GiBUU and Pluto (b). The dotted black vertical lines indicate different polar angle regions, while the dotted black horizontal lines indicate different regions of constant momentum in the laboratory frame.

In order to confirm the reliability of the correction procedure, a self-consistency check was carried out on the basis of two different models. For this purpose, the correction matrices obtained separately for each model were compared. For the comparison a double-differential correction was chosen. The correction of the experimental data is based on Pluto simulations, while GiBUU simulations [BGG+12] (Section 3.7) were used to validate the correction method. The same areas and binning were used as for Pluto. If one compares the ϕ double-differential distribution for $\pi^- + \mathrm{C}$ collisions based on an unfiltered Pluto simulation shown in Fig. 6.2 (a) with the one based on GiBUU shown in Fig. 6.5 (a), it becomes clear that both models predict completely different distributions. Furthermore, it can be seen that the simulated number of ϕ mesons differs significantly, since GiBUU describes the entire reaction dynamics of the pion-nucleus reactions

and ϕ mesons are rarely produced. After a full-scale simulation with HGeant to consider the acceptance of the spectrometer, the digitization process and all analysis steps, the corresponding reconstructed simulations are presented in Fig. 6.2 (b) and Fig. 6.5 (b).

The acceptance and efficiency correction matrix based on GiBUU is shown in Fig. 6.6 (a). Since the statistics in the GiBUU simulation is significantly lower, efficiency values greater than the maximum efficiency based on Pluto simulations were excluded in order to reduce the effect of statistical fluctuations. The average correction value based on GiBUU corresponds to 5.5%, while that of Pluto is 5.1% in the overlap range. The ratios of the corresponding correction represented in Fig. 6.6 (b) for $\pi^- + \mathrm{C}$ collisions are distributed around one with an average value of 1.05. Although deviations between the Pluto and GiBUU corrections are observed, the reliability of the correction procedure based on Pluto simulations is still given. As the deviations of the correction are mainly due to statistical fluctuations in the correction based on GiBUU.

6.1.3 Systematic Uncertainties

In the following, the systematic uncertainties that are caused by the measurement itself or by the applied analysis method were evaluated. Therefore, the invariant mass binning was varied with respect to the standard analysis and the order of the polynomial used to fit the background was changed from third to second order. The systematic uncertainty of this variations was estimated with the help of the minimal and maximal deviation. In addition, the correction uncertainty corresponding to 3% for each kaon (Section 3.6.4) was considered.

6.2 Results and Discussion

6.2.1 Inclusive ϕ Production Cross-Section

In Section 6.1 the procedure was explained for obtaining efficiency corrected ϕ yields. The total number of corrected ϕ mesons for the $p_T - y$ analysis within the HADES acceptance in $\pi^- + \mathrm{C}$ reactions is equal to $N_C^\phi = 11826 \pm 716(\mathrm{stat})^{+513}_{-663}(\mathrm{syst})$ and in $\pi^- + \mathrm{W}$ reactions is equal to $N_W^\phi = 7085 \pm 665(\mathrm{stat})^{+303}_{-301}(\mathrm{syst})$.
After the correction for the branching ratio and applying the absolute normalization (Section 3.4), the integrated differential ϕ production cross sections ($\Delta\sigma$) within the HADES acceptance ($0.4 \leq y < 1.0$ and $150 \leq p_T < 650$ MeV/c) for $\pi^- + \mathrm{C}$ and $\pi^- + \mathrm{W}$ collisions were extracted, which are listed in Table 6.2.

Table 6.2: Target, particle species and cross-section for ϕ ($0.4 \leq y < 1.0$, $150 \leq p_T < 650$ MeV/c). Error values shown are statistic (first), systematic (second) and normalization (third).

Target	Particle	$\Delta\sigma$ [μb]
C	ϕ	$41 \pm 2 \pm 2^{+6}_{-5}$
W	ϕ	$112 \pm 10 \pm 5^{+18}_{-14}$

The total number of corrected ϕ mesons for the $p - \theta$ analysis within the HADES acceptance in $\pi^- + \mathrm{C}$ reactions is equal to $N_C^\phi = 12038 \pm 756(\mathrm{stat})^{+511}_{-545}(\mathrm{syst})$ and in $\pi^- + \mathrm{W}$ reactions is

equal to $N_W^{\phi} = 8104 \pm 772(\text{stat})^{+346}_{-357}(\text{syst})$. Deviations in the total corrected ϕ yields compared to $p_T - y$ analysis may be attributed to statistical fluctuations.

6.2.2 ϕ Meson Absorption

Pion-nucleus reactions allow for a quantitative study of open and hidden strange hadron production and properties at a well defined nuclear density. Of particular interest is the ϕ meson ($s\bar{s}$) with no-net strangeness. According to the Okubo-Zweig-Iizuka (OZI) rule [Oku77, Zwe64, Iiz66] quark exchange and hence the interaction of the ϕ meson with ordinary (non-strange) baryonic matter is suppressed. Consequently, the ϕN cross-section is assumed to be small [SB16]. On the contrary, measurements of the modification of the ϕ production rates in proton- and photon-induced reactions point to a rather sizeable ϕN interaction cross-section [I$^+$05, W$^+$10, P$^+$11, H$^+$12].
The employed pion-nucleus reactions are superior to the previously studied proton- and photon-induced reactions. Due to the large πN inelastic cross section ($\sigma_{\pi N} = 35$ mb) and therefore small mean free path ($\lambda_\pi = 1.8$ fm), hadron production occurs close to the upstream surface of the nucleus [A$^+$73, B$^+$09c], leading on average to a longer path of the produced hadrons inside nuclear matter. Because of the much lower production cross-section of the ϕ meson in proton-induced reactions (Fig. 6.7 (a)), secondary processes are non-negligible, causing shorter path lengths, just as in photon-induced reactions where the incident photons penetrate deeply into the nucleus.
Commonly, the ϕ meson absorption is investigated by comparing the inclusive ϕ production off heavy and light nuclei in terms of the transparency ratio, which will be presented in Section 6.2.2.1 together with results of ANKE and CLAS. In addition, the momentum-dependent ϕ production cross-sections and transparency ratio is compared to the predictions of a collision model [Par18].
Furthermore, a direct indication of ϕ absorption can be obtained by comparing the ϕ/K^- ratio, measured in collisions with the heavy target (W) and the lighter target (C). In the ratio ϕ/K^- the K^- acts as a reference particle for the strange hadron absorption, due to its large absorption cross section (Section 5.2.5). The evidence of significant ϕ absorption based on the ϕ/K^- ratio is discussed in Section 6.2.2.2.
In Figure 6.2.2.3 the ϕ decay probability within the heavy nucleus (W) and the influence of the final state interaction of the ϕ meson decay products, K^+ and K^-, on the observed ϕ absorption is addressed.

6.2.2.1 Extracted Transparency Ratio

Insights on the in-medium ϕ meson absorption can be deduced by comparing the ϕ production cross-section off heavy and light nuclei. Therefore the ϕ absorption can be quantified in terms of the transparency ratio (Eq. (6.1)).

$$T(\sigma_{\mathrm{W}}^{\phi}/\sigma_{\mathrm{C}}^{\phi}) = \frac{12}{184}\frac{\Delta\sigma_{\mathrm{W}}^{\phi}}{\Delta\sigma_{\mathrm{C}}^{\phi}}, \tag{6.1}$$

with

$\Delta\sigma_{\mathrm{W}}^{\phi}/\Delta\sigma_{\mathrm{C}}^{\phi}$: integrated differential cross-section for the inclusive ϕ production in $\pi^- + \mathrm{W}$ and $\pi^- + \mathrm{C}$ collisions

The effect of the ϕN coupling, hence the in-medium absorption, is increasing with increasing the nucleus size [P$^+$11], since the ϕ mesons are exposed to higher densities on average. Therefore, the production off heavy nuclei (W) should be suppressed with respect to the light one (C) and hence the transparency ratio should decrease with increasing nucleus size.

The transparency ratio of the ϕ meson measured in collisions with heavy targets (A) compared to lighter ones (C) as a function of the excess energy ε relative to the free nucleon threshold is shown in Fig. 6.7 (b). The result of this work (full circle) with a value of $T(\sigma_{\mathrm{W}}^{\phi}/\sigma_{\mathrm{C}}^{\phi}) = 0.18 \pm 0.02(\mathrm{stat}) \pm 0.01(\mathrm{syst})^{+0.04}_{-0.03}(\mathrm{norm})$ is significantly smaller than the results obtained in $p+A$ by ANKE [P$^+$11] (open circle) and $\gamma + A$ by CLAS [W$^+$10] (full star) for slightly bigger nuclei ($T_{ANKE} = 0.29 \pm 0.01(\mathrm{stat}) \pm 0.02(\mathrm{syst})$, $T_{CLAS} = 0.46 \pm 0.12(\mathrm{stat}) \pm 0.13(\mathrm{syst})$). The presented normalization uncertainty is a conservative estimate as most contributions to error are expected to cancel in the ratio (Appendix B). The lower transparency ratio found in pion-induced reactions may be attributed to the already mentioned large πN reaction cross-section and the negligible contribution of secondary reactions due to the comparatively large ϕ production cross-section (Fig. 6.7 (a)), that lead to ϕ production near the upstream surface, allowing the hadron to travel a longer path within the nucleus than in proton- and photon-induced reactions.

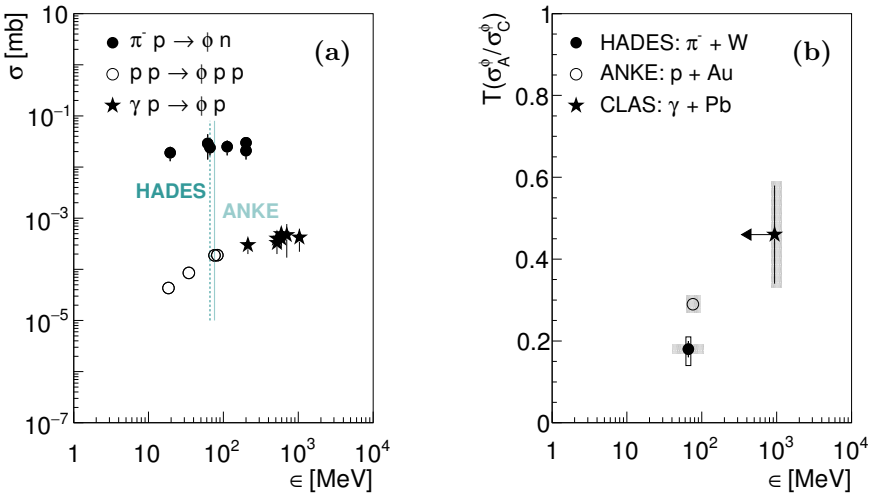

Figure 6.7: (a) The total cross sections for $\pi^- + p \to \phi n$ [Sch08a], $p + p \to \phi pp$ [H$^+$06, B$^+$01] and $\gamma + p \to \phi p$ [Sch08b] reactions as a function of the excess energy ε above the free nucleon threshold. The vertical lines indicate the excess energy of this experiment (blue dotted line) and ANKE [P$^+$11, H$^+$12] (cyan solid line). (b) Comparison of the ϕ meson transparency ratio normalized to carbon as a function of the excess energy ε relative to the free nucleon threshold. The full circle resembles the transparency ratio of this work. The statistical, systematic and normalization uncertainties are given by the error bars, hashed areas and open boxes, respectively. The open circle resembles the result in $p + A$ by ANKE [P$^+$11], while the star indicates measurement in $\gamma + A$ by CLAS [W$^+$10].

To extract information about the ϕN interaction cross-section, the transparency ratio has to be compared with theoretical models. The transparency ratios by CLAS [W$^+$10] were analyzed within a Glauber model yielding to $\sigma_{\phi N}$ in the range of $16-70$ mb. Also the ϕ meson momentum depended analysis of the transperency ratios measured in $p + A$ collisions by the ANKE Collaboration point in the same direction with an effective ϕN absorption cross-section of $14 - 21$ mb [H$^+$12].

In the following the inclusive ϕ production in $\pi^- + \mathrm{C}$ and $\pi^- + \mathrm{W}$ reactions is compared to the collision model [Par18]. The model considers the effects of the effective scalar ϕ and nucleon

potentials, which comprise a real and imaginary part. While the strength of the real part of the potential is connected to a in-medium mass shift, the imaginary part describes the absorption in the medium. An attractive effective scalar potential of $U_\phi = -20$ MeV (ρ_0) was considered for the ϕ meson corresponding to a mass reduction of 2% within matter. For the outgoing neutron besides, a repulsive effective scalar potential of $U_\phi = 25$ MeV (ρ_0) corresponding to sightly increased mass ($< 2\%$) also the case without potential ($U_N = 0$ MeV) was examined. In addition, both primary ($\pi^- + p \rightarrow \phi n$) and secondary ($\pi + N \rightarrow \phi N$) reactions are considered. However, it was found that the primary production channel is dominant at a beam moment of 1.7 GeV/c within the HADES acceptance. The model makes it possible to test different ϕN absorption cross-sections $\sigma_{\phi N}$. Figure 6.8 shows the differential production cross-section ϕ as a function of the momentum in collisions with light (C) and heavy (W) targets in the polar angle range of $10° - 45°$. The solid, long-dashed and dashed curves correspond to the ϕN absorption cross sections $\sigma_{\phi N}$ of 10 mb (weak), 20 mb (relatively weak) and 30 mb (strong), respectively. In addition, for the heavier target (W), the contribution of the secondary reactions is indicated by a dark cyan long-dashed curve (Fig. 6.8 (b)). As expected, the effect of the different ϕN absorption cross sections is more pronounced for the heavy system (W). Also the choice of the (final) neutron mass in the nuclear matter has influence on the calculated differential ϕ cross-section, as it is observed for the light cyanic solid curve ($U_N = 25$ MeV) with respect to the dark cyanic dotted curve ($U_N = 0$ MeV). Therefore the modification of the neutron mass can mask the determination of the ϕN absorption cross-section.

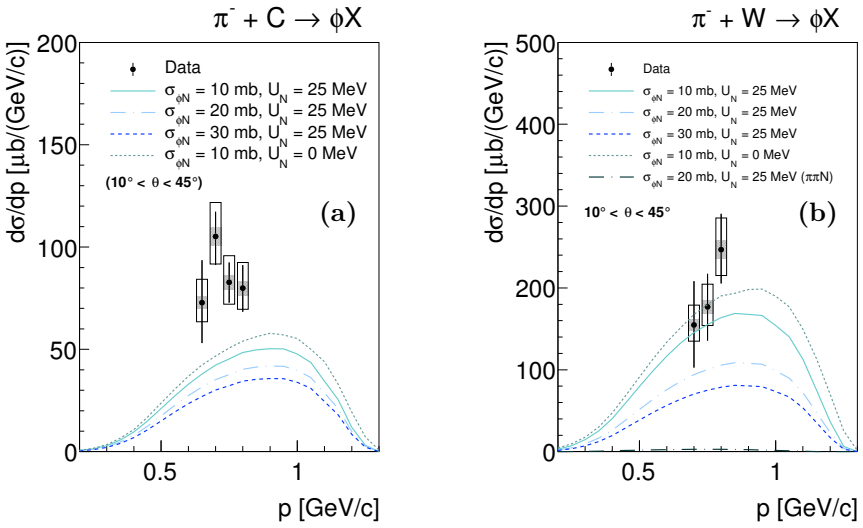

Figure 6.8: Differential cross-section for the production of ϕ mesons as function of momentum in $\pi^- + \mathrm{C}$ (a) and $\pi^- + \mathrm{W}$ (b) collisions in the polar angle range of $10° - 45°$ in the laboratory frame. The statistical, systematic and normalization uncertainties are given by the error bars, hashed areas and open boxes, respectively. The curves correspond to theoretical calculations taken from [Par18] for different values of the ϕN absorption cross-section (10 mb, 20 mb and 30 mb) and secondary neutron effective scalar potentials at density ρ_0 ($U_N = 0$ MeV, $U_N = 25$ MeV).

The experimental cross sections indicated by the black data points were extracted on the basis of the procedure explained in Section 6.1. Only the modeling of the background was changed from a third-order polynomial together with a Gaussian function to an ARGUS function. The latter proved to be more robust against statistical fluctuations. Details can be found in Appendix G. The statistical errors are represented by the error bars. As systematic uncertainty the correction

uncertainty corresponding to 3% for each kaon was considered. The systematic and normalization errors are represented by hashed areas and open boxes, respectively. It can be seen that the experimental cross-section for the ϕ production off carbon is larger than the theoretical curves (Fig. 6.8 (a)), while for the heavier target it is almost in agreement with the theoretical predictions of a weak ϕ absorption cross-section of $\sigma_{\phi N} = 10$ mb (Fig. 6.8 (b)). Therefore, no conclusive picture can be drawn for the production and absorption of the ϕ mesons according to the model by Paryev [Par18]. This is partly caused by the small amount of reconstructed ϕ mesons.

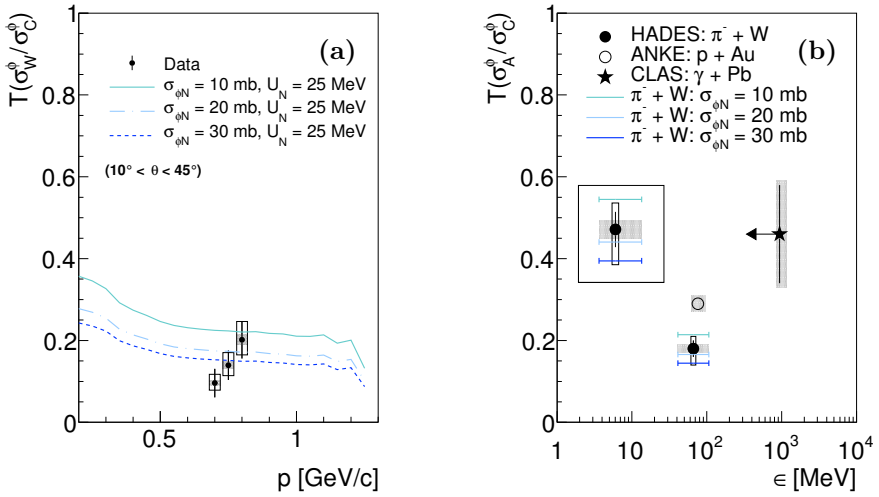

Figure 6.9: (a) ϕ meson transparency ratio as function of the momentum off tungsten normalized to carbon in the polar angle range of $10° - 45°$ in the laboratory frame. The statistical uncertainties are indicated by the error bars, the systematic uncertainty by the hashed areas and the normalization uncertainty by the open boxes. The curves correspond theoretical calculations taken from [Par18] corresponding to different values of the ϕN absorption cross-section (10 mb, 20 mb and 30 mb). (b) Comparison of the ϕ meson transparency ratios normalized to carbon as function of the excess energy ε above the free nucleon threshold. The full circle resembles the transparency ratio measured in this work. The statistical, systematic and normalization uncertainties are given by the error bars, hashed areas and open boxes, respectively. The open circles resembles the result in $p + A$ by ANKE [P$^+$11], while the star indicates measurement in $\gamma + A$ by CLAS [W$^+$10]. The horizontal lines represent momentum integrated theoretical calculations taken from [Par18].

Moreover, the momentum-dependent transparency ratios is investigated. In the transparency ratio the role of the meson in-medium modification is probably negligible [Par18]. In addition, the ratio should be less sensitive to the implemented elementary πN cross-sections. In Figure 6.9 (a) the predicted transparency ratio is presented as a function of the momentum for three different cases of the ϕN absorption cross-section (10 mb, 20 mb and 30 mb). As expected, the transparency ratio decreases with increasing ϕN absorption cross-section. Besides, also a decrease with increasing momentum of the ϕ meson is predicted. The experimental transparency ratios are represented by the black data points along with the statistical and systematic uncertainties. As most contributions to error are expected to cancel in the ratio, the presented normalization uncertainties are a conservative estimate (Appendix B). In contrast to the predictions of the collision model, the experimental transparency ratio increases with increasing ϕ momentum. Thus, the absorption seems to be stronger for ϕ mesons with low momentum, similar to the observation of K^- absorption based on the double ratio $(K^-/K^+)_{\mathrm{W}}/(K^-/K^+)_{\mathrm{C}}$ (Fig. 5.24). Nevertheless, also on the basis of the momentum-dependent transparency ratio, no quantitative statement can

be made about the ϕN absorption cross-section. In addition, the extracted momentum integrated transparency ratio (black circle) as function of the excess energy is compared to the collision model predictions in Fig. 6.9 (b). Here we find that the experimental data within the combined statistical and systematic uncertainty agree with a ϕ absorption cross-section of $\sigma_{\phi N} = 20$ MeV.

Future experiments with pion beams with higher statistics of ϕ mesons may allow to the determine the ϕN absorption cross-section based on the momentum-dependent ϕ production cross-section or/and transparency ratio similar to the results by ANKE [H$^+$12] presented in Section 1.5. Besides, new measurements would allow to systematically study the dependence on the mass number A, which in combination with theoretical calculation should provide complementary information to photon- and proton-induced measurements. To the present, the data in proton- and photon-induced reactions have been compared with calculations by Mühlich and Mosel [MM06], Magas et al. [MRO05], Paryev [Par09] and Cabrera et al. [CRO$^+$04] to extract the inelastic ϕN cross-section and the in-medium ϕ width (Section 1.5). However, the interpretation of the transparency ratio is rather model-dependent [MM06, C$^+$17] implying in-medium propagation, initial and final state interactions that have to be taken into account to extract final conclusions.

6.2.2.2 Extracted ϕ-to-Antikaon Ratio

The comparison of the ϕ/K^- ratio measured in collisions with the heavy target (W) and the lighter target (C) can give a direct indication of ϕ absorption inside the nuclear medium. The K^- acts this time as a reference particle for the strange hadron absorption due to its large absorption cross-section (Section 5.2.5).

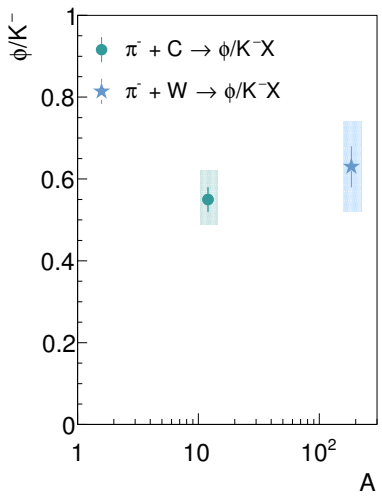

Figure 6.10: ϕ/K^- ratio as a function of atomic number A inside the HADES acceptance for $\pi^- + \mathrm{C}$ (circle) and $\pi^- + \mathrm{W}$ (star) reactions. The statistical uncertainties are shown by the error bars, while the systematic errors are indicated by the hashed areas.

The ϕ/K^- ratio was evaluated for both collision systems inside the HADES acceptance. For this investigation it has to be considered that the K^- and ϕ phase space coverage of HADES is different ($0.4 \leq y_\phi < 1$ and $0.2 \leq y_{K^-} < 1$, $150 \leq p_{T,\phi} < 650$ MeV/c and $90 \leq p_{T,K^-} < 330$ MeV/c). As shown in Fig. 5.12 the shape of the K^- rapidity distributions does not depend on the target. To demonstrate that also the ϕ distributions share the same feature, GiBUU [BGG$^+$12] simulations

were carried out for $\pi^- + \mathrm{C}$ as well as $\pi^- + \mathrm{W}$ collisions and no bias due to the HADES geometrical acceptance was found (Appendix H.1). The measured ϕ/K^- ratio within the HADES acceptance is $0.55 \pm 0.04(\mathrm{stat})^{+0.06}_{-0.07}(\mathrm{syst})$ for $\pi^- + \mathrm{C}$ and $0.63 \pm 0.06(\mathrm{stat})^{+0.11}_{-0.11}(\mathrm{syst})$ for $\pi^- + \mathrm{W}$ collisions. The main systematic error arises from the difference in the $p_T - y$ and $p - \theta$ analyses. In Figure 6.10 the ϕ/K^- ratio is shown as function of the atomic number A. Within errors the two ϕ/K^- ratios are in agreement. Since the double ratio $(K^-/K^+)_\mathrm{W}/(K^-/K^+)_\mathrm{C}$ (Fig. 5.24) clearly indicates a larger K^- absorption in the W target and since the ϕ/K^- ratios are the same for both targets, also a stronger ϕ absorption in W is observed. This demonstrates that both resonant (ϕ) and non-resonant (K^+K^-) channels are affected in the medium in the same way.

6.2.2.3 Influence of (Anti)Kaon Final-State Interaction

In Figure 5.2.4 it was demonstrated that the kaon do undergo final state interaction due to elastic scattering processes and the moderate repulsive KN potential. Besides, also the antikaon interacts with the nuclear matter via elastic scattering and via strangeness exchange processes, which lead to non negligible absorption (Section 5.2.5). Therefore, it is relevant to investigate how the final state interaction of (anti)kaons originating from ϕ decays may influence the reconstruction of the latter. If one considers that the ϕN cross-section would be small, and the life-time of the ϕ fixed to the vacuum life-time ($\tau_{vac} = 46.5$ fm/c, $\Gamma_{vac} = 4.3$ MeV), only few ϕ meson would decay inside the target nucleus.

By taking into account geometry of the reaction one can estimate the path of the produced ϕ mesons and thus their probability of decaying within the nucleus. The mean free path of the incident pions ($p_{\pi^-} = 1.7$ GeV/c) at normal nuclear density is around $\lambda \approx 2$ fm ($\sigma_{\pi N} = 35$ mb). Further, also the impact parameter distribution of the incident pions has influence on the remaining path within the nucleus as sketched in Fig. 6.11 (a). Thus, the probability of the pion impact parameter based on GiBUU (geometrical assumption) have been considered in four intervals indicated in Fig. 6.11 (b). The intervals I-III correspond to 7% ($b = 0 - 2$ fm), 20% ($b = 2 - 4$ fm), 35% ($b = 4 - 6$ fm) and 36% ($b = 6 - 7$ fm).

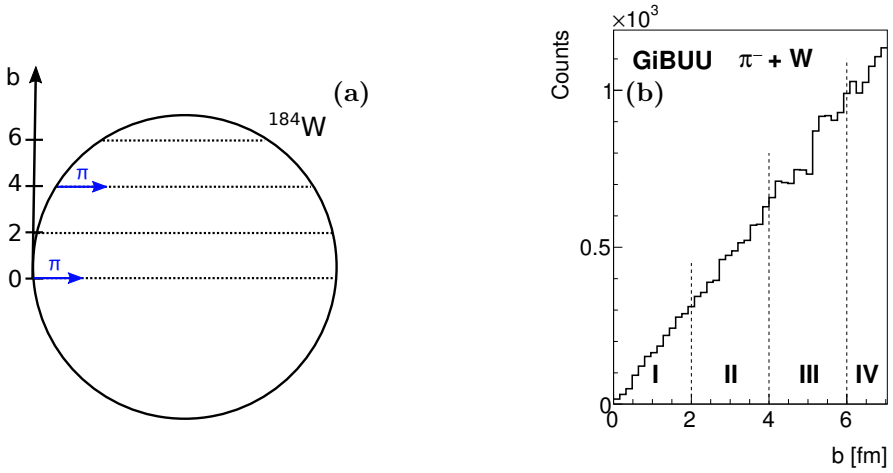

Figure 6.11: (a) Schematic of the π^- meson path length inside tungsten. (b) Impact parameter distribution in $\pi^- + \mathrm{W}$ reactions based on GiBUU.

To estimate the maximal path length of the ϕ meson inside tungsten, three polar angle θ intervals in combination with pion impact parameter b intervals were taken into account as sketched in

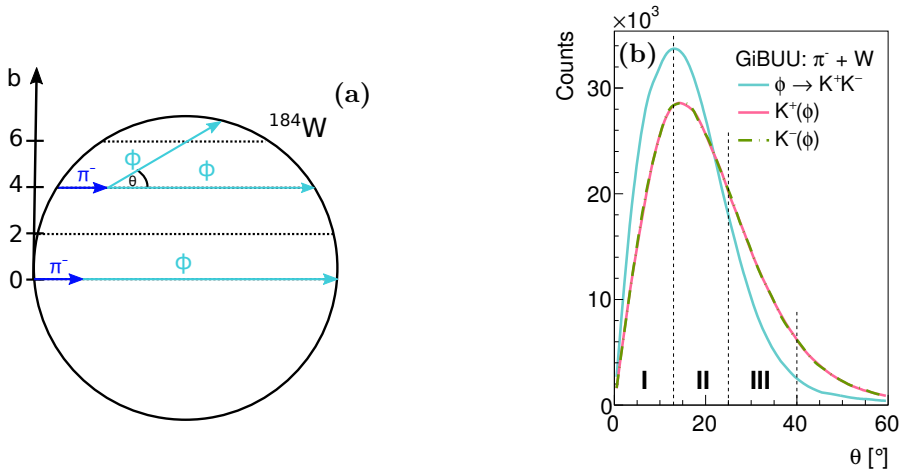

Figure 6.12: (a) Schematic of the ϕ meson path length inside tungsten. (b) Polar angle θ distribution of the ϕ meson (cyan curve) and daughter particles, K^+ (pink curve) and K^- (green dashed-dotted curve), originating from $\pi^- + \mathrm{W}$ reactions in GiBUU.

Fig. 6.12 (a). With increasing polar angle θ the path of the ϕ mesons is decreasing. The polar angle θ distribution of the ϕ meson based on GiBUU is shown in Fig. 6.12 (b) with the three intervals indicated. The probability to be in a certain polar angle θ interval is 43% $(0-13°)$, 40% $(13-25°)$ and 14% $(25-40°)$. For the polar angle θ range of $0-13°$ a maximal path length of the ϕ meson inside tungsten of 12 fm ($b = 0-2$ fm), 11 fm ($b = 2-4$ fm), 9 fm ($b = 4-6$ fm) and 5 fm ($b = 6-7$ fm) was estimated.

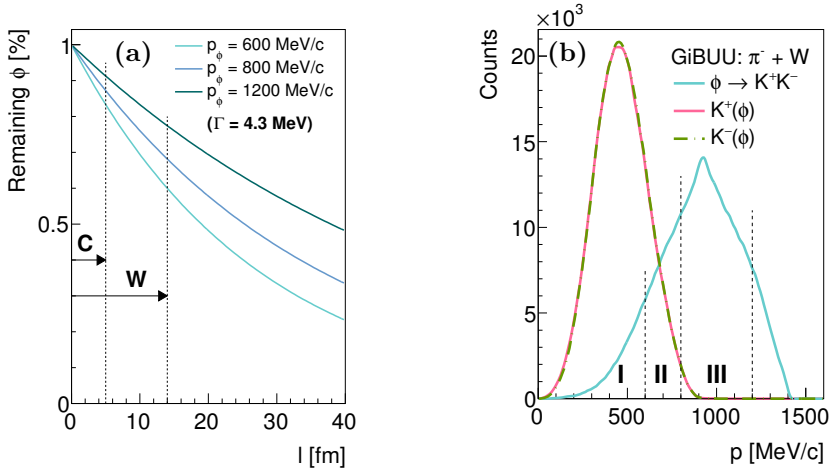

Figure 6.13: (a) Survival probability of the ϕ meson as a function path length l for three different momenta (600 (cyan curve), 800 (blue curve) and 1200 (dark cyan curve) MeV/c) assuming the vacuum life-time ($\tau_{vac} = 46.5$ fm/c, $\Gamma_{vac} = 4.3$ MeV). (b) Momentum distribution of the ϕ meson (cyan curve) and daughter particles, K^+ (pink curve) and K^- (green dashed-dotted curve), originating from $\pi^- + \mathrm{W}$ reactions in GiBUU.

The decay length of the ϕ mesons is not only dependent on its life-time but also on its momentum. Thus, the probability that the ϕ meson decays at the surface of tungsten was calculated in three momentum intervals. Further, the vacuum life-time ($\tau_{vac} = 46.5$ fm/c) has been assumed. Figure 6.13 (a) shows the survival probability of the ϕ meson as function of the path length for

three different momenta (see legend). The momentum distribution of the ϕ meson on the basis of GiBUU is depicted in Fig. 6.13 (b). The probability of the ϕ meson to be in a certain momentum interval is 11% ($0-600$ MeV/c), 22% ($600-800$ MeV/c) and 57% ($800-1200$ MeV/c) as indicated. The correlation between polar angle θ and momentum p was considered to be uniform. This results in an estimated overall probability that the ϕ decays inside tungsten of below 13%.

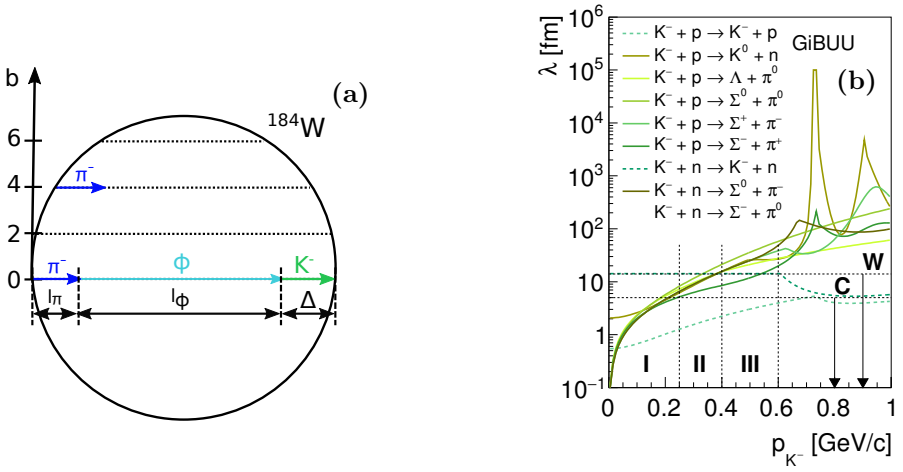

Figure 6.14: (a) Schematic of maximal path length of the K^- meson originating from ϕ meson decays inside tungsten. (b) Mean free path λ of elastic and inelastic reactions based on scattering cross-section parametriztaions for K^- implemented in GiBUU without resonance contribution.

To consider the effect of the re-scattering of (anti-)kaons stemming from ϕ decays inside tungsten one has to take into account that such scattering processes are hindered by Pauli-blocking [OVTR01, MFG+03] for low-energy (anti-)kaons originating from ϕ decay with momenta smaller than $100-150$ MeV/c of interest [Par05]. Besides, the probability for elastic scattering of (anti-)kaons from ϕ decays can be estimated on the basis of the mean free path λ at normal nuclear density ρ_0. The probability for the K^+ with a mean free path of $\lambda \approx 5$ fm (Fig. 5.14 (b)) is negligible. The mean free paths λ of the K^- are indicated in Fig. 6.14 (b) by (green) dashed curves. One can see that the mean free path of the elastic $K^- + p \rightarrow K^- + p$ reactions is rather small. We divided the distribution in three momentum intervals corresponding on average to a mean path λ of 1 fm, 2 fm and 4 fm. The probability of each momentum interval ($P(p_{K^-})$) is extracted from Fig. 6.13 (b) and listed in Table 6.3. As illustrated in Fig. 6.14 (a) the ϕ cannot exceed a certain path length inside tungsten in order to accommodate a mean free path of $\lambda = 4$ fm for the K^- ($\approx \Delta = d_W - l_\pi - l_\phi$). This criteria reduces the decay probability of the ϕ meson to 7%, which results in a maximal K^- re-scattering probability of $50\% \times 7\% = 3.5\%$ for this specific case. Considering all three scenarios listed in Table 6.3 an estimated overall re-scattering probability of the antikaons stemming from ϕ mesons below 6.4% is extracted.

In summary, the probability that the ϕ decays inside the nucleus is below 13%. If then the scattering of (anti-)kaons is considered maximally 6.4% of the ϕ mesons cannot be reconstructed via in the invariant mass technique. These numbers have been obtain considering the vacuum width of the ϕ meson ($\Gamma_{vac} = 4.3$ MeV).

Indeed, it was shown in Section 6.2.2.2 that the ϕ mesons disappear in nuclear matter by comparing the ϕ/K^- ratio measured in collisions with the heavy target (W) and the lighter target (C). As shown above, this effect cannot be attributed to final state interaction of the daughter particles, K^+ and K^-. Therefore, the disappearance of the ϕ mesons in the heavier target nucleus is a clear

Table 6.3: Elastic scattering mean free path, momentum intervals and corresponding probabilities for the K^-. Probabilities of remaining path (Δ) for the K^- after ϕ decay together with the overall elastic scattering probabilities.

$\lambda^{ES}_{K^-}(\approx \Delta)$ [fm]	p_{K^-} [MeV/c]	$P(p_{K^-})$ [%]	$P(\Delta)$ [%]	$P^{ES}_{K^-}$[%]
1	$0-250$	8	12	<1
2	$250-400$	29	10	2.9
4	$400-600$	50	7	3.5

signature of the inelastic interaction with the nucleons. Besides, assuming a free ϕN absorption cross-section of $\sigma_{\phi N} \approx 10$ mb and a ϕ momentum of $p \approx m$ (i.e. $\beta = 0.7$), one can calculate, in the low density approximation, a collision width of $\Gamma_{inel} = \hbar c \cdot \beta \cdot \sigma_{\phi N} \cdot \rho_0 = 197 \cdot 0.7 \cdot 1.0 \cdot 0.16 = 22.1$ MeV and find out that the inelastic width is much larger ($\Gamma_{inel} \approx 5 \cdot \Gamma_{vac}$). Hence the role of ϕ absorption is expected to be significant.

6.3 Summary of the Inclusive ϕ Production

The inclusive production cross-sections of ϕ mesons in $\pi^- + \mathrm{C}$ and $\pi^- + \mathrm{W}$ collisions at an incident beam momentum of 1.7 GeV/c were obtained within the HADES acceptance. The cross-sections should provide insights in the behavior of ϕ mesons in cold nuclear matter, which is complex and has been debated for decades. The ϕ meson ($s\bar{s}$) strongly couples to kaons and antikaons ($\phi \to K\bar{K}$ with $BR \approx 83\%$ [P$^+$16a]) and chiral effective field theory models predict a substantial modification of the in-medium width and thus reduced life-time, which arise from in-medium modification of kaon loop and direct ϕN coupling [GW15, CHBVV17]. Contrary, the ϕN coupling strength is expected to be suppressed based on the OZI rule [Oku77, Zwe64, Iiz66] hindering processes with disconnected quark lines. The ϕ mesons were reconstruced via their dominant charged decay channel ($\phi \to K^+K^-$ with $BR \approx 48.9\%$ [P$^+$16a]) employing the invariant mass technique. Besides, corrections for the reconstruction efficiency as a function of $p_T - y$ ($p - \theta$) within the HADES acceptance were evaluated and a strong dependence on the ϕ kinematics was found. Since the limited statistics does not allow for a double-differential analysis, each ϕ candidate was weighted with its corresponding correction factor and an integrated K^+K^- invariant mass spectrum was built. The same fitting procedure employed for the uncorrected K^+K^- invariant mass distribution to extract the raw ϕ yields was applied also to the corrected spectra. After the correction for the branching ratio and the applied absolute normalization the integrated differential ϕ production cross-sections ($\Delta\sigma$) within the HADES acceptance ($0.4 \leq y < 1.0$ and $150 \leq p_T < 650$ MeV/c) for $\pi^- + \mathrm{C}$ and $\pi^- + \mathrm{W}$ collisions were extracted and are summarized in Table 6.2.

In Section 6.2.2 the ϕ absorption, hence the ϕN coupling strength, was investigated by comparing the inclusive ϕ production off heavy and light nuclei in terms of the transparency ratio. Since the variation of the ϕ production cross-section with atomic number A depends on the attenuation of the flux in a nuclear target which is related to the in-medium width. The extracted ϕ transparency ratio of $\approx 18\%$ is lower than observed by ANKE [P$^+$11] and CLAS [W$^+$10] measurements in $p+A$ and $\gamma+A$ reactions, respectively. With the help of theoretical models the results by ANKE point to an effective ϕN absorption cross-section of $14-21$ mb [H$^+$12], compatible with $\sigma_{\phi N} = 16-17$ mb based on the results by CLAS [W$^+$10]. In addition, the momentum-dependent ϕ production

cross-section and transperancy ratio was evaluated and compared to a first collision model [Par18]. Neither based on the production cross-section nor the transparency ratio a conclusive picture on the ϕ absorption could be drawn, which may partly be caused by the low ϕ statistics. However, the interpretation of the transparency ratio is rather model-dependent.
Therefore, a direct indication of ϕ absorption inside the nuclear medium was extracted from the comparison of the ϕ/K^- ratio measured in collisions with the heavy target (W) and the lighter target (C). In the ratio the K^- serves as reference particle for the strange hadron absorption due to the observed strong absorption (Section 5.2.5). The measured ϕ/K^- ratios in $\pi^- + \mathrm{C}$ and $\pi^- + \mathrm{W}$ reactions within the HADES acceptance are found to be equal to $0.55 \pm 0.04(\mathrm{stat})^{+0.06}_{-0.07}(\mathrm{syst})$ and to $0.63 \pm 0.06(\mathrm{stat})^{+0.11}_{-0.11}(\mathrm{syst})$, respectively. The similar ratios measured in the two different reactions point to a non-negligible ϕ absorption. Furthermore, it was found that the final-state interactions of the decay products, K^+ and K^-, cannot account for the observed ϕ absorption. This first measurement of kaons and ϕ in the same reactions provides experimental evidence of the strong coupling between the ϕ and K^- dynamics within nuclear matter with direct consequences for an improved description of heavy-ion collisions and the equation-of-state of neutron stars.

7 Summary and Outlook

The properties of hadrons immersed in a strongly interacting environment have been intensively studied in recent decades. Several experiments have investigated the effects of nuclear matter in heavy-ion collisions (HIC), where densities of up to $2-3\,\rho_0$ at moderate temperatures can be reached. Since HICs are highly dynamic processes that make it difficult to address fundamental aspects directly, all observations are interpreted in a model dependent. Such effects are already expected in normal nuclear densities ρ_0, which can be investigated in hadron-nucleus reactions where the dynamics are less complex as they do not undergo such a large density and temperature evolution. The study of the hadron properties and hence their interaction in nuclear reactions is in particular relevant, since they are the key ingredient of the equation-of-state, which describes dense matter or even macroscopic phenomena like neutron stars (up to $8\,\rho_0$) and neutron star merger. Pion-nucleus reactions are in particular suitable for the detailed studies of hadrons in-medium properties. Due to the large πN inelastic cross-section ($\sigma_{\pi N} = 35$ mb) and therefore small mean free path ($\lambda_\pi = 1.8$ fm), (strange) meson production occurs close to the upstream surface of the nucleus [A$^+$73, B$^+$09c], leading on average to a longer path of the produced (strange) mesons inside nuclear matter. Moreover, due the (rather) large production cross-section of (strange) meson, secondary processes contribute less. For this purpose, the production and properties of $\pi^\pm$, $K^\pm$ and ϕ meson in cold nuclear matter generated in $\pi^- + \mathrm{C}$ and $\pi^- + \mathrm{W}$ reactions at an incident beam momentum of 1.7 GeV/c measured with HADES at SIS18/GSI was investigated in this work.

First, the (double-)differential distributions of both charged pions ($\pi^\pm$) were extracted and investigated in both collisions systems and in two-sets of kinematic variables ($p_T - y$, $p - \theta$) (Chapter 4). Strong scattering effects for both pions in heavier target (W) were observed as the rapidity density distributions dN/dy are shifted to backward rapidity with respect to the ones in the lighter target (C) (Section 4.2.2). Moreover, the integrated differential inelastic production cross-section ($\Delta\sigma$) for π^+ ($0 \leq y < 1.9(1.8)$) and π^- ($0.1 \leq y < 1.9$) inside the HADES acceptance in both collision systems was obtained (Table 4.2). The comprehensive experimental campaign performed by the HARP Collaboration [A$^+$09d] could be extended to lower incident pion beam momentum (1.7 GeV/c). Thereby, a significant dependence on the incoming beam momentum was found, which is stronger for the positively charged pions (Section 4.2.4). The comparison of three state-of-the-art transport models (GiBUU [BGG$^+$12], UrQMD [B$^+$99b] and SMASH [W$^+$16]) to the presented results, however, demonstrated that (currently) there is no satisfactory theoretical description of the (double-)differential charged pion cross-sections in pion-nucleus reactions (Section 4.2.5). While, the inclusive cross-section agrees rather well with GiBUU predictions for both charged pions in the lighter nucleus (C) pointing to correctly implemented elementary πN cross-section for the inelastic charged pion production channels, the description of (especially) scattering effects seems insufficient as the predictions deviate for the heavier target (W) as well as for the (quasi-)elastically scattered π^-. The backward scattering in the heavier nucleus (W) is reproduced by all three models. However, the contribution of the resonances decaying into charged pions and thus the branching ratios have to be re-tuned in UrQMD and SMASH.

Hence, the presented results can serve a reference of transport model calculations improving the interpretation of heavy-ion collisions in the few GeV energy range. In the context of astroparticle physics experiments, they can be used as ingriendient for calculations of the atmospheric neutrino flux [Bat01] and of the accelerator neutrino flux [BG06].

In addition, a (double-)differential analysis of charge (anti-)kaons (K^+, K^-) in π^-+C and π^-+W collisions was conducted for both sets of kinematic variables, $p_T - y$ and $p - \theta$ (Section 5.1.1). The rapidity density distributions were retrieved (Section 5.2.2) and revealed, that similar to the charged pions, (elastic) scattering shifts the K^+ distribution to target rapidity in the heavy target (W). On the contrary, the shape of the K^- is symmetric and comparable for both nuclear environments. For the antikaons not scattering effects, but absorption processes (e.g. $K^-N \to Y\pi$) are dominant. Furthermore, the integrated differential production cross-section ($\Delta\sigma$) for K^+ ($0 \leq y < 1.1$) and K^- ($0.2 \leq y < 1.0$) in π^-+C and π^-+W reactions inside the HADES acceptance was extracted (Table 5.3). For the kaons, the in-medium KN potential is of particular interest. Various experiments [B$^+$04, B$^+$09c, A$^+$10a, A$^+$14d] strongly support the existence of a repulsive in-medium KN potential of about $20 - 40$ MeV. In the comparision to the same three transport models, none is able to describe the experimental K^+ kinematic distributions (Section 5.2.4.1). In contrast to GiBUU, neither UrQMD nor SMASH contain mean-field NN potentials as well as in-medium KN potentials. As a detailed tuning of the elementary K^+ cross-sections would be needed, no conclusion about the presence of the in-medium KN potential could be drawn. In addition, the ratio of the inclusive kaon production cross-section $R(\sigma_A^K/\sigma_C^K)$, which is expected to be particularly sensitive to the effects of the KN potential, was compared to earlier measurements and predictions from GiBUU (Section 5.2.4.2). A similar trend of the ratio can be observed in comparison to the K^0 production cross-section ratio of FOPI [B$^+$09c] and the K^+ ratios of ANKE [B$^+$04]. Moreover, a better agreement with GiBUU including a in-medium ChPT KN potential is observed. For the K^- absorption processes are dominating. A direct indication of absorption was extracted from the comparison of the K^-/K^+ ratio measured in both nuclear environments (Section 5.2.5.2). In the double ratio $(K^-/K^+)_\mathrm{W}/(K^-/K^+)_\mathrm{C}$ the K^+ serves as a reference particle for the strange hadron production due to its very small absorption cross-section [D$^+$75]. Indeed, the measured double ratio of $(K^-/K^+)_\mathrm{W}/(K^-/K^+)_\mathrm{C} = 0.319 \pm 0.009(\mathrm{stat})^{+0.014}_{-0.012}(\mathrm{syst})$ is far below the expected (anti-)kaon production reference based on elementary πN reactions (Section 5.2.5.1), directly indicating a sizable K^- absorption in heavy nuclei (W) with respect to light nuclei (C). The predictions for K^- in GiBUU are promising, whereas UrQMD significantly overestimates the experimental cross-sections. SMASH is able to reproduce the K^- cross-section in the heavier system (W), although it underestimates the production off carbon as demonstrated in Section 5.2.5.3. The strong K^- absorption within nuclear matter has not only direct consequences for an improved description of heavy-ion collisions, but also for the equation-of-state of neutron stars in terms of kaon condensates star and in connection to hyperon stars.

In this context, also the ϕ production and absorption off light and heavy nuclear targets is of particular interest. On this account, the inclusive production cross-sections of ϕ mesons should provide insights in the behavior of ϕ mesons in cold nuclear matter, which is complex and has been debated for decades. The ϕ meson ($s\bar{s}$) strongly couples to kaons and antikaons ($\phi \to K\bar{K}$ with $BR \approx 83\%$ [P$^+$16a]). Hence, chiral effective field theory models predict a substantial modification of the in-medium width, which arise from in-medium modification of kaon loop and direct ϕN coupling [GW15, CHBVV17]. Contrary, according to the OZI rule [Oku77, Zwe64, Iiz66], which hinders processes with disconnected quark lines, the ϕN coupling strength is expected to be suppressed. The ϕ mesons were reconstruced via their dominant charged decay channel ($\phi \to K^+K^-$ with $BR \approx 48.9\%$ [P$^+$16a]) employing the invariant mass technique (Section 6.1).

After the correction for the branching ratio and the applied absolute normalization the integrated differential ϕ production cross-sections ($\Delta\sigma$) within the HADES acceptance ($0.4 \leq y < 1.0$ and $150 \leq p_T < 650$ MeV/c) for $\pi^- + \mathrm{C}$ and $\pi^- + \mathrm{W}$ collisions were extracted and are summarized in Table 6.2. Whereby, the ϕ production cross-sections off heavy and light nuclei normalized to the mass numbers are compared to each other in terms of the transparency ratio (Section 6.2.2.1). The latter is expected to increase with increasing nucleus size, due the effect of the ϕN coupling. The extracted ϕ transparency ratio of $T(\sigma^{\phi}_{\mathrm{W}}/\sigma^{\phi}_{\mathrm{C}}) = 0.18 \pm 0.02(\mathrm{stat}) \pm 0.01(\mathrm{syst})^{+0.04}_{-0.03}(\mathrm{norm})$ is lower than observed by ANKE [P$^+$11] and CLAS [W$^+$10] measurements. Theoretical models allowed to extract the effective ϕN absorption cross-section, which is found to be $14 - 21$ mb on the basis of the ANKE results [H$^+$12], compatible with $\sigma_{\phi N} = 16 - 17$ mb based on the results by CLAS [W$^+$10]. In addition, a direct indication of ϕ absorption with nuclear matter was extracted from the comparison of the ϕ/K^- ratio measured in collisions with the heavy target (W) and the lighter target (C). Here, the K^- serves as reference particle for the strange hadron absorption due to the observed strong K^- absorption. The measured ϕ/K^- ratios in $\pi^- + \mathrm{C}$ and $\pi^- + \mathrm{W}$ reactions within the HADES acceptance are found to be equal to $0.55 \pm 0.04(\mathrm{stat})^{+0.06}_{-0.07}(\mathrm{syst})$ and to $0.63 \pm 0.06(\mathrm{stat})^{+0.11}_{-0.11}(\mathrm{syst})$, respectively. The similar ratios measured in the two different reactions point to a non-negligible ϕ absorption. The experimental evidence of the strong coupling between the ϕ and K^- dynamics within nuclear matter is relevant to provide more realistic EoS of dense nuclear matter with hyperon content, in heavy-ion collisions, but possibly also in neutron stars. Since, the ϕ meson can act as mediator of hyperon-hyperon interactions.

In general, the presented kinematic distributions for the comprehensive meson set (π^+, π^-, K^+ and K^-) in comparison to the state-of-the-art transport models showed larger deviations. As these models are often used for interpretation of heavy-ion collision data an adjustment of these models becomes crucial. The presented results, published in [AM$^+$19b], highly contribute to understanding of K^- and particularly ϕ in-medium behavior in the context of the strong interaction. Due to the uniqueness of the pion-induced reactions with their large inelastic cross-section, which lead to hadron production near the surface, in-medium effects are expected to be more significant. The simultaneous measurement of K^+, K^- and ϕ opened up the possibility to extract and interpret particle ratios off light and heavy nuclei, which in fact showed for the first time a strong ϕN in-medium coupling without (any) model assumptions. The latter effect has a significant influence on our understanding and interpretation of ϕ mesons as probes in heavy-ion reactions.

Future experiments with pion-nucleus collisions with higher statistics of ϕ mesons may provide (double-)differential ϕ cross-sections and thus allow further investigation of the ϕN in-medium coupling. In fact, the upgrade of the RICH detector [M$^+$17] provides an improved single photo electron detection efficiency, which may allow to study the ϕ meson via the e^+e^- decay channel. Therefore, complementary information about the in-medium behavior of ϕ meson will be obtained. In addition, new measurements would make it possible to investigate the dependence of meson absorption on the mass number A and on the momentum for the K^- and ϕ meson. However, in current beam-time proposal of HADES for 2021, the beam momentum is below the ϕ production threshold.

A Appendix to Primary Vertex

The current analysis framework of the HADES experiment, HYDRA2, provides a primary vertex reconstruction methods, which requires at least two fully tracked particles (t=2) in all MDC chambers in combination with a matching hit in the META. Single track events (t=1) were also considered in the analysis and in these cases the primary vertex was reconstructed by the distance of closest approach (DCA). This allowed to obtain the primary vertex for at least one fully reconstructed charged particle. All primary vertex distribution are shown below and the obtained resolutions are listed in Table A.1.

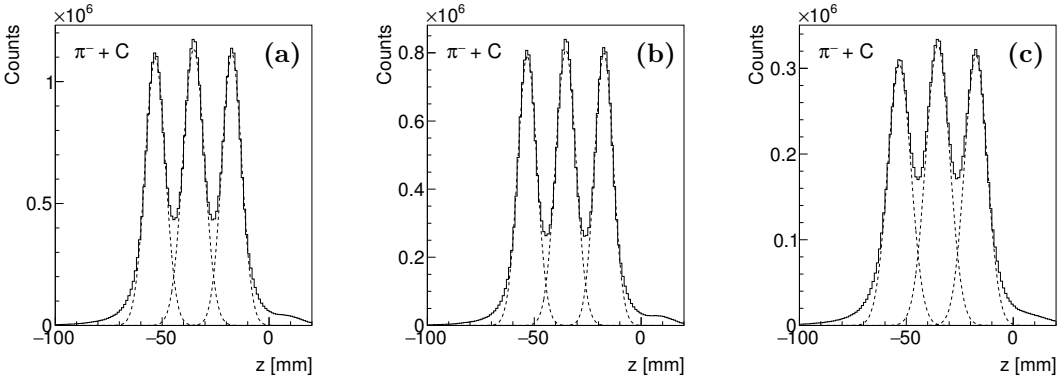

Figure A.1: Primary vertex distribution in z-direction in $\pi^- + \mathrm{C}$ reactions for at least one fully reconstructed charged particle (a), for at least two fully reconstructed charged particles (b) and for single track events (c).

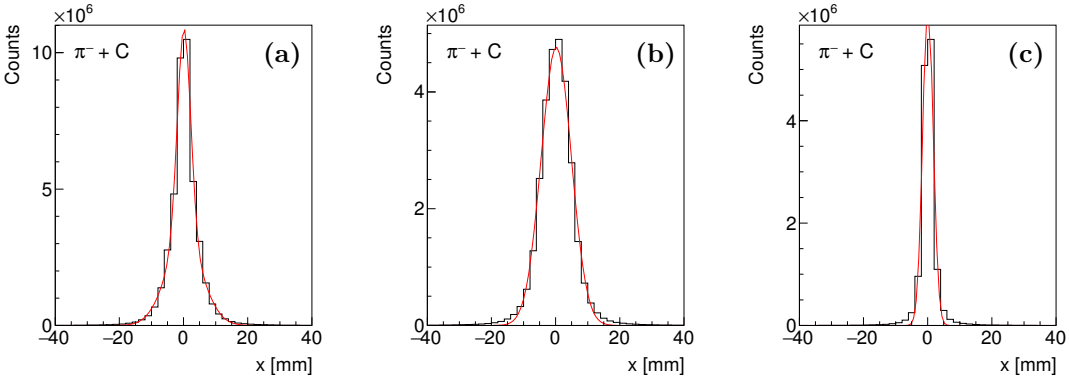

Figure A.2: Primary vertex distribution in x-direction in $\pi^- + \mathrm{C}$ reactions for at least one fully reconstructed charged particles (a), for at least two fully reconstructed charged particle (b) and for single track events (c).

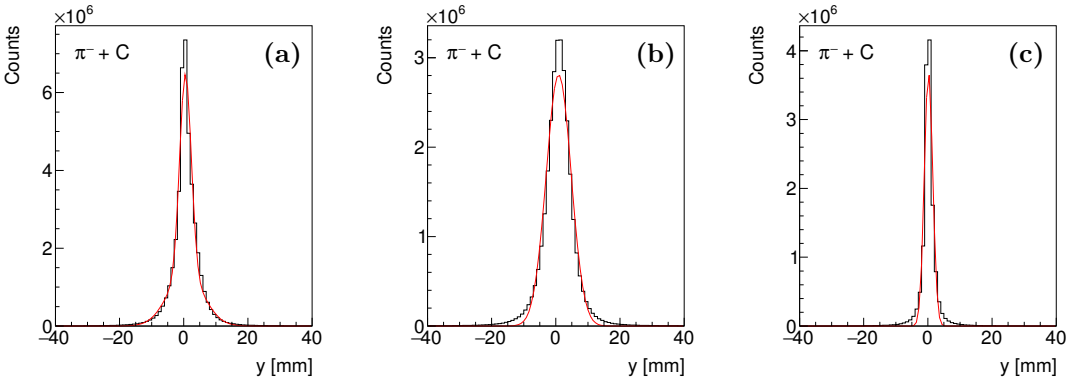

Figure A.3: Primary vertex distribution in y-direction in $\pi^- + \mathrm{C}$ reactions for at least one fully reconstructed charged particle (a), for at least two fully reconstructed charged particles (b) and for single track events (c).

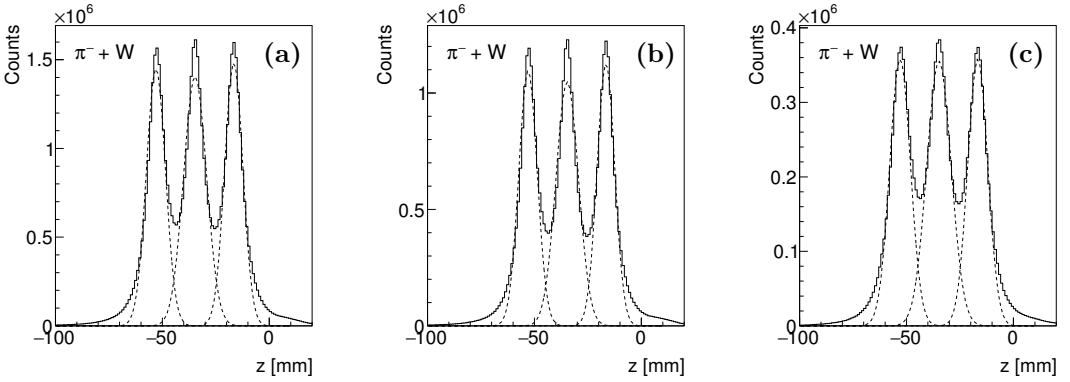

Figure A.4: Primary vertex distribution in z-direction in $\pi^- + \mathrm{W}$ reactions for at least one fully reconstructed charged particles (a), for at least two fully reconstructed charged particle (b) and for single track events (c).

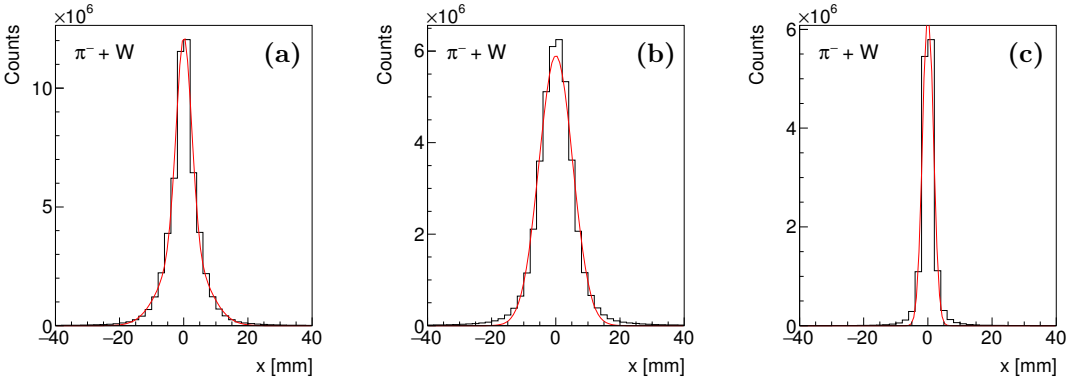

Figure A.5: Primary vertex distribution in x-direction in $\pi^- + \mathrm{W}$ reactions for at least one fully reconstructed charged particles (a), for at least two fully reconstructed charged particle (b) and for single track events (c).

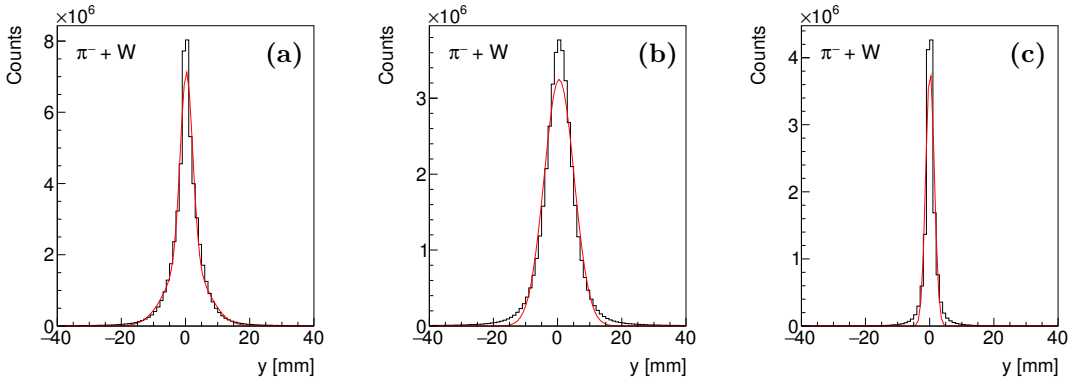

Figure A.6: Primary vertex distribution in y-direction in $\pi^- + \mathrm{W}$ reactions for at least one fully reconstructed charged particles (a), for at least two fully reconstructed charged particle (b) and for single track events (c).

Table A.1: Primary vertex resolution in z-, x- and y-direction for single track events ($t = 1$), for at least one ($t \geq 1$) and two ($t \geq 2$) fully reconstructed charged particle for both collision systems.

	$\sigma_{z_{PV}}$ [mm]			$\sigma_{x_{PV}}$ [mm]			$\sigma_{y_{PV}}$ [mm]		
	$t = 1$	$t \geq 1$	$t \geq 2$	$t = 1$	$t \geq 1$	$t \geq 2$	$t = 1$	$t \geq 1$	$t \geq 2$
C	5.4	4.7	4.5	1.6	3.1	4.7	1.3	2.6	3.9
W	5.1	4.7	4.6	1.6	3.5	5.2	1.3	3.0	4.7

B Appendix to Normalization

Another method to obtain the absolute normalization and hence the production cross-section of the reconstructed particles is based on the reaction cross-section σ_A^R and the number of events N_A^{evt}, as shown in Eq. (B.1). In the case of the pion-induced reaction at 1.7 GeV/c, the reaction cross-section σ_A^R can be evaluated with measurements of [A$^+$73].

$$\sigma_A^P = \frac{N_A^P \, \sigma_A^R}{N_A^{evt}}, \tag{B.1}$$

with

σ_A^P/N_A^P : cross-section and abundance of the particle of interest
σ_A^R : the total cross-section for pion-induced reactions
N_A^{evt} : number of events
A : mass number of the target nucleus

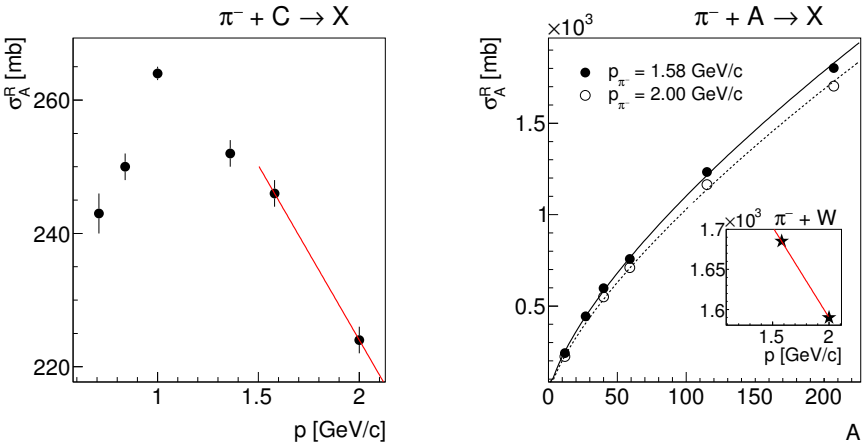

Figure B.1: Left: Reaction cross-section σ_A^R as a function of incident pion momentum for $\pi^- + \mathrm{C}$ reactions taken from [A$^+$73]. Right: Reaction cross-section σ_A^R as a function the mass number A of the target nucleus for two different incident pion momentum, 1.58 GeV/c (solid points) and 2 GeV/c (open points). Both black curves indicate a power law functions. Inset: Reaction cross-section σ_A^R as a function of incident pion momentum for $\pi^- + \mathrm{W}$ reactions exraoplated from measurements of [A$^+$73]. For details see text.

As shown in Fig. B.1 (left), the existing data points for $\pi^- + \mathrm{C}$ reactions at 1.58 GeV/c and 2 GeV/c were linearly interpolated to obtain the total cross-section at 1.7 GeV/c. Since no data are available for the heavy target (W), a power law function taken from [A$^+$73] ($\sigma_A^R = \; C \; A^n$, where A is the mass number) was used for the Sn and Pb target at 1.58 GeV/c and 2 GeV/c, respectively. Fig. B.1 (right) represents the corresponding data points and power law functions.

In this way, the so obtained total cross-section for the W target at 1.58 GeV/c and 2 GeV/c could be interpolated to deduce the total cross-section at 1.7 GeV/c as presented in Fig. B.1 right inset. A total cross-section in π^--induced reaction at 1.7 GeV/c of 239.7 mb for the light target (C) and 1657.9 mb for the heavy target (W) was extracted.

In order to compare the (standard) normalization method based on the beam particle multiplicity evaluated with the help of the target T_0 detector (Section 3.4) with the absolute normalization based on the reaction cross-section, the kaon production cross-section ratio $R(\sigma_A^K/\sigma_C^K)$ (Eq. (B.2)) evaluated on the basis of both normalization methods was investigated.

$$R(\sigma_A^K/\sigma_C^K) := \frac{\sigma_A^K}{\sigma_C^K} = \frac{N_A^K\ \sigma_A^R\ N_C^{evt}}{N_C^K\ \sigma_C^R\ N_A^{evt}}, \tag{B.2}$$

with

$$\sigma_A^K/N_A^K : \quad \text{kaon cross-section and number of reconstructed kaons}$$

The ratio of the inclusive K^+ production cross-section $R(\sigma_A^K/\sigma_C^K)$ measured in collisions with heavy targets (W) to lighter targets (C) as a function of the kaon momentum (Section 5.2.4.2), is shown in Fig. B.2 (red circles/stars). The red full circles are extracted based on the standard normalization method (Section 3.4), while the red full stars are obtained on the basis of the total reaction cross-section. Within the errors, both methods are equivalent in terms of ratio. Indeed, the comparable ratios on the basis of both normalization method indicate that the normalization uncertainty presented in Fig. B.2 are an conservative estimate as most contributions to error are expected to cancel in the ratio.

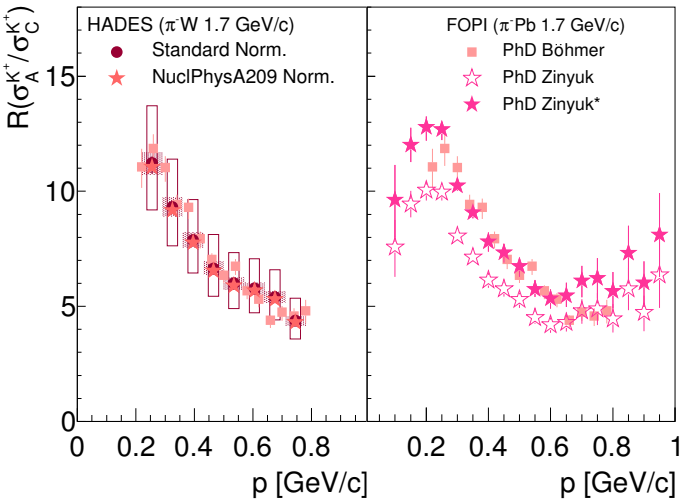

Figure B.2: Ratio of inclusive K^+ cross-sections produced by pions on heavy and light targets as a function of the kaon momentum. The red full circles (stars) resembles the ratio of K^+ in this work. The statistical errrors are smaller than the symbol size. The systematic and normalization uncertainties are given by the hased areas and open boxes, respectively. The latter uncertainties are only given for the standard normalization method. The pink full squares depict the ratio of K^+ produced on Pb and C targets measured by FOPI at an beam momentum of 1.7 GeV/c [Boe15] . While, the pink full (open) stars show as well the ratio of K^+ measured by FOPI taken from a different analysis [Zin16]. For details see text.

Besides, one can compare the results with the measurement of FOPI [Boe15] in π-induced reactions on a Pb target at 1.7 GeV/c represented by the pink full squares in Fig. B.2. Here the absolute normalization is based on the reaction cross-section. The observation of FOPI and HADES is compatible. Another independent analysis of the corresponding FOPI data [Zin16] is presented by the pink open stars in Fig. B.2. Both FOPI analyses differ from each other. However, it can be shown that the deviations result exclusively from the applied absolute normalization method. In the later analysis, the geometrical cross-section was used instead of the reactionl cross-section σ_A^R [A$^+$73]. If an absolute normalization based on the reaction cross-section (σ_A^R) is also applied to the latter FOPI analysis (pink full stars in Fig. B.2), both FOPI analyses agree over almost the entire momentum range.
In summary, a further normalization method based on the total reaction cross-section was introduced in pion-induced reactions at 1.7 GeV/c and within errors both methods are equivalent. In addition, our observed ratios are consistent with the FOPI measurement, although their measurement was performed with a slightly larger heavy target nucleus (Pb).

C Appendix to Minimum Bias

The META system consisting of the two time-of-flight detectors, RPC and TOF, determines the event multiplicity M. The first level trigger (LVL1) (Section 2.2.9) rejects all events that do not exceed the predefined event multiplicity. In the $\pi^- + A$ run the minimum charged particle multiplicity $M \geq 2$ ($M2$) (Section 2.2.9) had to be fulfilled resulting in an subset of selected events compared to the minimum bias events ($M0$). Such a selection may also lead to a selection of more central events, since the particle multiplicity is expected to increase due to a higher change of secondary particle production.

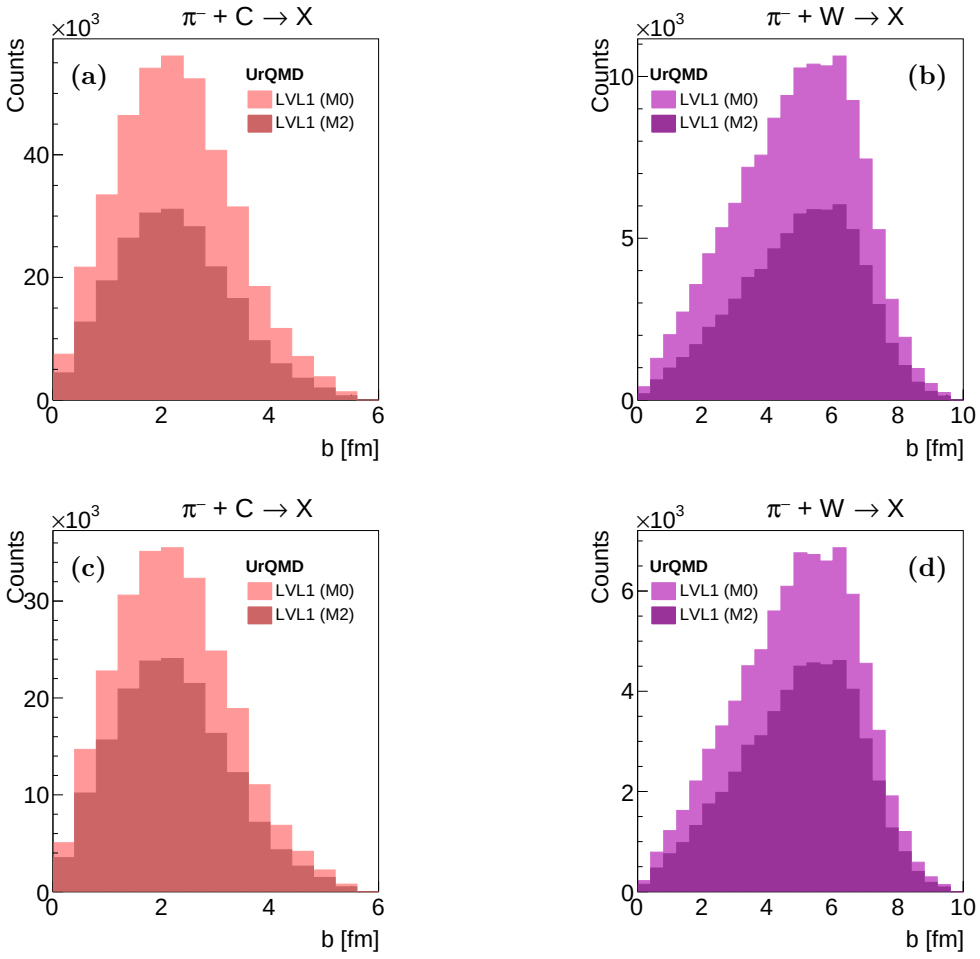

Figure C.1: Impact parameter distribution for minimum bias and LVL1 events for $\pi^- + \mathrm{C}$ (a,c) and $\pi^- + \mathrm{W}$ (b,d) collisions and with (a,b) and without (c,d) event selection based on UrQMD simulations.

In order to investigated in detail the influence of the trigger condition, UrQMD simulations with varying impact parameter b have been carried out and propagated through HGeant (Section 3.6.2)

and the whole reconstruction chain (Section 3.6). Figure C.1 shows the corresponding impact parameter distributions for two scenarios, the $M2$ and $M0$ trigger condition, in π^-+C (Fig. C.1 (a), Fig. C.1 (c)) and π^- + W (Fig. C.1 (b), Fig. C.1 (d)) collisions. The upper panels correspond to all events, whereas for the lower panels the event selection of Sections 3.1 and 3.2 has been applied. It can be seen for all cases that the $M2$ conditions does not introduce a selection of more central events, since in pion-induced reactions are dominated by primary reactions.

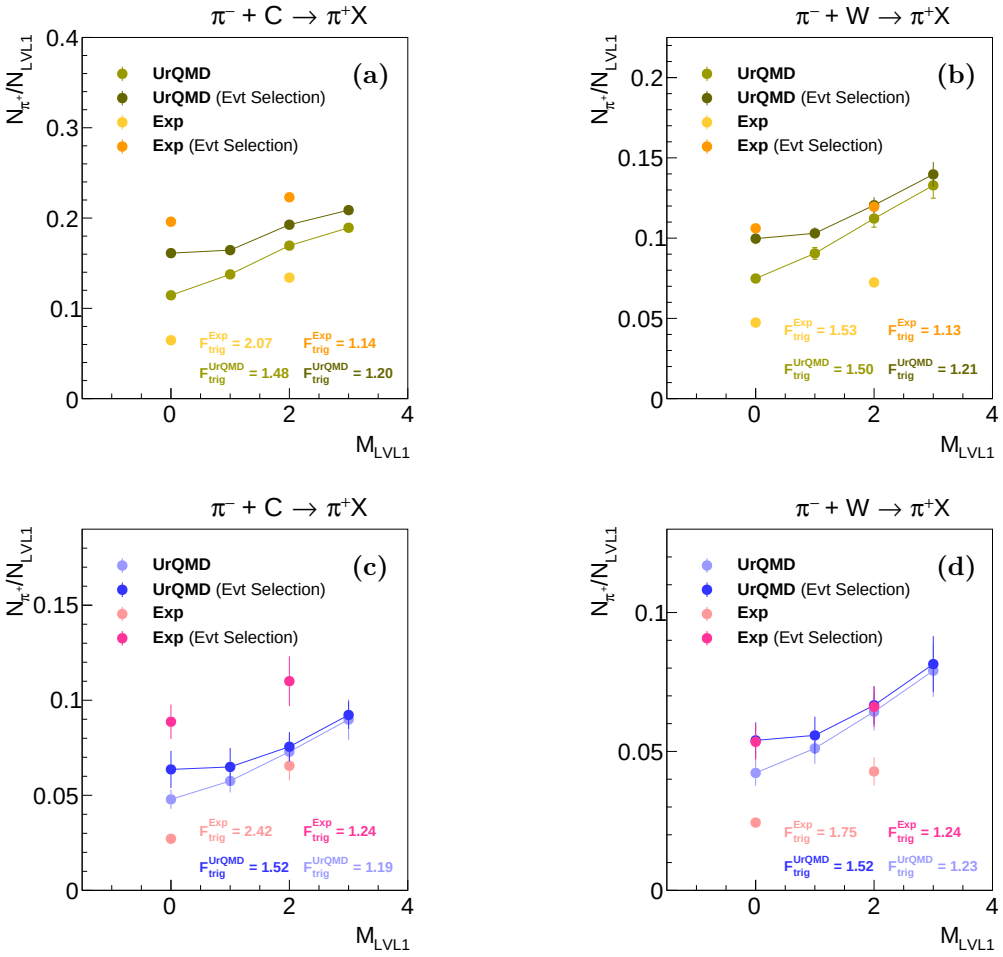

Figure C.2: Multiplicity dependence of positively charged pions on the selected trigger condition separately for π^- + C (a,c) and π^- + W (b,d) reactions. Both for experimental data (orange/pink points) and UrQMD simulations (green/blue points) based on two pion identification methods, β vs. momentum cut (a,b) and mass spectra (c,d). For details see text.

Nevertheless, the trigger condition influences the particle multiplicities as illustrated in Fig. C.2 for positively charged pions. The positively charged pion produced in $\pi^- + A$ reactions were identified based on two methods. In the following it has not been distinguished between the two time-of-flight detector systems, RPC and TOF. The first method is based on a β vs. momentum cut, whereas the second one by fitting the reconstructed mass spectra. For both pion reconstruction methods, the pion multiplicity is increasing with increasing multiplicity of the trigger condition. While on experimental side only two multiplicity classes, $M0$ and $M2$, are available, in the case of UrQMD the two additional multiplicity classes, $M1$ and $M3$, corresponding to minimum charged particle multiplicity of one and three were studied. To obtain the experimental multiplicity dependence

without the biases from background events due to the nature of the secondary pion beam, event selection criteria have to be applied and the raw distribution is just shown for comparison.

The trigger factor associated with trigger conditions $M0$ and $M2$, respectively, are defined as follows:

$$F_{trig} = \frac{N_{\pi^+}/N_{LVL1}(M2)}{N_{\pi^+}/N_{LVL1}(M0)}, \tag{C.1}$$

with

N_{π^+} : number of reconstructed pions
N_{LVL1} : number of selected events
$M2/M0$: trigger decision based on the multiplicity in the META sytem

By considering only the spectra with the applied event selection, one obtains an experimental value of $F_{trig}^{Exp,C} = 1.19 \pm 0.05$ and a value of $F_{trig}^{UrQMD,C} = 1.20 \pm 0.05$ for UrQMD averaged between both pion identification methods in $\pi^- + \mathrm{C}$ reactions. While in $\pi^- + \mathrm{W}$ reactions an experimental value of $F_{trig}^{Exp,W} = 1.19 \pm 0.06$ and a value of $F_{trig}^{UrQMD,W} = 1.22 \pm 0.01$ for UrQMD is extracted. Within errors the trigger factor of the experiment and UrQMD agree. The trigger effects will be included in the correction of the reconstruction efficiency during the analysis chain an thus no additional error for the minimum bias events has to be introduced.

D Appendix to Particle Identification

D.1 Appendix to Time-of-Flight Reconstruction

Charged particles can be identified by means of the correlation between the velocity and momentum information as described in Section 3.3.1. Since the purity of negatively charged pions is high, their particle identification criteria were also applied to the positively charged pions. The two-dimensional selections were calculated separately for the two time-of-flight detector systems, RPC and TOF. For each detector system the distribution was projected in momentum intervals of 36 MeV/c on the velocity axis. As presented in Fig. D.1, the projections are fitted with a Gaussian distribution (blue curve) to extract the mean μ and resolution σ of distribution. To extract starting values for the mean μ and amplitude, the theoretical velocity $\beta_{theo,min}$ of negatively charged pions was calculated based on Eq. (3.2) using the minimal momentum in each momentum slices. The mean μ was set to the corresponding $\beta_{theo,min}$ and the amplitude to height of the β distribution at $\beta_{theo,min}$. The fit range was limited to $\pm 20\%$ around the theoretical velocity $\beta_{theo,av}$ derived from the average momentum.

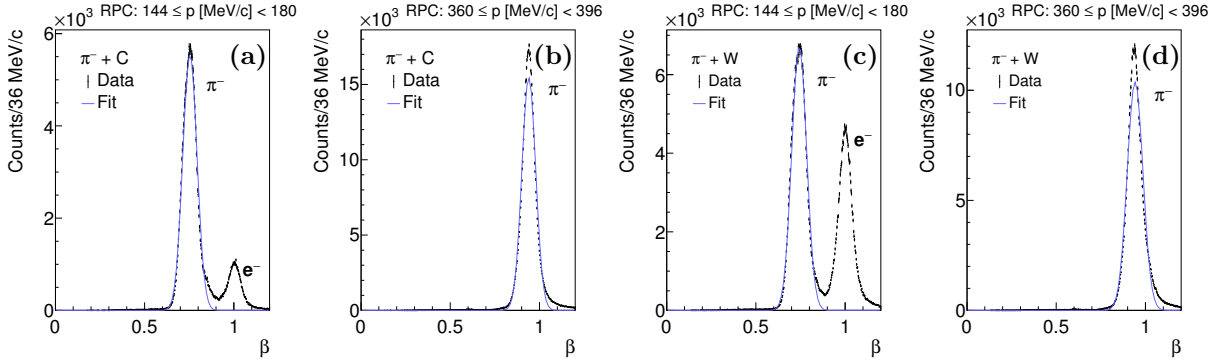

Figure D.1: Projection of the correlation between beta and momentum on the beta-axis for two different slices in momentum (see legend) in the RPC region to systematically extract the two-dimensional selection for pion identification in $\pi^- + \mathrm{C}$ (a,b) and $\pi^- + \mathrm{W}$ (c,d) collisions.

The so obtained mean μ follows with high accuracy the expected theoretical values according to Eq. (3.2), while the resolution of the RPC is better compared to the one of the TOF (Fig. 3.3 (a), Fig. D.2 (a)). As the velocity resolution σ as a function of momentum obtained in $\pi^- + \mathrm{C}$ reactions (Fig. 3.3 (a)) sightly deviates from those in $\pi^- + \mathrm{W}$ reactions (Fig. D.2 (a)), the two-dimensional selections was extracted for both collision systems. The assumption of an underlying Gaussian distribution is not fully justified in the region of low momenta as the distribution has a non-linear relation between β and p. This is the reason the resolution σ as function of momentum p deviates from the monotonic behavior. To overcome this issue the distribution has been fitted with a fourth-order polynominal function (see black dashed curves in Fig. 3.3 (a) and Fig. D.2 (a)) to extrapolated to the low momentum region and the resolution σ obtained from the fits were

further taken. The graphical selections were constructed as 2σ wide bands around the mean values. Fig. 3.4 and Fig. D.3 show the correlation between the velocity and momentum together with the resulting graphical selections used for both charged pions for RPC and TOF in $\pi^- + \mathrm{C}$ and $\pi^- + \mathrm{W}$ collisions, respectively. In order to guarantee that the simulation can be used to correct for the reconstruction efficiency, it is mandatory that both, experimental and simulated data, are treated in the same manner. Since the velocity resolution is not fully reproduced by the simulation (Fig. 3.3 (b) and Fig. D.2 (b)), the same procedure was performed for the simulated data, such that small differences between the resolution of velocity measurement in simulation and experimental data are taken care of and therefore the same pion fraction is selected.

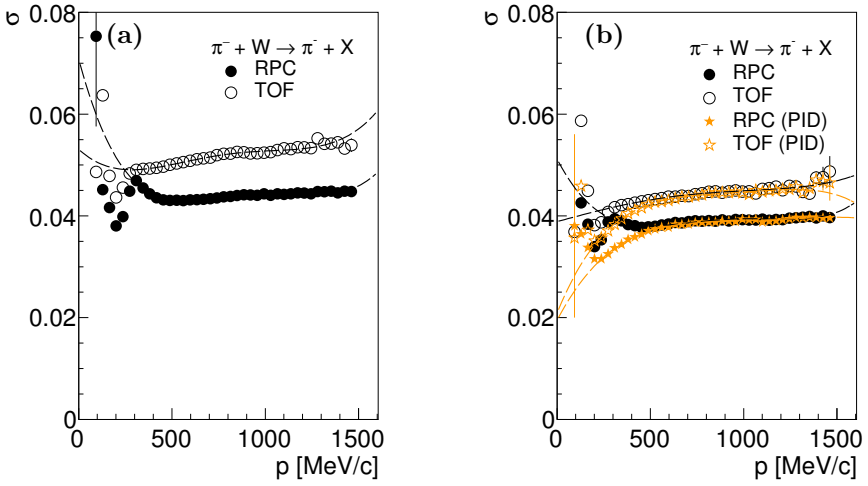

Figure D.2: Velocity resolution as a function of the momentum for negatively charged pions in the two time-of-flight detectors RPC (filed points) and TOF (open points) in $\pi^- + \mathrm{W}$ reactions for experimental data (a) and simulation (b). The stars correspond to the simulation containing only real pions (GEANT PID). The black (yellow) dashed lines correspond to a fourth-order polynominal fit.

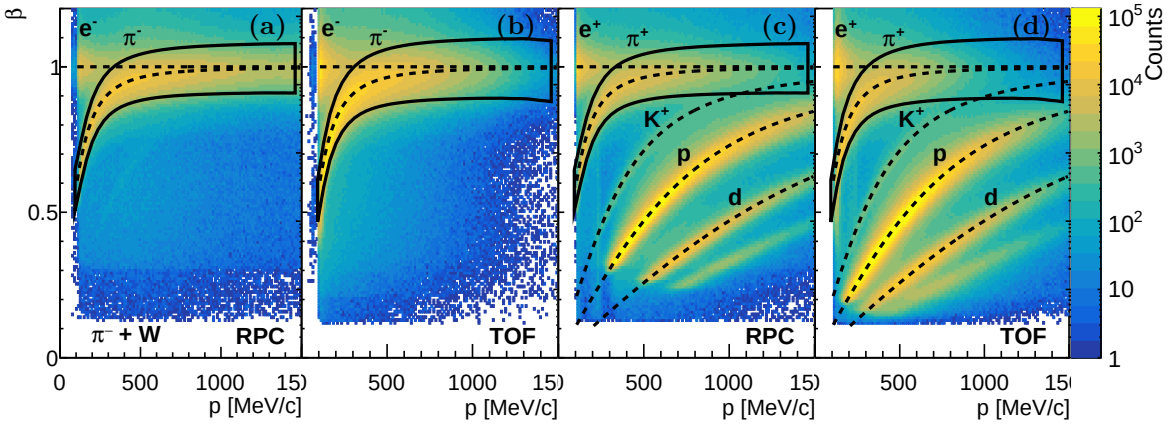

Figure D.3: Correlation between β and momentum for negatively (a,b) and positively (c,d) charged pions for RPC (a,c) and TOF (b,d) in $\pi^- + \mathrm{W}$ reaction. The black dashed lines correspond to the theoretical velocity β. The black solid curves resemble the applied two-dimensional selection.

As the particle identification is an important step of the inclusive pion analysis, which is supposed to select a high purity charged pion sample. Any removal of true charged pions or impurities due to this cut should be accounted for by the efficiency correction. In order to investigate if there are any residual differences between the experimental data and simulation, the systematic effects were investigated by using a broader (smaller) selection of 2.5σ (1.5σ) (Fig. D.4, Fig. D.5, Fig. D.6, Fig. D.7).

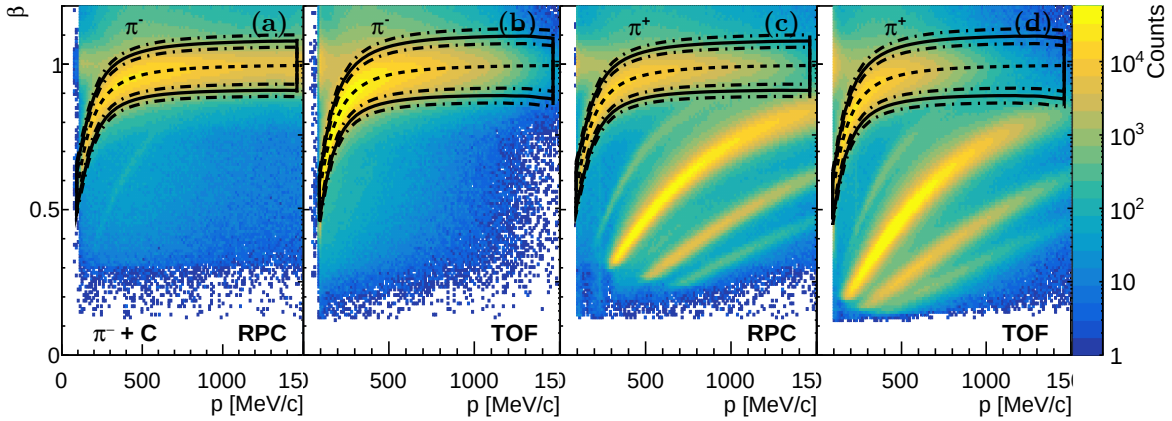

Figure D.4: Correlation between β and momentum for negatively (a,b) and positively (c,d) charged pions for RPC (a,c) and TOF (b,c) in $\pi^- + \mathrm{C}$ reaction. The black dashed lines correspond to the theoretical velocity β. The black curves resemble the applied two-dimensional selection. While the black dashed-dotted curves resemble the systematic variations.

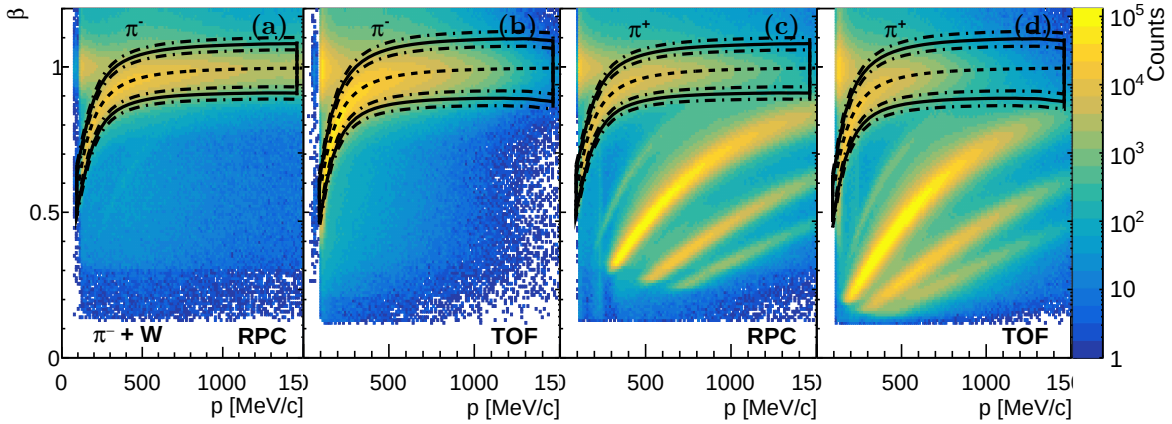

Figure D.5: Correlation between β and momentum for negatively (a,b) and positively (c,d) charged pions for RPC (a,c) and TOF (b,c) in $\pi^- + \mathrm{W}$ reaction. The black dashed lines correspond to the theoretical velocity β. The black curves resemble the applied two-dimensional selection. While the black dashed-dotted curves resemble the systematic variations.

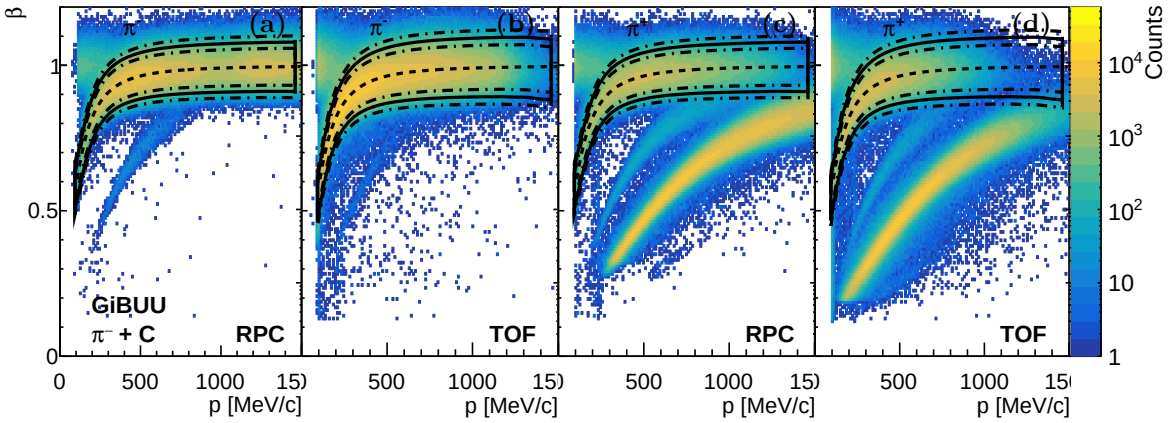

Figure D.6: Correlation between β and momentum for negatively (a,b) and positively (c,d) charged pions for RPC (a,c) and TOF (b,c) in $\pi^- + \mathrm{C}$ reaction for GiBUU based simulations. The black dashed lines correspond to the theoretical velocity β. The black curves resemble the applied two-dimensional selection. While the black dashed-dotted curves resemble the systematic variations.

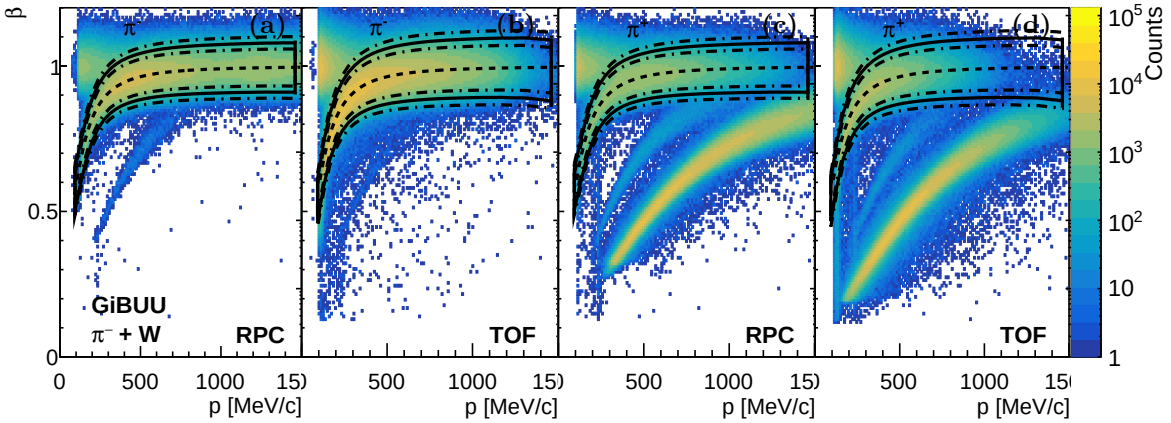

Figure D.7: Correlation between β and momentum for negatively (a,b) and positively (c,d) charged pions for RPC (a,c) and TOF (b,c) in $\pi^- + \mathrm{W}$ reaction for GiBUU based simulations. The black dashed lines correspond to the theoretical velocity β. The black curves resemble the applied two-dimensional selection. While the black dashed-dotted curves resemble the systematic variations.

D.2 Appendix to Specific Energy Loss Measurement

As explained in Section 3.3.2, charged particles can be identified based on the correlation of the specific energy loss in the MDC chambers and reconstructed momentum. The energy loss distribution can be described by a Landau (μ_L, σ_L) that is convoluted with a Gaussian (σ_G) distribution. The Landau function considers the specific energy loss while the Gaussian function represents the finite detector resolution.
Since kaons are less abundant than pions and protons (Fig. 3.6), the kaons have been pre-selected based on the correlation between β and momentum[1] (Fig. 3.2). The resulting correlation of dE/dx and momentum separated for the two different time-of-flight detectors (RPC/TOF) were each divided into momentum slices of 30 MeV/c and projected onto the dE/dx-axis for RPC and TOF. As shown in Fig. D.8 the spectra in different momentum ranges (see legend) of the RPC selection contain varying non-negligible contamination of pions and protons. Thus, dedicated background samples for each (background) particle species on the basis of the correlation between β and momentum were produced and fitted with a convoluted Landau-Gauss function. Following this procedure, initial values for the simultaneous fitting procedure of all three particle species (π^+: red curve, K^+: pink curve, p: yellow curve) were derived to extract the mean value ($\mu_{K^+} = \mu_{L,K^+}$) and the sigma ($\sigma_{K^+} = \sqrt{\sigma^2_{L,K^+} + \sigma^2_{G,K^+}}$) of the energy loss of the kaons for each momentum slice individually. The so obtained mean μ deviates from the theoretical values, whereas the deviation is more pronounced for the TOF detector (Fig. D.9). The kaon energy loss selection indicated by the solid black curve in Fig. 3.7 were constructed around μ_{K^+} with $+4\sigma_{K^+}$ and $-3\sigma_{K^+}$ to take into account the underlying asymmetric distribution (Fig. D.10).

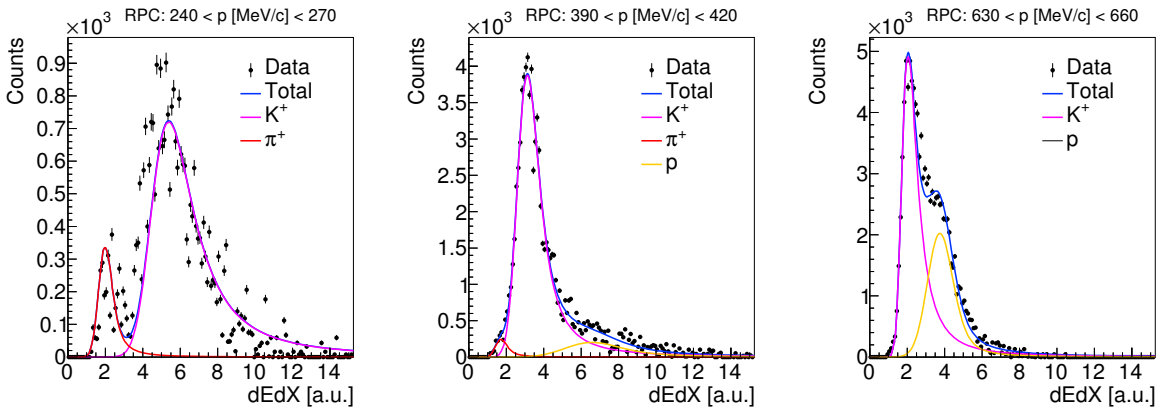

Figure D.8: Projection of the correlation between the specific MDC energy loss and momentum on the dE/dx-axis for three different slices in momentum (see legend) in the RPC region to systematically extract the two-dimensional selection for kaon identification.

For the subsequent detector response/efficiency correction, it is crucial that the simulated data is treated in the same way as the experimental data. Therefore, the selection efficiency of the graphical cuts must be the same for both. Since the energy loss resolution as a function of the momentum is not fully reproduced by the simulation, the same energy loss selection could not be applied to the simulation. Therefore, the same technique of extracting the two-dimensional

1 $p/\sqrt{p^2 + m_0^2}. \pm 0.05 \gtrless \beta_{RPC/TOF}$

energy loss selection was also applied to the simulation to ensure that the same kaon fraction was selected both in the simulation (Fig. D.11) and in the experiment (Fig. D.10). Still, in order to investigate if there are some residual differences between the experimental data and simulation, the investigation of the systematic error also considered the selection around μ_{K^+} in the interval of $+4.5\sigma_{K^+}$ ($+3.5\sigma_{K^+}$) and $-3.5\sigma_{K^+}$ ($-2.5\sigma_{K^+}$) (Fig. D.10, Fig. D.11).

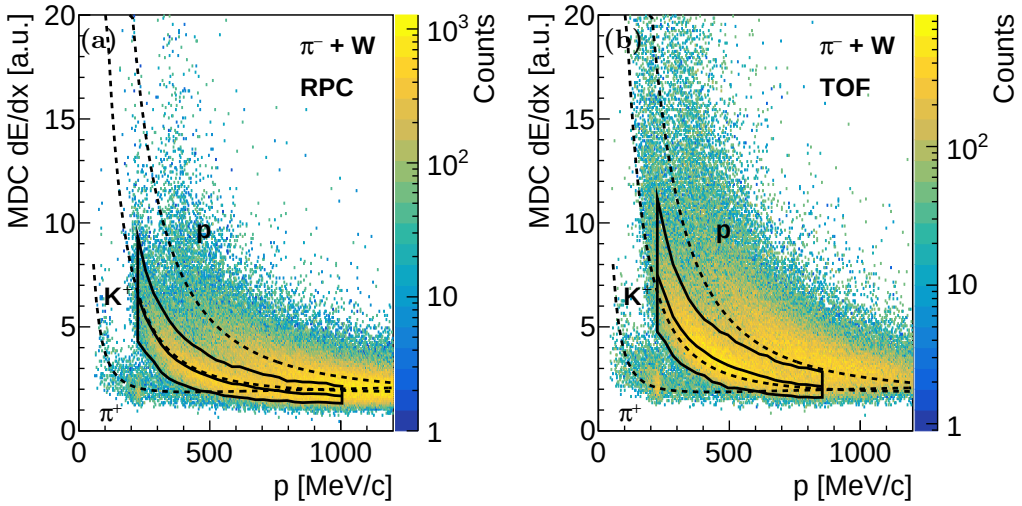

Figure D.9: Energy loss dE/dx in the MDCs as a function of the momentum for the reconstructed positively charged kaon candidates, separately for the two time-of-flight detectors RPC (a) and TOF (b). The contamination from other particle species has been reduced (for details see text). The dashed black lines correspond to the specific energy loss according to the theoretical Bethe-Bloch curves. The solid black line indicates the applied two-dimensional graphical selections for the kaon selection with the mean values indicated by the black curve in between the lower and upper boarder of the two-dimensional graphical selections.

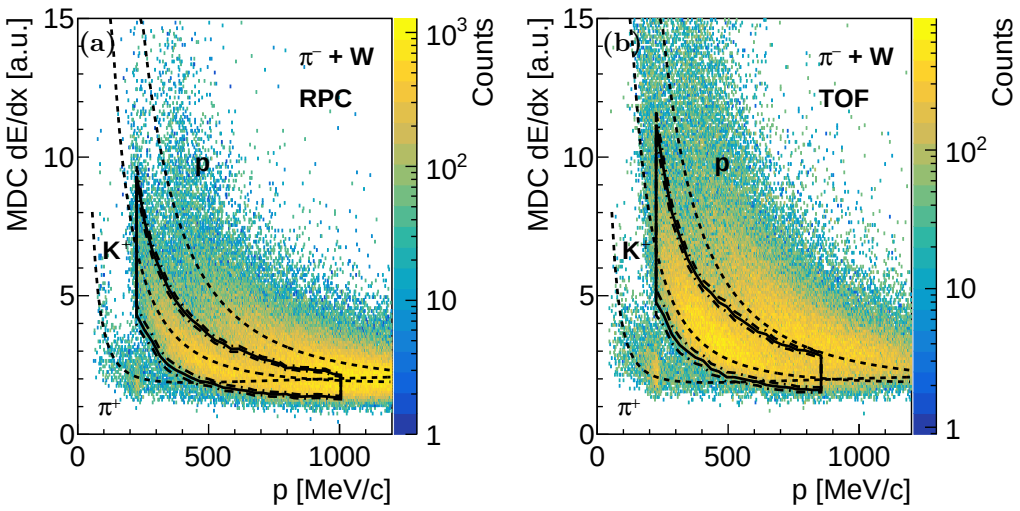

Figure D.10: Energy loss dE/dx in the MDCs as a function of the momentum for the reconstructed positively charged kaon candidates, separately for the two time-of-flight detectors RPC (a) and TOF (b). The contamination from other particle species has been reduced (for details see text). The dashed black lines correspond to the specific energy loss according to the theoretical Bethe-Bloch curves. The solid black line indicates the applied two-dimensional graphical selections for the kaon selection, while the dashed-dotted black lines correspond to the systematic variations.

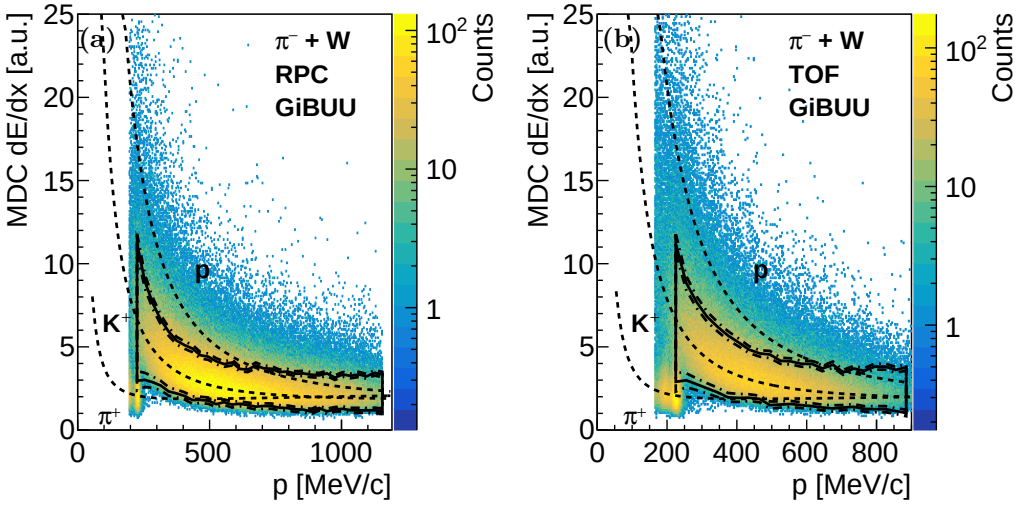

Figure D.11: Energy loss dE/dx in the MDCs vs. momentum for the reconstructed positively charged kaon candidates, separately for RPC (a) and TOF (b) for GiBUU based simulation. The contamination from other particle species has been reduced (for details see text). The dashed black lines correspond to the specific energy loss according to the theoretical Bethe-Bloch curves. The solid black line indicates the applied two-dimensional graphical selections for the kaon selection, while the dashed-dotted black lines correspond to the systematic variations.

E Appendix to Boltzmann Distribution

E.1 Pluto Simulation

To characterize the influence of the Fermi motion of the constitutes of the C nucleus on the K^+ transverse momentum spectra, Pluto simulations [F$^+$07, FGH$^+$10] (Section 3.6.1) have been carried out. The exclusive production channels of $\pi^- + p \to K^+K^-n$ and $\pi^- + p(\mathrm{C}) \to K^+K^-n(\mathrm{B})$ have been considered.

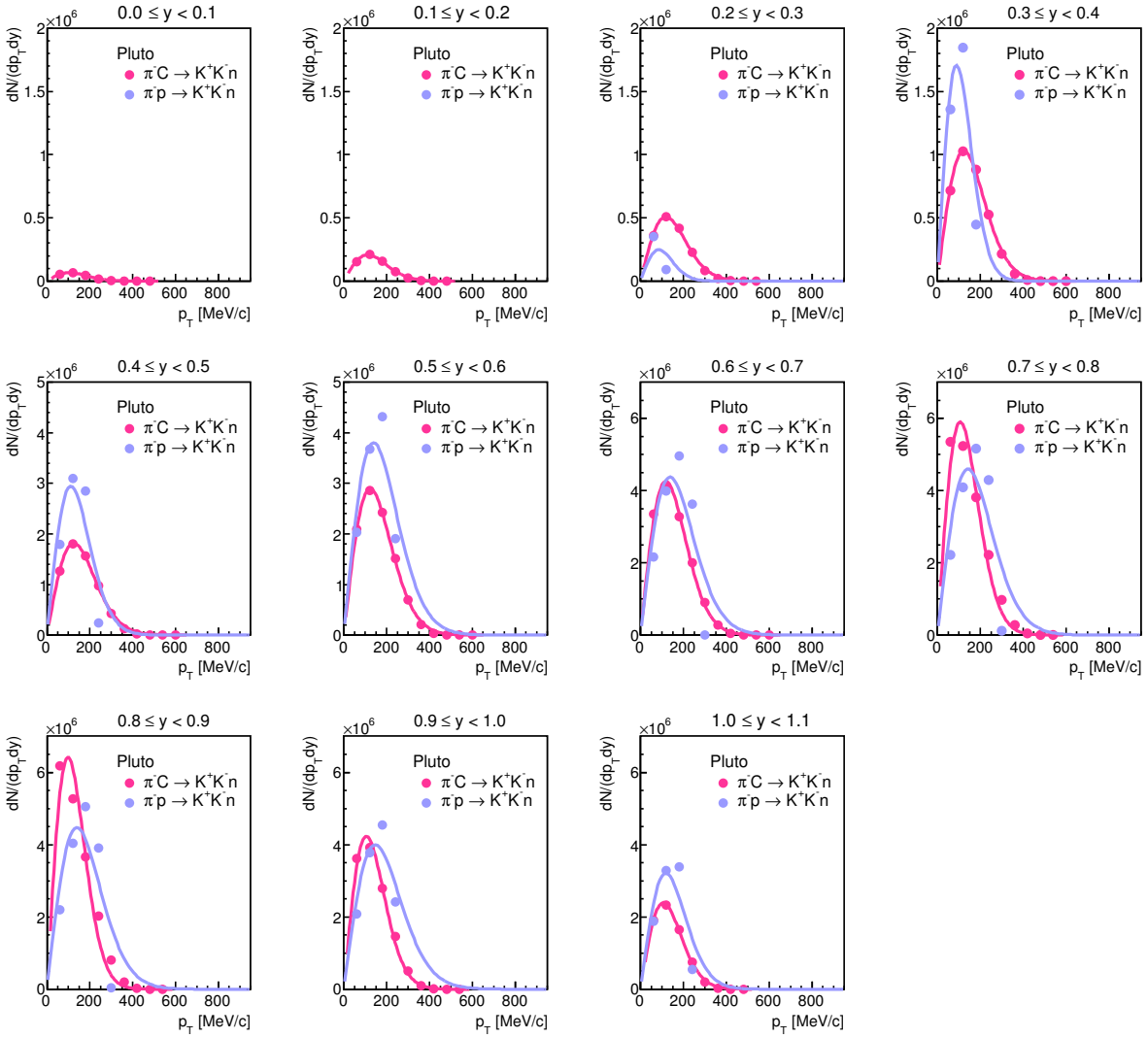

Figure E.1: Transverse momentum spectra of K^+ in $\pi^- + p$ (blue points) and $\pi^- + \mathrm{C}$ (pink points) reactions based on Pluto simulations. The solid lines indicate Boltzmann fits.

To the transverse momentum of both exclusive K^+ production channels a Boltzmann fit has been applied. One can see while in the case of elementary reaction channel ($\pi^- + p \to K^+K^-n$) the Boltzmann fit is not reproducing the simulated shape, this is not the case for the reaction off Carbon. This means, that the Fermi motion smears the distribution mimicking a Boltzmann like behavior.

E.2 Charged Pion Boltzmann Distribution

Based on corrected $p_T - y$ distributions of charged pions extracted in Section 4.1, the rapidity density distribution (dN/dy) can be obtained. For both charged pions, the p_T spectra reflect the yield within the acceptance, which depend on the selected rapidity interval. Figure E.2 shows the p_T distributions of π^+ in different rapidity regions (see legend) for in $\pi^- + \mathrm{C}$ reactions. As presented in Section 3.5 a Boltzmann fit (Eq. (3.8)) can be applied to the p_T spectra to extrapolate the yield in the uncovered kinematic regions. In case of the π^+ spectra in $\pi^- + \mathrm{C}$ collisions, the Boltzmann distributions (orange curves in Fig. E.2) reproduce the shape of the experimental distributions reasonably well. Although small deviations between the experimental data and the Boltzmann fit for $y < 0.4$ at intermediate p_T are observed in the heavier collision system. A similar trend is observed for $\pi^- + \mathrm{W}$ reaction (Fig. E.3).

For the π^- the extrapolation in the unmeasured kinematic regions is more complex, since here (quasi-)elastic scattering events have to be considered as well. Figure E.4 shows the p_T distributions for different rapidity regions (see legend) in $\pi^- + \mathrm{C}$ collisions. For the rapidity $0.3 \leq y < 0.4$ two contributions in the p_T spectra are visible. Negatively charged pions, which were either produced in inelastic reactions (low p_T) or (quasi-)elastically scattered (high p_T). Thus, the total fit function (dark blue solid curve in Fig. E.4) includes two contributions. Inelastic reactions are described by a Boltzmann function (dark blue dashed curve), while (quasi-)elastic scattered π^- are described by a Gaussian (light blue dashed curve). A good description of the experimental distribution with the combined, Boltzmann and Gaussian, fit was achieved. With increasing rapidity the p_T coverage within the HADES acceptance gets less. For $y \approx 0.9$, the part of the p_T distribution corresponding to (quasi-)elastically scattered π^- is outside the acceptance and thus only the inelastic part can be extrapolated. Here, the Boltzmann fit is consistent with the shape of the experimental distributions, as shown in Fig. E.4. For the entire measured rapidity range and for $\pi^- + \mathrm{W}$ collisions the employed fit, either combined Boltzmann and Gaussian or Boltzmann, reproduces the experimental data well (Fig. E.5).

Further, one can compare the shape of the inelastic scattering peak for both charged pions. Thus, the p_T spectra of π^+ were scaled to the integral of the p_T distributions of π^- in the range upto $p_T = 400$ MeV/c. Figure 4.14 depicts the comparison of p_T distributions for π^- (orange stars) and π^+ (blue points) in the same rapidity regions as shown above for in $\pi^- + \mathrm{C}$ reactions. The shapes of inelastic scattering peak for π^- and π^+ are (nearly) similar over the entire rapidity range. In $\pi^- + \mathrm{W}$ reactions (Fig. E.7) deviations between the inelastic scattering peak of π^- and π^+ are seen, however for forward rapidities the agreement is almost perfect.

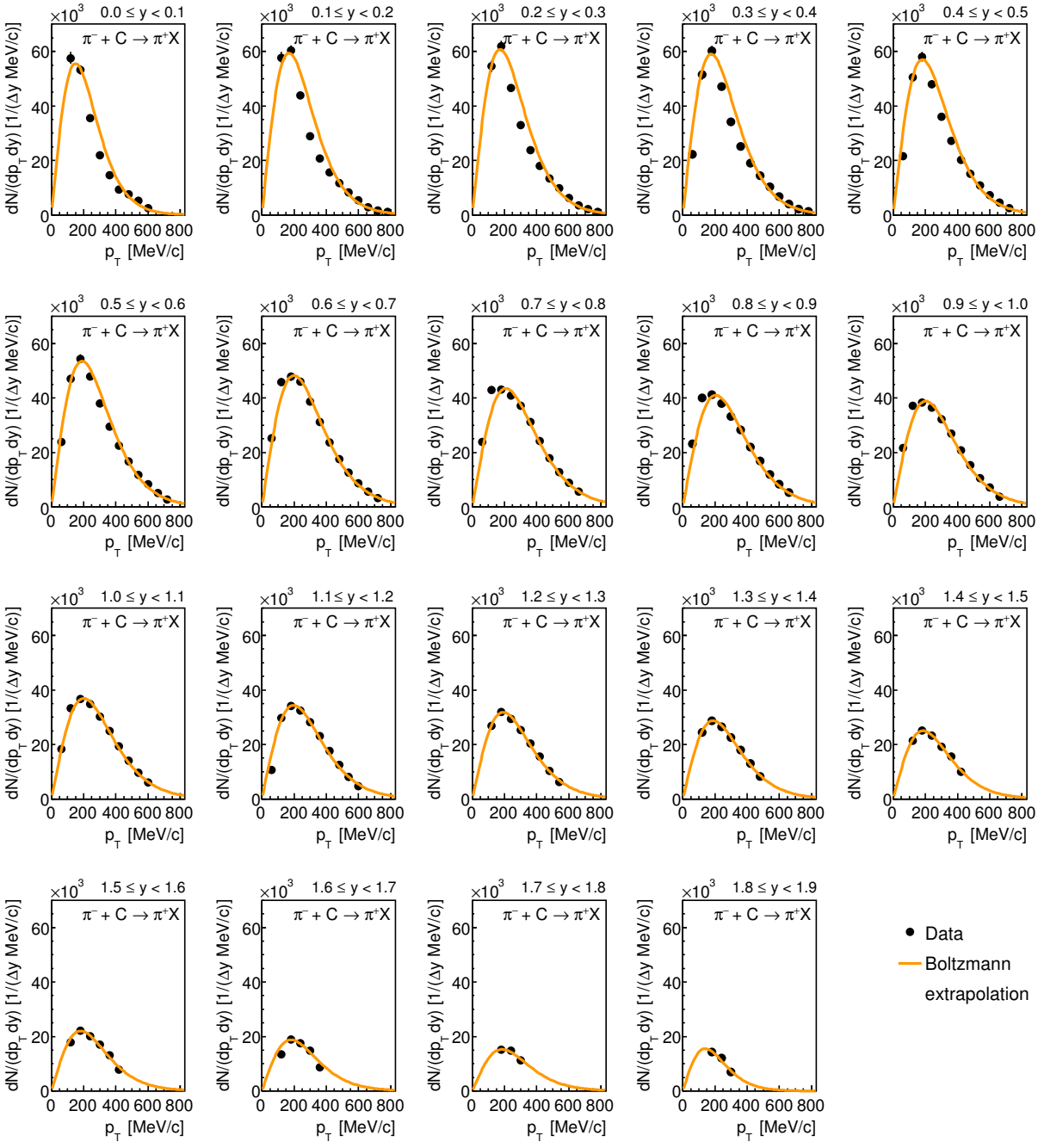

Figure E.2: Transverse momentum spectra of π^+ in $\pi^- + \mathrm{C}$ corrected for reconstruction efficiency within the geometrical acceptance in different rapidity regions (see legend). The solid lines indicate Boltzmann fits.

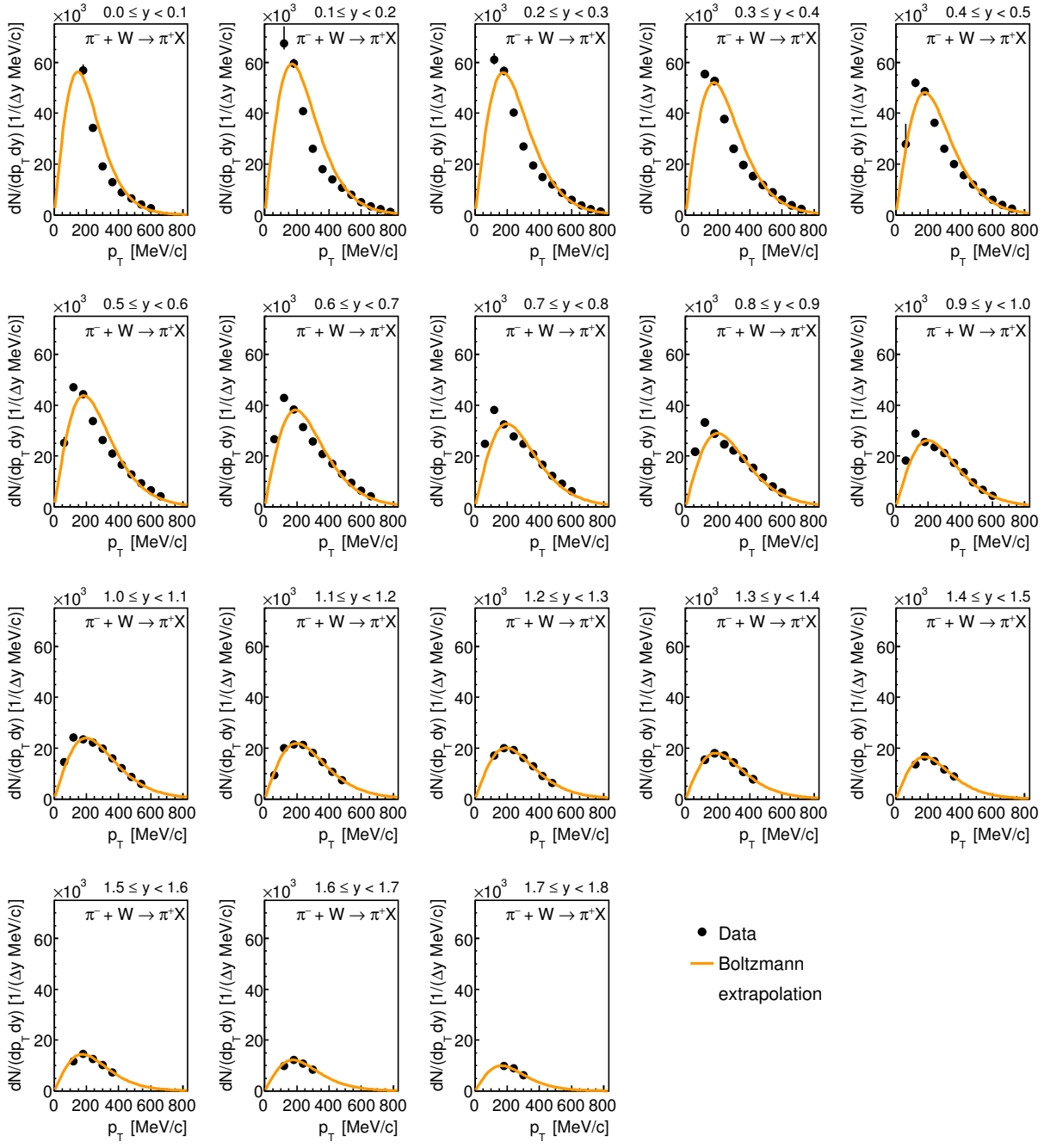

Figure E.3: Transverse momentum spectra of π^+ in $\pi^- + \mathrm{W}$ corrected for reconstruction efficiency within the geometrical acceptance in different rapidity regions (see legend). The solid lines indicate Boltzmann fits.

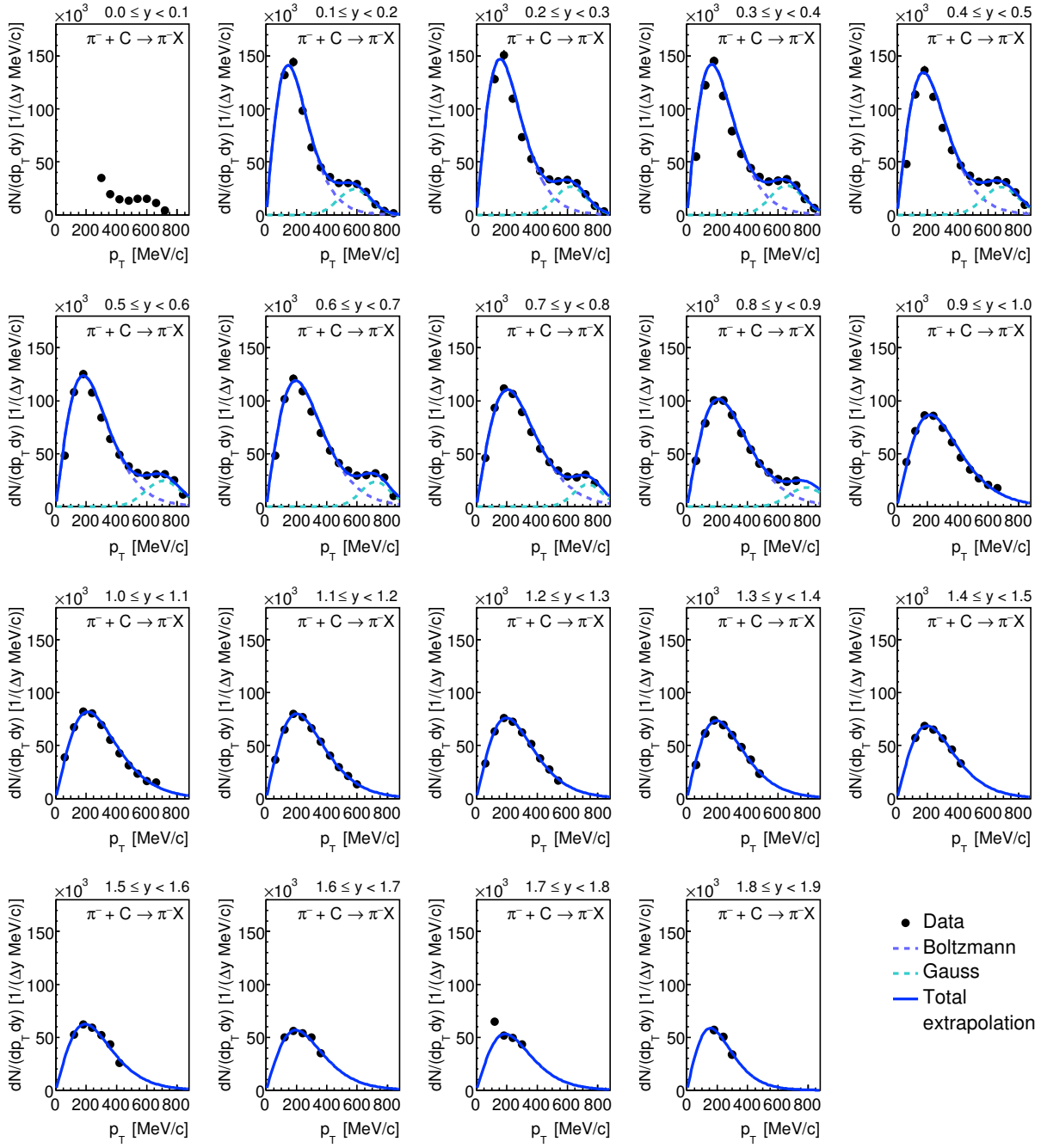

Figure E.4: Transverse momentum spectra of π^- corrected for reconstruction efficiency within the geometrical acceptance in different rapidity regions (see legend) in $\pi^- + \mathrm{C}$ reactions. The solid lines indicate the total fits. Until $y \approx 8$ dashed dark blue curve resembles the Boltzmann distribution for the π^- produced in inelastic reactions and dashed light blue curve the Gaussian distribution for elastic scattered π^-.

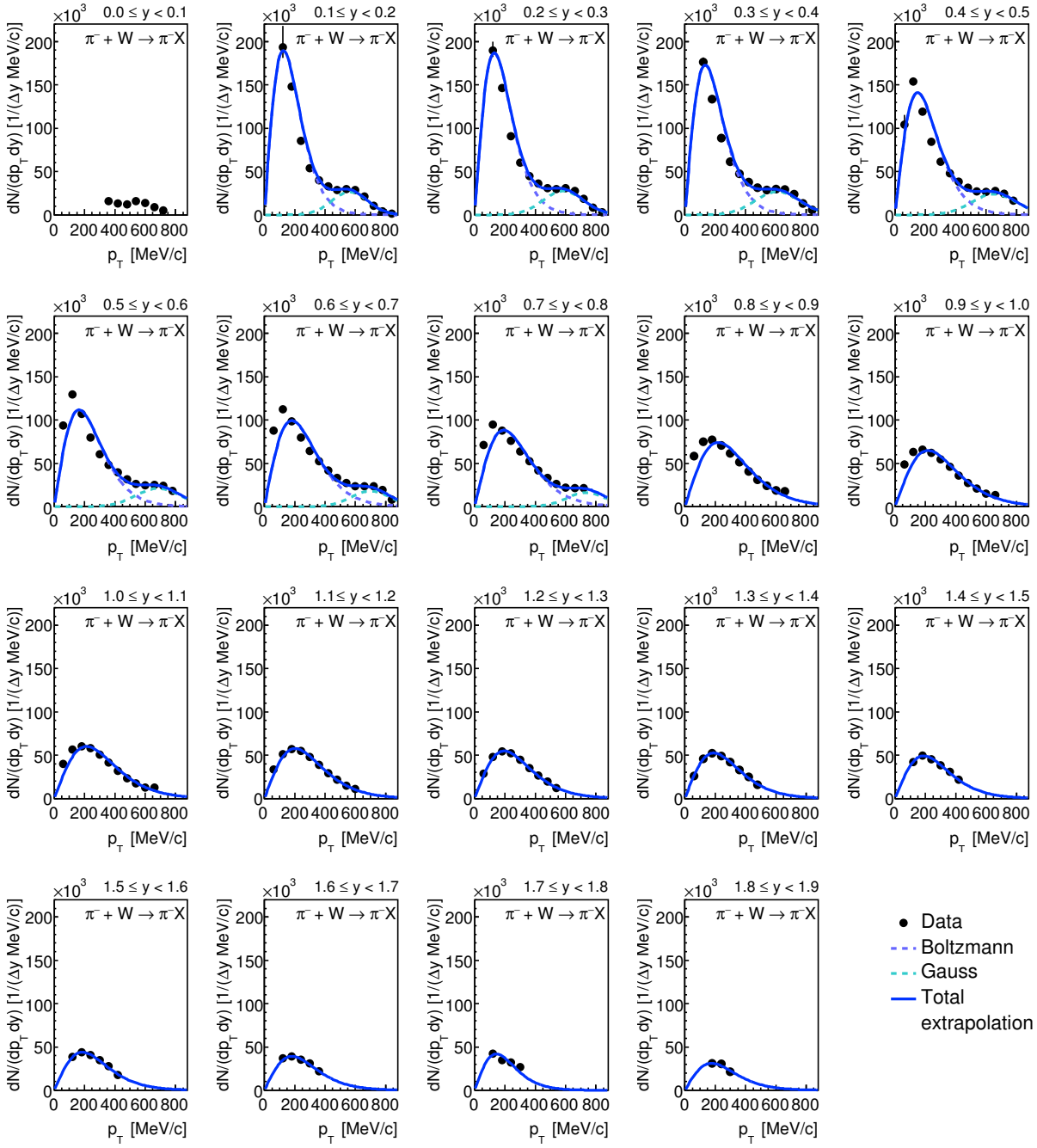

Figure E.5: Transverse momentum spectra of π^- corrected for reconstruction efficiency within the geometrical acceptance in different rapidity regions (see legend) in $\pi^- + \mathrm{W}$ reactions. The solid lines indicate the total fits. Until $y \approx 8$ dashed dark blue curve resembles the Boltzmann distribution for the π^- produced in inelastic reactions and dashed light blue curve the Gaussian distribution for elastic scattered π^-.

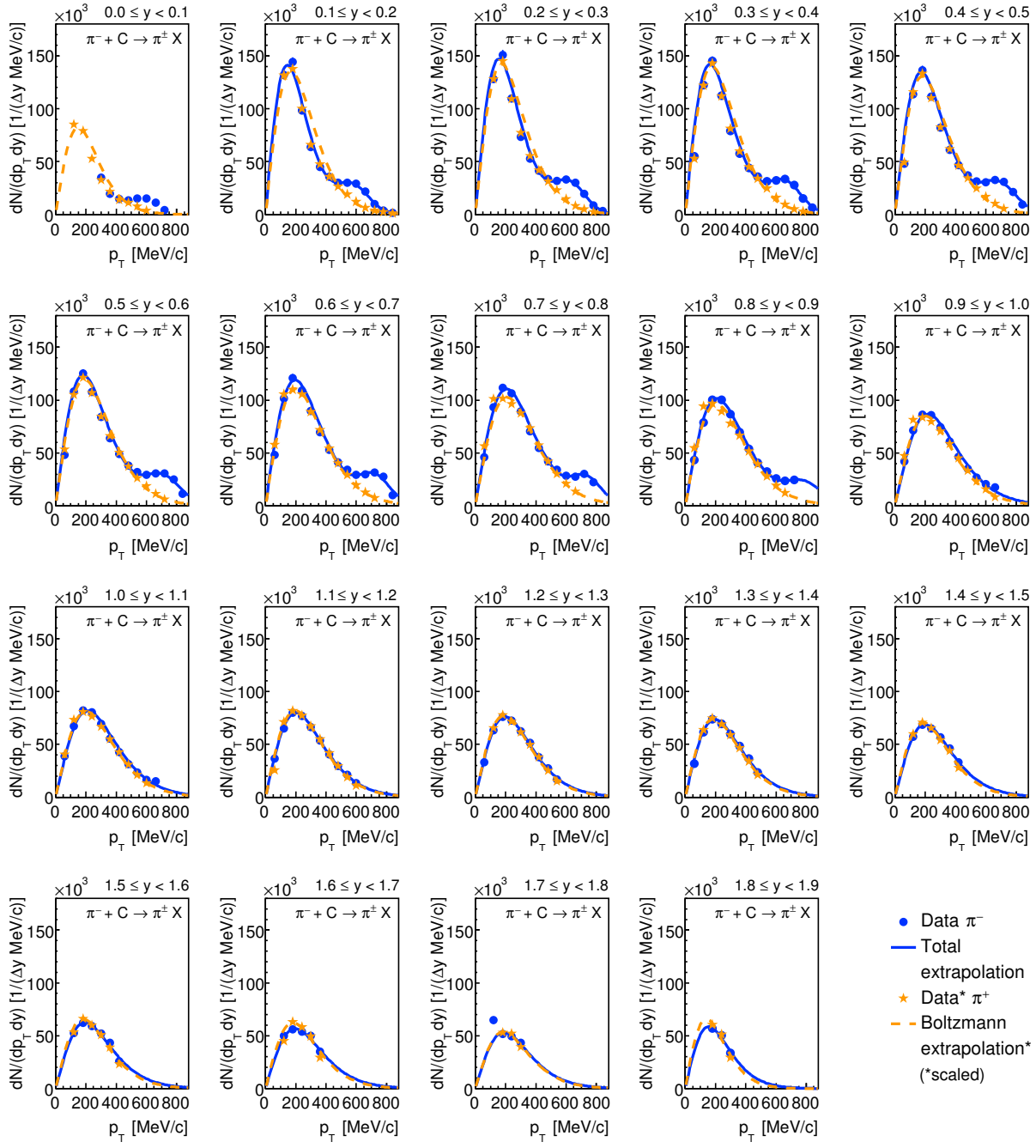

Figure E.6: Transverse momentum spectra of π^- (blue points) in different rapidity regions (see legend) in π^- + C reactions. The solid blue curves represent the total extrapolations of π^-. The corresponding scaled transverse momentum spectra of π^+ are resembled by the orange stars together with Boltzmann extrapolations (dashed orange curve).

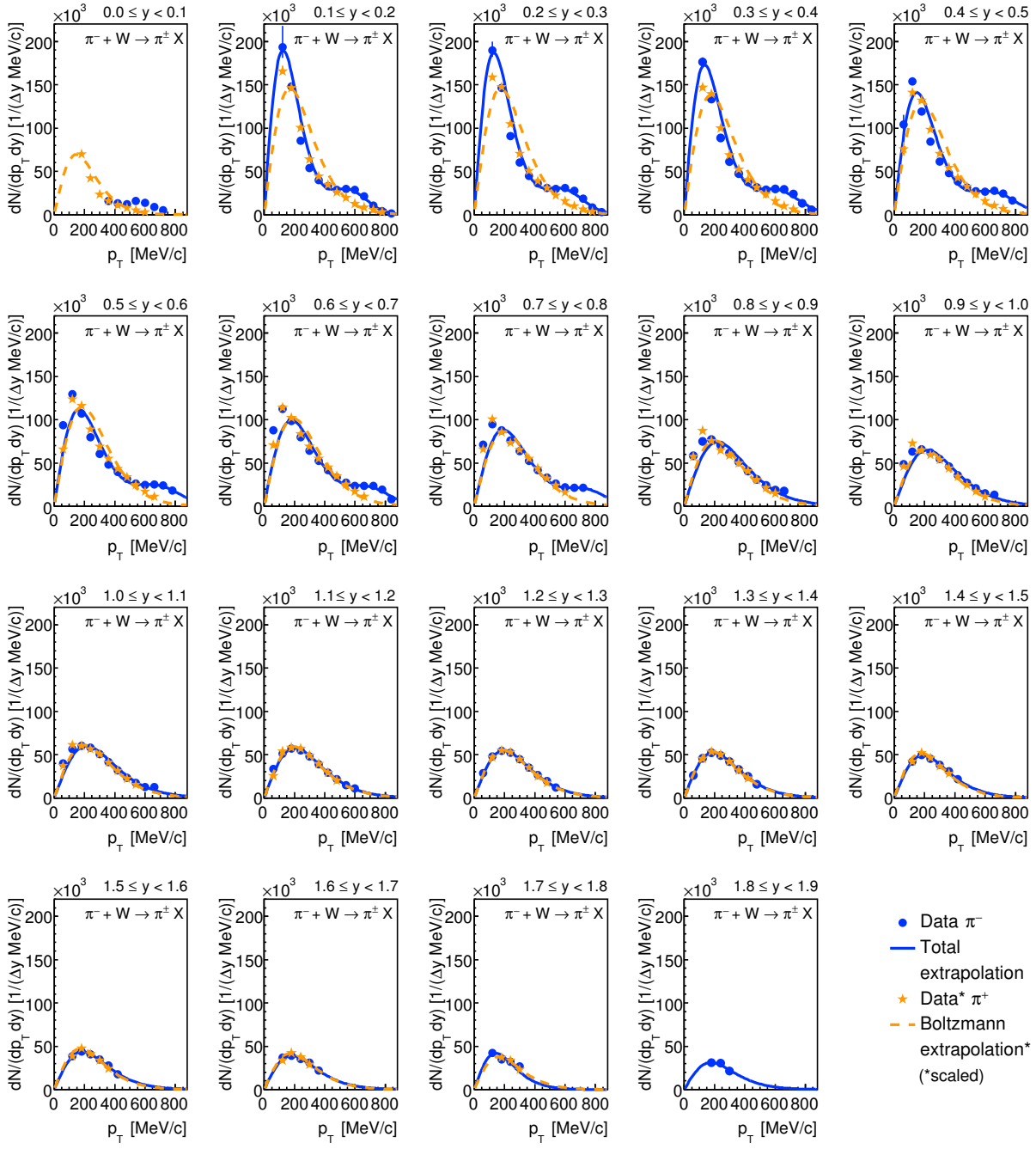

Figure E.7: Transverse momentum spectra of π^- (blue points) in different rapidity regions (see legend) in π^- + W reactions. The solid blue curves represent the total extrapolations of π^-. The corresponding scaled transverse momentum spectra of π^+ are resembled by the orange stars together with Boltzmann extrapolations (dashed orange curve).

E.3 (Anti-)Kaon Boltzmann Distribution

Based on the double-differential analysis the rapidity density distribution dN/dy of (anti-)kaons can be extracted. As explained in Section 3.5 a Boltzmann fit (Eq. (3.8)) can be applied to the measured p_T spectra and the yield in the uncovered regions can be estimated. As already mentioned, the comparison of K^+ transverse momentum spectra in the exclusive production channels of $\pi^- + p \rightarrow K^+K^-n$ and $\pi^- + p(\mathrm{C}) \rightarrow K^+K^-n(\mathrm{B})$ based on Pluto simulations [F$^+$07, FGH$^+$10] (Section 3.6.1) implied that the Fermi momentum of the nucleons leads to the Boltzmann-like behavior of transverse momentum spectra (Appendix E.1).

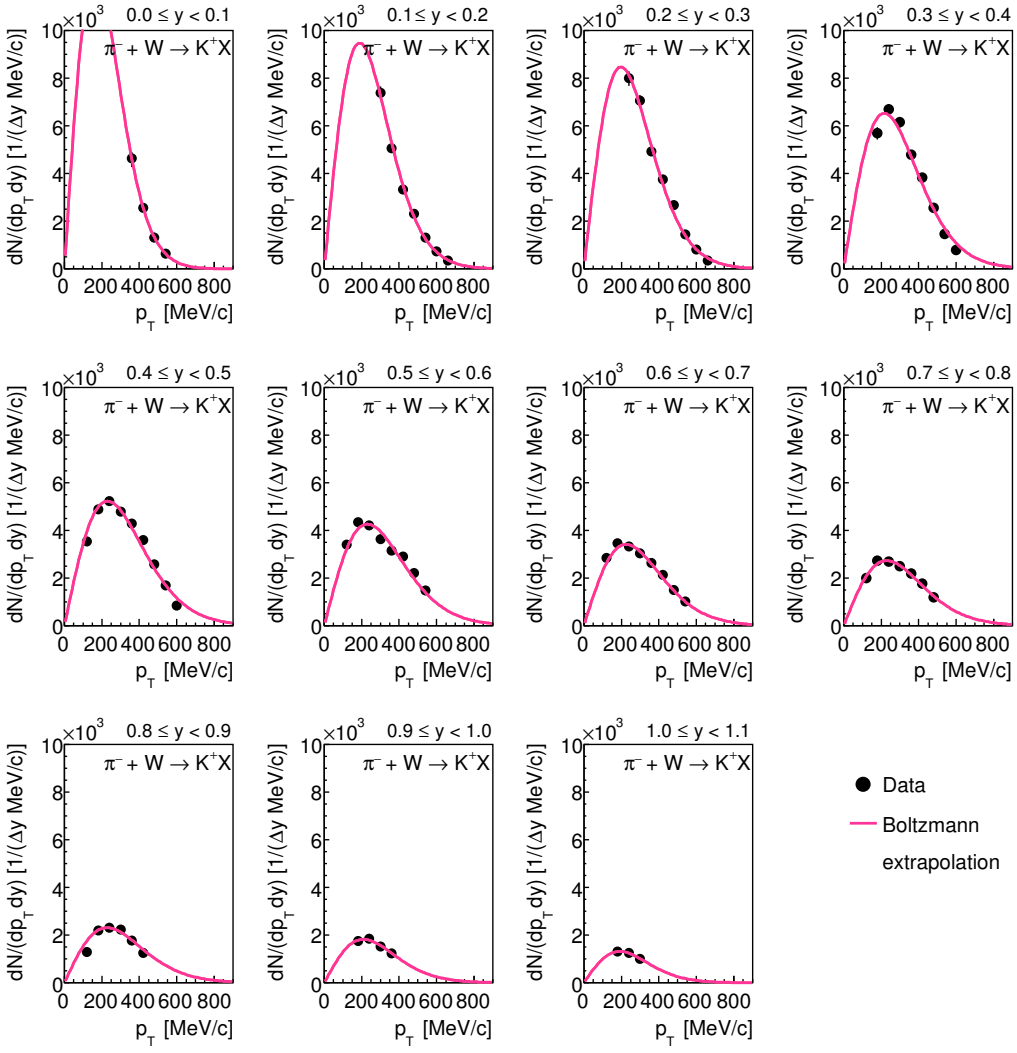

Figure E.8: Transverse momentum spectra of K^+ in $\pi^- + \mathrm{W}$ corrected for reconstruction efficiency within the geometrical acceptance in different rapidity regions (see legend). The solid lines indicate Boltzmann fits.

The Boltzmann distribution (pink curve) reproduces the shape of the experimental distribution for K^+ well over the entire rapidity range as demonstrated for $\pi^- + \mathrm{W}$ collisions in Fig. E.8. Since also the K^- transverse momentum spectra for $\pi^- + \mathrm{W}$ reaction are well described by the Boltzmann fit indicated by the green solid line in Fig. E.9, the same procedure was also applied

to the antikaons. A similar agreement is observed for the entire measured rapidity range for K^+ (Fig. 5.10) and K^- (Fig. 5.11) in $\pi^- + \mathrm{C}$ collisions.

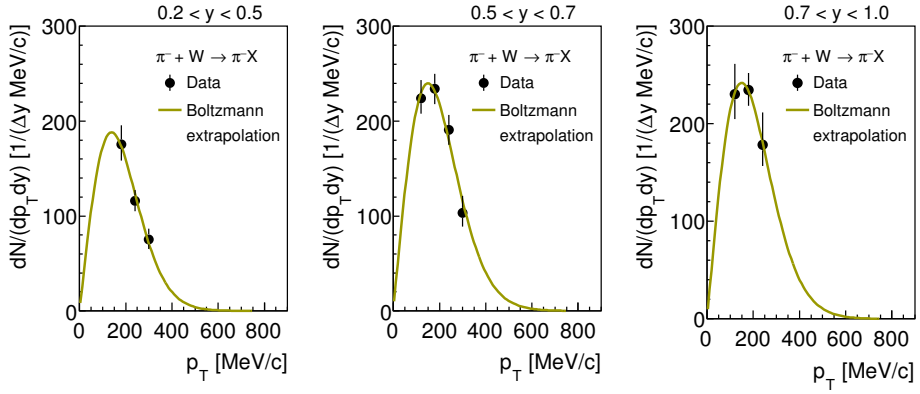

Figure E.9: Transverse momentum spectra of K^- in $\pi^- + \mathrm{W}$ corrected for reconstruction efficiency within the geometrical acceptance in different rapidity regions (see legend). The solid lines indicate Boltzmann fits.

F Appendix to Elementary Cross-Sections

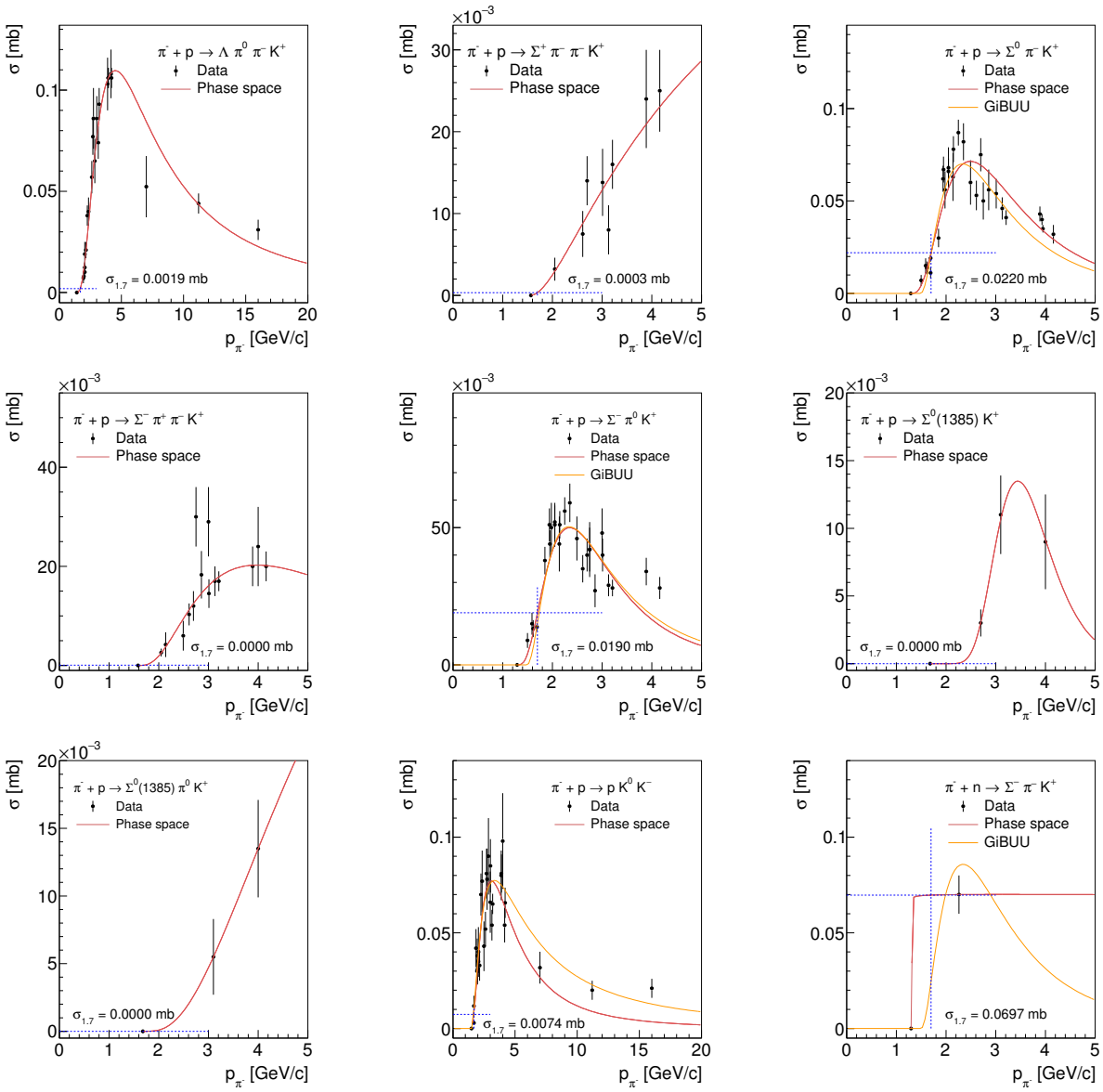

Figure F.1: Cross-sections measured by different experiments taken from the Landolt-Börnstein compilation [MS88] as a function of the incident pion momentum p_{π^-}. The red solid curve indicates the fit corresponding to a cross-section parametrization adapted from Sibirtsev *et al.* [SCK97, CBM+97], while the yellow solid curve pictures the parametrization employed in GiBUU [BGG+12]. The blue dashed lines represent the suggested cross-section by the fit at $p_{\pi^-} = 1.7$ GeV/c. For details see Section 5.2.5.

G Momentum-dependent ϕ Meson Reconstruction

The momentum-dependent experimental ϕ cross-sections were extracted on the basis of the procedure explained in Section 6.1. The invariant mass distributions of K^+K^- pairs including event-by-event reconstruction efficiency correction in $\pi^- + \mathrm{C}$ collisions for different momentum intervals (see legend) are shown in Fig. G.1. Only the modeling of the background was changed from a third-order polynomial together with a Gaussian function to an ARGUS function (Eq. (G.1)), since this function proved to be more robust against statistical fluctuations.

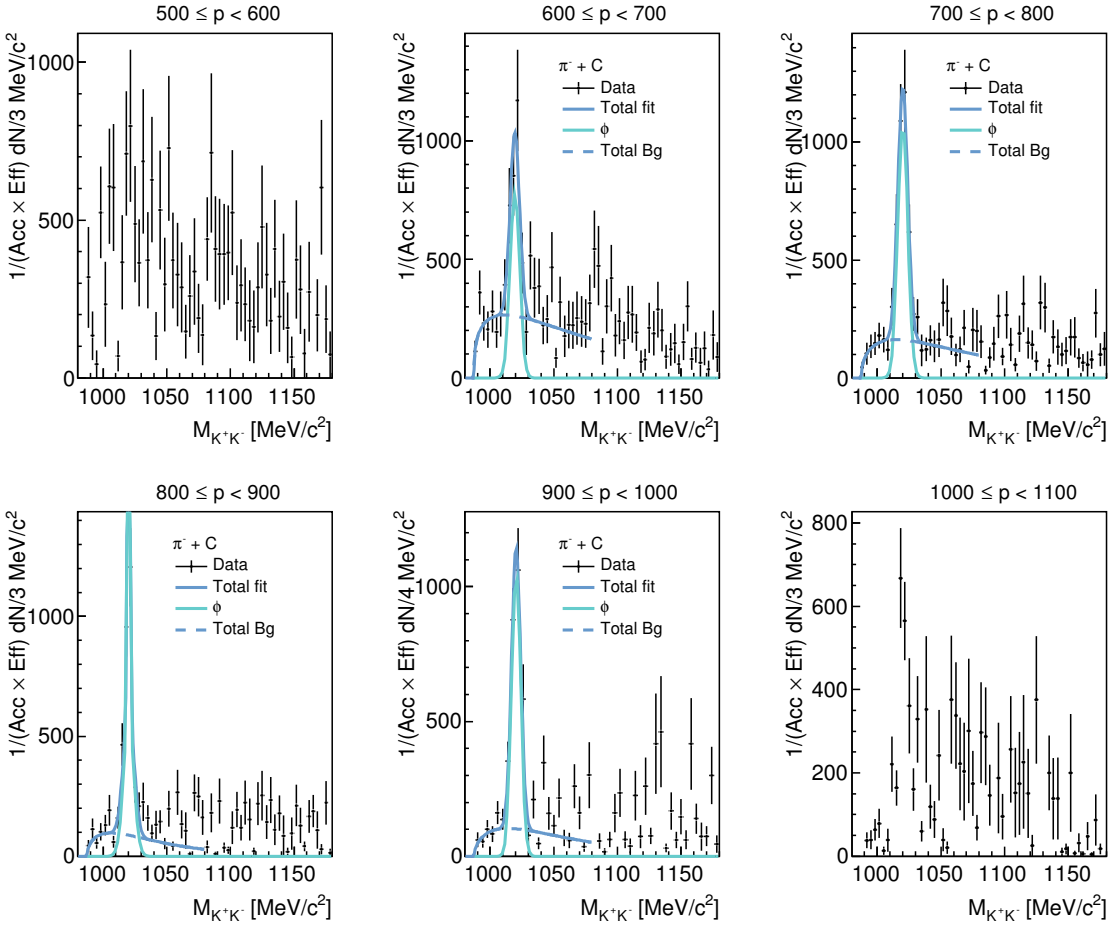

Figure G.1: Invariant mass distributions of K^+K^- pairs with event-by-event reconstruction efficiency correction produced in $\pi^- + \mathrm{C}$ collisions for different momentum intervals (see legend). The fit to the corrected experimental data consists of two Gaussian for the ϕ signal (light blue line) together with the background described by a ARGUS function (dashed curve).

$$
\begin{aligned}
x \leq 2m_0 : \; & f(x) = 0 \\
x > 2m_0 : \; & f(x) = z \cdot \left(1 - \frac{z^2}{[2]^2}\right)^{[0]} \cdot \exp\left([1] \cdot \left(1 - \frac{z^2}{[2]^2}\right)\right)
\end{aligned}
\tag{G.1}
$$

with

$$
\begin{aligned}
z : \quad & \text{variable } (z = 2 \cdot m_0 + [2] - x) \\
m_0 : \quad & \text{nominal charged kaon mass} \\
[0]/[1]/[2] : \quad & \text{fit parameters}
\end{aligned}
$$

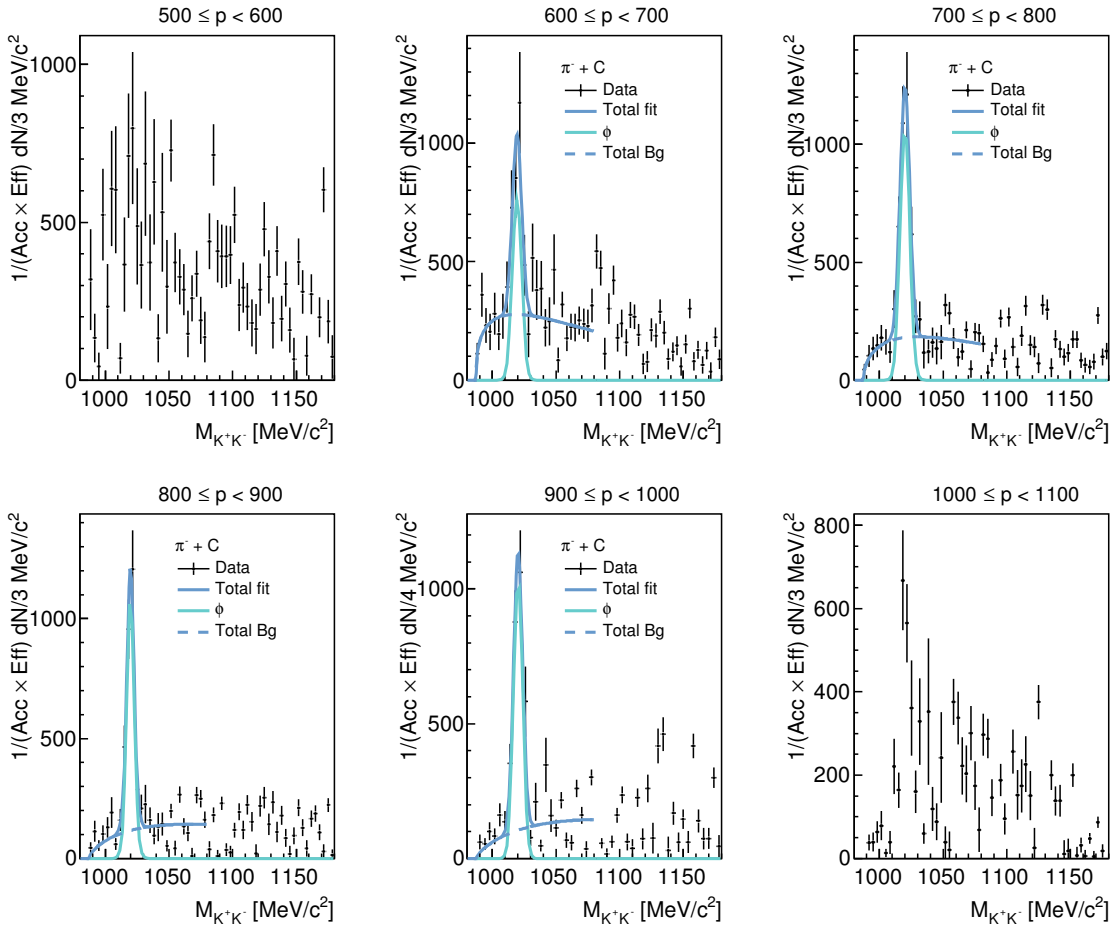

Figure G.2: Invariant mass distributions of K^+K^- pairs with event-by-event reconstruction efficiency correction produced in $\pi^- + \mathrm{C}$ reactions with reduced statistical fluctuations for different momentum intervals (see legend). The fit to the corrected experimental data consists of two Gaussian for the ϕ signal (light blue line) together with the background described by a ARGUS function (dashed curve). For details see text.

In Figure G.1 the total fit is represented by the blue solid curve, while the ϕ signal is represented by the cyan distribution and the background underneath the ϕ signal is represented by the blue dashed curve. One can see that especially with increasing momentum in the high invariant mass range ($M_{K^+K^-} > 1040$ MeV/c^2), outside the range of the ϕ signal, the background shows

significant statistical bin-by-bin fluctuations. This effect leads to an overestimation of the ϕ signal. Therefore, the statistical fluctuations were compensated by averaging the statistical error of the adjacent invariant mass bins in the high invariant mass region. In the following three invariant mass bins in front and behind each respective bin were considered. While the impact on the averaged statistical error is decreasing with increasing distance with respect to the respective bin. For the light target (C) this procedure was applied for the invariant mass range of $M_{K^+K^-} > 1050$ MeV/c^2. The resulting invariant mass distributions of K^+K^- pairs with event-by-event reconstruction efficiency correction are represented in Fig. G.2. One can clearly see that the statistical fluctuations of the background have less influence on the modeling of the later one. Therefore, not only the description of the background is more reliable, but also the extraction of the ϕ signal.

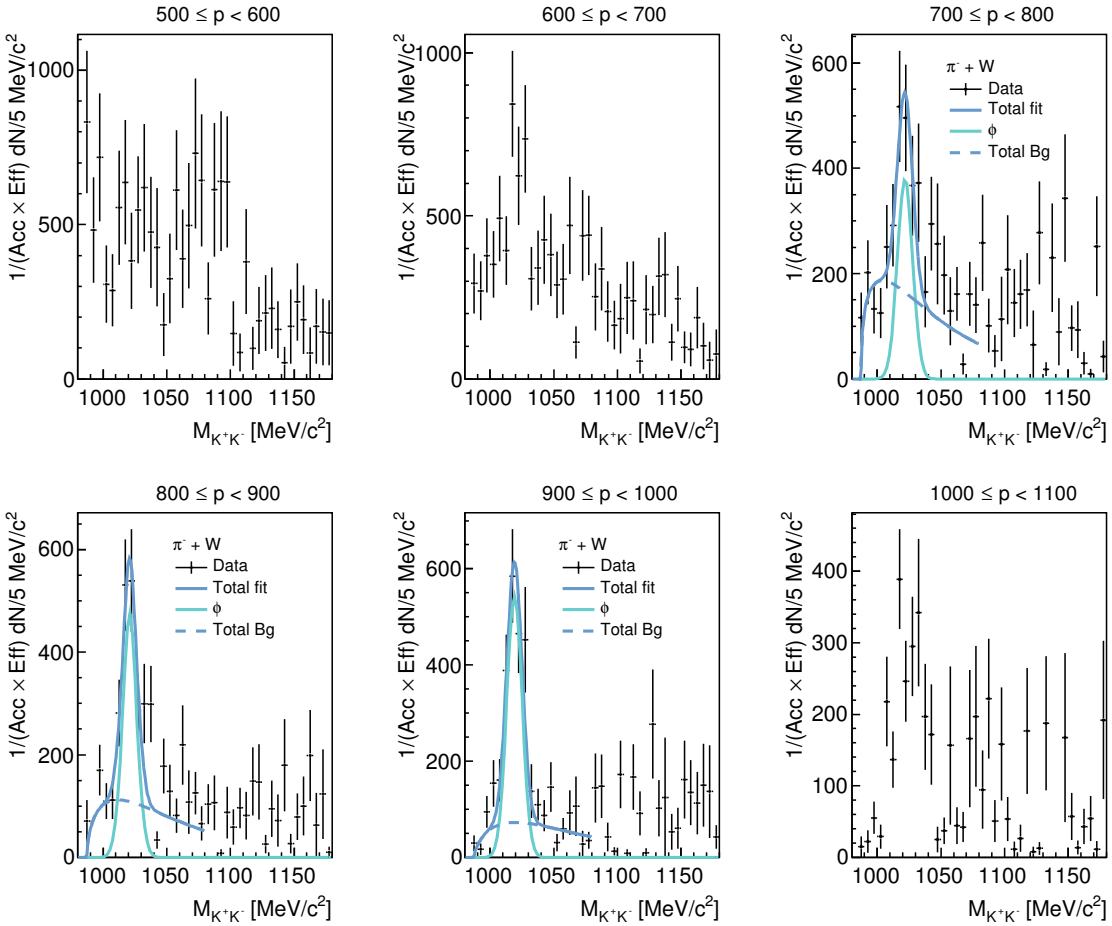

Figure G.3: Invariant mass distributions of K^+K^- pairs with event-by-event reconstruction efficiency correction produced in $\pi^- + \mathrm{W}$ collisions for different momentum intervals (see legend). The fit to the corrected experimental data consists of two Gaussian for the ϕ signal (light blue line) together with the background described by a ARGUS function (dashed curve).

Figure G.3 represents the invariant mass distributions of K^+K^- pairs with event by event reconstruction efficiency correction in $\pi^- + \mathrm{W}$ collisions for different momentum intervals (see legend). Also for the heavier target (W) an ARGUS function (Eq. (G.1)) was used to model the background. Similar to the ϕ production off carbon, statistical bin-by-bin variations in the invariant mass distribution of K^+K^- pairs are observed, causing an overestimation of the ϕ signal.

Therefore, the statistical fluctuations were compensated by averaging the statistical error of the adjacent invariant mass bins in the high invariant mass range of $M_{K^+K^-} > 1040$ MeV/c^2. In Figure G.4 the corrected invariant mass distributions of K^+K^- pairs thus obtained are shown. The statistical fluctuations of the sidebands have less influence on the modeling of the background and therefore its description is more reliable, but also the extraction of the ϕ signal.

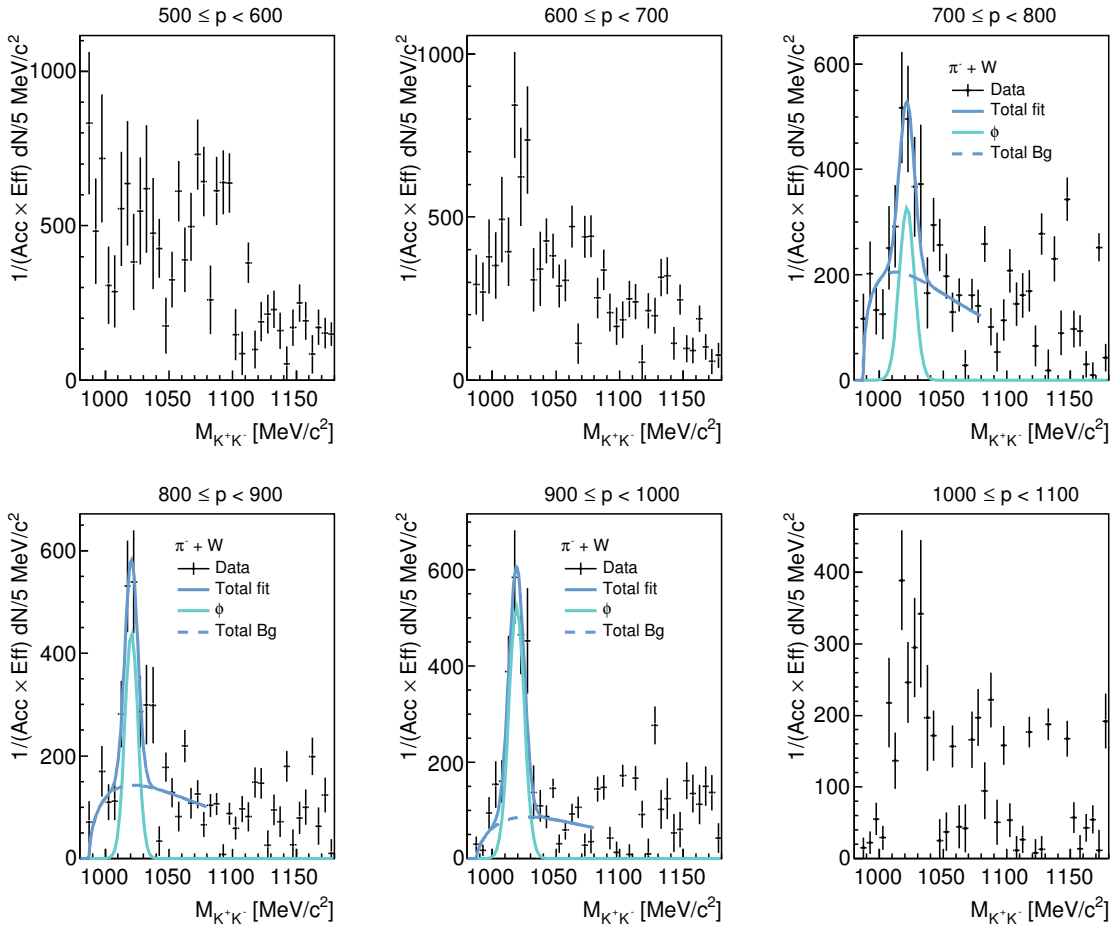

Figure G.4: Invariant mass distributions of K^+K^- pairs with event-by-event reconstruction efficiency correction produced in $\pi^- + \mathrm{W}$ reactions with reduced statistical fluctuations for different momentum intervals (see legend). The fit to the corrected experimental data consists of two Gaussian for the ϕ signal (light blue line) together with the background described by a ARGUS function (dashed curve). For details see text.

H Appendix to Transport Models

H.1 GiBUU: ϕ Phase Space Distribution

GiBUU [BGG+12] describes the entire reaction dynamics of the pion-nucleus reactions and ϕ mesons are rarely produced. In the following $\pi^- + \mathrm{C}$ and $\pi^- + \mathrm{W}$ reactions were simulated and the respective ϕ double-differential distribution are presented in Fig. H.1. It can be clearly seen that the ϕ meson distributions show no dependence on the target.

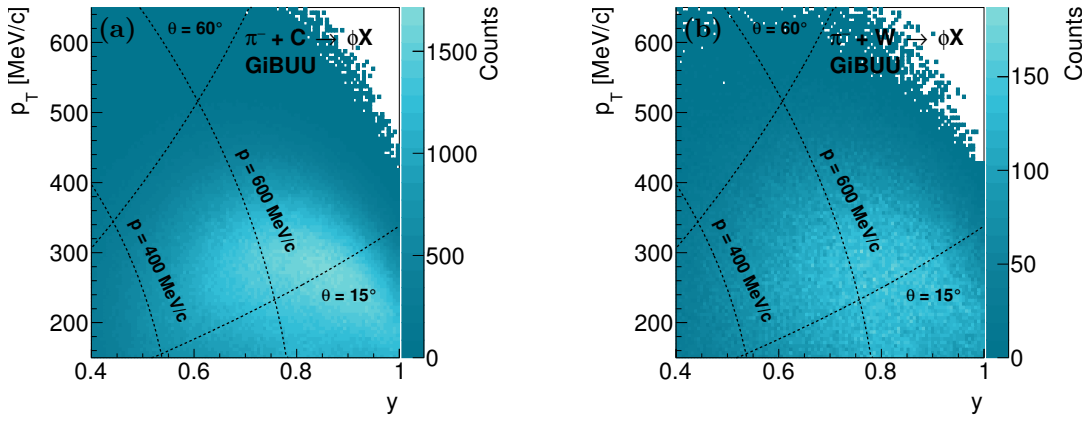

Figure H.1: ϕ meson distribution as a function of transverse momentum p_T vs. rapidity y for initial unfiltered simulation of $\pi^- + \mathrm{C}$ (a) and $\pi^- + \mathrm{W}$ (b) reactions based on GiBUU. The black dotted horizontal lines indicate the momentum at 400 and 600 MeV/c. The back dotted vertical lines denote the polar angle regions between $\theta = 15 - 60°$.

H.2 UrQMD: Resonance Contributions

For a resonance approach as exercised in UrQMD, $\pi^- + A$ reactions are of great interest, since they are more sensitive to the πN branching ratios than the usual NN collisions.

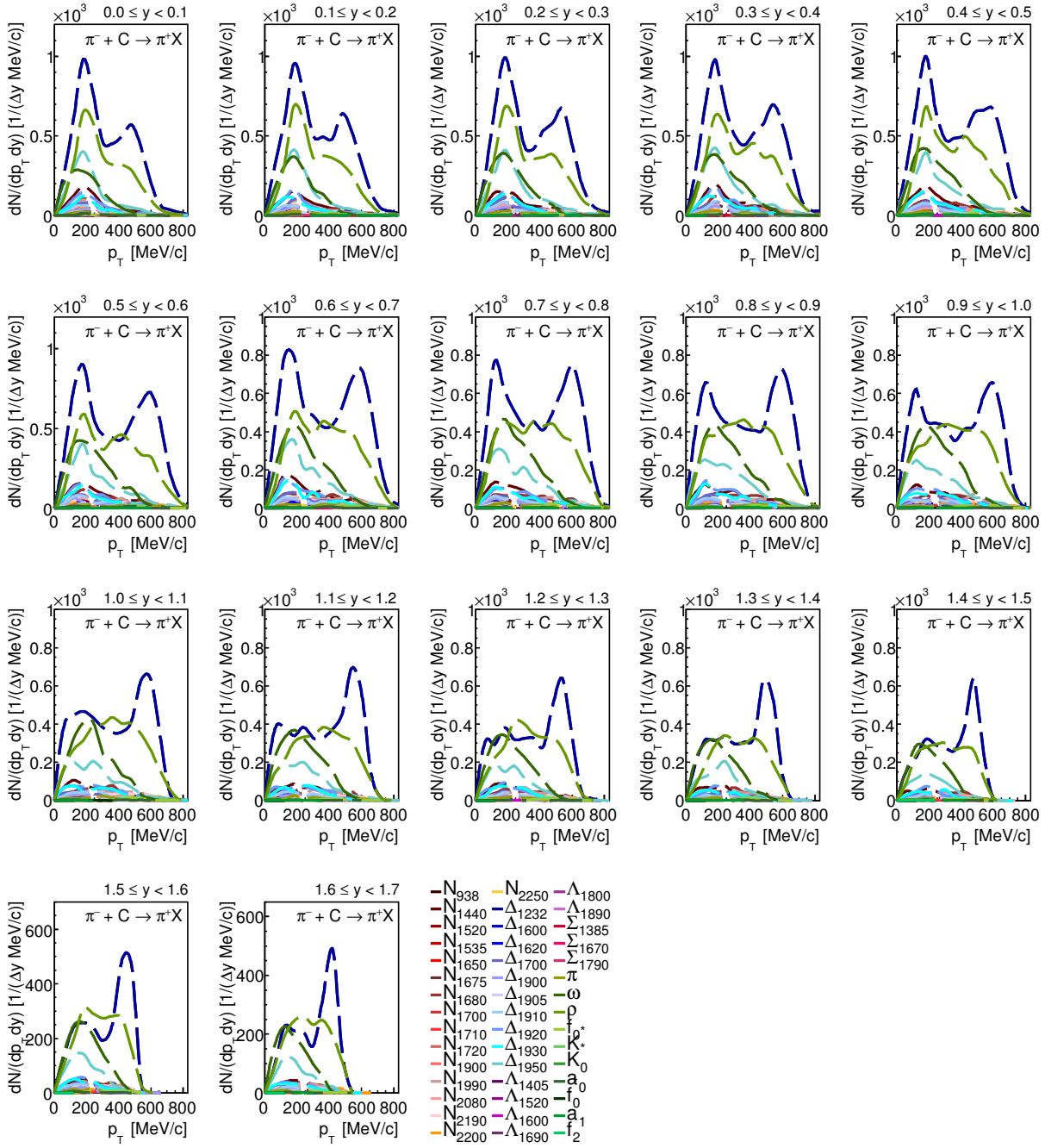

Figure H.2: π^+ transverse momentum spectra of UrQMD in $\pi^- + \mathrm{C}$ reactions for different rapidities (see legend). The different line colors indicate the contributions from the different resonances.

Figure 4.21 and Figure 4.22 present the experimental π^+ transverse momentum spectra in comparison to hadronic transport model predictions. While in the experimental data, the

transverse momentum distributions peak at low p_T, the spectrum predicted by UrQMD shows an unexpected two-peak structure. The second peak at high p_T can be attributed to the $\Delta(1232)$ resonance (Fig. H.2).

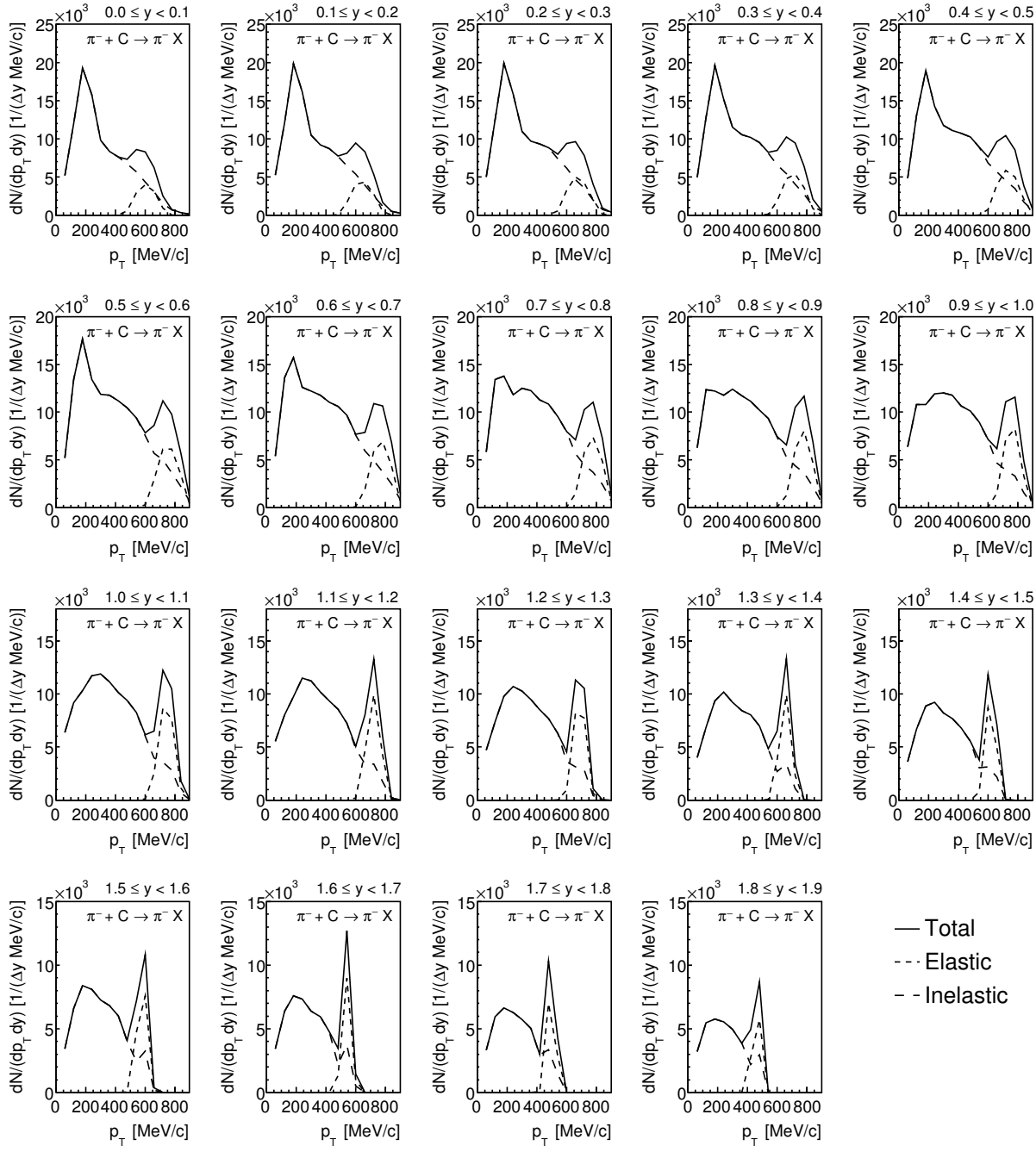

Figure H.3: π^- transverse momentum spectra of UrQMD in $\pi^- + \mathrm{C}$ reactions for different rapidities (see legend). The different curves correspond to the total (solid curve), elastic (dotted curve) and inelastic (dashed curve) yield.

For the π^- not only the inelastic, but also the (quasi-)elastic reactions, contribute to the total yield. While, the in-elastically produced π^- populate the low p_T region, the pronounced second peak at high p_T corresponds mainly the (quasi-)elastic scattered π^- (Fig. H.3).

Since in UrQMD (most) final state originate from the strong decays of intermediate resonances (e.g. Δ, N^*) with differences masses and widths, elastic meson-baryon cross-sections are determined by resonance excitation and decays (e.g. $\pi N \to \Delta \to \pi N$).

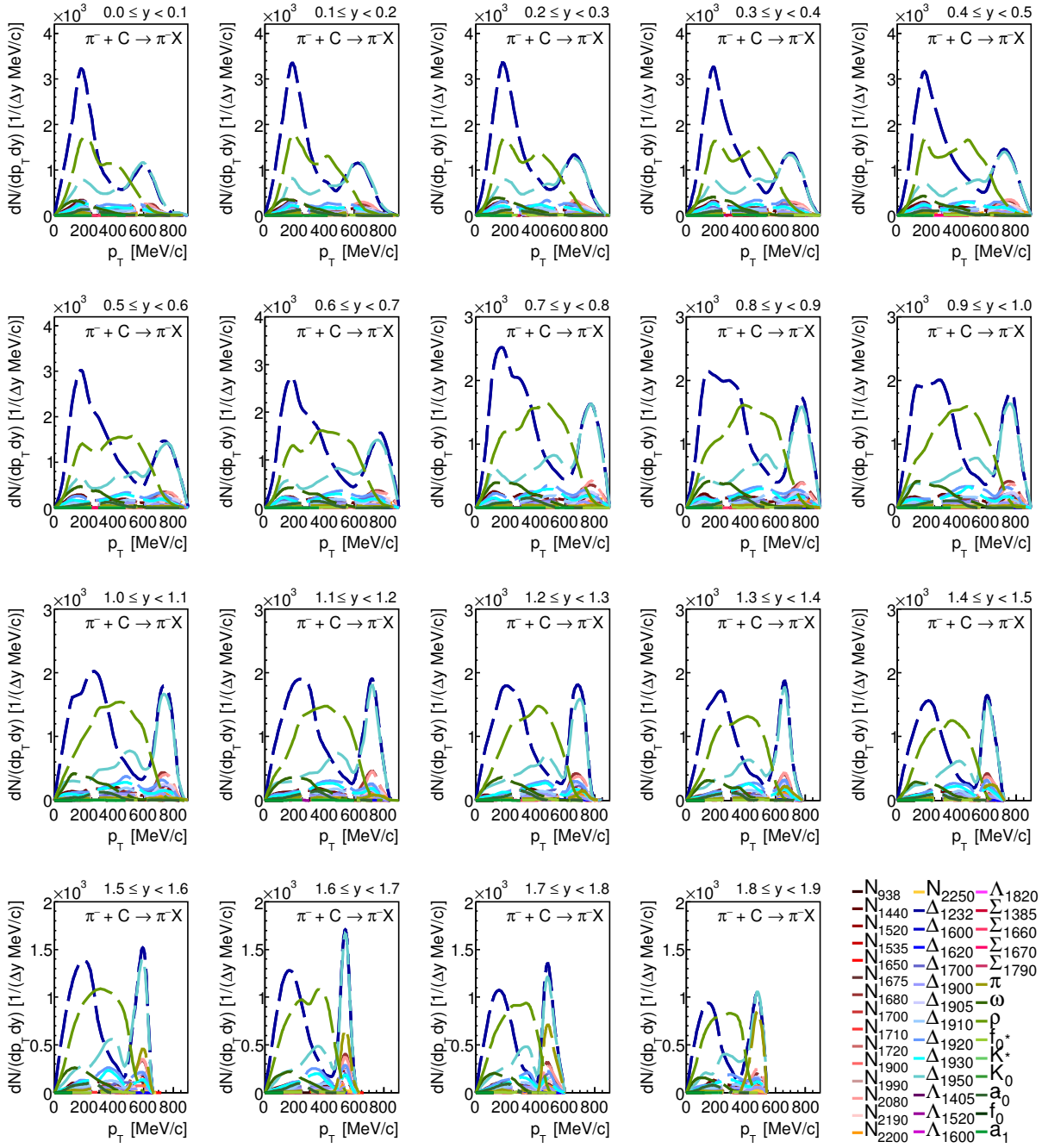

Figure H.4: π^- transverse momentum spectra of UrQMD in $\pi^- + \mathrm{C}$ reactions for different rapidities (see legend). The different line colors indicate the contributions from the different resonances.

In Figure H.4 one observes that the main resonance contributions to the elastic π^- yield arise from the $\Delta(1232)$ and $\Delta(1950)$ resonances. As presented in Fig. 4.24 and Fig. 4.25 for high p_T, the expected region of (quasi-)elastic events, the deviations between the experimental data and

UrQMD are striking. Hence, in order to reproduce the (quasi-)elastic scattering the contribution of the resonances with corresponding branching ratios into πN have to be re-tuned in UrQMD.

In Figure 5.18 and Figure 5.19 the experimental transverse momentum spectra of K^+ peak is shown as expected at low p_T in the forward rapidity region. Whereas in UrQMD, at higher rapidities an two-peak structure emerges, that is not observed in the experimental data.

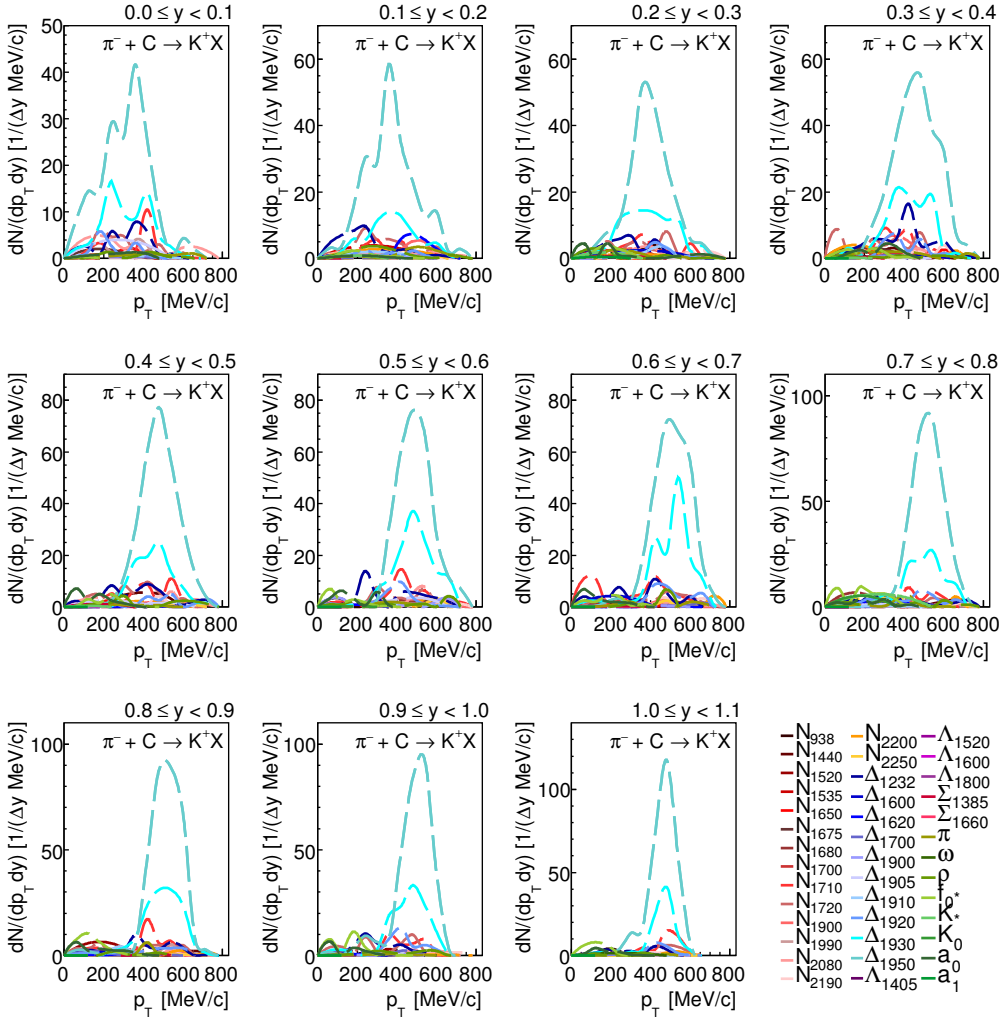

Figure H.5: K^+ transverse momentum spectra of UrQMD in $\pi^- + \mathrm{C}$ reactions for different rapidities (see legend). The different line colors indicate the contributions from the different resonances.

Investigations of the different resonance contributions to the K^+ spectra shown in Fig. H.5, reveal that the peak at high p_T arises from is from N^* and Δ resonance decays. Especially the $\Delta(1930)$ and $\Delta(1950)$ resonances contribute to the second peak at high transverse momenta. The two peak structure may have two possible reasons. First of all, the heavy resonance usually decay into two particles in the framework of UrQMD. One the one hand this allows to maintain detailed balance (e.g. $KY \leftrightarrow \Delta$), but one the other hand it may lead an overestimated p_T of the decay products such as K^+. Since in reality there should be more particles in the final state. A introduction of more decays containing more particles than two in the final state would lead to a higher abundance at low p_T. Nevertheless, it has the mentioned that N^* and Δ resonance decays are rarely measured and thus their associated branching ratios are not well constrained.

H.3 HSD: Transition Probability and Self-Energy

Based on in work of [CTAB14], the chiral effective scheme in dense matter developed in Refs. [TRO06, TCR08] was improved by incorporating the full self-consistent $s-$ and $p-$waves at finite density and temperature. In this way, in-medium meson-baryon cross-sections (amplitudes) for the strangeness sector ($S = -1$) were deduced containing the single-particle properties of hyperons, for example $\Lambda(1115)$, $\Sigma(1195)$, and $\Sigma(1385)$. In the model, the following channels are considered:

$$\begin{aligned} &K^- p \to K^- p, \bar{K}^0 n, \Lambda\pi^0, \Sigma^0\pi^0, \Lambda\eta, \Sigma^0\eta, \Sigma^-\pi^+, \Sigma^+\pi^-, K^+\Xi^-, K^0\Xi^0 \\ &K^- n \to K^- n, \Sigma^-\pi^0, \Sigma^0\pi^-, \Lambda\pi^-, \Sigma^-\eta, K^0\Xi^- \end{aligned} \tag{H.1}$$

In general, the calculation of dynamical quantities in transport theory will require an appropriate folding of reaction rates or transition probabilities with the spectral functions of the particles in the initial and final states. The integrated and differential transition probability (P_{ij}) have been extracted in [CTAB14] based on Eq. (3.21). Various temperatures ($T = 0 - 150$ MeV) and densities ($\rho = 1/8 - 11/4\ \rho_0$) as well as a wide range of total energy ($P_0 = 900 - 1854$ MeV) and momentum ($\vec{P} = 0 - 800$ MeV/c) of the meson-pair have been considered. However, due to the huge amount of data, which was deduced in [CTAB14] a straightforward implementation into the HSD (PHSD) transport model was not possible. In order to overcome this issue, the data was investigated in details. The grid size of the momentum was drastically reduced by one order of magnitude to $\Delta = 200$ MeV/c as no strong dependence was observed in particular for $P < 180$ MeV/c. On the other hand also the momentum range was further restricted as the data was dominated by numerical fluctuations for $P > 800$ MeV/c. Further also the grid size of the energy was reduced from $\Delta = 3$ MeV to $\Delta = 6$ MeV in the range of $P_0 = 900 - 1602$ MeV and even to $\Delta = 36$ MeV in the range of $P_0 = 1602 - 1854$ MeV.

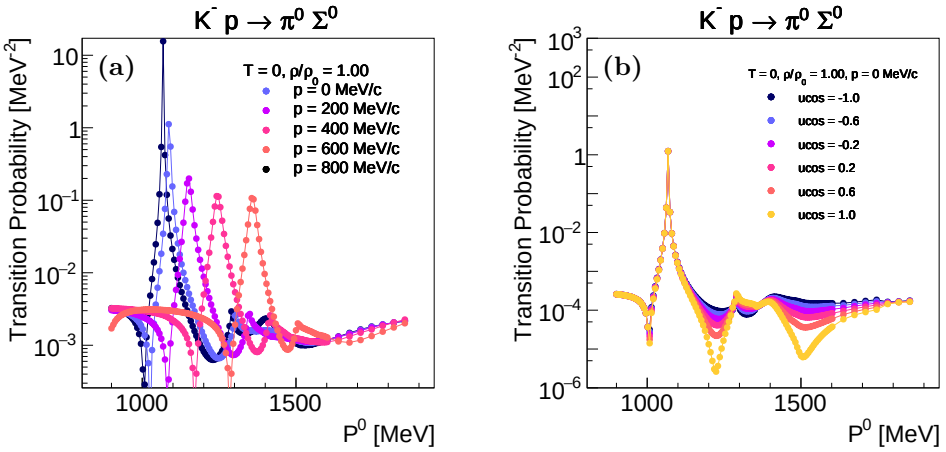

Figure H.6: Integrated (a) and differential (b) in-medium transition probability $P(s)$ based on [CTAB14] as function of the energy P_0 for the inelastic $K^- p \to \Sigma^0\pi^0$ reactions. At normal nuclear density ρ_0 and $T = 0$ MeV for different momenta P (see legend) in the integrated case and at $P = 0$ MeV/c for the differential case.

In Figure H.6 the obtained transition probability for inelastic $K^- p \to \Sigma^0\pi^0$ strangeness exchange reactions are shown. Whereas, Fig. H.6 (a) presents the integrated transition probability, Fig. H.6 (b) shows the differential one. The procedure allowed to significantly reduce the data

size from 6.8 MB to 440 kB per integrated strangeness exchange channel and from 141 MB to 2.6 MB in the integrated case. This opened up the possibility to consider them in the transport model HSD (PHSD) and the implementation of density and temperature dependent transition probabilities (cross-sections) is currently ongoing.

On the basis of the work presented in [TCR08], the $\bar{K}$ self-energy in the $(s+p)$ wave, spectral function, and nuclear optical potentials in a nuclear medium at same tempertures and densities over wide range of $\bar{K}$ energies ($E = 0 - 1500$ MeV) and momenta ($\vec{p} = 0 - 1000$ MeV/c) in the laboratory frame have been extracted [BCTS19]. The effective mass m^* and decay width Γ of the antikaon in matter are determined by the solution $E(k)$ of the in-medium dispersion equation ($c = 1$):

$$E^2 - m^2 - \vec{p}^{\,2} - Re(\Pi) = 0 \tag{H.2}$$

with

$E/\vec{p}$: energy and momentum of $\bar{K}$ in the laboratory frame [MeV]
m : nominal mass of $\bar{K}$ ($m = 495.67$ MeV [P$^+$16a])
$Re(\Pi)$: real part of the self-energy in $(s+p)$-wave [MeV^2]

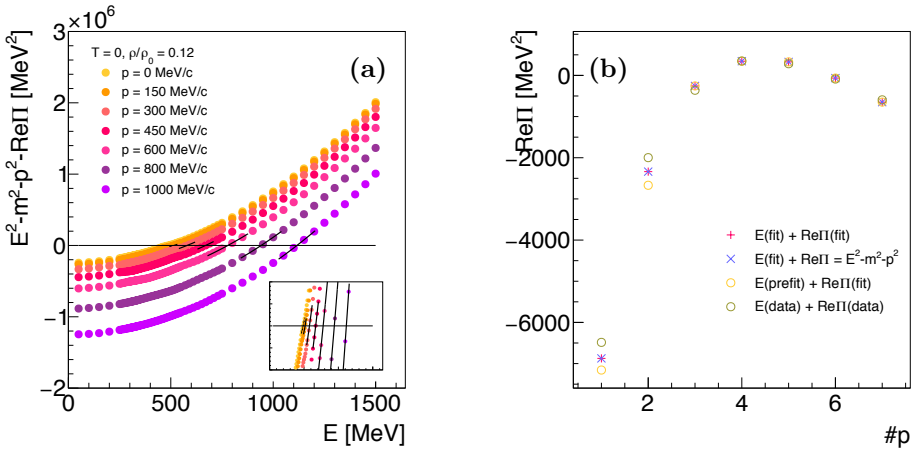

Figure H.7: (a) Relation between $\bar{K}$ energy, mass, momentum and the real part of the self-energy as function of the energy for different antikaon momenta (see legend). Results have been obtained at $T = 0$ and $\rho = 0.12\ \rho_0$, including $(s+p)$-wave contributions. [BCTS19] (b) Real part of the $\bar{K}$ self-energies for the different kaon momenta cases obtained on the basis of different methods (see legend and text for details).

To extract the solution of the dispersion relation (Eq. (H.2)), the relation between $\bar{K}$ energy, mass, momentum and the real part of the self-energy as function of the energy was investigated as presented in Fig. H.7 (a). For this purpose an interactive fitting procedure was applied. In the first step the distributions presented in Fig. H.7 (a) was fitted with a second order polynominal in order to constrain the $\bar{K}$ energy, which gives a exact solution of the dispersion relation. In the next step, the second-order polynominal fit was repeated in a limited region around the expected $\bar{K}$ energy as indicated by the black curves in Fig. H.7. One the basis of second-order polynomial, the real part (Fig. H.8 (a)) and the imaginary part (Fig. H.8 (b)) of the self-energy were retrieved at the expected $\bar{K}$ energy.

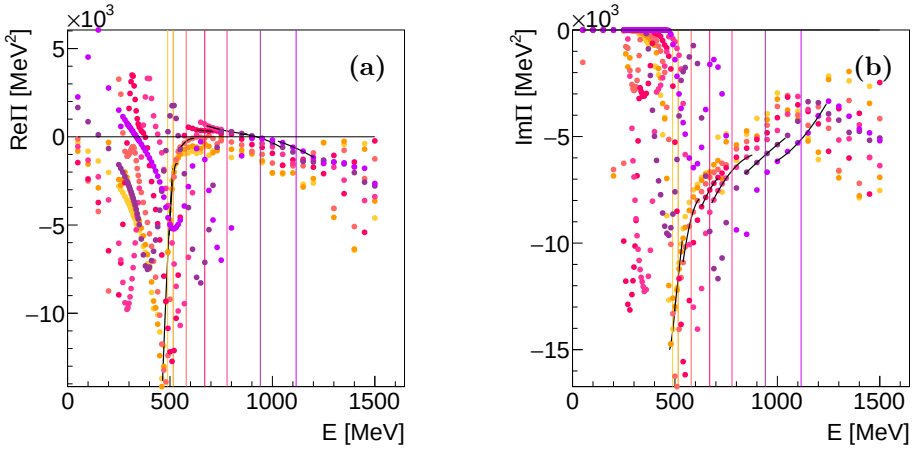

Figure H.8: Real (a) and imaginary (b) parts of the $\bar{K}$ self-energy as functions of the $\bar{K}$ energy for different antikaon momenta (see legend of Fig. H.7). Results have been obtained at $T = 0$ and $\rho = 0.12\ \rho_0$, including $(s + p)$-wave contributions. [BCTS19]

The reliability of this iterative method was confirmed in Fig. H.7 (b). The green points are obtained, if one relies on solely on the data. If one just adapts a second order polynominal to the distributions presented in Fig. H.7 (a) roughly around the expected $\bar{K}$ energy, the yellow points were deduced. Whereas, if one applies the iterative method to the extract the exact $\bar{K}$ energy, the real part of self-energy (pink dagger), which was evaluated at the obtained $\bar{K}$ energy, overlaps with the real part of the self-energy (blue cross), evaluated on the basis of exact solution of the dispersion relation.

The real and imaginary part of $\bar{K}$ self-energy as function of the normalized nuclear density ρ/ρ_0 at $T = 0$ MeV are presented in Fig. H.9 for the different antikaon momenta (see legend of Fig. H.7 (a)). It can be seen, that the real part of the self-energy strongly depends on the density and $\bar{K}$ momentum, whereas for the imaginary part the dependence on the density is stronger.

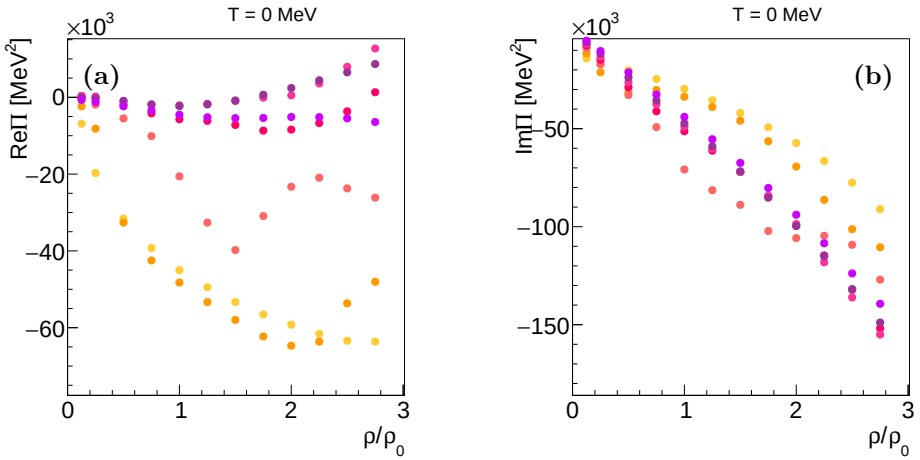

Figure H.9: Real (a) and imaginary (b) parts of the $\bar{K}$ self-energy as function of the normalized nuclear density ρ/ρ_0 for the different antikaon momenta cases (see legend of Fig. H.7). Results have been obtained at $T = 0$ including $(s + p)$-wave contributions.

Further, the $\bar{K}$ effective mass m^* and width Γ within nuclear matter were evaluated on the basis of Eq. (H.3). The corresponding distributions as function of the normalized nuclear density ρ/ρ_0 at $T = 0$ MeV are presented in Fig. H.10 for the different kaon momenta (see legend of Fig. H.7 (a)). Moreover, the real and imaginary part of the potential was deduced on the basis of Eq. (H.4). The implementation of density and temperature dependent potentials in the HSD model is currently ongoing.

$$m^* = \sqrt{m^2 + Re(\Pi)} \qquad \text{and} \qquad \Gamma = \frac{Im(\Pi)}{\sqrt{m^2 + \vec{p}^2}} \tag{H.3}$$

with

m^*/Γ : effective mass and width of $\bar{K}$
$Re(\Pi)/Im(\Pi)$: real and imaginary part of the self-energy in $(s+p)$ wave [MeV^2]
$m/\vec{p}$: $\bar{K}$ nominal mass [MeV/c^2] and momentum [MeV/c]

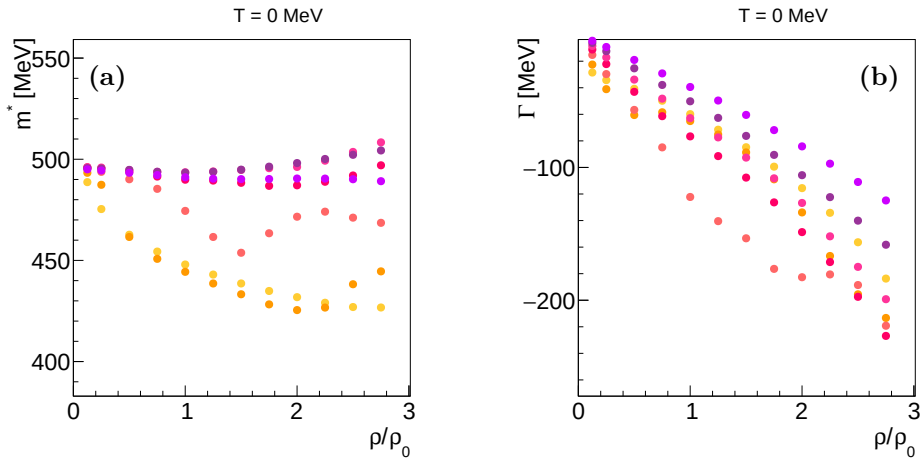

Figure H.10: Effective mass m^* (a) and width Γ (b) of $\bar{K}$ as function of the normalized nuclear density ρ/ρ_0 for the different kaon momenta cases (see legend of Fig. H.7). Results have been obtained at $T = 0$ including $(s+p)$-wave contributions.

$$Re(U)(Im(U)) = \frac{Re(\Pi)(Im(\Pi))}{2\sqrt{m^2 + \vec{p}^2}} \tag{H.4}$$

with

$Re(U)(Im(U))$: real (imaginary) part of the potential
m : nominal mass of $\bar{K}$ ($m = 495.67$ MeV[P$^+$16a])
$\vec{p}$: momentum of $\bar{K}$ in the laboratory frame [MeV]

Bibliography

[A+73] B.W. Allardyce et al.
Pion reaction cross sections and nuclear sizes.
Nuclear Physics A, 209(1):1 – 51, 1973.

[A+02] C. Agodi et al.
The HADES time-of-flight wall.
Nucl. Instrum. Meth. A, 492:14–25, 2002.

[A+07] G. Agakichiev et al.
Dielectron production in ^{12}C+^{12}C collisions at 2 AGeV with HADES.
Phys. Rev. Lett., 98:052302, 2007.

[A+08] G. Agakishiev et al.
Study of dielectron production in C+C collisions at 1 AGeV.
Phys. Lett. B, 663:43–48, 2008.

[A+09a] G. Agakishiev et al.
Deep sub-threshold Ξ^- production in Ar+KCl reactions at 1.76 AGeV.
Phys. Rev. Lett., 103:132301, 2009.

[A+09b] G. Agakishiev et al.
ϕ decay: A relevant source for K^- production at SIS energies?
Phys. Rev. C, 80:025209, 2009.

[A+09c] G. Agakishiev et al.
The High-Acceptance Dielectron Spectrometer HADES.
Eur. Phys. J. A, 41:243–277, 2009.

[A+09d] M. Apollonio et al.
Large-angle production of charged pions with incident pion beams on nuclear targets.
Phys. Rev. C, 80:065207, 2009.

[A+10a] G. Agakishiev et al.
In-Medium Effects on K^0 Mesons in Relativistic Heavy-Ion Collisions.
Phys. Rev. C, 82:044907, 2010.

[A+10b] G. Agakishiev et al.
$\Lambda - p$ femtoscopy in collisions of Ar+KCl at 1.76 AGeV.
Phys. Rev. C, 82:021901, 2010.

[A+10c] G. Agakishiev et al.
Origin of the low-mass electron pair excess in light nucleus-nucleus collisions.
Phys. Lett. B, 690:118–122, 2010.

[A+11a] G. Agakishiev et al.
Dielectron production in Ar+KCl collisions at 1.76 AGeV.
Phys. Rev. C, 84:014902, 2011.

[A+11b] G. Agakishiev et al.
Hyperon production in Ar+KCl collisions at 1.76 AGeV.
Eur. Phys. J., A47:21, 2011.

[A+12a] G. Aad et al.

Observation of a new particle in the search for the Standard Model Higgs boson with the ATLAS detector at the LHC.
Phys. Lett. B, 716(1):1 – 29, 2012.

[A+12b] G. Agakishiev et al.
Baryonic resonances close to the $\overline{K}n$ threshold: The case of $\Sigma(1385)^+$ in pp collisions.
Phys. Rev. C, 85:035203, 2012.

[A+12c] G. Agakishiev et al.
First measurement of proton-induced low-momentum dielectron radiation off cold nuclear matter.
Phys. Lett. B, 715:304–309, 2012.

[A+12d] G. Agakishiev et al.
Inclusive dielectron production in $p + p$ collisions at 2.2 GeV beam energy.
Phys. Rev. C, 85:054005, 2012.

[A+12e] G. Agakishiev et al.
Inclusive dielectron spectra in $p + p$ collisions at 3.5 GeV.
Eur. Phys. J., A48:64, 2012.

[A+13a] G. Agakishiev et al.
Baryonic resonances close to the $\overline{K}n$ threshold: The case of $\Lambda(1405)$ in pp collisions.
Phys. Rev. C, 87:025201, 2013.

[A+13b] G. Agakishiev et al.
Deep sub-threshold $K^*(892)^0$ production in collisions of Ar + KCl at 1.76 AGeV.
Eur. Phys. J., A49:34, 2013.

[A+13c] G. Agakishiev et al.
Inclusive pion and η production in $p + \mathrm{Nb}$ collisions at 3.5 GeV beam energy.
Phys. Rev. C, 88(2):024904, 2013.

[A+14a] G. Agakishiev et al.
Associate K^0 production in $p + p$ collisions at 3.5 GeV: The role of $\Delta(1232)^{++}$.
Phys. Rev. C, 90:015202, 2014.

[A+14b] G. Agakishiev et al.
Baryon resonance production and dielectron decays in $p + p$ collisions at 3.5 GeV.
Eur. Phys. J., A50:82, 2014.

[A+14c] G. Agakishiev et al.
Λ hyperon production and polarization in collisions of p(3.5 GeV)+Nb.
Eur. Phys. J., A50:81, 2014.

[A+14d] G. Agakishiev et al.
Medium effects in proton-induced K^0 production at 3.5 GeV.
Phys. Rev. C, 90:054906, 2014.

[A+15a] B. B. Abelev et al.
$K^*(892)^0$ and $\phi(1020)$ production in Pb-Pb collisions at $\sqrt{s_{NN}} = 2.76$ TeV.
Phys. Rev. C, 91:024609, 2015.

[A+15b] G. Agakishiev et al.
Analysis of pion production data measured by HADES in $p+p$ collisions at 1.25 GeV.
Eur. Phys. J., A51(10):137, 2015.

[A+15c] G. Agakishiev et al.
K*(892)$^+$ production in $p + p$ collisions at $E_{beam} = 3.5$ GeV.
Phys. Rev. C, 92(2):024903, 2015.

[A+15d] G. Agakishiev et al.
Partial Wave Analysis of the Reaction $p(3.5\ \mathrm{GeV}) + p \to pK^+\Lambda$ to Search for the

"ppK^-" Bound State.
Phys. Lett. B, 742:242–248, 2015.

[A+15e] G. Agakishiev et al.
Subthreshold Ξ Production in Collisions of p(3.5 GeV)+Nb.
Phys. Rev. Lett., 114:212301, 2015.

[A+19a] S. Acharya et al.
$p-p$, $p-\Lambda$ and Λ-Λ correlations studied via femtoscopy in pp reactions at $\sqrt{s} = 7$ TeV.
Phys. Rev. C, 99(2):024001, 2019.

[A+19b] S. Ajimura et al.
"K^-pp", a $\overline{K}$-Meson Nuclear Bound State, Observed in ^{3}He$(K^-, \Lambda p)n$ Reactions.
Phys. Lett. B, 789:620–625, 2019.

[AEF+06] Y. Aoki, G. Endrodi, Z. Fodor, S. D. Katz, and K. K. Szabo.
The order of the quantum chromodynamics transition predicted by the standard model of particle physics.
Nature, 443:675–678, 2006.

[Aic91] J. Aichelin.
Quantum molecular dynamics dynamical microscopic n-body approach to investigate fragment formation and the nuclear equation of state in heavy ion collisions.
Physics Reports, 202(5):233 – 360, 1991.

[AM+16] J. Adamczewski-Musch et al.
The Λp interaction studied via femtoscopy in $p+$Nb reactions at $\sqrt{s_{NN}} = 3.18$ GeV.
Phys. Rev. C, 94(2):025201, 2016.

[AM+17a] J. Adamczewski-Musch et al.
A facility for pion-induced nuclear reaction studies with HADES.
Eur. Phys. J. A, 53(9):188, 2017.

[AM+17b] J. Adamczewski-Musch et al.
$\Delta(1232)$ Dalitz decay in $p+p$ collisions at $T = 1.25$ GeV measured with HADES at GSI.
Phys. Rev. C, 95(6):065205, 2017.

[AM+17c] J. Adamczewski-Musch et al.
Inclusive Λ production in $p+p$ collisions at 3.5 GeV.
Phys. Rev. C, 95(1):015207, 2017.

[AM+18a] J. Adamczewski-Musch et al.
Deep sub-threshold ϕ production in Au+Au collisions.
Phys. Lett. B, 778:403–407, 2018.

[AM+18b] J. Adamczewski-Musch et al.
Σ^0 production in proton-nucleus collisions near threshold.
Phys. Lett. B, 781:735–740, 2018.

[AM+19a] J. Adamczewski-Musch et al.
Probing dense baryon-rich matter with virtual photons.
Nature Physics, 2019.

[AM+19b] J. Adamczewski-Musch et al.
Strong absorption of hadrons with hidden and open strangeness in nuclear matter.
Phys. Rev. Lett., 123(2):022002, 2019.

[AM+19c] J. Adamczewski-Musch et al.
Sub-threshold production of K^0_s mesons and Λ hyperons in Au+Au collisions at $\sqrt{s_{NN}} = 2.4$ GeV.

Phys. Lett. B, 793:457–463, 2019.

[AS60] V. A. Ambartsumyan and G. S. Saakyan.
The Degenerate Superdense Gas of Elementary Particles.
Sov. Astron., 4:187, 1960.

[B+75] H.-J. Behrend et al.
Photoproduction of ϕ-mesons at small t-values.
Phys. Lett. B, 56(4):408 – 412, 1975.

[B+97] R. Barth et al.
Subthreshold production of kaons and antikaons in nucleus-nucleus collisions at equivalent beam energies.
Phys. Rev. Lett., 78:4007–4010, 1997.

[B+98] S. A. Bass et al.
Microscopic models for ultrarelativistic heavy ion collisions.
Prog. Part. Nucl. Phys., 41:255–369, 1998.

[B+99a] S. Bart et al.
Σ hyperons in the nucleus.
Phys. Rev. Lett., 83:5238–5241, 1999.

[B+99b] M. Bleicher et al.
Relativistic hadron hadron collisions in the ultrarelativistic quantum molecular dynamics model.
J. Phys. G, 25:1859–1896, 1999.

[B+01] F. Balestra et al.
ϕ and ω meson production in pp reactions at $p_{\mathrm{lab}} = 3.67$ GeV/c.
Phys. Rev. C, 63:024004, 2001.

[B+04] Markus Buescher et al.
Inclusive K^+ meson production in proton-nucleus interactions.
Eur. Phys. J., A22:301–317, 2004.

[B+09a] M. Bazzi et al.
Kaonic helium-4 X-ray measurement in SIDDHARTA.
Phys. Lett. B, 681:310–314, 2009.

[B+09b] D. Belver et al.
The HADES RPC inner TOF wall.
Nucl. Instrum. Meth. A, 602(3):687 – 690, 2009.

[B+09c] M. L. Benabderrahmane et al.
Measurement of the in-medium K^0 inclusive cross section in pi^--induced reactions at 1.15 GeV/c.
Phys. Rev. Lett., 102:182501, 2009.

[B+11a] M. Bazzi et al.
A New Measurement of Kaonic Hydrogen X-rays.
Phys. Lett. B, 704:113–117, 2011.

[B+11b] M. Bazzi et al.
First measurement of kaonic helium-3 X-rays.
Phys. Lett. B, 697:199–202, 2011.

[Bac70] G Backenstoss.
Pionic atoms.
Annual Review of Nuclear Science, 20(1):467–508, 1970.

[Bat01] G. Battistoni.
Atmospheric neutrino flux calculations.

Nuclear Physics B - Proceedings Supplements, 100(1):101 – 106, 2001.

[BCTS19] E. L. Bratkovskaya, D. Cabrera, L. Tolós, and T. Song.
Private communication.
2018/2019.

[BG88] G.F. Bertsch and S. Das Gupta.
A guide to microscopic models for intermediate energy heavy ion collisions.
Physics Reports, 160(4):189 – 233, 1988.

[BG06] M. Bonesini and A. Guglielmi.
Hadroproduction experiments for precise neutrino beam calculations.
Physics Reports, 433(2):65 – 126, 2006.

[BGG+12] O. Buss, T. Gaitanos, K. Gallmeister, H. van Hees, M. Kaskulov, O. Lalakulich, A. B. Larionov, T. Leitner, J. Weil, and U. Mosel.
Transport-theoretical Description of Nuclear Reactions.
Phys. Rept., 512:1–124, 2012.

[BLR+98] G. E. Brown, G.-Q. Li, R. Rapp, M. Rho, and J. Wambach.
Medium dependence of the vector meson mass: Dynamical and/or Brown-Rho scaling?
Acta Phys. Polon., B29:2309–2321, 1998.

[Boe15] F. Boehmer.
Development of a GEM-based TPC for the Measurement of In-Medium Signatures in Kaon Momenta in a Combined Setup at FOPI.
PhD thesis, Technische Universität München, 2015.

[BTKR92] G. E. Brown, V. Thorsson, K. Kubodera, and M. Rho.
A Novel mechanism for kaon condensation in neutron star matter.
Phys. Lett. B, 291:355–362, 1992.

[C+06] F. Crawford et al.
A Survey of 56 Mid-latitude EGRET Error Boxes for Radio Pulsars.
Astrophys. J., 652:1499–1507, 2006.

[C+12] S. Chatrchyan et al.
Observation of a new boson at a mass of 125 GeV with the CMS experiment at the LHC.
Phys. Lett. B, 716(1):30 – 61, 2012.

[C+17] D. Cabrera et al.
ϕ meson transparency in nuclei from ϕN resonant interactions.
Phys. Rev. C, 96(3):034618, 2017.

[CB99] W. Cassing and E. L. Bratkovskaya.
Hadronic and electromagnetic probes of hot and dense nuclear matter.
Phys. Rept., 308:65–233, 1999.

[CBM+97] W. Cassing, E. L. Bratkovskaya, U. Mosel, S. Teis, and A. Sibirtsev.
Kaon versus anti-kaon production at SIS energies.
Nucl. Phys. A, 614:415–432, 1997.

[CHBVV17] D. Cabrera, A. N. Hiller Blin, and M. J. Vicente Vacas.
ϕ meson self-energy in nuclear matter from ϕN resonant interactions.
Phys. Rev. C, 95:015201, 2017.

[CRO+04] D. Cabrera, L. Roca, E. Oset, H. Toki, and M. J. Vicente Vacas.
Mass dependence of inclusive nuclear ϕ photoproduction.
Nucl. Phys. A, 733:130–141, 2004.

[CTAB14] D. Cabrera, L. Tolós, J. Aichelin, and E. Bratkovskaya.

Antistrange meson-baryon interaction in hot and dense nuclear matter.
Phys. Rev. C, 90:055207, 2014.

[D+75] C. J. S. Damerell et al.
K^+n Elastic and Charge Exchange Scattering Between 430 MeV/c and 940 MeV/c.
Nucl. Phys. B, 94:374–412, 1975.

[D+02] J. Diaz et al.
Design and commissioning of the GSI pion beam.
Nucl. Instr. and Meth., A478:511–526, 2002.

[D+10] P. Demorest et al.
Shapiro Delay Measurement of A Two Solar Mass Neutron Star.
Nature, 467:1081–1083, 2010.

[DBdT16] A. Deur, S. J. Brodsky, and G. F. de Teramond.
The QCD Running Coupling.
Prog. Part. Nucl. Phys., 90:1–74, 2016.

[DMGD91] C. B. Dover, D. J. Millener, A. Gal, and D. H. Davis.
Interpretation of a double hypernucleus event.
Phys. Rev. C, 44:1905–1909, 1991.

[DSW10] H. Djapo, B.-J. Schaefer, and J. Wambach.
On the appearance of hyperons in neutron stars.
Phys. Rev. C, 81:035803, 2010.

[Eff99] M. Effenberger.
Eigenschaften von Hadronen in Kernmaterie in einem vereinheitlichten Transportmodell.
PhD thesis, Justus-Liebig-Universität Gießen, 1999.

[EP95] S. V. Efremov and E. Ya. Paryev.
Subthreshold K^- production in pion nucleus reactions.
Z. Phys., A351:447–452, 1995.

[EYHK15] Paryev E. Ya, M. Hartmann, and Yu. T. Kiselev.
Non-resonant kaon pair production and medium effects in proton–nucleus collisions.
Journal of Physics G: Nuclear and Particle Physics, 42(7):075107, 2015.

[F+07] I. Fröhlich et al.
Pluto: A Monte Carlo Simulation Tool for Hadronic Physics.
PoS, ACAT:076, 2007.

[FG07] E. Friedman and A. Gal.
In-medium nuclear interactions of low-energy hadrons.
Physics Reports, 452(4):89 – 153, 2007.

[FGB93] E. Friedman, A. Gal, and C.J. Batty.
Density dependence in kaonic atoms.
Phys. Lett. B, 308(1):6 – 10, 1993.

[FGH+10] I. Fröhlich, T. Galatyuk, R. Holzmann, J. Markert, B. Ramstein, P. Salabura, and J. Stroth.
Design of the Pluto Event Generator.
J. Phys. Conf. Ser., 219:032039, 2010.

[FH11] K. Fukushima and T. Hatsuda.
The phase diagram of dense QCD.
Rept. Prog. Phys., 74:014001, 2011.

[Fuc06] Christian Fuchs.
Kaon production in heavy ion reactions at intermediate energies.

Prog. Part. Nucl. Phys., 56:1–103, 2006.

[G+16] P. Gasik et al.
Strange meson production in Al+Al collisions at 1.9 AGeV.
Eur. Phys. J., A52(6):177, 2016.

[GA12] N. Gupta and P. Arumugam.
Role of higher order couplings in the presence of kaons in relativistic mean field description of neutron stars.
Phys. Rev. C, 85:015804, 2012.

[GMOR68] M. Gell-Mann, R. J. Oakes, and B. Renner.
Behavior of Current Divergences under $SU_3 \times SU_3$.
Phys. Rev., 175:2195–2199, 1968.

[GSLB14] G. Graef, J. Steinheimer, F. Li, and M. Bleicher.
Deep sub-threshold Ξ and Λ production in nuclear collisions with the UrQMD transport model.
Phys. Rev. C, 90:064909, 2014.

[GW15] Philipp Gubler and Wolfram Weise.
Moments of ϕ meson spectral functions in vacuum and nuclear matter.
Phys. Lett. B, 751:396–401, 2015.

[H+89] R. S. Hayano et al.
Evidence for a bound state of the ${}^{4}_{\Lambda}$He hypernucleus.
Phys. Lett. B, 231(4):355 – 358, 1989.

[H+06] M. Hartmann et al.
Near-Threshold Production of ϕ Mesons in pp Collisions.
Phys. Rev. Lett., 96:242301, 2006.

[H+12] M. Hartmann et al.
Momentum dependence of the ϕ meson nuclear transparency.
Phys. Rev. C, 85:035206, 2012.

[HADa] HADES.
Superconducting toroidal magnet of HADES.
https://www-hades.gsi.de/?q=node/17
accessed on 20-Jun-2019.

[HADb] HADES.
The HADES simulation package HGeant.
https://www-hades.gsi.de/?q=computing
accessed on 20-Jun-2019.

[Hig64] Peter W. Higgs.
Broken symmetries and the masses of gauge bosons.
Phys. Rev. Lett., 13:508–509, 1964.

[HJ12] T. Hyodo and D. Jido.
The nature of the $\Lambda(1405)$ resonance in chiral dynamics.
Prog. Part. Nucl. Phys., 67:55–98, 2012.

[HOA03] Ch. Hartnack, H. Oeschler, and J. Aichelin.
What Determines the K^- Multiplicity at Energies Around $(1-2)$ AGeV?
Phys. Rev. Lett., 90:102302, 2003.

[HOL+12] Ch. Hartnack, H. Oeschler, Y. Leifels, E. L. Bratkovskaya, and J. Aichelin.
Strangeness Production close to Threshold in Proton-Nucleus and Heavy-Ion Collisions.
Phys. Rept., 510:119–200, 2012.

[HPK+13] J. Haidenbauer, S. Petschauer, N. Kaiser, U. G. Meissner, A. Nogga, and W. Weise.
Hyperon-nucleon interaction at next-to-leading order in chiral effective field theory.
Nucl. Phys. A, 915:24–58, 2013.

[HR62] W. E. Humphrey and R. R. Ross.
Low-energy interactions of K^- mesons in hydrogen.
Phys. Rev., 127:1305–1323, 1962.

[HTB+17] M. Hanauske, K. Takami, L. Bovard, L. Rezzolla, J. A. Font, A. Galeazzi, and H. Stöcker.
Rotational properties of hypermassive neutron stars from binary mergers.
Phys. Rev. D, 96:043004, 2017.

[I+05] T. Ishikawa et al.
ϕ photo-production from Li, C, Al, and Cu nuclei at $E(\gamma) = 1.5$ GeV to 2.4 GeV.
Phys. Lett. B, 608:215–222, 2005.

[IHW11] Y. Ikeda, T. Hyodo, and W.Weise.
Improved constraints on chiral SU(3) dynamics from kaonic hydrogen.
Phys. Lett. B, 706(1):63 – 67, 2011.

[IHW12] Y. Ikeda, T. Hyodo, and W. Weise.
Chiral SU(3) theory of antikaon-nucleon interactions with improved threshold constraints.
Nucl. Phys. A, 881:98–114, 2012.

[Iiz66] J. Iizuka.
A Systematics and Phenomenology of Meson Family.
Prog. Theor. Phys. Suppl., 37-38:21–34, 1966.

[KBD+70] P. A. Katz, K. Bunnell, M. Derrick, T. Fields, L. G. Hyman, and G. Keyes.
Reactions of stopping K^- in helium.
Phys. Rev. D, 1:1267–1276, 1970.

[KH97] Y. Koike and A. Hayashigaki.
QCD Sum Rules for ρ, ω, ϕ Meson-Nucleon Scattering Lengths and the Mass Shifts in Nuclear Medium.
Progress of Theoretical Physics, 98(3):631–652, 1997.

[KLW90] S. Klimt, M. Lutz, and W. Weise.
Chiral phase transition in the SU(3) Nambu and Jona-Lasinio model.
Phys. Lett. B, 249(3):386 – 390, 1990.

[KMM09] M. Kotulla, V. Meta, and U. Mosel.
Hadronen im Medium.
Physik Journal, 8(3):41–46, 2009.

[KN86] D. B. Kaplan and A. E. Nelson.
Strange Goings on in Dense Nucleonic Matter.
Phys. Lett. B, 175:57–63, 1986.

[L+99] F. Laue et al.
Medium effects in kaon and antikaon production in nuclear collisions at subthreshold beam energies.
Phys. Rev. Lett., 82:1640–1643, 1999.

[LMOP47] C. M. G. Lattes, H. Muirhead, G. P. S. Occhialini, and C. F. Powell.
Processes involving charged mesons.
Nature, 159(4047):694–697, 1947.

[M+17] J. Michel et al.
Electronics for the RICH detectors of the HADES and CBM experiments.

Journal of Instrumentation, 12(01):C01072–C01072, 2017.

[Mau19] S. Maurus.
Λ and K_s^0 Production in Pion-Nucleus Reactions at 1.7 GeV/c.
PhD thesis, Technische Universität München, 2019.

[MDG88] D. J. Millener, C. B. Dover, and A. Gal.
Λ-nucleus single-particle potentials.
Phys. Rev. C, 38:2700–2708, 1988.

[MFG+03] P. Mühlich, T. Falter, C. Greiner, J. Lehr, M. Post, and U. Mosel.
Photoproduction of ϕ mesons from nuclei.
Phys. Rev. C, 67:024605, 2003.

[MFGJ95] J. Mares, E. Friedman, A. Gal, and B. K. Jennings.
Constraints on Σ nucleus dynamics from Dirac phenomenology of Σ-atoms.
Nucl. Phys. A, 594:311–324, 1995.

[MM06] P. Mühlich and U. Mosel.
Attenuation of ϕ mesons in $\gamma + A$ reactions.
Nucl. Phys. A, 765:188–196, 2006.

[MNP17] V. Metag, M. Nanova, and E. Ya. Paryev.
Meson–nucleus potentials and the search for meson–nucleus bound states.
Prog. Part. Nucl. Phys., 97:199–260, 2017.

[MRO05] V. K. Magas, L. Roca, and E. Oset.
ϕ meson width in the medium from proton induced ϕ production in nuclei.
Phys. Rev. C, 71:065202, 2005.

[MS88] O. Madelung and H. Schopper, editors.
Numerical Data and Functional Relationships in Science and Technology, volume 12A of *Landolt-Boernstein - New Series - Group I Nuclear and Particle Physics.*
Springer, 1988.

[N+78] R. J. Nowak et al.
Charged Σ hyperon production by K^- meson interactions at rest.
Nuclear Physics B, 139(1):61 – 71, 1978.

[N+98] T. Nagae et al.
Observation of a ${}^{4}_{\Sigma}$He Bound State in the ^{4}He(K^-,π^-) Reaction at 600 MeV/c.
Phys. Rev. Lett., 80:1605–1609, 1998.

[N+15] K. Nakazawa et al.
The first evidence of a deeply bound state of ${}^{14}_{\Xi^-}$N system.
Progress of Theoretical and Experimental Physics, 2015(3), 2015.

[NAS87] Bo Nilsson-Almqvist and Evert Stenlund.
Interactions between hadrons and nuclei: The Lund Monte Carlo - FRITIOF version 1.6.
Computer Physics Communications, 43(3):387 – 397, 1987.

[NK87] A. E. Nelson and D. B. Kaplan.
Strange condensate realignment in relativistic heavy-ion collisions.
Phys. Lett. B, 192(1):193 – 197, 1987.

[Oku77] S. Okubo.
Consequences of quark-line (Okubo-Zweig-Iizuka) rule.
Phys. Rev. D, 16:2336–2352, 1977.

[OP47] G. P. S. Occhialini and C. F. Powell.
Nuclear disintegrations produced by slow charged particles of small mass.
Nature, 159(4032):186–190, 1947.

[OV39] J. R. Oppenheimer and G. M. Volkoff.
On massive neutron cores.
Phys. Rev., 55:374–381, 1939.

[OVTR01] E. Oset, M. J. Vicente Vacas, H. Toki, and A. Ramos.
Test of ϕ renormalization in nuclei through ϕ photoproduction.
Phys. Lett. B, 508(3):237 – 242, 2001.

[P+11] A. Polyanskiy et al.
Measurement of the in-medium ϕ meson width in proton-nucleus collisions.
Phys. Lett. B, 695:74–77, 2011.

[P+16a] C. Patrignani et al.
Review of Particle Physics.
Chin. Phys., C40(10):100001, 2016.

[P+16b] K. Piasecki et al.
Centrality dependence of subthreshold ϕ meson production in Ni + Ni collisions at 1.9 AGeV.
Phys. Rev. C, 94(1):014901, 2016.

[P+18] K. Piscicchia et al.
First measurement of the $K^- n \to \Lambda\pi^-$ non-resonant transition amplitude below threshold.
Phys. Lett. B, 782:339 – 345, 2018.

[Par05] E. Ya. Paryev.
Subthreshold ϕ meson production and medium effects in proton nucleus reactions.
Eur. Phys. J., A23:453–471, 2005.

[Par09] E. Ya. Paryev.
Near-threshold ϕ meson production in proton-nucleus reactions and ϕ width in finite nuclei.
J. Phys., G36:015103, 2009.

[Par18] E. Ya. Paryev.
Momentum dependence of pion-induced ϕ meson production on nuclei near threshold.
Chin. Phys., C42(8):084101, 2018.

[Per47] D. H. Perkins.
Nuclear disintegration by meson capture.
Nature, 159(4030):126–127, 1947.

[PWC16] K. Piscicchia, S. Wycech, and C. Curceanu.
On the $K^{-4}He \to \Lambda\pi^{-3}He$ resonant and non-resonant processes.
Nucl. Phys. A, 954:75–93, 2016.

[R+07] W. Reisdorf et al.
Systematics of pion emission in heavy-ion collisions in the 1 AGeV regime.
Nucl. Phys. A, 781:459–508, 2007.

[RBW05] Th. Roth, M. Buballa, and J. Wambach.
Medium modifications of antikaons in dense matter.
2005.

[RCJ+05] Z. Rudy, W. Cassing, L. Jarczyk, B. Kamys, A. Kowalczyk, and P. Kulessa.
Transport analysis of K^+ production in proton-nucleus reactions.
The European Physical Journal A - Hadrons and Nuclei, 23(3):379–385, 2005.

[RSBW01] A. Ramos, J. Schaffner-Bielich, and J. Wambach.
Kaon condensation in neutron stars.
Lect. Notes Phys., 578:175–202, 2001.

[S+94] A. Schröter et al.
Subthreshold antiproton and K^- production in heavy ion collisions.
Zeitschrift für Physik A Hadrons and Nuclei, 350(2):101–113, 1994.

[S+96] P. Senger et al.
Kaon production in relativistic nucleus-nucleus collisions.
Acta Phys. Pol. B, 21:2993–3004, 1996.

[S+97] J. Schaffner et al.
In-medium production of kaons at the mean field level.
Nucl. Phys. A, 625:325–346, 1997.

[S+04] K. Suzuki et al.
Precision spectroscopy of pionic 1s states of Sn nuclei and evidence for partial restoration of chiral symmetry in the nuclear medium.
Phys. Rev. Lett., 92:072302, 2004.

[Sal18] P. Salabura.
Private communication.
2018.

[SB16] J. Steinheimer and M. Bleicher.
Sub-threshold ϕ and Ξ^- production by high mass resonances with UrQMD.
J. Phys., G43:015104, 2016.

[Sch03] Stefan Scherer.
Introduction to chiral perturbation theory.
Adv. Nucl. Phys., 27:277, 2003.

[Sch08a] H. Schopper, editor.
Physics and Methods. Theory and Experiments, volume 21A of *Landolt-Boernstein - Group I Elementary Particles, Nuclei and Atoms.*
Springer, 2008.

[Sch08b] H. Schopper, editor.
Physics and Methods. Theory and Experiments, volume 21B of *Landolt-Boernstein - Group I Elementary Particles, Nuclei and Atoms.*
Springer, 2008.

[Sch16] H. Schuldes.
Charged Kaon and ϕ Reconstruction in Au+Au Collisions at 1.23 AGeV.
PhD thesis, Johann Wolfgang Goethe-Universität, 2016.

[Sch17] T. Scheib.
Λ and K_s^0 Production in Au+Au Collisions at 1.23 AGeV .
PhD thesis, Johann Wolfgang Goethe-Universität, 2017.

[SCK97] A. A. Sibirtsev, W. Cassing, and C. M. Ko.
Anti-Kaon production in nucleon-nucleon reactions near threshold.
Z. Phys., A358:101–106, 1997.

[SCM97] A. Sibirtsev, W. Cassing, and U. Mosel.
Heavy meson production in proton-nucleus reactions with empirical spectral functions.
Z. Phys., A358:357–367, 1997.

[SMS06] T. Sjostrand, S. Mrenna, and P. Z. Skands.
PYTHIA 6.4 Physics and Manual.
JHEP, 05:026, 2006.

[SMS08] T. Sjostrand, S. Mrenna, and P. Z. Skands.
A Brief Introduction to PYTHIA 8.1.

Comput. Phys. Commun., 178:852–867, 2008.

[SSO+19] V. Steinberg, J. Staudenmaier, D. Oliinychenko, F. Li, Ö. Erkiner, and H. Elfner.
Strangeness production via resonances in heavy-ion collisions at energies available at the GSI Schwerionensynchrotron.
Phys. Rev. C, 99(6):064908, 2019.

[TCR08] L. Tolós, D. Cabrera, and A. Ramos.
Strange mesons in nuclear matter at finite temperature.
Phys. Rev. C, 78:045205, 2008.

[THF94] K. Tsushima, S.W. Huang, and Amand Faessler.
The role of the $\Delta(1920)$ resonance for kaon production in heavy-ion collisions.
Phys. Lett. B, 337(3):245 – 253, 1994.

[THF97] K. Tsushima, S. W. Huang, and Amand Faessler.
A Study of the $\pi B \to YK$ reactions for kaon production in heavy ion collisions.
Austral. J. Phys., 50:35–43, 1997.

[TNDO07] A. I. Titov, T. Nakano, S. Daté, and Y. Ohashi.
Differential cross section of ϕ-meson photoproduction at threshold.
Phys. Rev. C, 76:048202, 2007.

[Tol39] Richard C. Tolman.
Static solutions of einstein's field equations for spheres of fluid.
Phys. Rev., 55:364–373, 1939.

[TRO06] L. Tolós, A. Ramos, and E. Oset.
Chiral approach to antikaon s- and p-wave interactions in dense nuclear matter.
Phys. Rev. C, 74:015203, 2006.

[TSTL99] K. Tsushima, A. Sibirtsev, A. W. Thomas, and G. Q. Li.
Resonance model study of kaon production in baryon-baryon reactions for heavy-ion collisions.
Phys. Rev. C, 59:369–387, 1999.

[VD+16] O. Vázquez Doce et al.
K^- absorption on two nucleons and ppK^- bound state search in the Σ^0p final state.
Phys. Lett. B, 758:134–139, 2016.

[W+10] M. H. Wood et al.
Absorption of the ω and ϕ Mesons in Nuclei.
Phys. Rev. Lett., 105:112301, 2010.

[W+16] J. Weil et al.
Particle production and equilibrium properties within a new hadron transport approach for heavy-ion collisions.
Phys. Rev. C, 94(5):054905, 2016.

[Wad13] M. Wada.
$\phi(1020)$ and $\omega(782)$ mesons from dielectron decays at STAR.
Nucl. Phys. A, 904-905:1019c–1022c, 2013.

[WCSB12] S. Weissenborn, D. Chatterjee, and J. Schaffner-Bielich.
Hyperons and massive neutron stars: the role of hyperon potentials.
Nucl. Phys. A, 881:62–77, 2012.

[WKW96a] T. Waas, N. Kaiser, and W. Weise.
Effective kaon masses in dense nuclear and neutron matter.
Phys. Lett. B, 379:34 – 38, 1996.

[WKW96b] T. Waas, N. Kaiser, and W. Weise.
Low energy KN interaction in nuclear matter.

Phys. Lett. B, 365(1):12 – 16, 1996.

[Yuk35] H. Yukawa.
On the Interaction of Elementary Particles I.
Proc. Phys. Math. Soc. Jap., 17:48–57, 1935.

[ZG96] C. Zeitnitz and T.A. Gabriel.
The GEANT–CALOR Interface User's Guide.
ORNL, 1996.

[Zin16] V. Zinyuk.
Systematic Study of Strangeness Production and Dynamic Behaviour with the FOPI Experiment at SIS-18.
PhD thesis, Ruprecht-Karls-Universität Heidelberg, 2016.

[Zwe64] G Zweig.
An SU_3 model for strong interaction symmetry and its breaking.
CERN-TH-412, page 80, 1964.

Danksagung

Hiermit möchte ich mich bei allen bedanken, die mich in der vergangenen Zeit unterstützt haben. Ganz besonders danke ich Laura Fabbietti, die es mir schon seit meiner Bachelorarbeit ermöglicht hat an diesem spannenden Projekt mitzuwirken. Sie hat mich während meiner ganzen Zeit in ihrer Gruppe gefördert und unterstützt. Dies hat es mir ermöglicht über meine Grenzen hinaus zu wachsen und vorallem habe ich gelernt eigenständig zu Arbeiten. Insbesondere möchte ich ihr dafür danken, dass sie mir die Teilnahme an Konferenzen und Treffen mit Fachleuten ermöglicht hat. Ich habe nicht nur meine Präsentationsfähigkeit verbessert, sondern auch mein physikalisches Wissen erweitert. Darüber hinaus möchte ich ihr für die ausgezeichnete Vorlesung über Hadronenphysik danken, die einen enormen Beitrag zu meinem Verständnis geleistet hat. Vielen Dank auch für deine italienischen Kochkünste und den jährlichen Ausflug zur Wiesn und zum Christkindlmarkt!

Ebenso möchte ich mich ganz herzlich bei Volker Metag und Jürgen Friese bedanken, die meine Fragen stets ausführlich beantwortet haben und mir in zahlreichen Diskussionen neue Einblicke in physikalische Zusammenhängen ermöglicht haben. Auch der gesamten HADES Kollaboration, u.a. Manuel Lorenz, Georgy Kornakov, Tetyana Galatyuk, Jochen Markert, Romain Holzmann, Piotr Salabura, Pavel Tlusty, Wolfgang und Ilse König um nur ein paar Namen zu nennen, möchte ich herzlich für die stets freundliche und produktive Atmosphäre danken.

Vielen Dank auch an Marcus Bleicher, Jan Steinheimer, Hannah Elfner, Vincent Steinberg, Jan Staudenmaier und Theodorus Gaitanos für die hilfreichen Diskussionen im Hinblick auf die Beschreibung unserer Daten mit den theoretischen Modellen. Ein großer Dank gilt auch Elena Bratkovskaya, Jörg Aichelin, Laura Tolós und Taesoo Song für die gute Zusammenarbeit bei der Implementierung von Strangeness-Austauschprozessen in (P)HSD. Weiterer Dank gebührt Eduard Paryev für das Bereitstellen der theoretischen Beschreibung der Absorption von ϕ Mesonen.

Meinen Mitstreitern Dimitar, Andi und Berni möchte ich für die schöne und witzige Zeit im Büro sowie auf Dienstreisen Danke sagen. Großer Dank gilt auch Vale und Ante, die jeder Zeit meine Fragen, besonders "theoretische" Natur, mit Hingabe beantworten haben. Ein großes Dankeschön richtet sich auch an Petra, Ralf, Sissy und Sigrid, die mir stets mit Rat und Tat zur Seite standen. Die vielen Gespräche bei einem Tee oder anderen prikelnden Getänken habe ich stets genossen. In diesem Zusammenhang möchte ich mich bei Lukas nicht nur für die Teepausen, sondern Ausflüge zum Bierladen, Japaner und Augustiner, bedanken. Spezieller Dank gebührt auch meine ehemaligen Bürokollegen Tobias, Dominik und Rafal für die spannende Zeit, die unzähligen Gespräche und das Teamwork. Ich möchte mich auch bei allen bedanken, die im Laufe der Arbeit meinen Weg gekreuzt haben, insbesondere Jia-Chii, Martin, Oli und Ludwig, sowie allen E12ern und KTAlern. Ich bin dankbar, dass ich mit so sympathischen Menschen zusammen arbeiten darf. Ihr seit mir im Laufe der Jahre sehr ans Herz gewachsen.

Der allergrößte Dank gilt natürlich meinem Freund, Steffen, für die grenzenlose Unterstützung. Ich bin enorm dankbar dafür, dass wir diesen Weg gemeinsam bestreiten konnten, und freue mich auf neue gemeinsame Herausforderungen.

Letztlich möchte ich meinen Eltern Karin und Uwe, meinem Bruder Jannik, meiner Oma Victoria danken. Sie haben mich während meines gesamten Studiums unterstützt und mir immer vermittelt, dass ich stets auf sie zählen kann!

"In between goals is a thing called life, that has to be lived and enjoyed."

(Sid Caesar)